

**A Thesis Submitted for the Degree of PhD at the University of Warwick**

**Permanent WRAP URL:**

<http://wrap.warwick.ac.uk/145543>

**Copyright and reuse:**

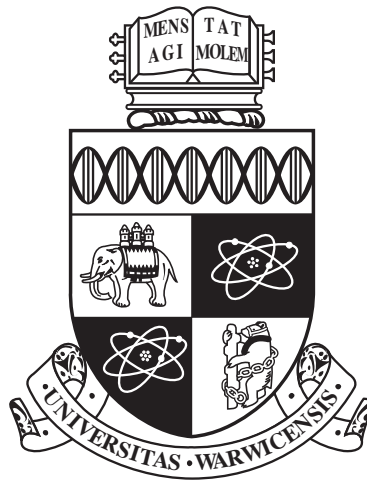
This thesis is made available online and is protected by original copyright.

Please scroll down to view the document itself.

Please refer to the repository record for this item for information to help you to cite it.

Our policy information is available from the repository home page.

For more information, please contact the WRAP Team at: [wrap@warwick.ac.uk](mailto:wrap@warwick.ac.uk)



**Development and Validation of a Water Separation  
model for AIS (Air Intake Systems) through PEPT  
experiments**

by

**Bram Vangestel**

**Thesis**

Submitted to the University of Warwick

for the degree of

**Doctor of Philosophy**

**University of Warwick, School of Engineering**

April 2019

THE UNIVERSITY OF  
**WARWICK**

...to Sara, my pillar

# Contents

<b>Acknowledgments</b>	<b>vi</b>
<b>Abstract</b>	<b>viii</b>
<b>Chapter 1 Introduction</b>	<b>1</b>
<b>Chapter 2 AIS - Air Intake System</b>	<b>3</b>
2.1 Description and main functions of an AIS . . . . .	3
2.2 Geometry of an AIS . . . . .	4
2.3 Factors influencing Water Separation . . . . .	5
2.3.1 Air velocity and turbulences . . . . .	5
2.3.2 Droplet Impact . . . . .	5
2.3.3 Droplet Rainwater Conditions . . . . .	8
2.3.4 Droplet Lab Conditions . . . . .	8
2.3.5 Location of the AIS orifice . . . . .	9
2.3.6 Materials used for the AIS construction . . . . .	9
2.4 Water Separation Techniques . . . . .	11
2.4.1 Orifice inlet velocity . . . . .	11
2.4.2 Louvres . . . . .	11
2.4.3 Standing edges . . . . .	11
2.4.4 Gravity enabled separation . . . . .	12
2.4.5 Rotary Flow . . . . .	13
2.5 Surface treatment . . . . .	13
<b>Chapter 3 PEPT: Positron emission particle tracking</b>	<b>15</b>
3.1 PEPT Introduction . . . . .	15
3.1.1 PEPT alternative techniques . . . . .	15
3.1.2 PEPT state of the art . . . . .	16
3.1.3 PEPT algorithm . . . . .	17
3.1.4 Labelling Tracers Particles . . . . .	20
3.1.5 PEPT Cameras . . . . .	21
3.1.6 Extraction of information from PEPT . . . . .	22
3.1.7 Conclusion of PEPT Introduction . . . . .	23
3.2 Experimental Setup and Methods . . . . .	24
3.2.1 Scaled down AIS (Air Intake System) . . . . .	24



3.2.2	Tracers . . . . .	26
3.3	Data analysis . . . . .	26
3.3.1	Pre-processing . . . . .	26
3.3.2	Lagrangian velocity . . . . .	27
3.3.3	Calibration . . . . .	28
3.4	Results and Conclusion of Experiments . . . . .	28
3.4.1	Position . . . . .	28
3.4.2	Tracers compared . . . . .	29
3.4.3	Velocities . . . . .	31
3.4.4	Effect of surface treatment . . . . .	34
<b>Chapter 4</b>	<b>Numerical Method - Introduction</b>	<b>36</b>
4.1	CFD Introduction . . . . .	36
4.2	The Navier-Stokes Equations . . . . .	37
4.3	Turbulence of the main air phase . . . . .	37
4.3.1	The k-epsilon turbulence model . . . . .	38
4.4	Multiphase Models . . . . .	38
4.4.1	Multiphase models: Lagrangian multiphase or LMP . . . . .	39
4.4.2	Multiphase Models: Eulerian Multiphase - VOF . . . . .	41
4.4.3	Multiphase Models: Fluid Film . . . . .	42
4.5	Multiphase Interaction Models . . . . .	43
4.5.1	Multiphase interaction model: LMP - VOF . . . . .	43
4.5.2	Multiphase interaction model: Fluid Film - VOF . . . . .	43
4.5.3	Multiphase interaction model: Fluid Film - LMP . . . . .	44
4.5.4	Multiphase interaction model: Surface Tension . . . . .	50
<b>Chapter 5</b>	<b>CFD - Validation with PEPT for the Scaled Down Inlet Box</b>	<b>56</b>
5.1	CAD and CFD Model . . . . .	57
5.2	Validation of the CFD model - Main Air Phase . . . . .	58
5.2.1	Mesh Independence Study . . . . .	58
5.2.2	Velocity - Measured . . . . .	60
5.2.3	Velocity - Simulated . . . . .	60
5.2.4	Pressure Loss - Measured . . . . .	62
5.2.5	Pressure Loss - Simulated . . . . .	64
5.3	Validation of the CFD model - Water Behaviour . . . . .	65
5.3.1	Water Phase - Setup CFD . . . . .	66
5.3.2	Water Phase - Experimental . . . . .	68
5.3.3	Water Phase - Mesh independence study . . . . .	69
5.3.4	Convective Courant number . . . . .	69
5.3.5	Parcel size independence study . . . . .	71
5.3.6	Effect of Bai-Gosman . . . . .	71
5.3.7	Description of final setup and result . . . . .	73
5.4	Conclusion on validation of the CFD setup with PEPT result . . . . .	78
5.5	Further Analysis on the scaled down inlet box . . . . .	79

5.5.1	Effect of Injector Droplet initial velocity . . . . .	79
5.5.2	Effect of Injector Droplet diameter . . . . .	80
5.5.3	Effect of Injector Cone Angle . . . . .	85
5.5.4	Effect of main air phase flowrate . . . . .	89
5.5.5	Conclusion from further investigation on the scaled down inlet box . . . . .	99
<b>Chapter 6</b>	<b>Applying the validated CFD setup to a large scale AIS</b>	<b>100</b>
6.1	CAD and Mesh model . . . . .	101
6.2	Rainwater Injection Setup . . . . .	105
6.3	CFD Methods to simulate Water behaviour . . . . .	106
6.4	Method 1 - Steady method with coefficient of restitution . . . . .	107
6.4.1	Free flowing - wall absorption . . . . .	108
6.4.2	Dripping . . . . .	112
6.4.3	Splashing . . . . .	114
6.4.4	Conclusion - Impingement with coefficient of restitution . . . . .	115
6.5	Method 2: method validated by work in Chapter 5 - Transient method with Fluid Film/VOF . . . . .	116
6.5.1	Further mesh refinement . . . . .	116
6.5.2	Simulation Setup . . . . .	117
6.5.3	Available steps to optimize the transient solution time . . . . .	124
6.5.4	Results and analysis - effect of contact angle . . . . .	126
6.6	Effect of Pressure (power) washing on water separation . . . . .	133
6.7	Effect of main air phase flowrate in the full-scale AIS . . . . .	136
<b>Chapter 7</b>	<b>Conclusion</b>	<b>140</b>
<b>Appendix A</b>	<b>PEPT test setup</b>	<b>145</b>
<b>Appendix B</b>	<b>Fanjet properties</b>	<b>154</b>
<b>Appendix C</b>	<b>CFD - Mesh Settings</b>	<b>158</b>
<b>Appendix D</b>	<b>CFD Settings - Mesh and Physics</b>	<b>172</b>
D.1	Simulation Settings - Small Scale Model . . . . .	172
D.2	Simulation Settings - Full Scale Model . . . . .	174
<b>Appendix E</b>	<b>CFD - Post processing Settings</b>	<b>177</b>
E.1	MAIN FLOWFIELD . . . . .	177
E.1.1	CAD preparation and boundary types . . . . .	177
E.1.2	Mesh preparation . . . . .	177
E.1.3	Coordinate systems . . . . .	178
E.2	Lagrangian Injector . . . . .	178
E.2.1	Optimize the Lagrangian solution time . . . . .	178
E.3	Fluid Film Settings . . . . .	179
E.3.1	Fluid Film Physics . . . . .	179
E.3.2	Fluid Film Boundary Conditions . . . . .	183

E.3.3	Fluid Film - Create phase . . . . .	184
E.3.4	Multiphase interaction . . . . .	184
E.4	Solver Settings . . . . .	185
E.5	Stopping criteria . . . . .	185
E.6	Post processing . . . . .	185
E.6.1	Isosurface settings . . . . .	186
<b>Appendix F CFD - Results</b>		<b>189</b>
<b>Appendix G Measured Results</b>		<b>195</b>
G.1	Measured Velocity - Small Scale Box: Inlet . . . . .	195
G.2	Measured Velocity - Small Scale Box: Outlet . . . . .	198

# Acknowledgments

This thesis was typeset with  $\text{\LaTeX} 2_{\epsilon}$ <sup>1</sup> by the author.

This part-time PhD programme has been a very rewarding experience in my academic and professional career. Let's first start with what has been a big impact not only on this PhD but my life as whole. During the summer of 2012 I was diagnosed with cancer. Because of this I was forced to withdraw from this PhD program. My believe in (medical) science was proven correct, I recovered well from the treatment and declared fit again to resume my daily activities, including this program that I resumed in 2013. This PhD experiencep proved to me how an individual can sacrifice many of the worldly-pleasures and dedicate work to something that happens in a niche area but with an unknown effect on the broader surroundings and it has helped me realize that research is more than solving equations and running simulations. It is the hope that your work will help someone else to better understand the world or universe we live in, even if this thesis is only 1 in a very large stack of publications. I take this opportunity to show respect for all the PhD students and professors who are working day and night to make our planet a better place to live in. The peaceful nights of many people are the result of your sleepless nights in the research labs. This thesis has reached completion through my interaction with lot of people who have supported and encouraged me to give my best. I take this opportunity to thank all the people who have helped me directly or indirectly. First, I would like to thank my supervisors Prof. Peter J. Thomas, Dr Yongmann M. Chung and Prof. Jan Baeyens. Their dedication to achieve excellence and belief to be a constructive part of the whole have inspired me to put that extra effort and motivated me to keep going despite failures. I owe them lots of gratitude for having me shown this way of research. They could not even realize how much I have learned from him. A special thanks to my sponsor and employer Donaldson for believing in the value of this research and enabling me to take on this part-time program. I would like to thank my committee members Prof. Bob Critoph and Prof. Jennifer Wen for reviewing my work and providing valuable suggestions. My sincere thanks to the StarCCM support group: Thijs Scheeve, Leonardo Palma, Vincent Keromnes and Mathieu Stasia. You have been very helpful and cooperative. I would like to specially thank Peter Martens

---

<sup>1</sup> $\text{\LaTeX} 2_{\epsilon}$  is an extension of  $\text{\LaTeX}$ .  $\text{\LaTeX}$  is a collection of macros for  $\text{\TeX}$ .  $\text{\TeX}$  is a trademark of the American Mathematical Society. The style package warwickthesis was used.

at Europlasma for providing me with free of charge plasma treated PE samples. Peter Gajdatsy, Filip de Coninck and Emmanuel Moreau for their letters of reference. Kerrie Hatton, research Degrees Secretary at the School of Engineering, to support me in all special requests that came from being a part time student. A special thanks To Donaldson Company Inc. for sponsoring this project. Finally, this thesis would not have been possible without the encouragement and support of my wife Sara (your passion and zeal for life have taught me how simple it is to be happy), my parents Eduard Vangestel and Christiane Rits (my career is a result of your sacrifices and belief in me), and Penelope, Isabella and Caterina (daughters). It is hard to put in words how much I love you all.

# Abstract

An experimental investigation of the flow through a scaled down mock-up of an Air Intake System (AIS) of a heavy goods vehicle are presented. The main goal being to identify the locations where small water droplets that enter the system together with the air will get deposited and to evaluate details of drainage film flows that are established on the inclined louvres in the orifice of the system in order to validate the predictions of a computational model. A single particle was tracked using the positron emission particle tracking (PEPT) technique, a method that determines the location of a particle through the triangulation of gamma photons emitted by a radioactive tracer particle. The experiments were performed at the Positron Emission Particle Tracking facility at the University of Birmingham for flow down inclined flat surfaces. The materials used for the test surfaces were manufactured from the same materials that are considered for use for the full-scale commercial systems to be designed. The surfaces of the plates were plasma treated to achieve laboratory conditions for the surface energy closely representing those to be encountered under typical operational conditions for vehicles on the road. The simulation was then solved by means of commercial CFD multiphase models developed as part of the research. The information obtained from the experiments is then used for the validation of the CFD set-up for an identical geometry as used during the experiments, the main air phase in the model is validated through measurements on the air (velocity in multiple areas of the geometry, and pressure reading at the beginning and end of the ductwork), the water phase is then validated with the experimental velocity data obtained during the PEPT experiments. The results show that the surface energy significantly effects the drainage flows established. Finally the validated CFD model is then applied to a true scale commercially available Air Intake System and findings on this design exploration are reported. Those findings can then be used in future investigations to improve new Air Intake Systems.

Keywords: Lagrangian Particle Tracking, Positron Emission Particle Tracking (PEPT), Inclined Plate, Air Intake Systems (AIS), Surface treatment, Multiphase flow, Fluid Film, Volume of Fluid

# Chapter 1

## Introduction

The objective of the research is to further develop and/or improve existing CFD water drainage models used in the design of air intake systems (both for commercial vehicles and industrial filtration). Preventing water to reach a filter medium is fundamental for good and durable filtration results. Minerals dissolved in the fluid (e.g. salts) can clog the filter medium, and/or can be batch-wise released due to sudden pressure waves or air fluctuations etc. Minerals entering the ICE (internal combustion engine) need to be avoided. Other reasons to avoid water entrainment are the restriction rise (pressure difference between in and outlet of the system) by icing of the filter media, the corrosion of engine components and a potentially hydro-locked engine.

CFD simulations are used to provide a better understanding of the fluid flow (droplet coalescence, re-entry, accumulation, instability) and to provide fundamental insights to develop and improve separation techniques such as inclined louvres. To develop and validate the numerical water drainage model, the thesis will use experimental PEPT-results to serve as a validation tool for the CFD setup (in order to comply with the PEPT laboratory safety regulations this is done on a scaled down air inlet system). Once validation is established this CFD setup is then extended to a full scale air intake system. The experimental part captures the behaviour of the water phase, the spatial time transport of water through the system provides us with information to validate existing CFD models and where needed to adapt these or develop new models. Important parameters that affect the experimental results are airflow rate, water concentration and surface tension (surface tension will be altered with plasma treatment). For the numerical part a CFD model is developed that is validated with the outcome from the experimental phase. The object under investigation is initially a scaled down air inlet system and after validation is proven a full air intake system is considered. The amount of detail required for the specific models will drive the size of the meshed zone. Next to accuracy, also time is a driving factor. For industrial use with limited time between design iterations it is crucial to get results in a timely manner. Although faster results could require a decrease in accuracy, they would still be valuable for A-to-B comparison (frequent use during early design stage). The combination of multiple CFD physics models will be needed: in order of appearance these are, Lagrangian discrete water droplets that represent to rain water at the intake orifice, Fluid Film on the intake surface to represent the wetted surfaces, VOF (volume of fluid) fractions that consider the contact angle and zones with relatively high film heights. These 3 main CFD models would interact with each other and with the surrounding continuous air phase. This study is aimed at engineers from the automotive sector in fields such as water drainage on

external vehicle components (such as windscreens and car bodies) and water drainage in vehicle intake solutions. However other engineers may find parts of this study interesting for subjects such as: gas turbines intakes, industrial dust collection, HVAC and process filtration.

This thesis is structured as follows. The background and review of Air Intake Systems are given in Chapter 2. Detailed descriptions of different drainage techniques and its applications are discussed. In Chapter 3, the PEPT (positron emitted particle tracking) experiment is described, starting from the setup where polymer plates with different contact angles are prepared to the processing of the measured results into plots that represent the migration of the particle down an inclined plate. In Chapter 4, a numerical introduction is given that outlines the different models used throughout the following chapters. Most important here are the different phase interaction models and their benefits and limitations towards their use in industrial scenarios. Chapter 5 describes the validation and development of the CFD drainage models with the PEPT experimental results from Chapter 3, further investigation is then done to extend the use of the CFD model to other user scenarios. Chapter 6 applies the validated CFD models from Chapter 5 on a true scale air inlet system and examines the effect of multiple variables on the water behaviour. Chapter 7 is conclusion and wrap-up.



## Chapter 2

# AIS - Air Intake System

This chapter gives a broader explanation on air intake system (AIS). It starts with describing the function of an AIS as used in the automotive world. An AIS can come in a wide array of forms often due to space constraints that are becoming tighter with the years (the internal combustion engine and all the environmental aids take up more space due to ever increasing strict legislation). Multiple contaminants are treated in an air intake system, however this thesis focusses on water, the main factors that influence water separation are described (air velocity and turbulences, rainwater parameters such as droplet size, velocity and volumetric flowrate and the location of the inlet orifice on the vehicle. Of special interest is the material that the inlet is made of, since its surface energy will influence the water behaviour once it makes contact. The final subsection describes the historical methods used to achieve better water separation, yet these were all obtained through trial and error, the goal of this thesis is to come up with a CFD method that avoids constructing the costly prototypes for this trial and error approach.

### 2.1 Description and main functions of an AIS

The AIS (Air Intake System) has two main purposes, the first is to guide the incoming air to the cylinders in which the air will take part in the combustion process, the second is to clean the air from contaminants. A typical location in the automotive world is in the front part of the engine room under the bonnet, directly behind the front grill where the company emblem is mounted. How much air is needed for the combustion process is influenced by several variables but mainly one can say that speed and acceleration contribute the most to the need for air. If a vehicle accelerates from low to high speed, the fuel consumption increases and hence the engine needs more oxygen (air). The unit that controls the air suction rate (MAF, mass airflow sensor) is located after the AIS in the clean air duct. This unit is very sensitive to water and if exposed to water it might malfunction and thus, give wrong air flow rates to the engine. Cleaning the incoming air from particles such as dust, leaves, snow and other contaminants is done by using a filter in the filterbox section in which the dirt will be trapped, and the standard requirement of a filter is to clean 99.8 percent the incoming dust. Another function of the filter is to reduce noise from the engine. Note that this description is a broad and general outline of an intake system. In real life the intake system may come in a plethora of different shapes and variations. Vehicles in general and lorries in particular, have an extensive air intake system for both engine-, compressed- and cabin-air (see figure 2.1). These filters are intended to remove fine particles from the inlet air, but suffer from

water ingress (rain, spray, wash) in the main filter body. Currently water drainage systems are installed prior to the cellulose or polymer filters, but a better understanding of the drainage process is needed. The installed solutions intend to achieve better water removal, yet their design is based on a trial and error process during the prototype phase. The ultimate objective of this research is the development of a numerical model that would allow for a more accurate design prior the prototype phase. Yet, before using such a numerical model, a validation of the phenomena with experimental values is essential. The experimental determination of the validation values is one of the chapters of this thesis.

## 2.2 Geometry of an AIS

The intake system that is used as starting point to develop the water separation model in this thesis is in production and installed in a Donaldson OE client lorry and has been on the market for several years. It is located just behind the cabinet of the lorry close to the engine compartment. The system is divided into three sections and are named (see figure 2.1).

1. inlet and intake orifice
2. rubber bellow
3. filter housing + duct to engine (not shown)

Figure 2.1 shows a plot of the inlet taken from the side. The intake orifice is located in the top left in the figure, from which the air is guided into the top inlet compartment where the first and most important steps of water separation occur at the louvres which protects from snow and heavier dust particles and also functions as a first and main barrier against water ingress, air is able to enter in between the louvres that give a direction to it to facilitate the further separation steps. The intake system is also equipped with a drainpipe, with the hose mounted at the bottom of the intake orifice directly after the louvres. Its function is to lead the incoming water downwards and out of the system before it enters the filter-box. The drainpipe orifice is visible directly under the louvres (raised object under the green louvres). On the right image the outer shell has been made transparent, the orange part is a reversed inlet duct that forces the air and the suspended water particles over a standing edge. The air is then led through the main duct that is separated from the filter housing by a rubber below (mechanical decoupling), to the filter located in the black box (not visible in the image). Note that most of the inlet parts are not visible in a typical driving configuration where a trailer is attached to the lorry.

Due to the radioactive nature of the PEPT test that will be used for the experimental validation, it was decided to use a scaled down version of the inlet orifice and to model only 1 larger louvre where the surface properties could be easily adapted (by exchanging a polymer plate on top of the louvre). The environmental conditions were also scaled so that it would still represent the inlet condition from the larger air intake system (around 5 m/s at the intake orifice).

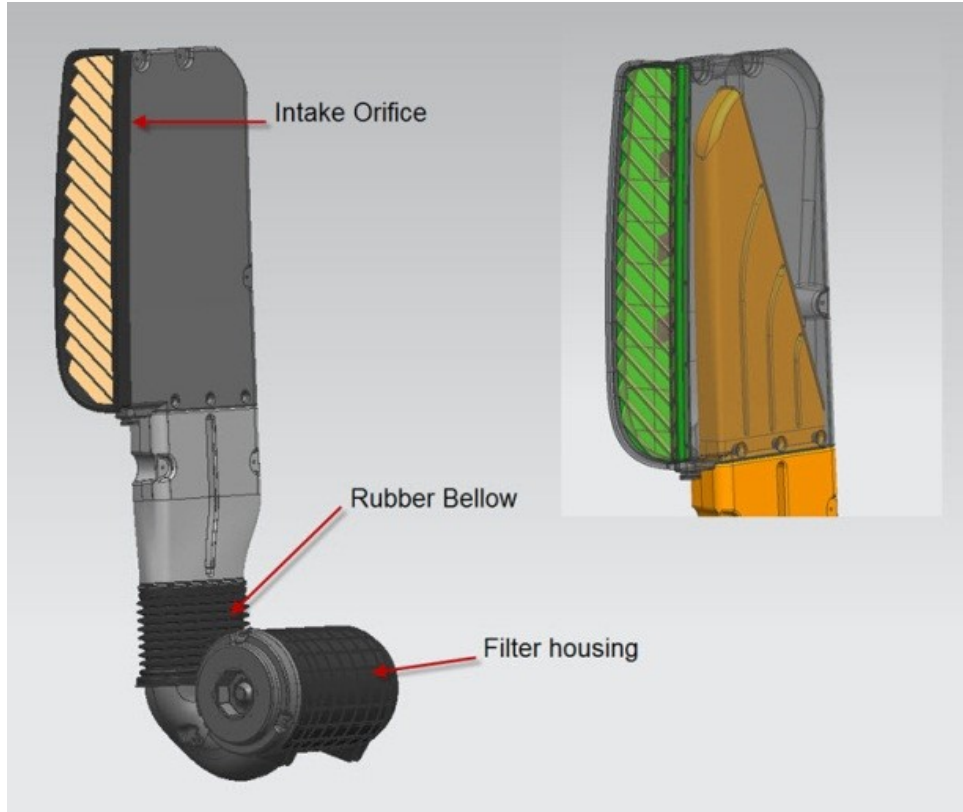


Figure 2.1: AIS (Air Intake System) used on larger lorries. Core parts are the filter housing with the filter media inside and a dirty air channel with several pre-separation methods incorporated.

## 2.3 Factors influencing Water Separation

### 2.3.1 Air velocity and turbulences

Air velocity and turbulences at the orifice and at other locations throughout the AIS (Air Intake System) will influence the water droplets suspended in the main airflow and in the water film formed on the AIS surface. It is beneficial to keep the intake velocity around the orifice below a certain threshold (typically 5m/s) in order to reduce droplets entrainment to a minimum. The remaining droplets that do enter the AIS are then separated by means described in later chapters.

### 2.3.2 Droplet Impact

Rain water droplets fall when their falling velocity exceeds the upward wind speed or lift velocity of the air [7]. When a water droplet impacts on to a solid surface, it splashes, spreads or breaks into smaller particles. There are plenty of examples of water droplets hitting a solid surface; rainfall is a natural example that can be observed everywhere. Also, inkjet printing provides another example of a drop impact application [8]. Typically when a water droplet hits on a solid it creates a splash, spreading or bouncing [9] (depending on the properties of the impact surface solid). One could summarize the behaviour of a water droplet based on three primary factors, the nature and inclination of the surface, the properties of the liquid and the velocity and the size of the droplet [10]. From the materials view, droplet behaviour is determined by kinetic energy, the surface energy of the drop, and the energy created by the internal motion of the water droplet [9]. A droplet only holds kinetic energy before the impact and will exhibit different impact behaviours:

Deposition, when a droplet attaches to the surface. Spreading occurs when the drop touches the surface and the surface area of the droplet increases because the impact will deform the droplet and the water will spread quickly away from the centre of the impact.

Rebound, when depending on the droplets initial kinetic energy, the surface tension will absorb the energy upon impact like a spring, and the forces of restitution will make the drop to recoil away from the surface. The deformation will create a jet shape in the centre of the impact which can cause part of the droplet to lift off and bounce back [9]. It can either partially rebound or it can completely rebound. If it is a complete rebound, the entire droplet elevates away off the surface. If it partially rebounds, part of the droplet sticks to the surface while other parts will elevate away from the surface.

Splash, whereby the small secondary droplets form up on impact, occurs when the surface tension is not adequate to stop the outward motion after the drop spreads upon impact. Hence, the deformation will create a rim while the centre part will flatten to the surface. Thus, the outward velocity of the particle will exceed the surface tension, as a result the main rim breaks and creates smaller droplets [11].

In actuality, the mechanics of fluid droplet behaviour will depend on many other characteristics that are beyond the scope of this project [12]. Drop behaviour is determined by two dynamical dimensionless numbers, the Reynolds number ( $Re$ ), which balances inertia with viscous effects, and the Weber number ( $We$ ), which balances inertia with capillary effects (if the drop diameter is  $D = 2R_0$  and velocity at impact is  $V_0$  then:

$$We = \frac{\rho D v_0^2}{\lambda} \quad (2.1)$$

$$Re = \frac{\rho D V_0}{\nu} \quad (2.2)$$

Where  $\rho$  is the liquid density,  $\lambda$  is the surface tension coefficient and  $\nu$  is the kinematic viscosity of the fluid. If  $We > 1$ , inertial forces are higher and will likely cause the drop shape to change up on impact. If  $We < 1$ , the surface tension is higher and the drop will be stable upon impact [11]. To explain the Weber number: the liquid inside the droplet is held together by the surface tension of the liquid (see figure 2.2) and the droplet shape can be deformed if the surface tension changes. Also, the change of inertia created by the impact will affect the shape of the droplet. The ratio between the inertial force and the surface tension will govern the amount of the deformation.

Apart from the Weber and Reynolds number, several other factors influence the energy dissipation of a droplet upon impact such as viscous dissipation and contact angle hysteresis. And after the lift-off, a droplet might rotate and/or oscillate thereby dissipating internal energy. Calculating the droplet diameter is virtually impossible because several factors influence the size of the droplet. For rainwater the typical size is a minimum droplet diameter of around 0.1 mm and a maximum around 5 to 7 mm. Droplets any larger will break apart during the fall. The lower limit of 0.1 mm is defined because a droplet has to overcome the updraft (or the lift) of the wind [7]. The shape of the droplet depends on the magnitude of its diameter as well. Perfect spherical shapes at terminal velocity are only observed in droplets that are less than 0.3 mm. Droplets that are larger than 1 mm look alike spheroids with flat bases. The terminal velocity of a droplet

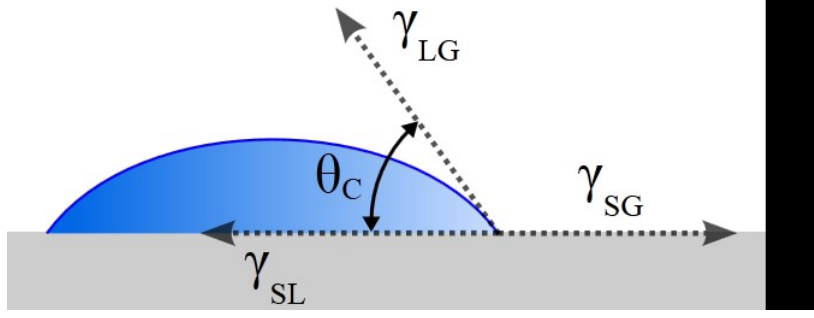


Figure 2.2: Water droplet on a solid surface and the tension-active forces occurring at each interface: Solid-air, Liquid-solid and Air-liquid. The point of contact of air, liquid and solid is in equilibrium. Because the tension-active forces are a function solely of the ratios of cohesive and adhesive forces, the angle of contact will take a value that achieves equilibrium (minimum energy). At a given temperature, the contact angle depends solely on the materials involved

is very important for the rainwater penetration test, as the behaviour of the droplet on impact is dependent upon the droplet's terminal velocity. The motion of the droplet is affected by the gravitational force and drag/lift forces of the air.

$$m_D \frac{du}{dt} = F_g - F_D \quad (2.3)$$

$$m_D \frac{du}{dt} = m_D \cdot g - \frac{C_d \rho_a v^2 A}{2} \quad (2.4)$$

Where,  $m_D$  = mass of the droplet,  $u$  = droplet velocity,  $C_d$  = drag coefficient in air (function of  $Re$ ),  $\rho$  = density of air,  $v$  = wind velocity,  $A$  droplet area. However, the droplet shape is not going to be a perfect sphere every time; therefore, the area cannot be calculated precisely. The area of the droplet can be estimated using the Reynolds number.

$$m_D \frac{du}{dt} = m_D \cdot g - \frac{\pi}{8} v Re C_d D (u - v) \quad (2.5)$$

Where,  $v$  is the kinematic viscosity,  $D$  droplet diameter.

The terminal velocity is the maximum vertical velocity a rain particle can obtain. However, this is assuming that there are no horizontal forces acting up on the droplet, as these would affect the shape of the droplet and create additional drag [7]. Since the terminal velocity of a droplet is hard to calculate, an approximation for the formula was obtained using the data collected [13]. Hence, the terminal velocity of a droplet can be approximated as a function of the droplets diameter.

$$V_t \approx 9.40 [1 - e^x (-1.57 \times 10^3 D^{1.15})] \quad (2.6)$$

Where,  $V_t$  is the terminal velocity and  $D$  is the droplet diameter in meters.

When a droplet impacts there is a difference in velocity before and after the impact in the case of a rebound. This measure is called the coefficient of restitution (see also chapter 6) and it is denoted by  $c$ ,

$$c = \frac{V_f}{V_i} = \sqrt{\frac{h}{H}} \quad (2.7)$$

Where,  $V_f$  and  $V_i$  is the velocity before and after the impact. Also,  $h$  is the height the drop bounce

after impact and  $H$  is the height from which the droplet was originally released. The coefficient of restitution is dimensionless number between 0 and 1. Calculating the diameter of a droplet after an impact is a cumbersome process. Hence, several estimates have taken this into account, and the following formula gives the maximum diameter on a hydrophobic surface [11].

$$D_{max} \approx D_0 We^{1/4} \quad (2.8)$$

Where,  $D_0$  is the initial diameter. A hydrophobic material will repel water on the molecular level upon impact. These materials repel water by making large contact angles on the droplet surface (see figure 2.2). The contact angle is the geometrical angle created by the interaction of the liquid-solid interface [14]. Some materials are super-hydrophobic and they can create contact angles up to 170 degrees [9]. Therefore, in super-hydrophobic materials, there will be very little contact with surface of the droplet and solid. Hence, bouncing and splashing happens more frequently. As the surface interaction is low, it assists the droplet to leave the surface, creating a bouncing behaviour, or the droplet simply breaks apart creating increased splashing behaviour.

### 2.3.3 Droplet Rainwater Conditions

In 1851, George Gabriel Stokes derived an expression, now known as Stokes' law, for the frictional force (also called drag force) exerted on spherical objects with very small Reynolds numbers in a viscous fluid. Stokes' law makes the following assumptions for the behaviour of a particle in a fluid: Laminar flow, spherical particles, homogeneous (uniform in composition) material, smooth surfaces and particles do not interfere with each other. Stokes' law is derived by solving the Stokes flow limit for small Reynolds numbers of the NavierStokes equations. For our setup one could argue that the larger diameter drops see higher Reynolds numbers however the empirical formulas in [71] are also applied. The terminal velocity of a droplet is very important for the rainwater penetration test, as the behaviour of the droplet on impact is dependent upon the droplet's terminal velocity. The motion of the droplet in the atmosphere is due to gravitational force and drag/lift forces of the air. The terminal velocity is the maximum velocity a rain particle can obtain while falling to the earth's surface. However, this is assuming that there are no horizontal forces acting up on the droplet, as these would affect the shape of the droplet and create additional drag. The terminal velocity of the droplet was calculated in function of its diameter. With  $F_D$  being the Stokes upward drag force,  $F_g$  being the downward weight force as described in figure 2.3,  $D$  the droplet diameter and  $V_t$  the terminal velocity the formulas result in the values described in table 2.1.

$$F_D = 3\pi\mu Dv \quad (2.9)$$

$$F_g = \rho \frac{4}{3}\pi \left(\frac{D}{2}\right)^3 \quad (2.10)$$

### 2.3.4 Droplet Lab Conditions

The distribution of droplet sizes is due to the interaction with air, which deforms larger drops and causes them to fragment into smaller drops, effectively limiting the largest raindrops to about 7 mm diameter [1] [2]. Droplets in lab conditions are generated according ASAE S-572 (see table

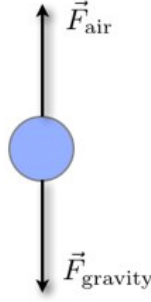


Figure 2.3: Forces on water droplet at terminal velocity

Table 2.1: typical rain droplet diameters and their terminal velocity [2]

Diameter [mm]	Type of Particle	Terminal Velocity [m/s]
0.02	typical cloud drop	0.012
0.10	large cloud drop	0.304
0.20	large cloud drop/small drizzle	0.763
0.40	typical drizzle	1.65
0.50	drizzle / small rain drop	2.068
1.0	typical raindrop	3.92
1.5	typical raindrop	5.404
2.0	typical raindrop	6.564
5.0	Large rain drop—will break apart	9.082

2.2) to mimic real life scenarios [3]. Described by Volume Median Diameter(VMD) in microns, 50 percent of the spray volume is made up of droplets less than the VMD, and 50 percent is made up of droplets exceeding the VMD. Droplet size is correlated with the chances of droplet drift, as smaller droplets are more prone to be carried on by the main airflow, larger droplets have less probability to be picked up by the airflow due to their inertia. For the experiments it was decided to focus on the range of fine drizzle to light rain.

### 2.3.5 Location of the AIS orifice

The orifice or inlet mouth position can be located on several places of the lorry as illustrated in figure 2.4. Due to location and dimensional constraints it is not always possible to locate this orifice in the most beneficial locations. When located in the front, spray coming from the road (a secondary effect) will become more prominent. A position behind the cab will reduce this effect but could place the inlet in a local low pressure zone due to vehicle aerodynamics. And an elevated position at the side would be more prone to water spray during a car-wash (lateral jets).

### 2.3.6 Materials used for the AIS construction

Due to the injection moulding production process of the air intake system and its louvres, the material choice is limited. This in combination with the state of the moulding tool, the potential additives to optimize surface tension and the potential presence of glass fibres that are used to reinforce the matrix material, all lead to an end product that has characteristic surface properties. When this solid surface is combined with the water that needs to be drained and the surrounding air it leads to a certain contact angle unique for the setup (see figure 2.2). Surface tension in

Table 2.2: ASAE S-572 droplet size characterization based on approximate Volume Median Diameter (VMD) [3]













ASAE Standard				Comparative Size		
Symbol	Category	Code	Apx. VMD	Relative Size	Comparative Size	Atomization
VF	Very Fine	Red 	<100		Point of Needle (25 Microns)	Fog
F	Fine	Orange 	100-175		Human Hair (100 Microns)	Fine Mist
M	Medium	Yellow 	175-250		Sewing Thread (150 Microns)	Fine Drizzle
C	Coarse	Blue 	250-375			
VC	Very Coarse	Green 	375-450		Staple (420 Microns)	Light Rain
EC	Extremely Coarse	White 	>450		#2 Pencil Lead (2000 Microns)	Thunderstorm



Figure 2.4: Potential inlet locations for an AIS: 1:side 2:front 3:behind cab



3 regions are governing the behaviour of the drainage solution: water-solid, water-air, air-solid. Yet only the contact areas where the solid is involved is subject to modifications off the drainage solution. The contact angle quantifies the wettability of a solid surface by a liquid via the Young equation [4]. A given system of solid, liquid, and vapor at a given temperature and pressure has a unique equilibrium contact angle.

## 2.4 Water Separation Techniques

Historically water drainage and separation techniques were based on trial and error and often involved having a full scale final product available, hence of low value during an initial design phase where only virtual CAD models are under investigation. In recent years findings of these experiments were invalidated due to the geometry of the AIS that are very different from one another (due to the clients design envelopes that are ever more limited in size).

### 2.4.1 Orifice inlet velocity

When dimensional constraints from the end-user do not limit the intake orifice size, a solution to water separation is increasing the orifice cross sectional area until the intake air velocity is reduced to 5 m/s or below. For the experiments this 5 m/s was considered as the default intake velocity. Increasing the inlet area reduces the inlet velocity (with paramount effect on primary water ingress such as rain)

### 2.4.2 Louvres

As illustrated in figure 2.1 the inclined louvres are meant to capture the water in the intake air (and guide it to a drain point) while preventing re-entrainment. The current construction of the inclined louvres, is typically manufactured in a polymer material with optional additives that can affect the surface energy. To achieve different surface energies for our validation study, we used surface activation (see figure 2.7) on a base polyethylene (PE) plate. To examine the effect on water drainage, 3 different surface conditions were created on the PE plate (default PE, hydrophobic and hydrophilic). For the results of surface treatments please consult table 3.2. Net contributions from gravity, surface effects, airflow and the inclination of the louvres create a range of down flow behaviours [5][6]. Three common types are known as Gravity flow, Rivulet flow and Dry Patch. Figure 2.5 shows schematics of these three types of down flow behaviour. The pattern above the impingement line XX is common to all. Where downward momentum dominates surface tension the flow forms a stable falling film of width W, which is here termed gravity flow (figure 2.5a). The film width may change gradually. In cases where surface tension is significant, two behaviours can arise: rivulet flow (figure 2.5b), where the liquid forms a narrow tail, and dry patch formation (figure 2.5c), where the falling film splits.

### 2.4.3 Standing edges

Further downstream, standing edges (e.g. orange part in figure 2.1) act as deposit surface: the remaining water in the main flow impacts or attaches on the flat surface and/or standing edges that prevent it from crossing the barrier further into the AIS (se also figure 2.6b). Drain channels

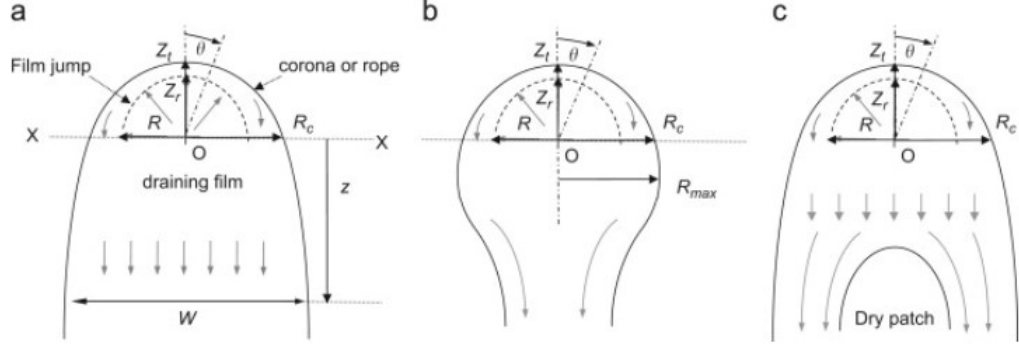


Figure 2.5: Schematics of flow patterns, generated by a jet impinging on a vertical plate.  $O$  is the jet impingement point,  $\tau$  is the polar coordinate,  $R$  is the radius of the film jump,  $R_c$  is the radius of the corona or rope at the impingement level (XX).  $Z_r$  is the height of inner radial zone above  $O$  and  $Z_t$  is the maximum height of the film above  $O$ . The grey arrows show the flow pattern, radial from  $O$  to the jump and tangential around the rim[5][6].

then guide the water to a drain point. Again surface properties in combination with topology make the difference between good drainage or re-entrainment in the main airflow.

#### 2.4.4 Gravity enabled separation

When the water is collected by the previously described methods, and further downstream against the walls of the AIS, it still needs to travel to drain points where the water is discharged through one-way valves that open once a threshold weight of the water above it is achieved and are closed due to negative pressure inside the ductwork. Several drain points exist throughout the AIS, the first one behind the louvres (see figure 2.1). A second one at the lowest point of the whole system (figure 2.6a), and a third in the filter housing itself (figure 2.6c). These are constructed so they form the lowest point in their respective sub-component. Yet also here the effect of surface properties will influence water re-entrainment.

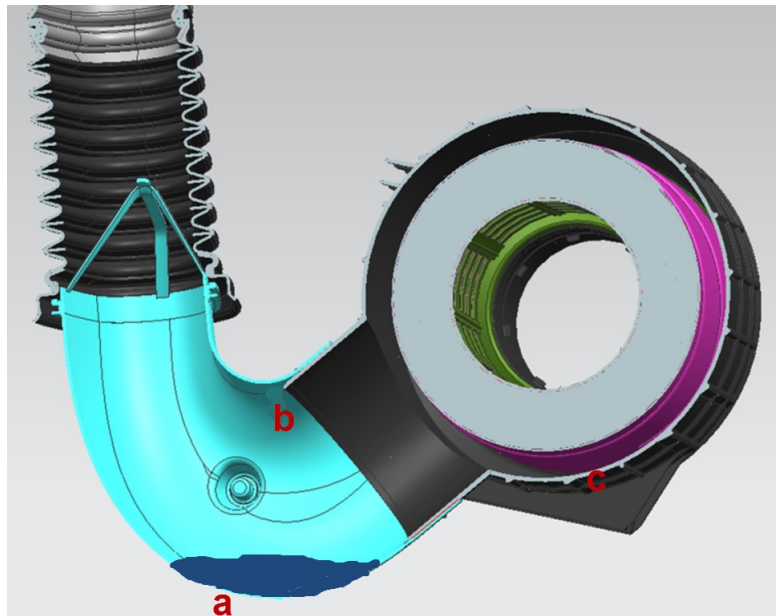


Figure 2.6: Gravity enabled separation

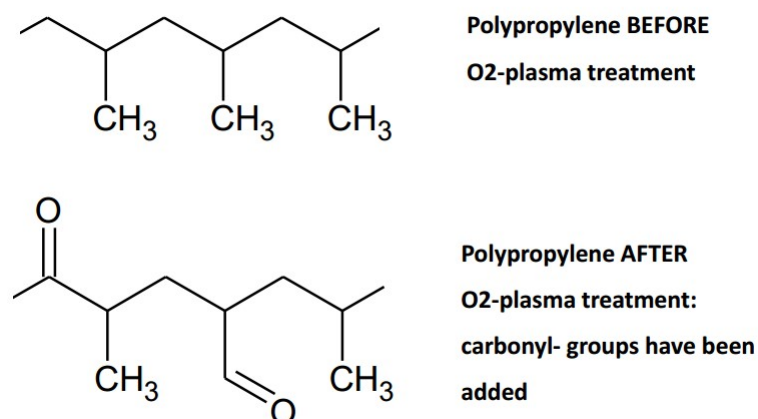


Figure 2.7: Activation of a polymer with hydrophilic end result

### 2.4.5 Rotary Flow

As mentioned the last drain point is the filter housing itself, again at the lowest point of this sub-component. Due to the rotary flow in the filter house itself and the conical shape of the element (conical shape raises or lowers the available cross sectional area, thus affecting the rotational speed), the remaining water is forced to a drainage point.

## 2.5 Surface treatment

For the results of surface treatments please consult table 3.2. There are many ways to treat surfaces: cleaning (decontamination, grease removal), activation (adherence or anti-adherence properties), etching, functionalization (electrical conductivity, protection against corrosion, chemical barrier...). Note that the cleaning and activation steps often precede the deposition phase, and the surface quality is determinant for the coating quality. The effect of each treatment step is as follows:

1. Cleaning: removal of molecular contamination layers from a surface
2. Etching: removal of surface material (several nm up to 1  $\mu\text{m}$ )
3. Activation: non-permanent chemical modification of surface
4. Functionalization: permanent chemical modification of surface
5. Coating: polymerization of chemical species on the surface

Surface activation, as illustrated in figure 2.7 consists in grafting chemical functions (plasma active species) on the material surface in order to give it specific properties by varying its surface energy. The plasma composition influences the surface properties of the treated material. For example, an argon oxygen plasma leads to the grafting of polar and hydrophilic functions (oxygen groups), which increase the material surface energy. This kind of activation is useful to prepare the surface before other treatments: metallization, painting, printing, coating, sticking and bonding. On the other hand, an Ar-CF<sub>4</sub> plasma leads to the surface fluorination and induces anti-adherence properties. Spectroscopic analysis of the treated surfaces (FTIR, XPS) can link the surface energy evolution to the surface composition and the chemical bounds. Atmospheric plasma can treat

various materials even those that are stable, such as polymers. The surface activation remains stable over a quite long period: treated substrates can thus be stored. Nevertheless, handling a sample between two treatment steps can damage the surface. Then, it is interesting to integrate the plasma system into the production line. For our experiments we used an external partner of the thesis sponsor, however not all details of the treatment can be shared due to an NDA in place.

## Chapter 3

# PEPT: Positron emission particle tracking

In order to build a good CFD model, it is required to validate this with experimental values. The experimental method that was selected for this validation exercise is PEPT (Positron Emission Particle Tracking). This chapter begins with the principles, background and state-of-the-art of Positron Emission Particle Tracking (PEPT). The second section covers the setup of our experiment in the Birmingham PEPT laboratory. Section 3 discusses the methods applied for processing the obtained result into data that usable for later validation of the CFD model, in the case of PEPT for fluid systems this means that spatial time data of a tracer is outputted by the test rig and can then be processed to obtain velocity plots in function of the tracer location (how the tracer follows the water is explained). At the end of this chapter the results are then discussed, the conclusion being that PEPT is a viable technique to study the flow of water in an air intake system and is able to produce data that can be used for validation of a CFD model. Chapter 5 then uses the outcome of this PEPT chapter (spatial time information on the tracers) as validation for the velocity data of the water phase in the CFD model.

### 3.1 PEPT Introduction

To give the reader a sound understanding of the technique, a comprehensive description of PEPT development in Birmingham, the location algorithm, particle labelling and recent developments in the camera system are given in this section.

#### 3.1.1 PEPT alternative techniques

Laser Doppler Velocimetry (LDV) and Particle Image Velocimetry (PIV) were introduced after the invention of laser in the 1960s. The optical methods have been extensively used by a number of researchers and substantial improvement of the understandings of phase interactions has been achieved. Meanwhile, the performance of the optical methods has improved rapidly with the development of laser and camera techniques, and Laser Doppler anemometry (LDA) and PIV are currently the most widely used techniques. However, the optically-based experimental measurements are constrained to transparent systems resulting in limited practical use for many industries, so alternative techniques are desirable for most non-Newtonian fluids and multiphase systems which

are opaque. The Lagrangian tracking techniques such as the Positron Emission Particle Tracking (PEPT) and Computer Automated Radioactive Tracking (CARPT) are two promising techniques to investigate the localized information for the opaque systems. The Ultrasonic Doppler Velocimetry (UDV) technique has also been used to measure the velocity field in multiphase setups.

### 3.1.2 PEPT state of the art

The well-known method of Positron Emission Tomography (PET) has been used in nuclear medicine for decades. This technique offers a non-intrusive way of monitoring the metabolic activity inside a patients body. The use of PET is limited to slow moving systems since a lot of data are required to reconstruct images of the flow of the fluid tracer. Hence, it was not possible to use PET to study dynamic systems that are present in most engineering equipment. However, [32] suggested that if the positron camera is used to track a single particle instead of looking at the flow of fluid as a whole, it is possible to locate the position of the particle more accurately since fewer data are required. The new technique of tracking a single particle was named Positron Emission Particle Tracking (PEPT) and this increased the range of equipment that can be studied. Since then PEPT has been used extensively to study both granular and liquid systems e.g. fluidized beds, stirred vessels and extruder's. The table below gives some comparison between PET and PEPT.

PET	PEPT
Image of the bulk material can be obtained	Track the motion of a single particle
Large amount of data is required for image reconstruction	Suitable for dynamic systems
Data collection: 2D image takes 1 minute and 3D image takes 1 hour	Real time motion of particle can be observed
Resolution of MWPC camera for PET imaging: 8 mm	Particle moving at $0.1\text{ m/s}$ can be located to within 2 mm or less, 25 times per second and a faster particle moving at $1\text{ m/s}$ can be located to within 5 mm at 250 times per second
Not suitable for fast dynamic systems	Accurate tracking for velocities of up to $2\text{ m/s}$

Positron emission particle tracking (PEPT) is used to study particle dynamics, granular systems and multiphase flows. PEPT allows a non-invasive 3D spatial detection of a single radioactive particle as it moves through the system under study. Because this study involves the impact of surface energy on the fluid flow, an experimental method was needed that would allow the use of the original intake orifice materials including mostly opaque materials (PA, PP), PEPT allows for this. PEPT has been compared to other used visualization techniques [33] and showed good agreement and again benefit for the opaque systems. As there is only one point-like source particle within the field of view, the statistics necessary to provide a precise location are much less than the equivalent required for a volume image. Thus, the time-scale over which data becomes statistically significant is greatly reduced and comparable to typical physical and engineering time-scales. Dynamic systems can hence be studied using positron imaging techniques. Under optimum conditions the PEPT technique can measure locations along the trajectory of a particle moving with speeds up to  $10\text{ m/s}$  at intervals of around 1 ms. The particle location can be measured with

precision of around 0.5 mm in 3D. Since it was first introduced in 1988, PEPT has been used for the study of both granular and fluid flow in a wide range of engineering equipment. Numerous examples of PEPT application can be found such as mixers [36], fluidised beds [26], granular systems [25] and validation with CFD [30] to name a few, [23] gives a comprehensive review on recent work of PEPT.

### 3.1.3 PEPT algorithm

The PEPT camera (together with a computer) calculates the location of the particle through an iteration process performed by the PEPT algorithm. Before running the experiment, a single particle is taken from the bulk powder and labelled with a radionuclide. The radioactive particle (also known as tracer particle) is then mixed with the bulk powder inside the equipment which is in turn placed between the positron cameras. For a liquid system (e.g. stirred tank), a particle which is neutrally buoyant in the liquid is labelled with the radionuclide. The radionuclide decays by emitting positrons and when a positron collides with an electron a pair of back to back 511 keV gamma rays is produced (figure 3.1a). Those gamma rays are detected by the positron cameras (figure 3.1c) and the information is then sent to a computer. The data are processed by the computer which calculates the location of the particle by triangulation (figure 3.1d). The line joining coincident pairs of gamma rays is referred to as the line of response. In practice, not all lines of response (1 pair of detected gamma rays = 1 event) actually pass through the exact location of the particle. Erroneous reconstruction (figure 3.2) is unavoidable since the emitted gamma rays experience Compton scattering when travelling between the tracer particle and the photon cameras. To eliminate as many erroneous events as possible and minimize the error when calculating the location of the particle, a location algorithm was written [32] to process the data. Full details of the algorithm are available [30] [32]. The algorithm outputs the results in a text file. Figure 3.4b is an example of a PEPT file with information on the motion of the particle. These data can further be processed to obtain information on the particle and system being studied. The following information is present in the file (columns from left to right):

1. Time (ms)
2. X location (mm)
3. Y location (mm)
4. Z location (mm)
5. Error (mm)
6. Angle (Not used in work presented in the thesis)
7. Torque (Not used in work presented in the thesis)
8. Number of events used to calculate location

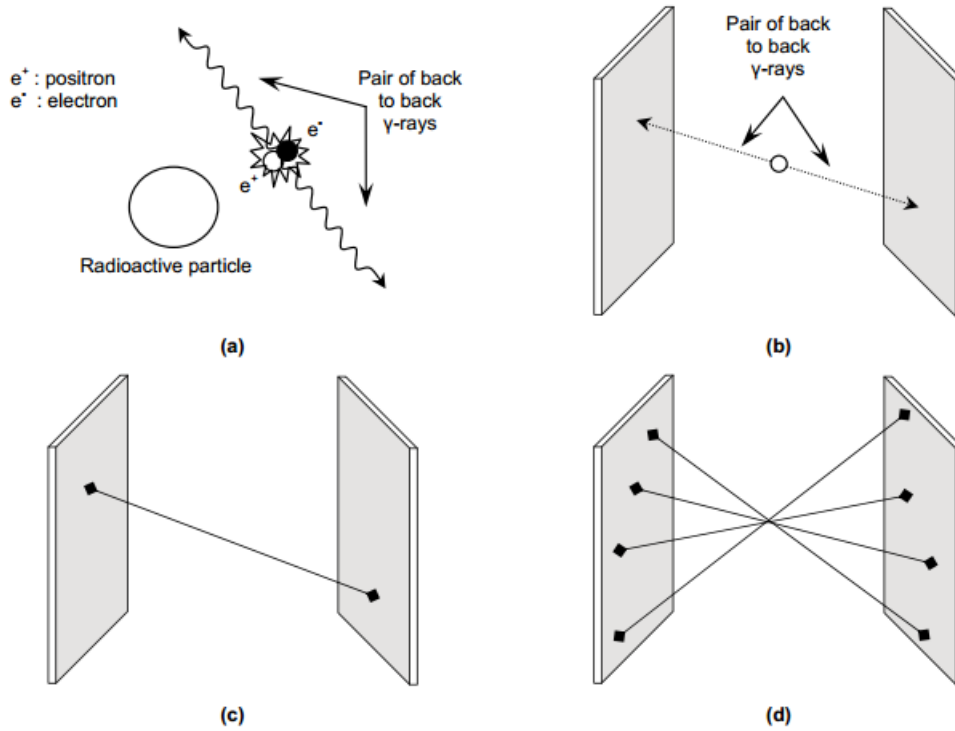


Figure 3.1: The above diagrams show how the PEPT camera is used to detect the location of the tracer particle. (a) The radionuclide decays by emitting positrons which on collision with an electron annihilates each other and produces a pair of back to back gamma rays. (b) Particle emits a pair of back to back gamma rays. (c) The gamma rays are detected by the camera. (d) The location of the particle is calculated by the method of triangulation[23].

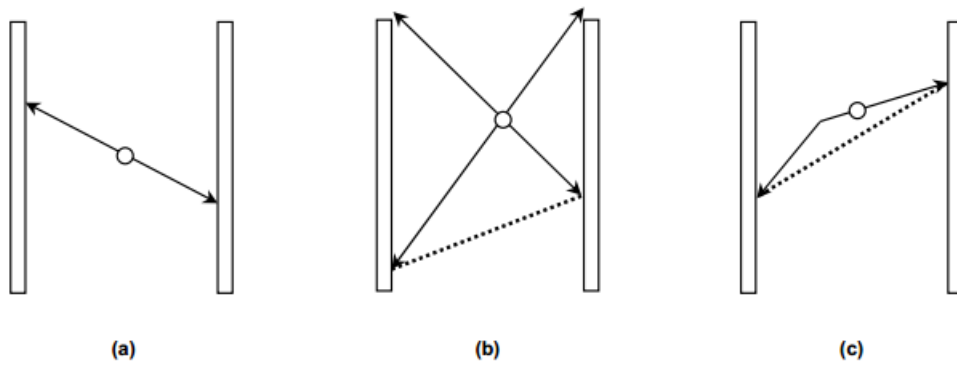


Figure 3.2: An illustration of possible erroneous reconstructions. (a) True pairing. (b) Random pairing. (c) Scattered gamma rays[23]



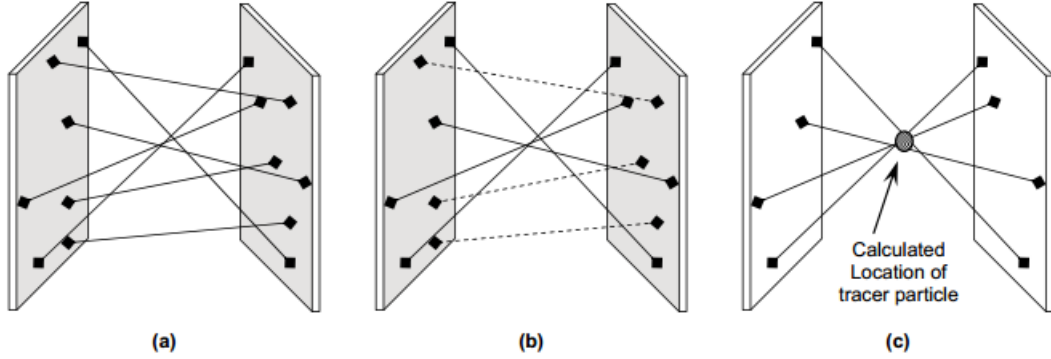
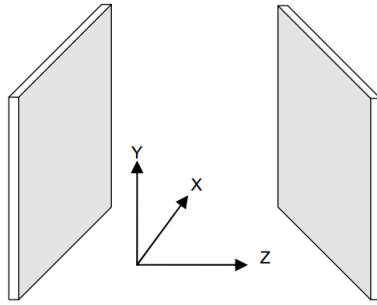


Figure 3.3: Calculating the location of the particle using the location algorithm. (a) A set number of events are chosen (Defined by Events per slice). (b) Events furthest from the minimum perpendicular distance to all the trajectories are discarded. (c) Location of particle is calculated when only a percentage of events are left (Defined by the value of fopt)[23].



(a)

youvan02 - WordPad  
 File Edit View Insert Format Help  
 Sand 19/10/06 5cm/s  
 Separation= 395  
 f(opt) : 0.200 Displacement parameters : 300, 400, 1500  
 Fixed slices: 150 events/slice, 1 locations/slice

3.9	342.1	181.7	184.5	1.5	0.0	0.00	30
11.5	341.7	181.4	184.0	1.4	0.0	0.00	26
18.3	342.9	181.2	182.0	1.2	0.0	0.00	26
26.1	342.6	181.3	186.4	1.4	0.0	0.00	26
33.6	342.7	181.2	182.3	1.3	0.0	0.00	26
41.0	342.4	181.6	183.0	1.6	0.0	0.00	26
48.1	342.9	181.4	183.3	1.4	0.0	0.00	26
56.0	342.0	181.5	185.0	1.2	0.0	0.00	26
62.6	341.4	180.6	186.4	1.4	0.0	0.00	26
70.5	341.7	180.6	183.6	1.4	0.0	0.00	26
76.5	342.1	180.7	185.8	1.2	0.0	0.00	26
83.8	342.5	181.4	183.5	1.4	0.0	0.00	26
91.0	342.8	181.6	185.5	1.3	0.0	0.00	26
97.3	341.8	181.5	181.7	1.4	0.0	0.00	26
105.5	340.9	181.2	184.3	1.1	0.0	0.00	26
112.6	341.5	181.9	182.8	1.2	0.0	0.00	26
120.2	341.8	181.8	183.2	1.3	0.0	0.00	26
127.9	342.1	182.1	182.2	1.2	0.0	0.00	26
134.6	341.0	181.5	183.3	1.4	0.0	0.00	26
141.3	341.4	181.7	184.1	1.3	0.0	0.00	26
148.1	340.8	180.7	180.2	1.4	0.0	0.00	26
153.9	341.3	180.1	182.1	1.3	0.0	0.00	26

For Help, press F1 NUM

(b)

Figure 3.4: (a) Direction of axis relative to the positron cameras. (b) Example of the output text file as obtained from PEPT which shows the location of the particle with time[23].

### 3.1.4 Labelling Tracers Particles

During PEPT experiments, the motion of a single particle is tracked and recorded. The shape, size, density and other physical properties of the tracer particle will affect its behaviour in the equipment being studied. Hence it is important for the tracer particle to have near identical properties to that of the bulk mass. In the case of liquid systems, a neutrally buoyant particle is usually used. Thus, it is essential to be able to label a wide range of particles in terms of size and material for PEPT applications. So far, 3 different techniques have been used to label particles with radioisotope [33] [40] [41]. For our experiments two types of tracers particles were used: a resin tracer particle and an  $Al_2O_3$  tracer particle.

For the resin tracer, fluorine-18 is first produced by bombarding deionised water with the  $^3He$  beam from the cyclotron giving rise to a diluted solution of fluoride ions. Particles of strong base anion exchange resins are then mixed with the solution and during the process, the radioactive fluoride ions are adsorbed onto the surface of the resins through ion-exchange. The resins can then be used as tracer particles. The radioactivity achieved on the particle depends on the chemical and physical properties of the resin, the contact time, the concentration of  $^{18}F$  in the solution and the type and number of other anions present in the solution.

Advantages Ion Exchange	Disadvantages Ion Exchange
Very small particles can be labelled. Minimum size is about $60\ \mu m$ .	Only particles that have a high affinity for $^{18}F$ ions can be labelled.
High activity can easily be achieved (13 to 40 MBq.)	Tracer particles can last long in dry conditions or in organic solvents, but in aqueous surroundings, the activity tends to leach away (painting can prevent this).

The  $Al_2O_3$  tracer particle was created by modifying the surface of the material first, followed by ion-exchange. Surface modification helps improve the selective adsorption of  $^{18}F$  onto the surface of the material used as tracer particle. This is carried out by introducing metallic ions on the surface of the solid to act as a bridge and encourage  $^{18}F$  ions to bind onto the surface through ion-exchange.

Advantages Surface Treatment	Disadvantages Surface Treatment
Very small particles can be labelled, minimum size is about $60\ \mu m$ .	This process takes more time compared to the other two methods.
Wider range of materials can be labelled with $^{18}F$ compared to ion-exchange only.	Tracer particles can last long in dry conditions or in organic solvents, but in aqueous surroundings, the activity tends to leach away (painting can prevent this).

The ability of the tracer to study the water flow patterns is justified by the balance of forces in the system. The forces acting on the tracer particle are drag forces against gravity, adhesion by Van der Waals forces, and water-induced adhesion forces.

$$(Drag) = (Gravity) + (VanderWaals) + (Adhesion) \quad (3.1)$$

Table 3.1: Stokes values for 2 types of resin

	$Stk$	$\rho_p$	$d_p$	$\mu_f$	$d_c$	$U_0$
$Al_2O_3$	0.4	2500	0.000012	0.001	0.001	0.2
<i>resin</i>	0.36	1000	0.000018	0.001	0.001	0.2

In the event of a wetted surface, forces of adhesion, electrostatics and Van der Waals are negligible, and both gravity and shear forces dominate. It is hence obvious that the tracer particle, adhered to the surface in dry conditions, will follow the streamlines of the water droplets when the surface is wetted. Additionally the Stokes dimensionless number allows qualification of the tracer to follow the flow [35], with  $\tau_p$  the particle response time,  $\tau_f$  the fluid response time,  $\rho_p$  as particle (tracer) density,  $d_p$  as particle diameter,  $\mu_f$  as water dynamic viscosity,  $d_c$  as characteristic dimension and  $U_0$  as water velocity.

$$Stk = \frac{\tau_p}{\tau_f} = \frac{\rho_s d_p^2 / 18 \mu_f}{d_c / U_0} \quad (3.2)$$

When  $Stk \ll 1$ , the particle is considered as following the flow, when  $Stk \gg 1$  the particles inertial forces will start to affect the particle movement. The max velocity  $U_0$  was obtained with the 6 point method described in the subsection on Lagrangian velocity and depended on the surface energy of the inclined plate. Characteristic dimension  $d_c$  for the inclined plate was considered as the thickness of the film when the plate was fully and homogeneously covered. Stokes values obtained are described in table 3.1.

The layers in the fluid film closest to the wall boundary are moving slowest, so it is expected that the particle will prefer these layers as Stokes numbers become more beneficiary. In the CFD validation to follow these experiments, the recorded max velocity  $U_0$  will be considered as closer to the wall boundary vs the outer layers of the film.

### 3.1.5 PEPT Cameras

Since the technique was first introduced, three different positron cameras have been used at the Positron Imaging Centre for PEPT, the multi wire proportional counter (MWPC) that is no longer used, the ADAC Forte (figure 3.5) that was used for this thesis and the Modular PEPT camera.

The ADAC Forte (developed by ADAC Laboratories) consists of a pair of NaI(Tl) gamma camera heads on motorised gantry which allows rotation about a horizontal axis. Each head contains a single sodium iodide crystal which is 590 mm x 470 mm with truncated corners and 16 mm thick. The face to face separation of the camera heads can be adjusted to between 250 mm and 800 mm and hence is more flexible and can accommodate bigger equipment compared to the MWPC camera. The location of a gamma ray colliding with the crystal in the camera head is determined by the software and hence compared to an analogue system like the MWPC camera there is less distortion near the edge of the camera. The main advantage of the ADAC Forte over the old MWPC camera is in the data logging rate (up to 100k events per second), as very fast pulses can be used and signals from different areas of the crystal can to some extent be processed in parallel. The increase in data logging rate also increases the spatial resolution of the camera.

Key features of the ADAC Forte camera:

1. Useful detector area: 510 mm x 380 mm. Separation of camera heads: 250 mm to 800 mm



Figure 3.5: (a) Picture of the ADAC Forte camera. (b) Camera heads can be rotated about a horizontal axis to accommodate different types of equipment

2. Camera heads can be rotated about a horizontal axis.
3. Maximum data logging rate: 100k events per second
4. Particle moving at 1 m/s can be located to within 0.5 mm 250 times per second.
5. A slow moving particle can be located to within 100  $\mu\text{m}$  50 times per second.
6. Full digital readout
7. Photopeak efficiency: 16 percent. Photopeak efficiency is a measure of the ratio of the number of events registered by the detectors that contribute to the full energy peak (in the case of PEPT, 511 keV gamma photons) to the total number of events incidents upon the detector.

### 3.1.6 Extraction of information from PEPT

This section gives a brief account on the type of information that can be obtained by processing the raw data from PEPT. As explained previously, the only information available directly from PEPT is the location of the tracer particle with time. To help PEPT users extract some basic information from raw PEPT data the Positron Imaging Centre created a program named Track. Figure 3.6 shows some examples of the type of information that can be obtained by processing the raw PEPT data through Track. Figure 3.6a is an example of part of the full trajectory of the tracer particle inside a fluidised bed as seen from the X-Y plane. This can also be viewed in the other two planes i.e. X-Z and Y-Z. This view offers the user the ability to visualise the real-time motion of the particle within a set timeframe. Figure 3.6b illustrates the velocity map of the solids inside a fluidised bed. The arrows indicate the direction of flow of the solids and the length of the arrow is proportional to the average velocity of the particle at different points inside the equipment. The third example (figure 3.6c) shows the occupancy plot of the tracer particle in a vertically stirred mill. The grey density indicates the average amount of time spent in each region of the vessel. A grey scale normally accompanies the occupancy plot but it has been excluded in the figure.

As described above, Track effectively allows users to extract valuable information from the raw PEPT data. However, the type of analysis and presentational information that it can produce

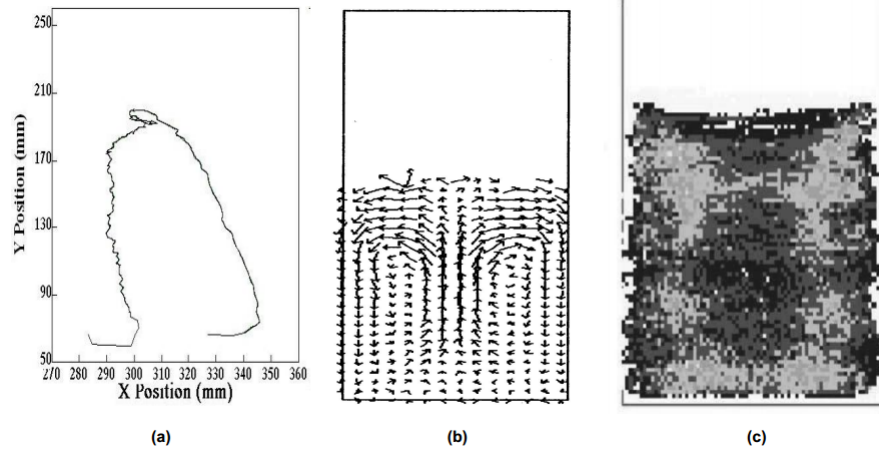


Figure 3.6: Examples of type of information that can be obtained by processing raw PEPT data with TRACK. (a) Part of the particle trajectory as seen on the X-Y plane. (b) Velocity map of solids as seen through PEPT. (c) Occupancy plot of grinding media inside a vertically stirred mill [23].

is limited to the functions which it has been programmed to deliver. In general, PEPT users use Excel spreadsheets to perform simple calculations with small amounts of data, or if a large number of PEPT files that contain hundreds of thousands of data points are to be processed, programs like Matlab or C are normally used. Most of the information calculated from PEPT is time-averaged, but individual trajectories can also be analysed to give detailed information on the tracer behaviour in particular regions. The calculations on PEPT data presented in this thesis are modified versions of the previous mentioned methods. Details of how the data has been processed are outlined in each individual results chapter.

### 3.1.7 Conclusion of PEPT Introduction

PEPT is a very powerful technique that can be used to monitor the motion of a single particle with time through opaque systems. The gamma rays emitted by the tracer particle are so penetrative that they can even go through relatively thick steel walls which is the preferred material used for most engineering equipment. Both liquid and granular systems can be studied using PEPT. For liquid systems, a neutrally buoyant particle is used as tracer and for granular systems, one particle from the bulk powder or a particle which has very similar properties to that of the bulk can be labelled and used as tracer. The algorithm for processing PEPT data eliminates all pairs of gamma rays not associated with the location of the particle and thus prevents erroneous reconstruction. Three different methods can be employed to label particles with the radionuclide and recent developments made labelling of smaller (down to  $60\text{ }\mu\text{m}$ ) and a wider range of particles possible. The amount of information available from the raw PEPT data only is relatively limited. However, by further processing the particle trajectories through Track or programs like Matlab and C, it is possible to obtain more detailed information on the equipment e.g. dispersion, velocity fields, residence time, etc.

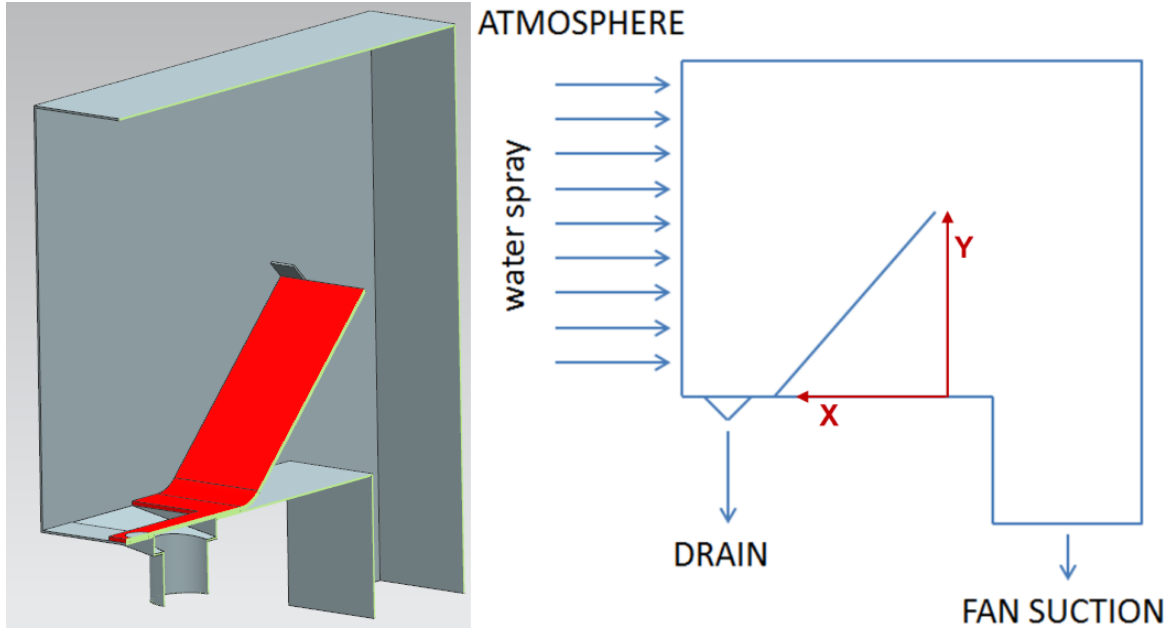


Figure 3.7: Left: stainless steel inlet box (grey) with surface treated PE plate (red) mounted against its support surface. Right: a fan located downstream of the inlet box is regulated so a 5[m/s] airflow is generated at the orifice. The generated water spray is partially pulled in and impacts on the inclined plate, where it flows influenced by the force balance downwards to the drain, X is fore-aft and Y is vertical movement relative to the CFD and PEPT coordinate system

## 3.2 Experimental Setup and Methods

This PEPT section explains how the experimental setup was made in the PEPT facility at Birmingham university. As already mentioned prior there are safety regulations that need to be respected since radio-active particles are used. It is important that these are located and retrieved at all times to avoid contamination outside the laboratory, on the bodies of persons involved or on personal belonging. For this reason a scaled down test rig was used rather than a full scale air intake system, to avoid running very high airflow that could blow the radioactive particles through the lab. The radioactive tracers that were used come in two forms  $Al_2O_3$  and an ion exchange resin. Theoretically both would be able to follow the water flow, later on these results are then also compared and proven that this statement is valid, only the hydrophilic case is proven to be an exception (hydrophilic is less relevant since no real-life AIS exist with pure hydrophilic materials).

### 3.2.1 Scaled down AIS (Air Intake System)

A stainless steel filter inlet of 300 x 400 x 150 [mm] was constructed with a welded inclined plate that acts as support for the treated PE plates (see figure 3.7), where X represents the fore-aft movement and Y the vertical movement of the particle on this inclined plate. The tracer particle was manually positioned at the top of the inclined plate. When the data acquisition was started, the water spray and airflow were started. Water spray is generated by a spray nozzle, generating rain-like conditions as described in chapter 2. Several plates with different contact angles were prepared through plasma treatment of the base PE plates (see table 3.2). The whole setup was then positioned inside the PEPT rig (see figure 3.8).

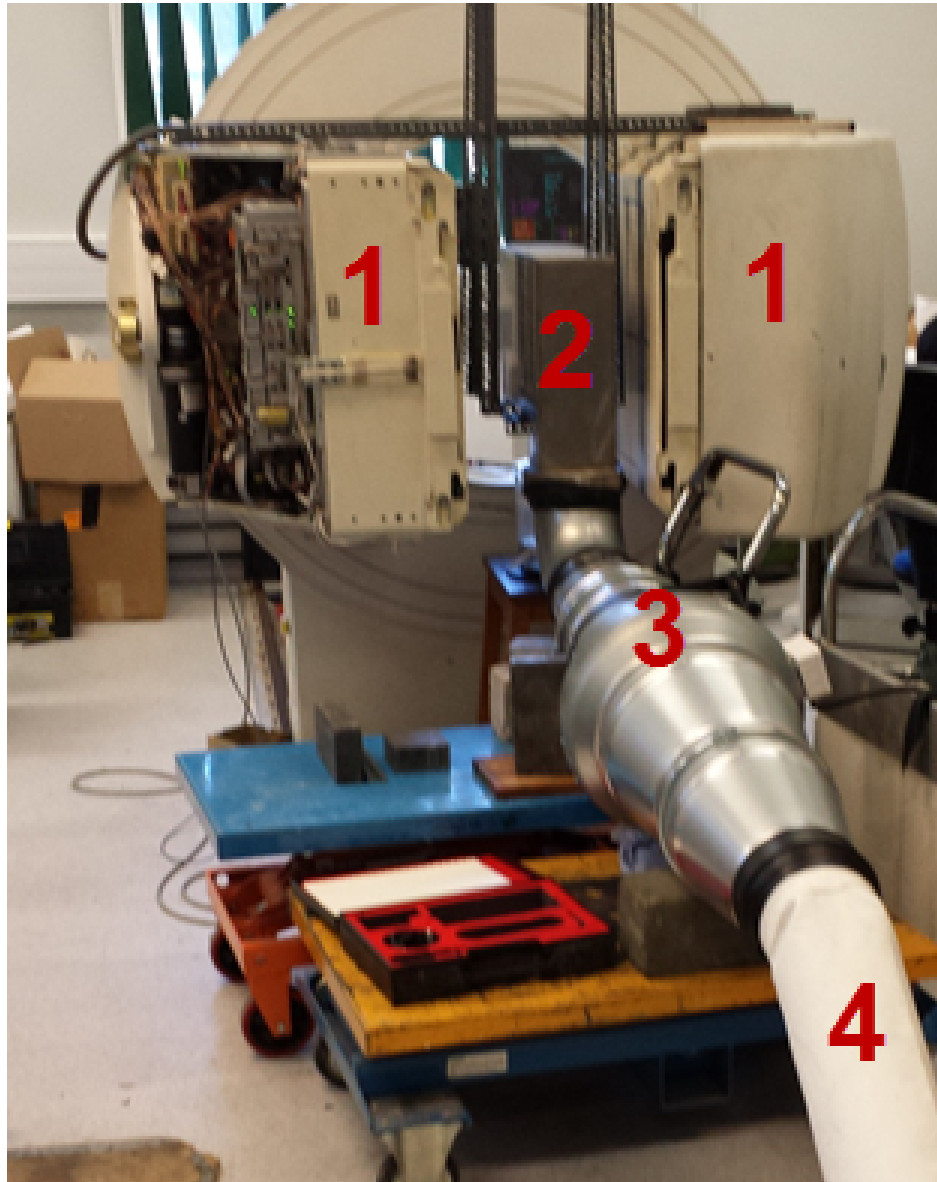


Figure 3.8: 1:cameras 2:inlet box with inclined plate (surface treated) 3:fan to simulate intake air flow 4:filter bag to trap tracer particle if escaped from 2

Table 3.2: Contact angles of the plasma treated inclined plates as measured by the goniometric method: several plates were created and all showed consistency through the measurements

plate	contact angle[deg]
hydrophobic	110
default PE	95
steel	72
hydrophilic	0

### 3.2.2 Tracers

An  $F_{18}$  radioisotope which decays by a form of beta-decay involving emission of a positron is incorporated into the tracer particle. Once emitted from the nucleus, the positron annihilates with an electron, releasing energy in the form of two 511 keV gamma-rays which are emitted back-to-back, 180 degrees apart to within about 0.5 degrees. The tracer particle is introduced into the system under study, which is mounted between the two detectors of the positron camera. Each detector is able to detect incident gamma-rays and determine their interaction coordinates to within a few mm. Only coincidence events in which gamma-rays are simultaneously detected in both detectors are recorded. From a small number of such detected events the tracer position can be determined by triangulation. The gamma-rays are quite penetrating (50 percent are transmitted through 11 mm steel) so that tracking is possible inside real process equipment. Some gamma-rays are scattered prior to detection, but the tracking algorithm used is able to discard these events. It should be noted that all measurements are made in three dimensions, and that the accuracy quoted is limited by the difficulty in determining the position along the axis normal to the detector faces. A single tracer was inserted at the start of each experiment, on top of the inclined plane, which corresponded to the centre of the detectors. This method was preferred over putting the tracer in the water reservoir of the spray nozzle as it would pose additional safety risks when working with the radioactive material. For the experiments, 2 types of tracer were used:

1.  $Al_2O_3$  (density 2500-2800  $kg/m^3$ , size 80-120  $\mu m$ )
2. Ion exchange resin (density 1000  $kg/m^3$ , size 100-180  $\mu m$ ), the resin particle is painted to prevent leakage of Fluorine-18 ( $^{18}F$ ), yet also causing some surface energy effects itself [34].

## 3.3 Data analysis

The PEPT section on data analysis starts from the pre-processing that occurs in the cameras itself, the output file that is then generated contains raw information on the particle coordinates in function of the time. This output file is then converted to velocity plots in function of the position on the slope using the 6 point method as described earlier. Calibration is also being discussed yet this is fairly straight forward for a static test rig like ours (it requires guiding the tracer over the contours of the rig to establish this).

### 3.3.1 Pre-processing

The two PEPT cameras each produce a two dimensional image of both end of the gamma rays. With an algorithm developed in Birmingham [37] this data is transformed in 3D raw location data.



This data is then further processed specifically for this experiment through following steps:

1. Because the location errors would propagate badly through the 6 point method described in subsection on Lagrangian velocity, an initial step removed all data with a spatial location error higher than 2 mm. (Trim stationary events at beginning and end of experiments as these are not containing any data valuable to the experiments (markers were put in the raw data during the experiments))
2. Due to the construction of the steel inlet box, particles could get stuck in the weld-lines where the inclined plate was connected to the box, these experiments were ignored.
3. Other reasons why experiments were ignored from the 51 runs in total were: double particles present during recording (depositing the particles did not always guarantee a single particle was picked)
4. Experiments were the particle dislodged from the plate before the water spray was turned on
5. Particles that escaped through small openings between the inclined plate and the surrounding box (as in reality the air intake louvres form one body with its surroundings due to injection moulding)

The position of the tracer particle when it is moving along the inclined plate is captured by the detectors. The position is stored as raw coordinates over time. When the tracer particle is moving in the test setup, this is visualized as a change in co-ordinates. In Matlab with some post processing it is also possible to generate residence time plots (for more information refer to the appendices). Once the particle started the decent of the inclined plate, the velocity increased rapidly, this in combination with the constant acquisition time of the PEPT cameras could lead to too large time intervals in between 2 measurement points. As the slope was linear for most of the slope area (see figure 3.7) and the PEPT results showed the particle to follow this path, no further interpolation was introduced. For the lower part of the inclined plate where the slope was no longer linear, an interpolation method was used to optimize results [36]. This interpolation was applied when measurement locations where in between 0.5 and 2 mm apart. These values are derived from requirements for the Eulerian velocity analysis.

### 3.3.2 Lagrangian velocity

The instantaneous Lagrangian velocities along the trajectory of the tracer can be directly determined using the 6-point method [16]:

$$\begin{aligned} \vec{v}_i = & 0.1 \left( \frac{\vec{P}_{i+5} - \vec{P}_i}{t_{i+5} - t_i} \right) + 0.15 \left( \frac{\vec{P}_{i+4} - \vec{P}_{i-1}}{t_{i+4} - t_{i-1}} \right) + 0.25 \left( \frac{\vec{P}_{i+3} - \vec{P}_{i-2}}{t_{i+3} - t_{i-2}} \right) + 0.25 \left( \frac{\vec{P}_{i+2} - \vec{P}_{i-3}}{t_{i+2} - t_{i-3}} \right) \\ & + 0.15 \left( \frac{\vec{P}_{i+1} - \vec{P}_{i-4}}{t_{i+1} - t_{i-4}} \right) + 0.1 \left( \frac{\vec{P}_i - \vec{P}_{i-5}}{t_i - t_{i-5}} \right) \end{aligned} \quad (3.3)$$

where  $\vec{v}_i$  is the velocity calculated for location  $i$  along the particle trajectory,  $\vec{P}_i$  represents the position of the particle at location  $i$  and  $t_i$  gives the time of the location. This method

introduces a small amount of smoothing to the velocity data but is preferred as the effects of PEPT measurement error are greatly reduced.

### 3.3.3 Calibration

The test setup was fixed at its outer locations, the contours of the inclined plate where recorded by moving a tracer particle in its container over the outer edges of the plate. This resulted in an outline with the 4 corners well defined (see table 3.3).

Table 3.3: Corners of the inclined plate

[mm]	X	Y	Z
Top Left	210	290	120
Bottom Left	390	160	120
Top Right	210	290	270
Bottom Right	390	160	270

## 3.4 Results and Conclusion of Experiments

From the processed data of the PEPT experiment several plots are created that can tell us more on the behaviour of the water as it moves down the slope. The test was run for 4 different test plates with each their own surface energy (hydrophilic, steel, PE and hydrophobic) and this is also observed in the generated plots as there is clear difference in the velocity as the water moves down the slope as shown in figure 3.16. Because PEPT generates data for 3 axis the plots can be generated for multiple viewpoints (fore-aft, lateral and vertical movement) as shown in figures 3.10, 3.11 and 3.12, as well as position plots or plots on residence time. As explained in prior sections there are 2 type of tracers selected to follow the water flow, when comparing these plots we see good agreement as explained by theory as shown in figure 3.13 (with the exception being the hydrophilic case).

### 3.4.1 Position

Figure 3.9 shows the position of a tracer ( $Al_2O_3$  on hydrophobic plate) over the complete recording time. The actual movement down the inclined plate occurs in a narrow window around  $t=26s$ . Until the water supply is switched on and the plate is sufficiently wetted, the particle is stagnant. Then a sliding down the plate occurs, followed by yet another stagnant time were the particle arrived in the collector bottle. Figure 3.10 zooms in around the time where the particle starts to move. The rapid increase in X location indicates that the tracer is suddenly moving forward, the rapid decrease in Y location indicates the tracer moving down the slope. The fluctuation in Z direction, indicates that the lateral movement is rather limited. X and Y position have a fairly similar starting value due to position of the inlet box in between the cameras. This was positioned in such a way that the centre top of the inclined plate was corresponding to roughly the centre of the cameras. In figure 3.11 the Y direction represents the vertical motion of the particle, while X represents the horizontal fore-aft motion. At the end of the plate ( $X=370$  mm) the curvature of the bended plate becomes visible and as such confirms that our particle is following the plate contour.

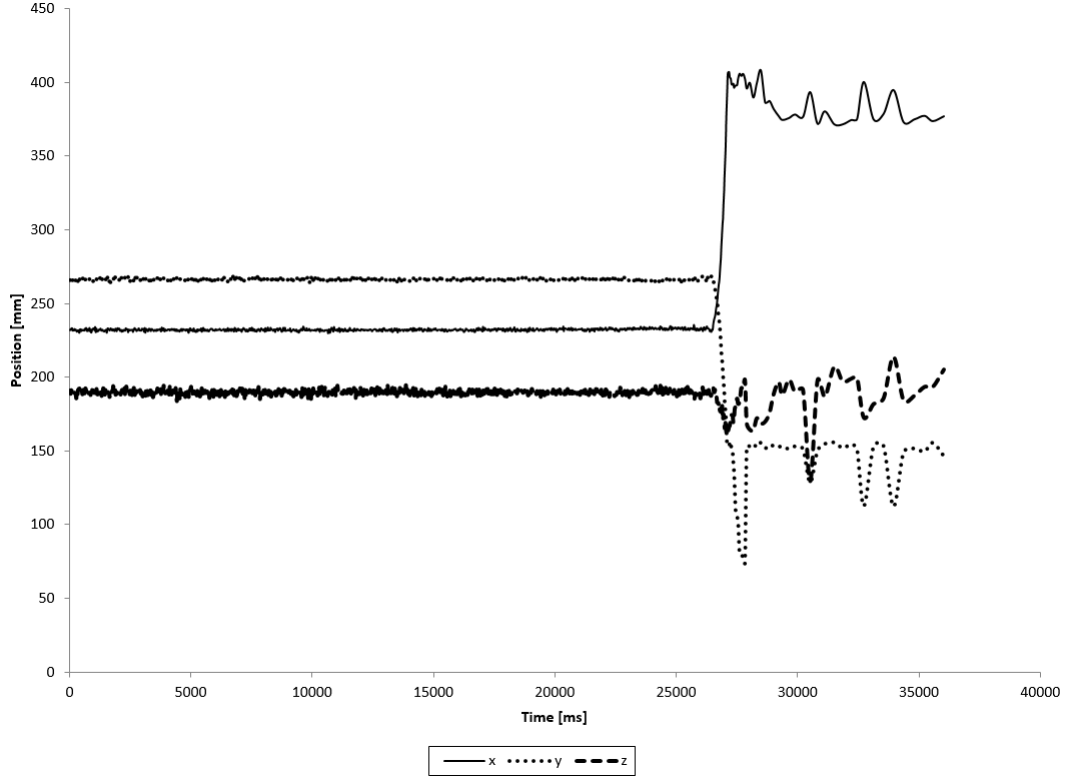


Figure 3.9: Position of one run plotted against time - actual movement down the slope occurs in a narrow window

Sudden spikes or drops would imply that the particle is no longer located in the plane of the plate. In figure 3.12 the Z direction represents the lateral movement: the particle when descending also changes lateral position and does not drop in a straight line. The left image corresponds to a frontal view of the setup. At the bottom ( $y=150$  mm) the particle has reached the collection point and is shown floating around until it falls into the drain and the measurement is stopped. The right image represents a top view of the setup. Again at the end of the descent ( $x=450$  mm), the particle reaches the collection point.

### 3.4.2 Tracers compared

According to the Stokes numbers in table 3.1, both tracer particles would have to follow the water flow. However they do have different size and density, therefore it was decided to compare the behaviour over the 3 main axis between the  $Al_2O_3$  and the resin tracer particle. In figure 3.13 velocities are non-dimensionalised with respect to the maximum overall velocity observed per direction. Each column represents the surface condition of the inclined plates, rows indicate the velocities, respectively  $Vx(t)$  (fore-aft),  $Vy(t)$  (vertical),  $Vz(t)$  (lateral). Orange colour represents the resin particle, blue represents the  $Al_2O_3$  particle. Several observations were made: For lateral speeds there is an anomaly observed for resin at the default plate (third row, third column), max speed for non-dimensional speeds will not be based on this result, but rather on a06. The horizontal axis that represent the time in which the particle descends shows a decrease in time from left to right. This behaviour follows also table 3.4, where the hydrophobic plate corresponds with the fastest descend. The hydrophilic plate shows the lowest speeds relative to the max speed for all

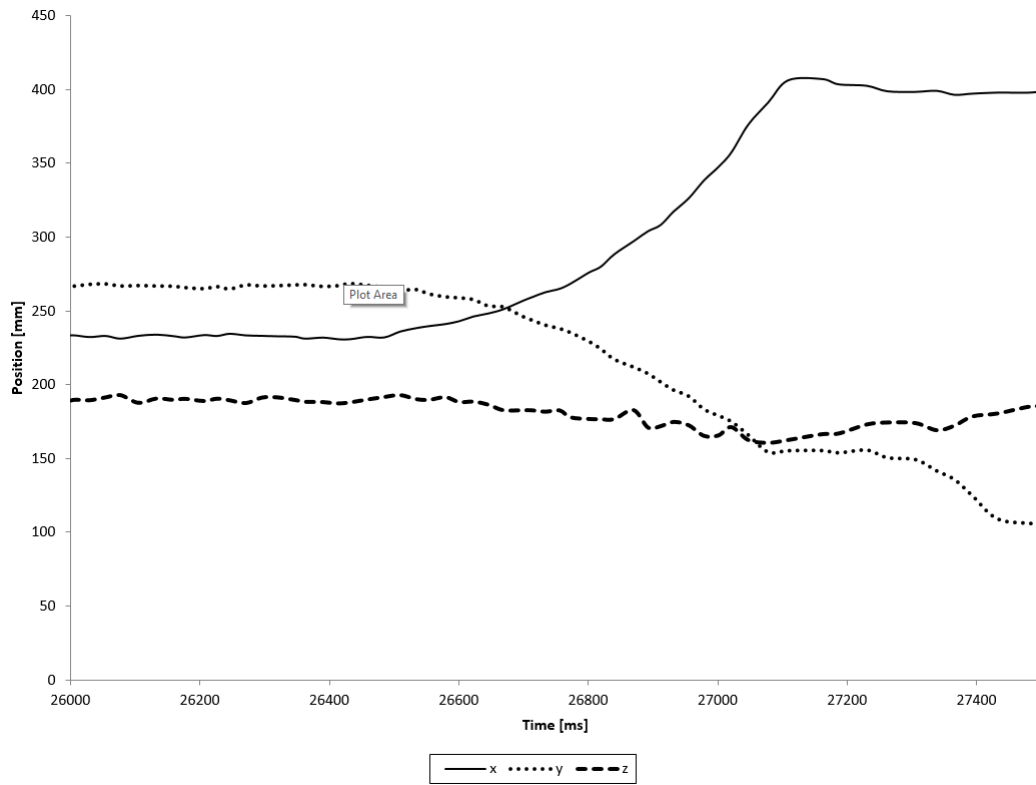


Figure 3.10: Position plotted against time - zoomed in around the time where movement occurs

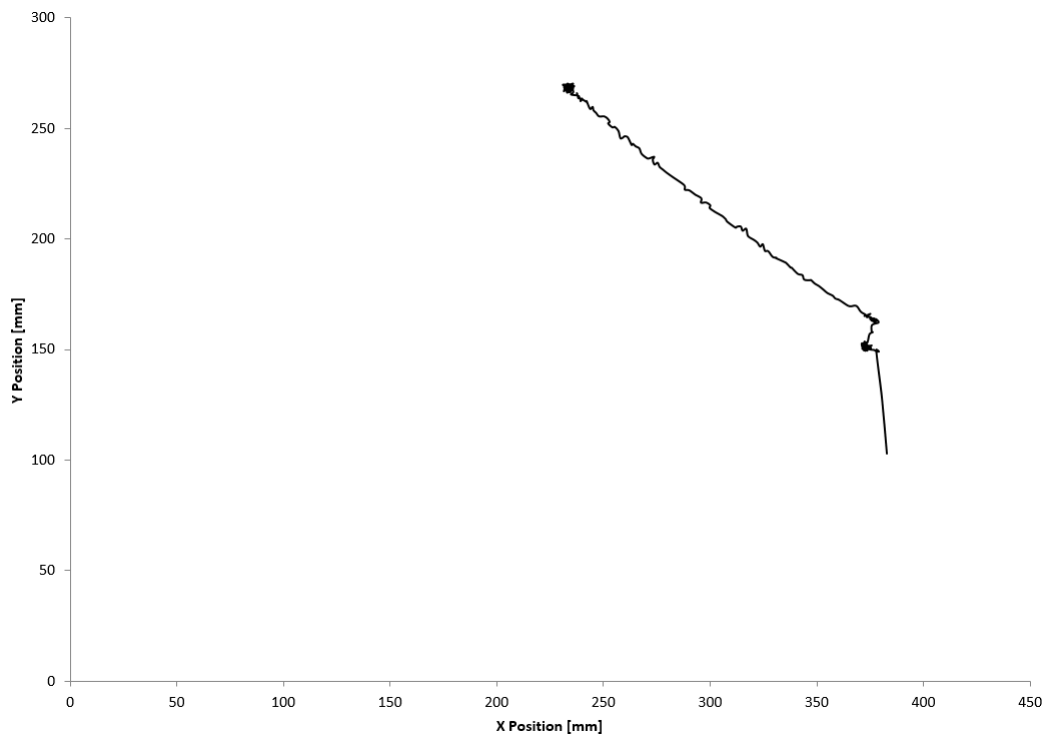


Figure 3.11: Position in X direction (fore-aft) against Y direction (vertical) - Side view on the test setup looking perpendicular to the slope

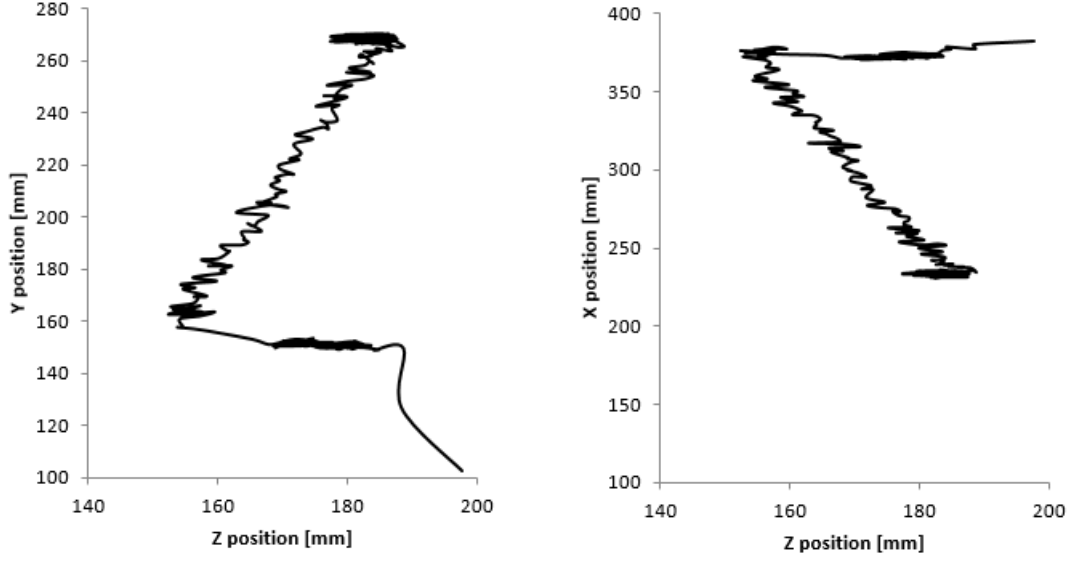


Figure 3.12: left image: frontal view into orifice, Y direction (vertical) against Z direction (lateral) - right image: top view on the test setup looking perpendicular to the roof, X direction (fore-aft) against Z direction (lateral) -

directions, also the time to descend is the longest of the 4 conditions. This would imply the particle has difficulty descending the plate even when a high quantity of water has been injected. This also explains the high variability in the hydrophilic charts, because of the very low overall speeds any small change in direction causes a large relative disruption in the chart. Important to note for the hydrophilic column is the difference between the two tracers, the resin (orange) tracers clearly shows more random behaviour, this can be explained by the fact that the resin particle is painted to prevent leakage of Fluorine-18 ( $^{18}F$ ), yet also causing some surface energy effects itself. For the lateral speeds  $V_z(t)$ , the lateral centre point of the cameras was aligned with the lateral centre of the inclined plate. This has as result that speeds can be both negative and positive as the particle moves left or right from the centreline. For the default PE plate (3rd column) both  $V_x(t)$  and  $V_y(t)$  show a slight offset between the resin and  $Al_2O_3$  particle, they do start in the same matter and achieve fairly similar amplitudes, yet the resin particle takes longer to achieve this top speed. An explanation could be that the resin particle encountered a dry patch and then continued its way down after the area was again sufficiently wetted, achieving in the end the same amplitude as the  $Al_2O_3$  particle. The overall trend for the  $Al_2O_3$  and the resin particle is fairly similar, both max amplitudes and slopes don't show much difference. For the hydrophilic plate, we see a lot of fluctuation due to small absolute changes having a large relative impact, but even here overall amplitudes are similar.

### 3.4.3 Velocities

Because the flow and the tracer particle follow a 45 degree inclined plate, a Cartesian coordinate system was used in this analysis. Due to the 45 degree slope it is expected to find symmetry in the vertical (Y) and fore-aft (X) behaviour. Figure 3.14 shows the velocity in the 3 axes in function of the X position (low X position is at beginning of the slope, high X at the end where the drain is located). Lateral speeds in Z direction are fairly constant during the descent relative to the other 2 direction X (fore-aft) and Y (vertical) that increase during the movement down the plate. The

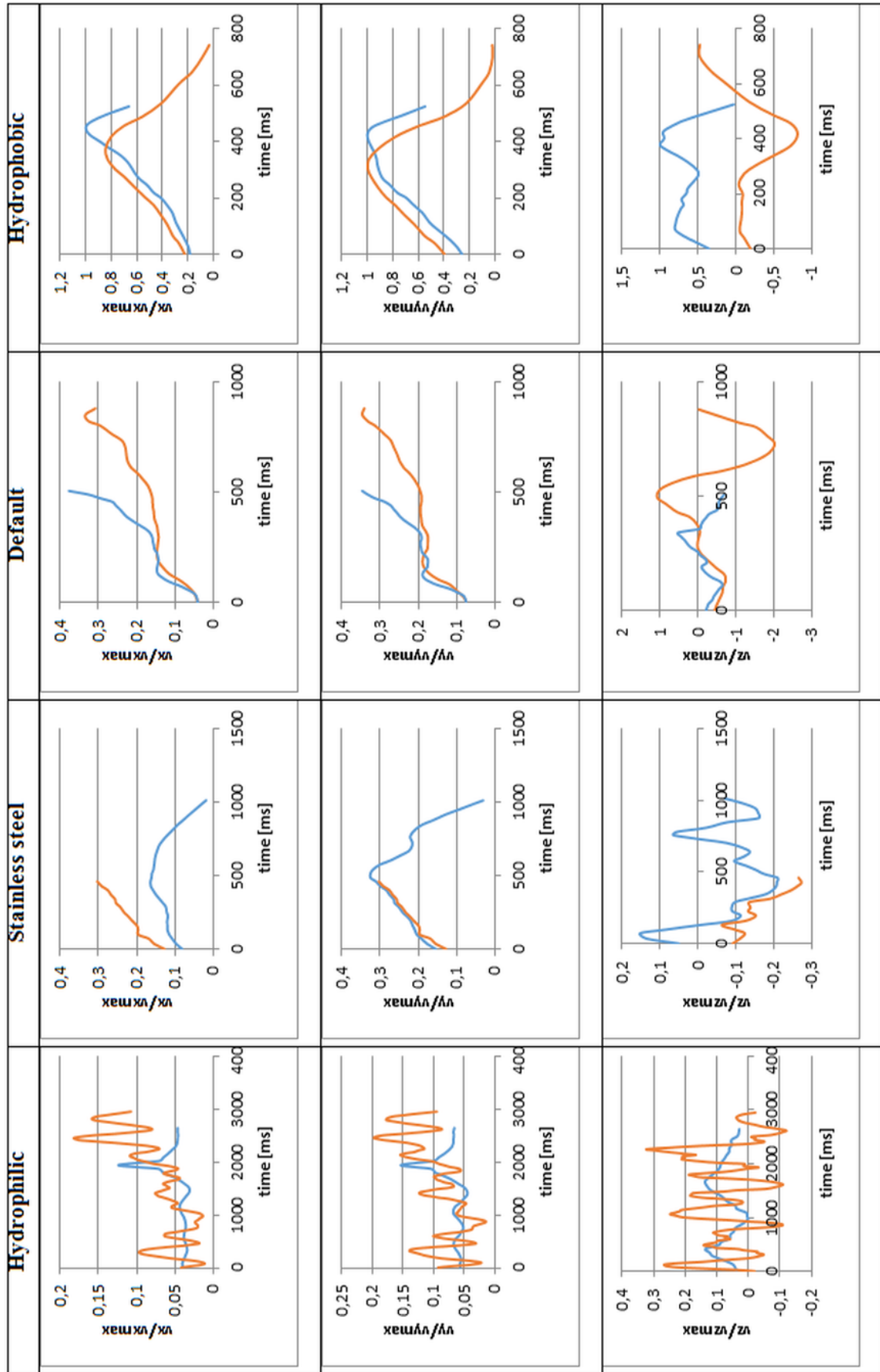


Figure 3.13:  $Al_2O_3$  (blue) and Resin (orange) tracer compared in terms of velocities while moving down the slope:  $V_x$  is the fore-aft velocity,  $V_y$  is the vertical velocity and  $V_z$  is the lateral velocity. Read section 3.4.2 for more detail.

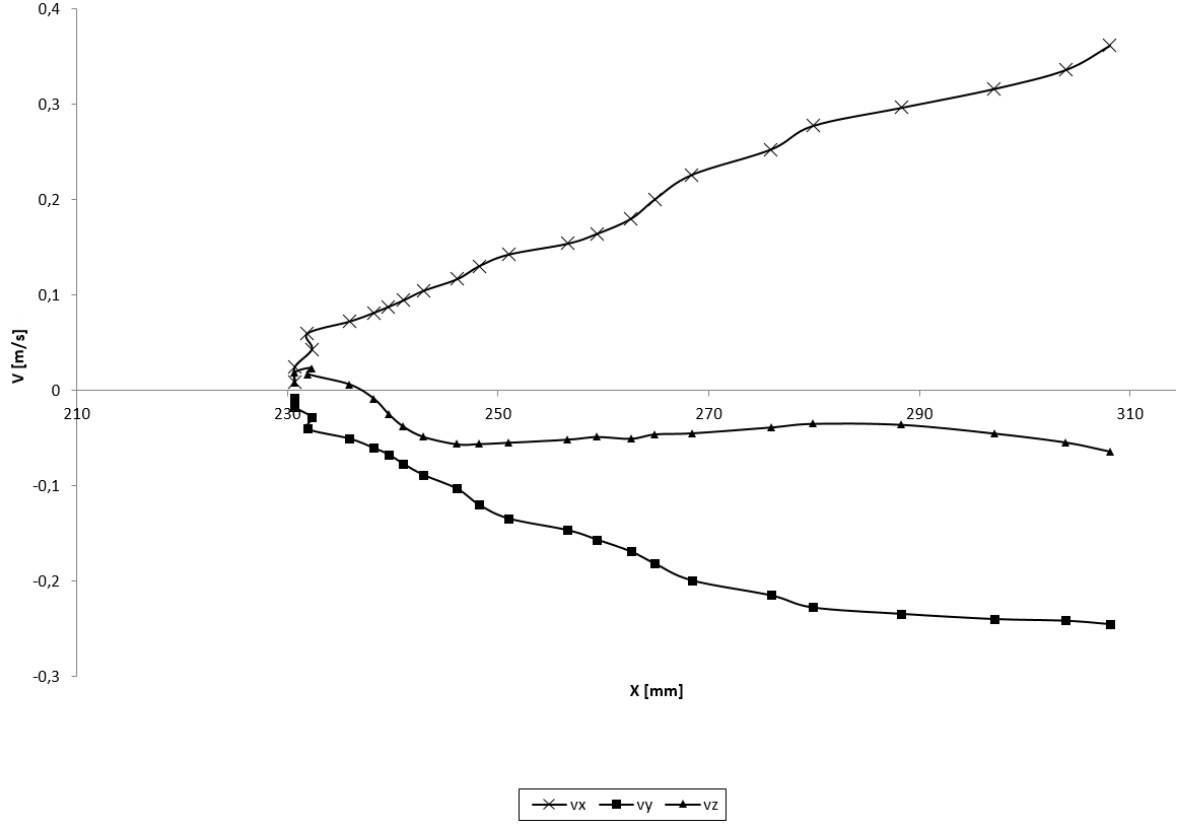


Figure 3.14: Typical tracer velocities of a single measurement in function of the tracer position on the X axis

approximate mirrored image between the 2 datasets is explained by the downwards movement on the slope. Due to the 45 degree angle and the effect of the force balance, it is expected that both X and Y velocities are more or less equal ( $V_x = V_y$  on 45 slope). The lateral speeds observed are always a fraction of the main axis X and Y. The 2 directions that govern the descent of the particle on the inclined plate and indicate best the effect of the surface treatment on the velocity of the particle are fore-aft (X) and vertical (Y). The force balance from the previous chapter indicate that under circumstances a terminal velocity can be achieved that would be characterized by a stabilization of the velocity before the particle reached the slope end, this stabilization does not necessarily have a bad impact on drainage efficiency, but it does need to be spotted in this experiments as it would have an impact on the physics used in the CFD validation following these experiments, for our experiments this is not observed. Figure 3.15 Shows  $V_{xy}$ , with  $V_{xy} = \sqrt{(V_x^2 + V_y^2)}$ , relative to the highest speed ( $V_{xy}$ ) measured across the 4 surface conditions. Highest velocities are observed at the bottom of the inclined plate: this means no critical velocity is reached that would cause the particle to slow down before the bottom is reached. Residence time plots indicate the absolute time the particle spends across the full descent of the inclined plate. The plots can help to indicate the effect of surface treatment by observing the max value of the heat-scale. Because of the 45 degree slope and the linear increase of both vertical and for-aft velocity without reaching a terminal velocity, it will be so that the longer residence times will occur on top of the slope, and that when the particle picks up speed at the end of the descent there the residence time intervals will decrease.

Table 3.4: Median values of velocity for each type of surface condition

Median vel [mm/ms]	$V_x$	$V_y$	$V_z$	spd
Hydrophobic	0.263421	-0.19323	-0.02246	0.32207
Hydrophilic	0.019659	-0.01544	-0.00407	0.02483
Default PE	0.067289	-0.05023	0.016163	0.090121
Stainless steel	0.059012	-0.058	0.003696	0.083357

#### 3.4.4 Effect of surface treatment

To get a better understanding of the effect of the surface treatment, four measurements representing each individual surface condition (default PE, hydrophobic, hydrophilic and stainless steel plate) were selected and overlaid. Measurements showed consistent results for each plate. When we zoom in on the time-frame where the actual motion is occurring we see a distinctive difference between the plates, confirming that the PEPT measurement was able to capture the phenomena we were looking for (influence of surface energy on spatial time distribution of particles). Table 3.4 represents the median values for these parameters. And figure 3.15 plots these differences relative to the position X. Previously it was already discussed and showed that there is minimal difference between the 2 types of tracers. To help create clearer plots in following chapters it was decided to average the values from both tracers for each surface condition. Figure 3.15 was simplified and figure 3.16 was obtained, this will be the plot used for further study. The hydrophilic case showed to be the most unstable during PEPT testing, also in later chapters during simulation it will show high instability during the calculations, in reality this type of surface condition (contact angle = 0 degrees) will never occur in air intake systems, hence the results for the hydrophilic plate are plotted here for reference only.



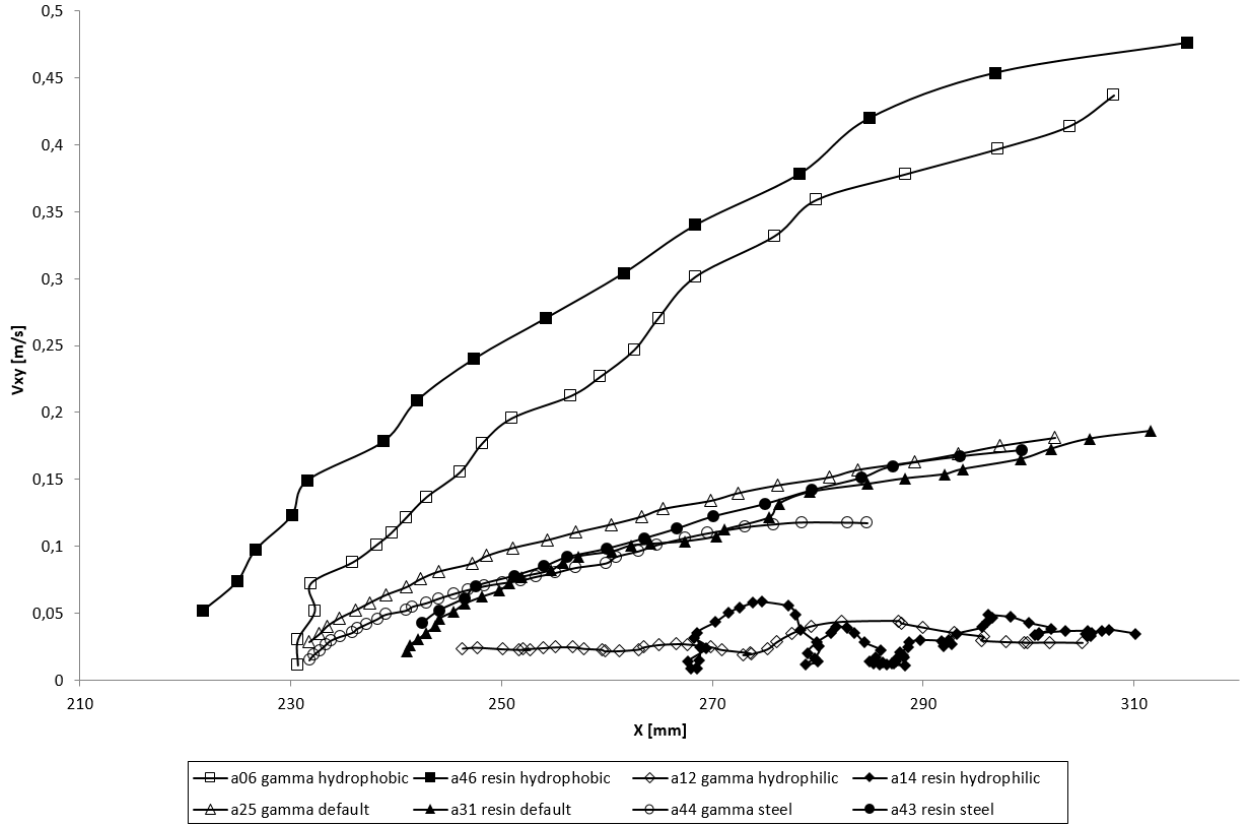


Figure 3.15: Speed down the slope  $V_{xy}$  in function of the position on the slope in horizontal direction  $X$  for both tracer types ( $Al_2O_3$  and resin) and for the 4 different surface conditions

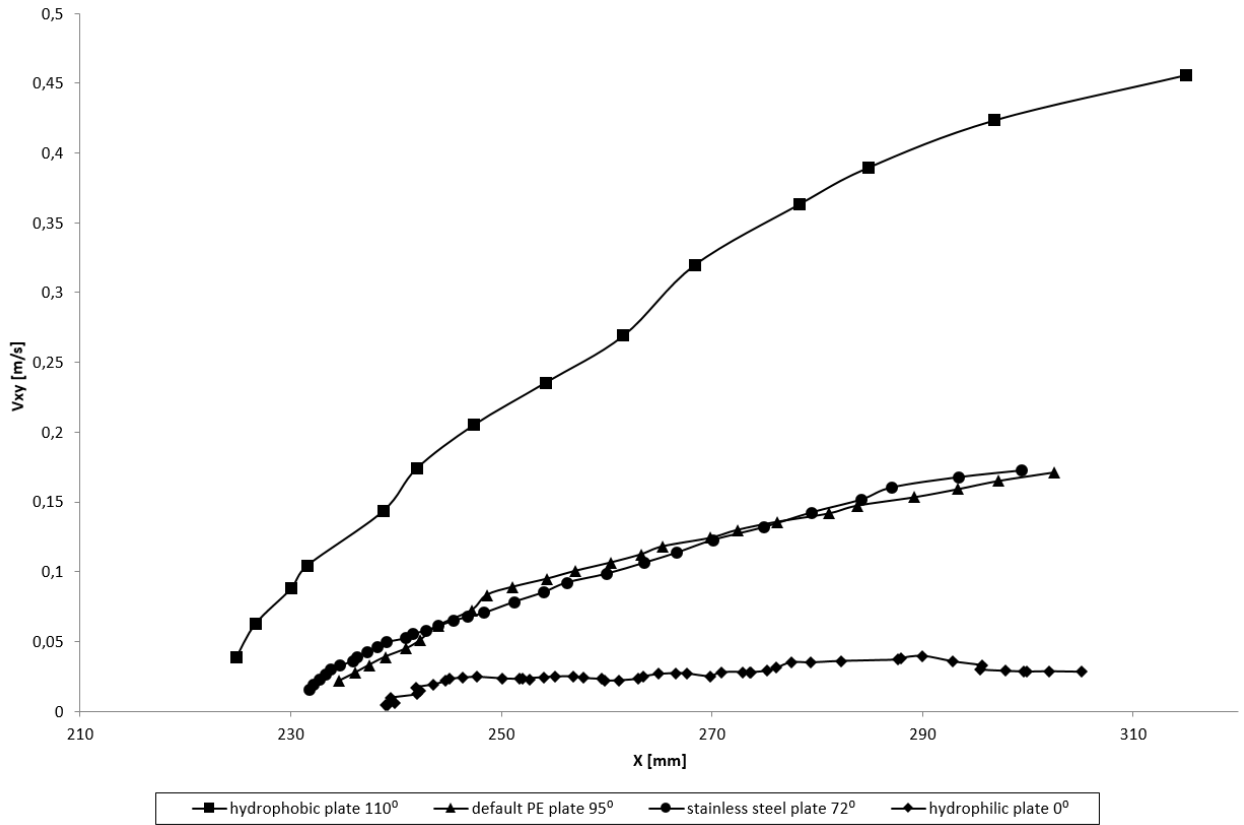


Figure 3.16:  $V_{xy}$  averaged between 2 tracer types for each surface condition

## Chapter 4

# Numerical Method - Introduction

This chapter is dedicated to an introduction of the CFD models as used for our investigation (water ingress into an air intake system going from impingement to draining). For the actual settings of the models and the boundary conditions please refer to chapter 5 for the small scale experimental and to chapter 6 for the full scale AIS, also refer to appendix C and D for the full detail on these parameters. The first 3 sections are dedicated to the main air phase that is present in our model (it is the air moving through the intake system when the engine is running) although it is not the topic of this research it does need to be modelled in order to match the experimental conditions as used in the PEPT laboratory. Since this air phase is solved as a steady state case and then used to initialize the transient case for solving the water migration, limited information is presented on how to model this (for more information on how to model steady state cases in CFD please refer to other works on this topic or when using a commercial CFD code refer to the help files). In section 4 more detail is given to modelling of the water in the air intake system, starting from models that are able to solve the movement of the rain droplets (Lagrangian parcels) into the system over to the water film and VOF models that can tackle the surface energy effect on the behaviour when the water is moving down the slope. In section 5 the possible interaction between those models are discussed, since these will be required to fully simulate the water in all its forms. Subsection 4.5.3 discusses the Lagrangian - Fluid film interaction that is important for our setup, on 1 side for modelling the impingement of the impinging raindrops into the fluid film and secondly the droplet stripping behaviour if the film would be to break up again. Section 4.5.4 covers the models that are available in the CFD code to cover the main research topic being the effect of surface energy on the water behaviour once it is deposited on the slope, both the static and dynamic contact angle method are presented, it is important to mention that for this topic the static method was selected.

### 4.1 CFD Introduction

Fluid dynamics is the study of fluid flow, convective heat transfer and species mass transfer. When fluid dynamics concepts are applied within a computational environment (CFD), a set of mathematical methods are used to obtain an approximate solution for a particular application [43]. Fluid Dynamics are governed by three principles; the conservations of mass, Newton second law and the conservation of energy. For this thesis multiple CFD models were used, however the 2 main parts were the setup for the main air phase and the setup for the liquid phase. For the main air

phase further detail on CFD can always be found in textbooks and help-files of the respective CFD software packages. The part of the multiphase setup is discussed in more detail as it is important for the topic under investigation.

## 4.2 The Navier-Stokes Equations

The governing equations of fluid dynamics are based on three equations; Conservation of mass, conservation of momentum and conservation of energy. The governing equations for unsteady, three dimensional, compressible, viscous flow is:

Conservation of Mass,

$$\frac{d}{dt}M(V_c) = \dot{M}_{in} - \dot{M}_{out} \quad (4.1)$$

Where  $\dot{M}$  is the mass flow rate

Conservation of Momentum,

$$\frac{d}{dt}P(V_c) = L\dot{M}_{in} - L\dot{M}_{out} + \sum F_{ext} \quad (4.2)$$

Where,  $LM$  is the linear momentum and  $\sum F_{ext}$  is the external forces acting on the particle

And conservation of energy,

$$\frac{d}{dt}E(V_c) = E\dot{N}_{in} - E\dot{N}_{out} + \dot{W}_{ext} + \dot{Q}_{in} \quad (4.3)$$

where,  $E\dot{N}$  is energy flux,  $\dot{W}$  is work done per unit time and  $\dot{Q}$  is the heat added per unit time. The derivations of these equations are further explained in this chapter.

## 4.3 Turbulence of the main air phase

This section contains a description of the characteristics of turbulence and the specification of the turbulence model that will be used in this thesis. Since the droplets in our experiments are suspended in the air surrounding them, the turbulence model mentioned here is used for the main air phase. Typical air filtration equipment is seeing turbulent behaviour around the intake orifices and inside the air intake system itself. The behaviour and characteristics of a fluid in motion is mainly dependent on the Reynolds number which is a dimensionless parameter and defined as

$$Re = \frac{vL}{\nu} \quad (4.4)$$

where  $v$  is the velocity,  $L$  is the characteristic length and  $\nu$  is the kinematic viscosity of the fluid. The equation is a ratio between the inertial and viscous forces in the fluid that determines the regime of the flow. When viscous forces dominate, the fluid travels smoothly in the domain and the forces acting for rapid fluctuations is suppressed by the forces acting to keep the flow in a steady behaviour. The flow is then said to be laminar. On the other hand when the inertial forces dominate over the viscous forces and the Reynolds number is sufficiently large, the flow will become unsteady and fast fluctuations in the flow will occur.

In industrial and automotive practices, when environmental air is moving through an air intake system this falls largely in the turbulent regime. A number of turbulent eddies of different length scales and intensities exist throughout the intake systems in the turbulent flow. The motion of the turbulent eddies play a significant role in promoting the ingestion of water, therefore, the turbulent regime is generally adding difficulty. The behaviour of turbulent flows are more difficult predict than laminar flows since the presence of turbulence will make the flow unsteady. A mathematical approach in CFD to handle turbulent flow is to introduce two-equation turbulence models where two more transport equations are modelled and solved together with the continuity and momentum equations. The choice of right turbulence model is crucial since some of the models are very CPU and time demanding. One of the most common turbulence models is the k-epsilon model and is described in the next section.

### 4.3.1 The k-epsilon turbulence model

The  $k - \epsilon$  model adds an additional two transport equations which are solved simultaneously with the continuity and momentum equations. The model has three versions which all solve for the turbulent kinetic energy ( $k$ ) and the turbulent dissipation rate ( $\epsilon$ ) but the approach to solve these equations are different for all of them. The simplest of these models is the standard  $k - \epsilon$  model and was the first one to be developed. The standard model has its strengths but also weaknesses, and improvements from this model have been made and the outcome is the Re-normalization Group (RNG)  $k - \epsilon$  model and the realizable  $k - \epsilon$  model. In this thesis we will use the realizable  $k - \epsilon$  two layer model. The main difference between the realizable model and the other two is that the realizable satisfies certain mathematical constraints on the Reynolds stresses, which in the standard and RNG model may become negative although by definition it is positive. The transport equations for the turbulent kinetic energy  $k$  and dissipation  $\epsilon$  to solve are the following:

$$\frac{\partial}{\partial t}(\rho k) + \nabla \cdot (\rho k \bar{v}) = \nabla \cdot \left[ \left( \mu + \frac{\mu_t}{\sigma_k} \right) \nabla k \right] + G_k + G_b - \rho \epsilon - Y_m + S_k \quad (4.5)$$

$$\frac{\partial}{\partial t}(\rho \epsilon) + \nabla \cdot (\rho \epsilon \bar{v}) = \nabla \cdot \left[ \left( \mu + \frac{\mu_t}{\sigma_k} \right) \nabla \epsilon \right] + \rho \epsilon C_1 S + \rho C_2 \frac{\epsilon^2}{(k + \sqrt{\nu \epsilon})} + C_{1\epsilon} \frac{\epsilon}{k} C_{3\epsilon} G_b + S_\epsilon \quad (4.6)$$

Where  $G_k$  and  $G_b$  represents the generation of turbulent kinetic energy due to the mean velocity gradients and the generation of turbulent kinetic energy buoyancy respectively.  $Y_m$  is the contribution of fluctuating dilatation in compressible turbulence to the overall dissipation rate,  $\sigma_k$  and  $\sigma_\epsilon$  are the turbulent Prandtl numbers for  $k$  and  $\epsilon$  respectively and  $S_k$  and  $S_\epsilon$  are user defined source terms.

## 4.4 Multiphase Models

The term phase usually refers to the thermodynamic state of matter (Solid, Liquid or Gas) In modelling terms, it can also refer to other characteristics, i.e. liquids of different density, bubbles of different size, solid granules of different size and/or weight. Concerning multiphase flows, DNS and LES have been employed in very few studies, and RANS is more suitable and has received extensive attention. In the RANS approach, the Eulerian-Lagrangian approach (Euler-Lagrange,

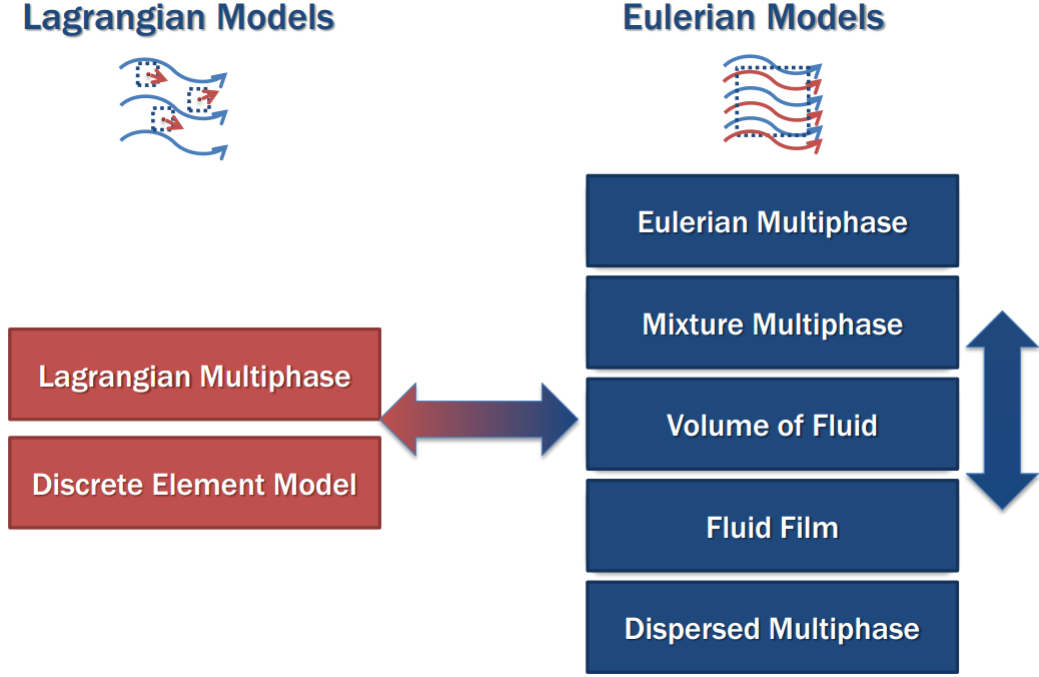


Figure 4.1: overview of multiphase models

Lagrangian Multiphase, LMP) where the observer tracks parcels of particles as they move through space and time, simulates the solid phase as a discrete phase and so allows particle tracking, in addition, the physical effects such as the particle-turbulence interaction on the particle motion can be modelled. However, the effect of surface tension on a discrete particle cannot be considered. The multi-fluid Eulerian-Eulerian model (Euler-Euler, Eulerian Multiphase, EMP) where the observer considers the particles, bubbles, or droplets to be a continuum passing through a fixed volume is capable of predicting the effect of surface tension.

#### 4.4.1 Multiphase models: Lagrangian multiphase or LMP

The Navier-Stokes equations are solved for the continuous phase while the equations of motion are solved for representative parcels of the dispersed phase as they pass through the system. Well suited for cases where the volume fraction of the dispersed phase is relatively small, and where interaction with solid boundaries is important, i.e. vehicle soiling, spray coating, cyclone separation, erosion, aerosol dispersion, liquid fuel combustion, spray cooling.

Lagrangian specification uses the initial position of a fluid particle as a reference to identify changes to a moving particle [45]. In other words, the measuring instrument or the computational mesh is not in a fixed position, instead, the mesh computes and reports the fluid changes while moving through the fluid domain [50]. Thus, every fluid particle has a unique equation following its path. Since, the fluid domains have infinite numbers of particles, the position of any individual particle is identified by stipulating its position  $x_0$  at time  $t = 0$ . Hence this equation can be used to locate the position of individual particle  $x$  at any given time  $t$  [47].

$$x = x(t, x_0) \quad (4.7)$$

When Lagrangian specification follows large distortions of the fluid domain it attempts to

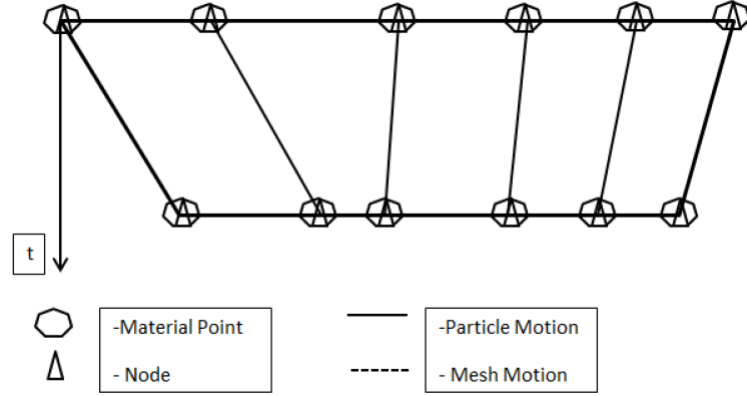


Figure 4.2: Lagrangian method

regenerate the meshing operations recurrently. As a result, this will consume large amounts of computing power when creating the mesh [51]. For instance, let's consider an example of measuring the temperature of a flowing stream of a river using a thermometer. Also, the thermometer is fixed in to a very light boat and the boat moves at exactly the same rate as the flowing stream. In this example, because the thermometer moves with the fluid particle, it will be reading the temperature of the same fluid particle with respect to time [47]. Hence, the distorted areas of the mesh will frequently regenerate with time.

The generic term particle is used in the CFD code to describe solid particles, liquid droplets, gas bubbles and massless (virtual) particles. Valid for dilute dispersed phases like motion dominated by interaction with the continuous phase rather than interaction with other particles. Coupling can be one or two way. There can be an arbitrary number of dispersed phases, for each dispersed phase, particle-like elements known as parcels are followed through the continuum.

On these parcels there are several forces acting: drag force, shear lift due to velocity gradient normal to relative motion, pressure gradient force due to difference in pressure across a particle due to its size (also includes the effects of buoyancy), virtual mass force is the force on a particle as it accelerates through the surrounding continuous phase, coulomb force is the electrostatic force acting on charged particles and can be used with field charging to simulate particles charging in an electric field, turbulent dispersion employs random walk to synthesize effect of turbulent velocity field on the dispersed phase(s), user-defined body force allows user to customize particle momentum equation by adding a term.

Mass and heat transfer can also act on these parcels: droplet evaporation and condensation with single and multi-component options, coal combustion simulates the transport, gasification, and combustion of coal particles, particle reaction includes particle combustion and de-volatilization with the option for user depletion criteria to remove particles from the domain, heat transfer with the continuous phase and heat transfer between Lagrangian particles and wall boundaries can be accounted by the impingement heat transfer model, Radiation accounts for the scattering and absorption of radiation due to particles and calculates the radiation that is emitted from the particles themselves.

Since the water ingestion model is a multiphase model (gas-liquid phase) and water droplets will be injected into the computational domain, the CFD code solves the equations of motion for water droplets. In a Lagrangian reference frame the CFD code solves the equation by integrating

the force balance on the particle. The force balance equates the particle inertia with the forces acting on the particle and is given in vector form below.

$$\frac{\partial \bar{v}_p}{\partial t} = F_D(\bar{v} - \bar{v}_p) + \frac{\bar{g}(\rho_p - \rho)}{\rho_p} + \bar{F} \quad (4.8)$$

where  $v_p$  is the velocity of the particle,  $F_D$  is the aerodynamic drag force,  $v$  is the fluid velocity,  $g$  is gravity,  $\rho_p$  is the particle density,  $\rho$  is the fluid density and  $\bar{F}$  is an additional force term due to the pressure gradient and virtual mass, this term contains the force required for accelerating the fluid surrounding the particle and forces due to pressure gradients in the fluid. The term on the left hand side represents the acceleration of the particle, the first on the right hand side represents force due to aerodynamic drag and the second due to gravity.

The CFD code has different kinds of particle types and each particle type is associated to different physical laws of heat and mass transfer. All simulations that have been done with discrete particles, uses an inert particle type. The inert particle type activates the inert heating or cooling laws when the particle temperature is less than the vaporization temperature,  $T_{vap}$ , and when the volatile fraction,  $f_{v0}$ , of a particle has been consumed.

The two conditions may be written as  $T_p < T_{vap}$  and  $m_p \leq (1 - f_{v,0})m_{p,0}$  where  $T_p$  is the particle temperature,  $m_{p,0}$  is the initial particle mass and  $m_p$  its current mass. When using an inert particle and the above condition, the particle temperature is related to a simple heat balance equation. In all the CFD code simulations the energy equation has been deactivated and hence there is no temperature simulation.

#### 4.4.2 Multiphase Models: Eulerian Multiphase - VOF

According to the Encyclopaedia of Computational Mechanics, Eulerian specification is broadly used in mathematical modelling of fluid dynamics simulations [51]. Eulerian method involves measuring the fluid motion with respect to fixed instruments [45]. In other words, the measurement instrument or computational mesh is considered to be fixed and the fluid domain is moving relative to the mesh. Mathematically, the velocity  $v$  at every spatial point  $x$  in the fluid domain can be calculated at any instant of time  $t$  using equation [47].

$$v = v(x, t) \quad (4.9)$$

A trivial example would be identifying the velocity of stream flow in a river using a flow meter [48]. Depending on the river bank location that the flow meter is fixed, the velocity of the flow could be either fast or slow at any given time. Also, the flow meter is measuring the velocity of the fluid particles as they pass a fixed point. Hence, the fluid domain is not calculated as it changes; instead, the calculations are centred on a fixed three-dimensional domain, and the fluid flows through it [47].

This model is mainly used to track the motion of the interfaces between immiscible fluids as seen in free surface flows. Typically used where the interface between the phases is well defined such as large free surfaces present in hydrodynamic simulation. The volume of fluid approach is classed as a Eulerian multiphase model but is more generally referred to as VOF. It is well suited for: marine hydrodynamics and sea-keeping, fuel tank sloshing, oil and gas flow assurance and internal combustion engine cooling. It is also suited for immiscible fluids: Grids capable of re-

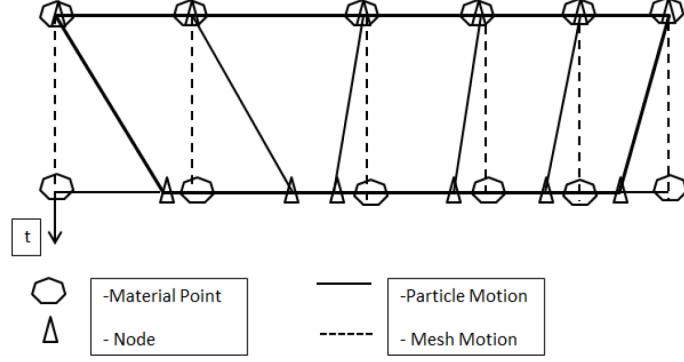


Figure 4.3: Eulerian method

solving phase interface, sharp resolved interface between phases with no need to model inter-phase interaction on a sub-grid scale as with Eulerian Multiphase. It can also include contact angle, predefined VOF waves for marine simulations and phase change (boiling, evaporation/condensation, solidification/melting, cavitation). An important parameter that is not used for this thesis is the dynamic contact angle (see also section 4.5.4): the contact angle can be set as a dynamic rather than a static value through the Kistler model [42]. Advantages are separate advancing and receding contact angles with blended treatment in-between, alternatively a new field function for capillary number is available, it allows user defined dynamic models, other laws such as Tanner’s law can be set up via field functions (see also section 4.4.4).

#### 4.4.3 Multiphase Models: Fluid Film

Fluid film modelling is a component of the Eulerian Multiphase framework in the CFD code. It does not occupy a physical volume, instead it is represented as a thickness value on the surface. Used for modelling the distribution of a thin layer of fluid on a solid surface it takes into account accumulation, removal and transportation. It has multiple application areas: vehicle soiling, condensation, fuel spays, lubrication, spray coating deposition and wing icing. The fluid film model solves transport equations for mass, momentum, energy, species- and volume-fraction. The model exists on a shell region so it does not occupy volume, blockage is numerically accounted for and it does not change the effective shape of the wall.

The Fluid Film models the thickness and flow of a thin layer of liquid, it can receive mass from impinging Lagrangian, Eulerian or Dispersed Multiphase droplets and shed droplets back into Lagrangian or Dispersed Multiphase phases via wave and edge stripping. Films of variable thickness can be modelled with the VOF-Film multiphase interaction model.

The conservation equation for the wall film particles includes momentum, mass and energy (energy not used in our setup). If only the wall film height and its velocity are of interest, is it enough to study the momentum equation and reads:

$$\rho h \frac{d\vec{v}_p}{dt} + h(\nabla_s p)_\alpha = \tau_g \vec{t}_g + \tau_w \vec{t}_w + \dot{P}_{imp,\alpha} - \dot{M}_{imp,\alpha} \vec{v}_p + \dot{F}_{n,\alpha} + \rho h(\vec{g} - \vec{a}_w) \quad (4.10)$$

Where  $\alpha$  denotes the current face on which the particle resides,  $h$  is the current film height at the particle location,  $\nabla_s$  is the gradient operator restricted to the surface, and  $p$  is the pressure on the surface of the film,  $\tau_g$  is the magnitude of the shear stress of the gas flow on the surface



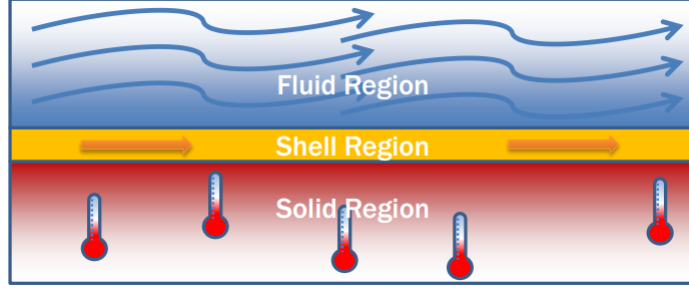


Figure 4.4: The Fluid Film exists on a shell region which has boundary conditions which are exactly the same as a full 3D region, except flow enters or exits along an edge rather than through a surface

of the film,  $\vec{t}_g$  is the unit vector in the direction of the relative motion of the gas and the film surface,  $\tau_w$  is the magnitude of the stress that the wall exerts on the film,  $\vec{t}_w$  is the unit vector in the direction of the relative motion of the film to the wall and  $\rho h(\vec{g} - \vec{a}_w)$  is the body force term where  $\vec{a}_w$  corresponds to the acceleration rate seen in simulations with moving boundaries. The remaining expressions are  $\dot{P}_{imp,\alpha}$  which denotes the impingement pressure on the film surface,  $\dot{M}_{imp,\alpha}$  is the impingement momentum source, and  $\dot{F}_{n,\alpha}$  is the force necessary to keep the film on the surface.

## 4.5 Multiphase Interaction Models

Each multiphase model is suited to a different regime whereas real flow problems cover multiple flow regimes. Therefore multiphase interaction models let you harness multiple phase models in a single simulation. Models can interact exchanging mass, momentum and energy by various mechanisms. It opens up many otherwise complex applications and allows users to make the best use of resources. Figure 4.5 illustrates the wide array of interaction models typically available.

### 4.5.1 Multiphase interaction model: LMP - VOF

This interaction reduces computational expense for applications where droplets otherwise have to be fully resolved. Lagrangian Impingement into VOF: The first step towards full interaction between Lagrangian droplets and VOF because modelling small droplets in VOF can become very expensive. When using Film-VOF models, Lagrangian droplets can impinge into both Film and VOF, it is available for both single and multicomponent droplets. Typical applications are: crankcase and gearbox sloshing, part dipping/coating, rainwater management (as will be used this thesis). In our study it represents the impingement of water droplets that represent the rain onto already existing surfaces of water inside the air intake system.

### 4.5.2 Multiphase interaction model: Fluid Film - VOF

Fluid film with VOF multiphase interaction as illustrated in figure 4.6 is a hybrid approach that dramatically reduces computational cost and mesh count. The interaction model selects the most suitable approach for local flow regime and resources available. The two-way transition is based on film thickness: fluid film transitions into VOF when it becomes thick compared to the mesh,

	<b>EMP</b>						
<b>VOF</b>	EMP-LSI Model EMP and VOF are incompatible, but above model is equivalent	<b>VOF</b>					
<b>MMP</b>	Incompatible	Incompatible	<b>MMP</b>				
<b>DMP</b>	Incompatible	Compatible, but no phase interaction	Compatible, but no phase interaction	<b>DMP</b>			
<b>LMP</b>	Incompatible	LMP -> VOF Impingement	Compatible, but no phase interaction	Compatible, but no phase interaction	<b>LMP</b>		
<b>DEM</b>	Incompatible	Compatible, but no phase interaction	Compatible, but no phase interaction	Compatible, but no phase interaction	Compatible, but no phase interaction	<b>DEM</b>	
<b>Fluid Film</b>	<ul style="list-style-type: none"> <li>EMP -&gt; Film Impingement</li> <li>Evaporation/Condensation</li> </ul>	VOF <-> Film Hybrid Film	Incompatible	<ul style="list-style-type: none"> <li>DMP -&gt; Film Impingement</li> <li>Film -&gt; DMP Stripping</li> </ul>	<ul style="list-style-type: none"> <li>LMP -&gt; Film Impingement</li> <li>Film -&gt; LMP Stripping</li> </ul>	Incompatible	<b>Fluid Film</b>

Figure 4.5: overview of multiphase interaction models, green are interactions that are expected to deliver good results, orange is possible but with limitations, and red are interaction models that are not possible

VOF transitions into Fluid Film when it becomes thin compared to the mesh. If the combined thickness of the film of VOF and Fluid Film fills more than half the cell, the Fluid Film portion will be converted into VOF, if the combined thickness of the film of VOF and Fluid Film fills less than half the cell, the VOF portion will be converted into Fluid Film, transitions occur at a finite rate so locally Fluid Film and VOF can coexist.

#### 4.5.3 Multiphase interaction model: Fluid Film - LMP

Impact of droplets into film as illustrated in figure 4.6 is referred to as impingement (the fluid film accepts mass from impinging Lagrangian, Eulerian (single or multi-component) or dispersed multiphase droplets), the reverse is referred to as stripping. The Lagrangian and Fluid Film interaction model is a hybrid approach for modelling droplets interacting with fluid films. It is computationally cheaper than the alternative VOF-Film approach, however more expensive than alternative DMP-Film approach because it includes more physics than DMP such as droplet bounce and breakup. Droplet stripping can occur in 2 conditions: wave, where droplets are stripped due to instabilities in (unresolved) waves in the fluid film and edge, where droplets are stripped when fluid film flows over a sharp edge. Previously stripped droplets can always re-impinge the fluid film. For our setup only the impingement will play a significant role, stripping is less important for this thesis, yet it does need to be considered when the AIS geometry has sharp corners and narrow areas in the duct work.

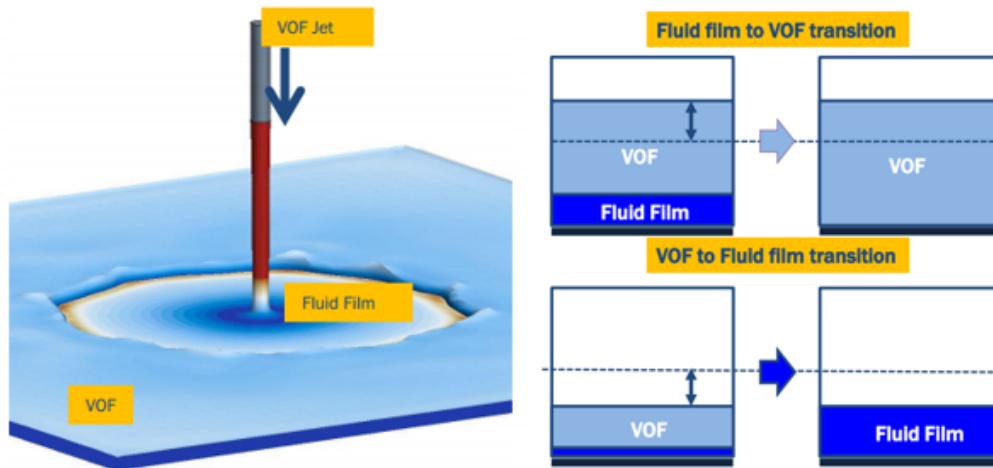


Figure 4.6: VOF jet impinging onto fluid film, which then undergoes a hydraulic jump back into VOF

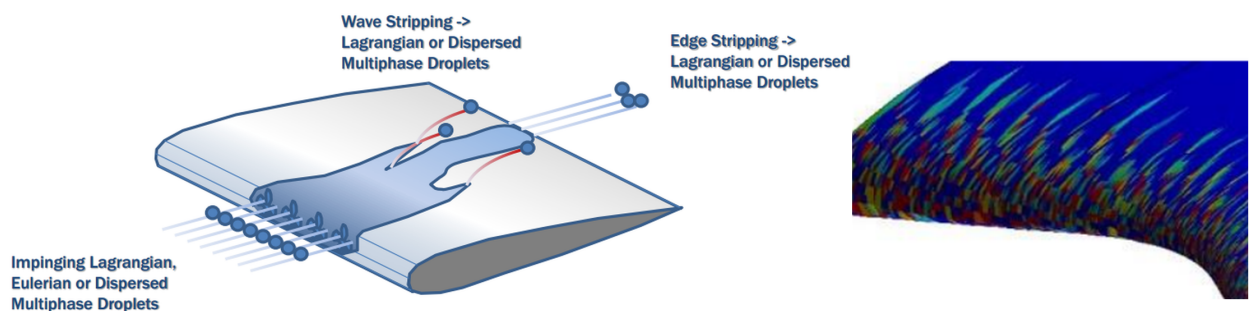


Figure 4.7: Left: Lagrangian impingement and stripping (both edge and wave) - Right: droplet impingement shows discrete impact zones

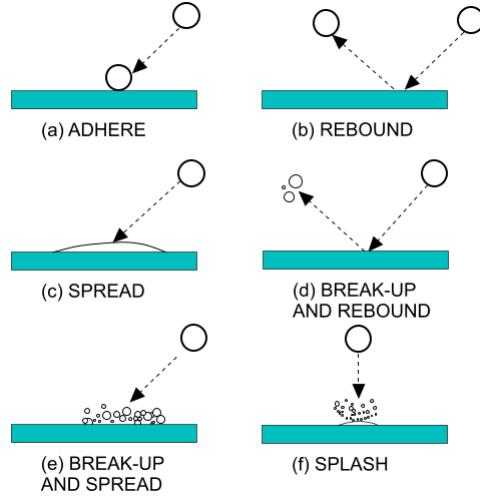


Figure 4.8: Lagrangian impingement regimes

### Bai-Gosman Impingement

When using Lagrangian parcels as the impinging phase, impingement can be patchy due to the discrete nature of the Lagrangian injections. To mitigate against this a large number of injection points are required together with some degree of randomization. This approach can be used to give a smooth impingement but is computationally expensive. Typically the Lagrangian injection is from a dense presentation grid (derived part), so it is not limited to the mesh density. A random selection of these points on this grid are used for injection at each timestep (Point inclusion probability with re-randomization.) Turbulent dispersion may also be used to further randomize impingement sites. All this combined gives a uniform impingement over time.

The impact of particles on rigid solid surfaces produce a variety of effects. These effects depend on the size, the velocity, the material of the impacting particles and they depend on the nature of the surface. A liquid droplet, for example, can stick, bounce, or splash. The liquid that is deposited on the wall can retain the droplet form or it can merge into a fluid film. The Bai-Gosman model aims to predict the outcomes of liquid droplets impacting an impermeable boundary (wall) or fluid film.

The Bai-Gosman model [60] [61] [62] categorizes possible outcomes as being in one of six possible regimes, illustrated in figure 4.8. For fluid film boundaries, momentum and kinetic energy lost by the droplets are gained by the film. The choice of regime for a given impingement event is made using four parameters:

- The incident Weber number  $We_I$ .
- The Laplace number  $La$ .
- The boundary temperature  $T_w$  (provided the Energy model is active in the physics continuum).
- The dry wall state (a boundary can be either wet or dry, for fluid film boundaries, this is determined by the presence or absence of a fluid film)
  - At Weber numbers below  $We_c$  and wall temperatures below  $T_{12}$  impinging droplets spread out on the wall.

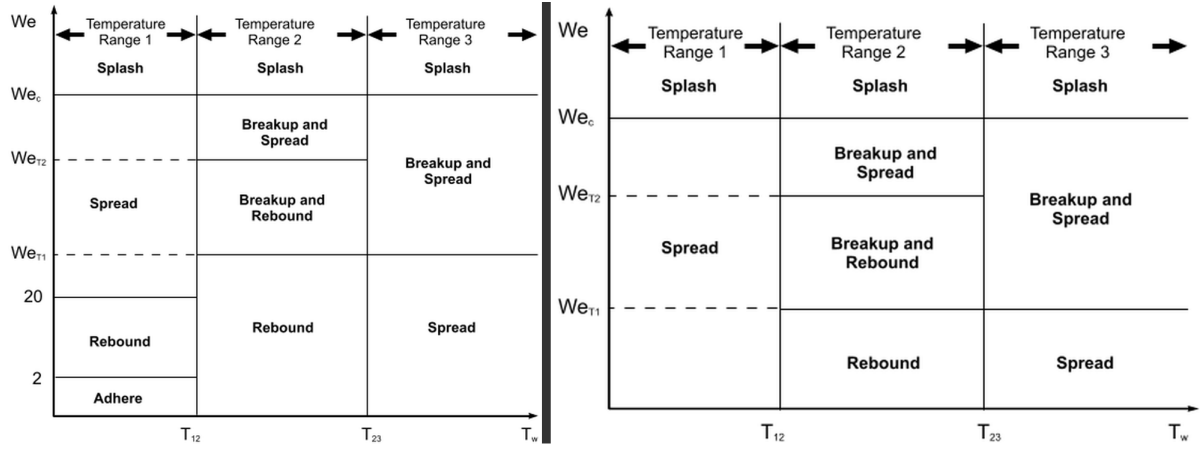


Figure 4.9: Left: The transition criteria for wetted walls - Right: for dry walls

- At higher Weber numbers or wall temperatures, droplets can spread, break up and spread, break up and rebound, or rebound.
- Above  $We_c$ , impinging droplets splash.
- The wet wall state
  - At Weber numbers below 2 and wall temperatures below  $T_{12}$ , impinging droplets adhere to the wall.
  - At higher Weber numbers or wall temperatures, droplets can spread, break up and spread, break up and rebound, or rebound.
  - Above  $We_c$ , impinging droplets splash.

$T_{12}$  separating range 1 from range 2, is expected to be approximately the boiling temperature of the droplet.  $T_{23}$  separating range 2 from range 3, is expected to be approximately the Leidenfrost temperature of the droplet.

### Droplet Stripping: Wave

Droplets can be stripped in 2 ways: wave stripping (as illustrated in figure 4.10) where droplets are stripped due to instabilities in (unresolved) waves in the fluid film and edge stripping (as illustrated in figure 4.11) where droplets are stripped when the fluid film flows over a sharp edge. With the current version of the CFD software it is possible to strip into Lagrangian or Dispersed Multiphase droplets (or to remove the stripped mass if accounting the mass is not important, which can be an important time gain during initial design iterations). Waves develop at the liquid-gas interface due to velocity difference at the interface. The waves become unstable and form cylinders of liquid which are ejected into the surrounding gas (Kelvin-Helmholtz instability). The cylinders then break up further forming spherical droplets (Rayleigh-Taylor instability). Surface break-up is determined by computing the resonance wavelength, which is a function of the body force acting on the film (including the inertial force)  $fb$ , the relative velocity between the film and the surrounding fluid  $v$  and the surface tension,  $\sigma$ . If the film height exceeds a minimum derived from this wavelength, stripping will occur. The film height stripped into an ejected cylinder is based on the surface wave amplitude. From this the stripped droplet diameter can be calculated.

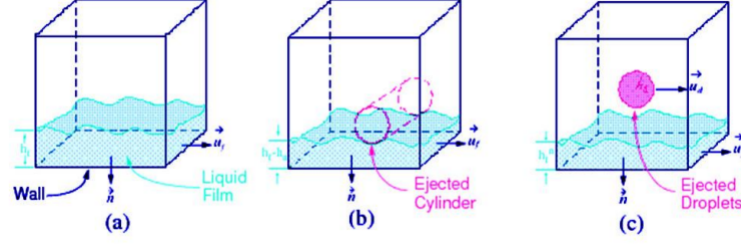


Figure 4.10: Wave Stripping: Droplet formation from wave

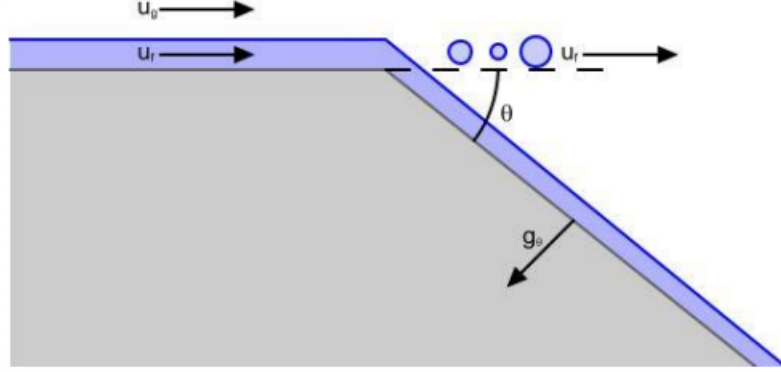


Figure 4.11: Edge Stripping: Droplet formation from sharp edge

### Droplet Stripping: Edge

If edge stripping is enabled, droplets are shed from edges where the corner angle is greater than the user-defined minimum corner angle,  $\tau$  as shown in figure 4.11. The break-up of the film is then modelled to give a droplet size distribution based on a force balance determined from: the film momentum flux, surface tension and gravity. The shed parent droplet size is a function of: the film height at the edge and the most unstable wavelength, the droplet size distribution is then based on the parent droplet size and a Rosin-Rammler size distribution.

Edge stripping models the break-up of the liquid film over a sharp edge. In [67] was proposed a model for the break-up of liquid films over a sharp edge. This model is based on the Rayleigh-Taylor instability and contains the break-up criterion and resulting droplet diameter distribution. However, in [68] questions were raised about the validity of the breakup criterion. Therefore, an alternative criterion is adopted, proposed in [69], that is based on a force balance. The droplet diameter distribution still follows [67].

The model is only applied at edges where the corner angle ( $\theta$  in 4.11) is greater than the user-defined minimum corner angle. If a boundary cell has multiple sharp edges, stripping occurs over all of them in a weighted manner. The force ratio  $FR$ , which is essentially the ratio of the film momentum flux to the surface tension and gravity force, is:

$$FR = \frac{We_f}{1 + \frac{1}{\sin\theta} + Bo_f \frac{L_b}{h_f \sin\theta}} \quad (4.11)$$

where  $We_f$  is the film Weber number,  $Bo_f$  is the Bond number,  $L_b$  is the break-up length and  $h_f$  is the film thickness.

The film Weber number is:

$$We_f = \frac{\rho_f v_f^2 h_f}{\sigma} \quad (4.12)$$

where  $\rho_f$  is film density,  $v_f$  is film velocity projected orthogonal to the stripping edge,  $h_f$  is film thickness and  $\sigma$  is film surface tension.

The film Bond number is:

$$Bo_f = \frac{\rho_f g_\theta h_f^2}{\sigma} \quad (4.13)$$

where  $g_\theta$  is the component of acceleration normal to the downstream wall.

In [70] the break-up length is given as:

$$L_b = 0.0388 h_f^{0.5} Re_f^{0.6} We_{rel}^{-0.5} \quad (4.14)$$

where  $Re_f$  is the film Reynolds number and  $We_{rel}$  is the relative Weber number.

The film Reynolds number is:

$$Re_f = \frac{\rho_f v_f h_f}{\mu_f} \quad (4.15)$$

where  $v_f$  is the film viscosity.

The relative Weber number is:

$$We_{rel} = \frac{h_f \rho_g (u_g - u_f)^2}{2\sigma} \quad (4.16)$$

where  $\rho_g$  is the gas density and  $u_g$  is the gas velocity projected orthogonally to the stripping edge.

The break-up is deemed to occur when  $FR > FRC$  where  $FRC$  is the user-defined critical force ratio. The critical force ratio default value is 1. Of the fluid crossing the edge, only a fraction  $x_S$  separates from the film. This fraction is approximated using the formula below:

0	$FR \leq FRC$
$0.44(FR - FRC)$	$FRC < FR \leq (FRC + 1.6)$
$0.057(FR - FRC - 1.6) + 0.704$	$(FRC + 1.6) < FR \leq (FRC + 6.792)$
1	$(FRC + 6.792) < FR$

which is based on the experimental data in [69]. For droplet formation, model in [69] is adopted, which estimates the parent droplet diameter  $D_d$  as:

$$D_d = c_1 \sqrt{\frac{\lambda h_f}{\pi}} \quad (4.17)$$

where  $c_1$  is a user-defined droplet diameter scale factor. This factor is set to 3.78 by default. The wave length  $\lambda$  is calculated from the wavenumber  $k$ ,

$$\lambda_m = 2\pi/k \quad (4.18)$$

with wavenumber  $k$  which maximizes the growth rate:

$$\omega = - \left( \frac{\sigma - (\rho_f - \rho_g)a/k^2}{2\mu_f h_f} \right) \left( \frac{(kh_f)\sinh(kh_f)\cosh(kh_f) - k^2 h_f^2}{\cosh^2(kh_f) + k^2 h_f^2} \right) \quad (4.19)$$

where the acceleration  $a$  is computed from:

$$a = \frac{u_f^2 \theta}{h_f(\pi + \theta)} \quad (4.20)$$

You can choose to provide an upper limit for the parent droplet diameter  $D_d$  by activating the limit parent droplet diameter property and supplying a value for the maximum diameter. According to the model, the cumulative droplet size distribution  $F(D)$  is a Rosin-Rammler distribution:

$$F(D) = 1 - e^{-(D/X)^q} \quad (4.21)$$

where  $q$  is a user-defined parameter, which is set to 1.5 by default, and:

$$X = \frac{D_d}{(3\ln 10)^{1/q}} \quad (4.22)$$

There are two options for determining the droplet diameter:

- Generate droplets with a deterministic diameter, namely the average of the size distribution that is:

$$D = X\Gamma\left(1 + \frac{1}{q}\right) \quad (4.23)$$

where  $\Gamma(x)$  represents the Gamma function

- Generate droplets with a randomized diameter  $D$

You can select these options by either activating or deactivating the Randomize droplet diameter property. The droplets are ejected at the film velocity speeds in terms of both magnitude and direction.

#### 4.5.4 Multiphase interaction model: Surface Tension

2 Methods exist to model Surface tension:

- When only considering a static contact angle you can use the computationally cheap method of Fluid Film Surface tension. This is the method used for this thesis (if limited validation with experimental data is obtained then the more costly contact angle method can be used)
- When considering a dynamic contact angle (not used in this thesis) you have to use the more computationally expensive VOF formulation.

Contact angle  $\tau$ , is a quantitative measure of wetting of a solid by a liquid. It is defined geometrically as the angle formed by a liquid at the three phase boundary where a liquid, gas and solid intersect. The well-known Young equation describes the balance at the three phase contact of solid-liquid and gas.



$$\gamma_{sv} = \gamma_{sl} + \gamma_{lv} \cos \phi_Y \quad (4.24)$$

The inter-facial tension from the equilibrium contact angle of wetting, many times referred as Young contact angle. It can be seen that the low contact angle values indicate that the liquid spreads on the surface while high contact angle values show poor spreading. If the contact angle is less than 90 degrees it is said that the liquid wets the surface, zero contact angle representing complete wetting. If contact angle is greater than 90 degrees, the surface is said to be non-wetting with that liquid. Contact angles can be divided into static and dynamic angles. Static contact angles are measured when droplet is standing on the surface and the three phase boundary is not moving. Static contact angles are utilized in quality control and in research and product development. Contact angle measurements are used in fields ranging from printing to oil recovery and coatings to implants. When the three phase boundary is moving, dynamic contact angles can be measured, and are referred as advancing and receding angles. Contact angle hysteresis is the difference between the advancing and receding contact angles. Contact angle hysteresis arises from the chemical and topographical heterogeneity of the surface, solution impurities absorbing on the surface, or swelling, rearrangement or alteration of the surface by the solvent [63] [64]. Advancing and receding contact angles give the maximum and minimum values the static contact angle can have on the surface. Difference between advancing and receding angles can be as high as 50 degrees. Dynamic contact angles and contact angle hysteresis has become a popular topic because of the recent interest in superhydrophobic and self-cleaning surfaces [65] [66], this is also being investigated at Donaldson, for this thesis it is not to be considered yet, however keep in mind to activate this model when superhydrophobic surfaces are being considered. This is important since small sliding angles (= angle the substrate has to be tilted to move the droplet) are needed for self-cleaning applications. Hysteresis is however also important in other situations such as intrusion of water into porous media, coating, and adsorption at liquid/solid interface.

### Fluid Film Surface tension - Static contact angle

At the interface between a fluid film and the gas phase, surface tension is caused by the greater attraction of fluid molecules to each other than to the gas molecules. The net effect is an inward force at the interface that causes the fluid film to behave as if its surface were covered with a stretched elastic membrane: that is, the surface is under tension. This tension is expressed using the experimentally determined surface tension coefficient  $\sigma$ . The magnitude of the surface tension between a given fluid and a given gas depends on the nature of the fluid and gas that are in contact and on the temperature. The surface tension coefficient is defined for each phase interaction. In CFD, surface tension model properties are defined as:

- Minimum Film Thickness: The minimum film thickness  $\delta_{min}$  that is used to determine the value of  $\omega$ . The default minimum film thickness is 0.01 mm.
- Alpha Tuning Parameter: The tuning parameter that is used in the capillary pressure calculation. This value is  $\alpha$ .
- Beta Tuning Parameter: The parameter that is used to calibrate the contact line force calculation with respect to experimental results. This value is  $\beta$ .

Each phase interaction is assigned its own surface tension coefficient  $\sigma$ . This coefficient is used to calculate the surface tension force between each of the defined phases in the phase interaction. It is entered as a scalar profile. The surface tension model for fluid film is used to model surface tension between the film and the surrounding fluid. It is also used to model surface tension across both the VOF phase and the fluid film phase in combined Fluid Film-VOF simulations. The surface tension formulation that is employed in the fluid film phase is based on the model that is introduced in [56]. There, the surface tension effects in the fluid film momentum transport are separated into two terms: capillary pressure and contact line force. The capillary pressure,  $p_\sigma$ , is expressed as:

$$p_\sigma = -\alpha\sigma (\nabla_s^2\delta) \quad (4.25)$$

where:

1.  $\sigma$  is the surface tension coefficient.
2.  $\nabla_s^2\delta$  approximates the curvature of the liquid surface with  $\delta$  being the fluid film thickness.
3.  $\alpha$  is a non-dimensional scale factor for the user to specify.

This force term has units of  $N/m^2$  and acts orthogonal to the bottom surface. This relationship is valid only for surfaces with slight curvature [57].

The contact line force is calculated as:

$$\tau_\sigma = \beta\sigma (1 - \cos\theta) \nabla w \quad (4.26)$$

where:

1.  $\theta$  describes the contact angle as a fundamental parameter of the wetting behaviour of the film.
2.  $w$  is defined as 1 wherever  $\delta > \delta_{min}$  (a user-specified minimum value) and 0 elsewhere.
3.  $\beta$  is an empirical parameter that is used to calibrate the model with respect to experimental results.

This force term has units of  $N/m^2$  and acts tangential to the bottom surface. The resulting surface tension force that is contributed to the momentum transport equation of the liquid film is:

$$F_\sigma = p_\sigma + \tau_\sigma \quad (4.27)$$

### VOF Surface tension - Dynamic contact angle

In this thesis the dynamic contact angle is not used for our CFD setup, however since Donaldson is currently investigating superhydrophobicity, this should be considered for future simulations when these materials are applied, hence the theory is described below. The contact angle  $\theta$  describes the influence of a solid wall on the free surface. By default, STAR-CCM+ uses a static value of contact angle for calculating the surface tension. In some applications, using a static contact angle can produce unrealistic free surface shapes. For these applications, you can define a dynamic contact

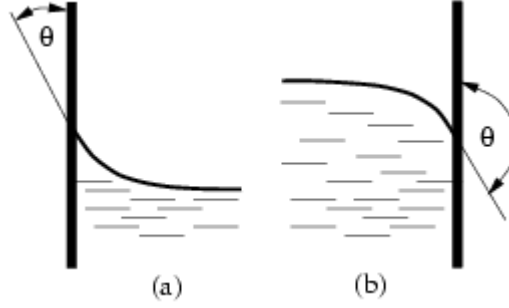


Figure 4.12: positive and negative contact angle

angle. The magnitude of the contact angle for a phase interaction depends on the pair of fluids and the solid that are in contact and on the temperature. The contact angle is measured at the triple line, which is the line where the wall and both fluid phases are in mutual contact. It is assumed that the specified value is with respect to the Primary Phase of the phase interaction. Values of contact angle smaller than 90 degrees mean that the phase is wetting the wall, as illustrated in part (a) of the following figure:

In order to comply with the usual convention on contact angle values, that are shown above, define a liquid phase as the primary phase of the interaction. You specify the contact angle at each wall boundary. The corresponding value node (Contact Angle) is activated when the surface tension option is selected in the Phase Interaction Model Selection dialog and after the Phase Interaction has been defined. You specify the contact angle as a scalar profile. The Kistler validation is suitable for both inertia- and capillary-dominated flows. However, you cannot use a Capillary number-driven dynamic contact angle method at slip walls. The triple line velocity is always evaluated to be 0 at slip walls, and therefore there is no variation in the contact angle. The same restriction applies to modelling the contact angle hysteresis. These simulations are not possible: no variation is observed in the contact angle as, by the definition of this phenomenon, the triple line is not moving. In some scenarios, oscillations can develop in the interfacial flow field for capillary-dominated flows. These oscillations can be damped or eliminated if a blending function is used in the dynamic contact angle specification. The Kistler method uses a blending function. In addition, you are recommended to activate the Interface Momentum Dissipation model in combination with a dynamic contact angle method in order to remove the parasitic currents at the interface. Specify a value of Interface Artificial Viscosity large enough to reduce parasitic currents, but keep the value as small as possible to avoid affecting the simulation results. If the interface shows much smearing, and other treatments (such as reducing the time-step size) do not improve the results, you can adjust the Sharpening Factor setting in the Volume of Fluid (VOF) model. Increasing this value from its default of 0 reduces the numerical diffusion at the interface. For surface tension dominated flows, setting a higher value can improve the resolution of the interface. Surface Tension Formulation: The surface tension force is a tensile force tangential to the interface separating two fluids. It works to keep the fluid molecules at the free surface in contact with the rest of the fluid. The surface tension force is an interfacial force, which is modelled as a volumetric force using the Continuum Surface Force (CSF) approach of Brackbill and others [58]. The magnitude of the surface tension force depends mainly on the nature of the fluid pair and on temperature. For a curved interface, the surface tension force  $f_\sigma$  can be resolved into two

components:

$$f_\sigma = f_{\sigma,n} + f_{\sigma,t} \quad (4.28)$$

Where:

$$f_{\sigma,n} = \sigma K n \quad (4.29)$$

And:

$$f_{\sigma,t} = \frac{\partial \sigma}{\partial t} t \quad (4.30)$$

Where:

1.  $\sigma$  is the surface tension coefficient.
2.  $n$  is the unit vector normal to the free surface and directed from liquid to gas.
3.  $t$  is the unit vector in the tangential direction to the free surface.
4.  $K$  is the mean curvature of the free surface.

For a constant surface tension coefficient  $\sigma$ , the tangential force is zero and the surface tension results in a force normal to the interface  $f_\sigma = f_{\sigma,n}$ . When the surface tension coefficient varies along the surface, which can be due to temperature differences, the tangential part does not vanish. In this case, Marangoni or Bnard convection can develop tangential to the free surface. In the VOF multiphase model case, the surface tension force is calculated according to the continuum surface force (CSF) model. That is, it uses the smooth field of the phase volume fraction  $\alpha_i$  to calculate a vector normal to the interface:

$$n = \nabla \alpha_i \quad (4.31)$$

The curvature of the interface can therefore be expressed in terms of the divergence of the unit normal vector  $n$ , as follows:

$$K = -\nabla \cdot \frac{\nabla \alpha_i}{|\nabla \alpha_i|} \quad (4.32)$$

Now the normal component of the surface tension force  $f_{\sigma,n}$  can be expressed as:

$$f_{\sigma,n} = -\sigma \nabla \cdot \left( \frac{\nabla \alpha_i}{|\nabla \alpha_i|} \right) \nabla \alpha_i \quad (4.33)$$

When the surface tension coefficient  $\sigma$  is constant,  $f_\sigma = f_{\sigma,n}$ . For a variable surface tension coefficient, the tangential force is evaluated as:

$$f_{\sigma,t} = (\nabla \sigma)_t |\nabla \alpha_i| \quad (4.34)$$

where  $(\nabla \sigma)_t$  is the gradient of the surface tension coefficient in the tangential direction.

The common quantity of many different dynamic contact angle validations is the triple line velocity. The triple line is the line where the wall and both fluid phases are in mutual contact. This quantity is related to the dimensionless capillary number  $Ca$  as:

$$Ca = \frac{V \cdot \mu}{\sigma} \quad (4.35)$$

where:

1.  $V$  is the triple line characteristic velocity.
2.  $\mu$  is the dynamic viscosity of the primary phase (usually a liquid phase).
3.  $\sigma$  is the surface tension force.

The triple line velocity is defined as:

$$V = -\langle \nu, \hat{n}_t \rangle \quad (4.36)$$

where:

1.  $\nu$  is the relative velocity of the fluid and the corresponding wall at the triple line.
2.  $\hat{n}_t$  is the normalized wall tangent pointing in the same direction as the volume fraction gradient of the primary phase ( $\nabla \alpha$ ).

STAR-CCM+ implements the Kistler validation [59], which is an empirical dynamic contact angle validation based on the capillary number  $Ca$  and utilizing the Hoffman function. The Kistler contact angle is defined as:

$$\theta_k = f_{Hoff} \left( Ca + f_{Hoff}^{-1}(\theta_s) \right) \quad (4.37)$$

where  $f_{Hoff}$  is the Hoffman function with  $f_{Hoff}^{-1}$  being its inverse:

$$f_{Hoff}(x) = \cos^{-1} \left( 1 - 2 \tanh \left( 5.16 \left( \frac{x}{1 - 1.31x^{0.99}} \right)^{0.706} \right) \right) \quad (4.38)$$

STAR-CCM+ uses a slightly modified definition of the Hoffman function to achieve a closed form for its inverse function. In the modified Hoffman function, the  $x^{0.99}$  term in the denominator is changed to a simple  $x$ . The closed form of the inverse function is valid for contact angle values in the range 0 to 176 degrees. Static advancing or receding contact angles that are larger than the upper bound are limited to 176 degrees. The static contact angle  $\theta_s$  is used in above equation as either the static advancing or receding contact angle, depending on the sign of the capillary number.  $\theta_s$  is specified as the Advancing Contact Angle or Receding Contact Angle in the Contact Angle Properties. To enhance the stability of the method that is implemented in STAR-CCM+, a range for the equilibrium capillary number ( $Ca_{eq}$ ) can be defined. Within the specified range  $-Ca_{ea} < Ca < Ca_{ea}$ , the resulting dynamic contact angle is blended with the equilibrium contact angle ( $\theta_e$ ) as a weighted average:

$$\theta_d = f\theta_e + (1 - f)\theta_k \quad (4.39)$$

While  $\theta_e$  is a user-specified value, the factor  $f$  is determined within the  $Ca_{eq}$  range as:

$$f = 0.5 + 0.5 \cos \left( \frac{Ca}{Ca_{eq}} \pi \right) \quad (4.40)$$

## Chapter 5

# CFD - Validation with PEPT for the Scaled Down Inlet Box

This chapter is the main area of investigation of this thesis, with figure 5.17 summarizing the validation findings. The PEPT experiments provided us with information on the behaviour of the water on the slope of the experimental inlet system in the form of raw spatial time data and processed velocity plots. This chapter will use the CFD models as explained in Chapter 4 and apply these to the geometry of the experimental setup. After selecting the correct models and fine-tuning the mesh and model settings, the model is post-processed to obtain data in the same form as the experimental setup (velocity plots in function of slope position). (See appendix C for the mesh details and appendix D for the full detail on the solvers and boundary conditions used for the simulation). When comparing these datasets it is concluded that the CFD setup is capable of simulating the experimental setup with the main proof for validity as shown in figure 5.17, the velocities observed in the CFD model are closely matching the PEPT experimental data. This chapter start with section 1 explaining how the raw CAD data is made into a valid CFD model. Section 5.2 is dedicated to the main air phase, although this air is not the area of investigation, it does need to be modelled correctly and needs to show proper mesh independence and convergence, since the solution of this main air phase will be used to initialize the transient part that simulates the water behaviour. In the subsection of 5.2 validation of the main air phase is based on the validation of pressure loss, velocity and airflow results with experimental measurements. Section 5.3 is the main interest of this thesis as it addresses the validation of the modelling we use for the water behaviour, in this section a lengthier explanation is given to the setup of the several models that handle water behaviour in the CFD code and again mesh independence is explained with finally validity of the CFD model in terms of water simulation explained as shown in figure 5.17. Section 5.4 gives a conclusion of the findings on validity for both the main air phase modelling and water phase modelling. Section 5.5 does some further design exploration on the scaled down inlet box such as the effect of changing the droplet diameter, droplet injector cone, droplet initial velocity and the effect of adjusting the main air phase flow-rate, these further investigations show that a good understanding of the boundary conditions are required when setting up a test rig, as they indicate an impact on the behaviour of the water (some parameters more outspoken than others)

## 5.1 CAD and CFD Model

(See appendix C for the mesh details and appendix D for the full detail on the solvers and boundary conditions used for the simulation). The domain of the CFD model for the scaled down inlet box is based on the CAD model from the experimental setup as represented also in Chapter 3. The CFD tool used was StarCCM v12 from CD-Adapco. Siemens NX was used for design and drafting purposes of the CAD models. Siemens NX direct modelling and Spaceclaim Engineer were used for preparing the CAD models for use in the CFD software. The purpose of a CAD model is to convey details to other parties such as, customers and product engineers. The original CAD drawing contained complex geometrical outlines and advanced design details down to small details such as, nuts, washers and tubing. Thus, it made the model very detailed and complex. However, for CFD simulations these advance details are not compulsory. Also, by including details which are insignificant to the CFD model, the calculation time will increase and the simulation will use more computing power.

The actual enclosure of the scaled down inlet is made out of sheet metal parts combined together. Thus, the enclosure of the original CAD model was designed using sheet parts as well. Unlike solid parts, models made out of sheet parts are not completely sealed. When the original CAD model was imported to StarCCM, it reported multiple water leak errors. Meaning, that there are internal and external leaks in the original CAD model and it is not impervious. The simulation requires the fluid domain to be waterproof; any open areas should be designated as boundary conditions such as inlets, outlets or pressure openings. Also, the sheet parts were not perfectly mated in the CAD software. Hence, improper mating of parts contributed to the water leak error as well. The CFD model was created as a replica of the original CAD model. Therefore, all the original dimensions were preserved in the CFD model. However, any parts that were not relevant to the fluid domain behaviour were removed.

The CFD model only considers the fluid domain (or empty space). Therefore, all the physical boundaries were built as solids and extrusion tools were used to construct individual shapes. For the purpose of waterproofing the model, the CFD model full scale assembly only contained solid parts. Moreover, when parts were imported, they were mated as coincident style. Also, all crucial components that control air flow, such as the front louvres, baffle plates and the drain were directly imported from the original CAD model as independent parts. In addition, any individual part that was imported from the original model was assembled as a coincident mating structure to avoid any leakage of the CFD model. However, it should be pointed out that the CFD model is not a 100 percent match to the original CAD model.

Consequently, inlet and outlet areas were extended by creating solid geometry, and lids were placed on top of the covers to seal the fluid domain. In a pressure opening, the flow will try to circulate back into the model and this is called the vortex effect, boundaries are extended far enough to avoid this effect. Finally, the model was tested for any water leaks or boundary condition errors using StarCCM. After testing, the inlet boundary condition was defined as a volumetric flow opening and the outlet boundary condition was defined as a pressure opening. Next sections describe the validation of the models and the setup of the physics.

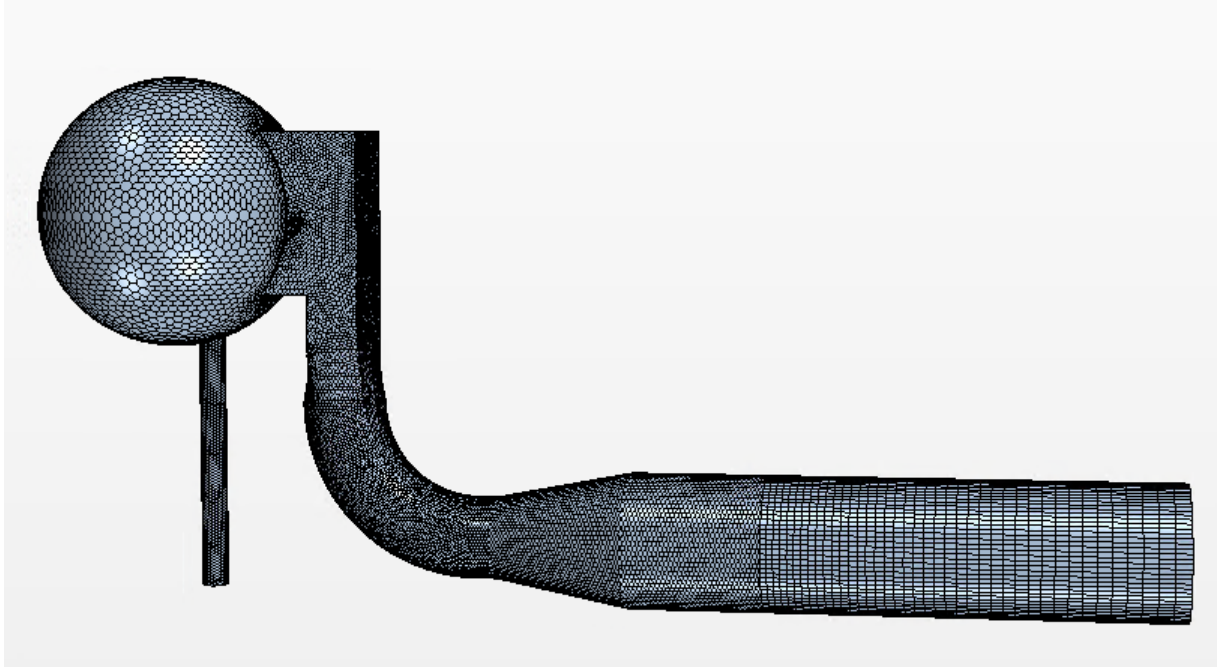


Figure 5.1: The mesh generated for the scaled down box, on the right the tube leading to the fan is extended to 6 times the diameter to enable better convergence of the simulation - once the simulation was validated for the main airflow, this duct section was cut off to reduce the domain size, the flow-field around the inclined plate was the area of investigation and the flow-field was shown to be stable around that area also with the tube removed

## 5.2 Validation of the CFD model - Main Air Phase

For the validation of the water phase which is the main area of investigation of this thesis see section 5.3. Given that, modelling and simulation are an approximation of the real application, the model needs to be validated before evaluating the data. Therefore, three common validation areas for the main air phase were examined; velocity points, air flow rate and pressure difference. Next to that there is the extra validation set that is the focus of this thesis, the PEPT experiment that allowed for an even more in depth validation study down to the level of the water particles itself. Data taken from experiments was compared to the theoretical data obtained from the simulation. However, it should be expected that these two sets of data will not be an exact match; instead, the simulated data will be an approximation of the experimental data and even the experimental data will have some inaccuracy in it due the factors like environment and measurement equipment.

### 5.2.1 Mesh Independence Study

For more information on the mesh settings used for the mesh independence study please refer to Appendix C, after the independence study a mesh of 2,250,000 cells was obtained, for the transient simulation where the water behaviour is studied this is further increased as described in section 5.3. Following sections study the validation between measured and simulated parameters, however these only make sense when the mesh of the CFD is fine enough to ensure numerical results are stable. At the same time a mesh that is too fine would lead to large solving times and this is for an industrial use of a CFD code not desired. A mesh independence study was therefore done by each time decreasing the mesh cell size and observing the main parameters during the iterative process,



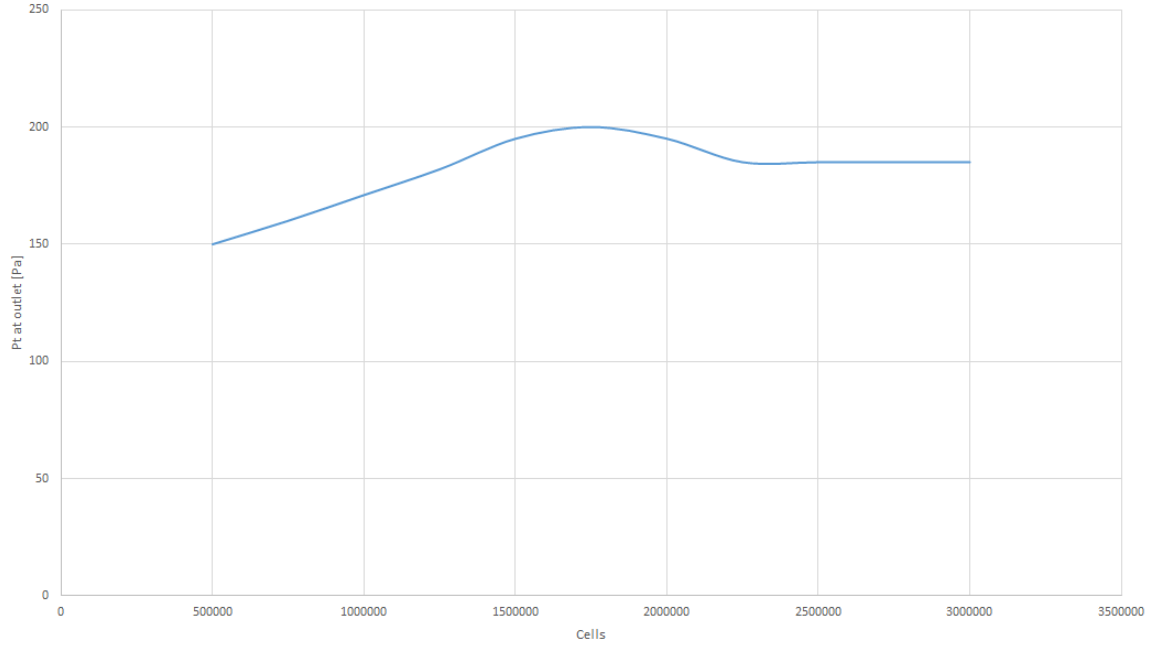


Figure 5.2: Evolution of  $P_t$  at outlet in function of the overall mesh cell count. Around 2,250,000 cells the value of 185 Pa does not change any more when increasing the mesh refinement indicating mesh independence. Table 5.1 shows also other variables that were monitored, for the plot of the other variables please consult Appendix C

Table 5.1: The table shows the variables that are monitored for the mesh independence study of the scaled down inlet box: the total pressure at both the inlet and outlet of the system are monitored and also the velocity at the outlet. Figure 5.3 shows the planar feature that represents the inlet area in the orifice. Figure 5.1 at the extreme right shows the outlet boundary. The optimal mesh setting is where none of the values no longer change upon further refinement

	coarse		medium		optimal	
cells	1000000		1750000		2250000	
	mag	var	mag	var	mag	var
$P_t$ inlet [Pa]	-4.86	0.5	-4.52	0.2	-3.12	0.05
$P_t$ outlet [Pa]	-176	0.5	-200	0.2	-185	0.05
$V$ inlet [m/s]	6.21	0.1	6.32	0.05	6.56	0.02

once they no longer showed variation the mesh was considered as optimal. It is shown that the mesh can be relatively coarse for validation in terms of velocity, pressure and flowrates, yet with the water behaviour being a phenomena influenced by wall conditions it does require a much finer mesh close to the boundaries (typically prism layers). Figure 5.2 shows the mesh independence achieved for the total pressure at the outlet of the system, the total pressure at the inlet orifice of the air intake and the velocity magnitude across that same orifice was also monitored for mesh independence, table 5.1 shows those variables. For more details consult the appendix C. Please consider that the boundary conditions for the mesh independence study (mass flowrate) were not yet set exactly like the test conditions, for the mesh independence study the value was set at a fixed flowrate of 0.1 kg/s and the goals was merely to examine the stabilization of the simulation. Since the final test setup was in the same order of velocities and flowrates the convergence was not influenced.

Table 5.2: Mesh settings for the optimal mesh for simulating the main air phase (this is further fine-tuned for the simulation where the water phase is solved as described in section 5.3.3) - resulting mesh was acceptable for parameters under investigation and also for residuals - With these settings all variables no longer show large fluctuations and computational time is still within limits

Mesh Global settings - Fine mesh settings	
Mesh Models	Extruder
	Prism Layer Mesher
	Polyhedral Mesher
	Surface Remesher
Base size	5mm
Number of prism layers	3
prism layer stretching	1.5
prism layer thickness	33.3% relative to base
surface size - relative min	10
Local mesh settings - Box around inclined face	
custom surface size min	5% relative to base
custom surface size max	100% relative to base
nr of prism layer	5
prism layer stretching	1.5
prism layer thickness	25% relative to base

### 5.2.2 Velocity - Measured

The test-rig was brought up to optimal load and the air speed was measured near the inlet grill and inside the outlet duct. The fan was then regulated to obtain an average inlet velocity of 5m/s. Measurements were taken at the air inlet using an anemometer that was placed on the plane at which air enters the enclosure, in other words the anemometer blades were perpendicular to the air flow (see fig 5.3). Moreover, for accuracy, the anemometer was fixed to a flat plate and that plate was placed parallel to the inlet orifice. The speed in the outlet duct was measured by creating a small hole in the duct, inserting a pitot tube and then sealing it to prevent air entering or exiting the test-rig. Due to the topology of the inlet box and the louvre located deeper into the box it is expected to get non uniform velocity data at the inlet, therefore the orifice was divided with an overlay point matrix, a measurement was made at each of this locations. For identification purposes, the inlet matrix points are referred to in 10 rows and 4 columns, top left is point A1 bottom right is point D10 (see table 5.3). Similarly, air speed was measured in the outlet duct as well (with a pitot tube that was inserted into the outlet duct). The outlet cross-section had also 16 equally divided data collection points (see table 5.4). The appendix contains more details about the data point locations and air speeds measured at those locations. The outlet tube has a diameter of 250 mm to connect smoothly to the fanset inlet that is also 250 mm, since our fan was running at 225 l/s, the expected velocity in that 250 mm duct would be 4,58 m/s.

### 5.2.3 Velocity - Simulated

(See appendix D for the full detail on the solvers and boundary conditions used for the simulation). The simulation was set-up as a steady state simulation for validation of the velocities and pressure losses of the main air phase. Velocities at the inlet orifice were visualized using a contour plot (see

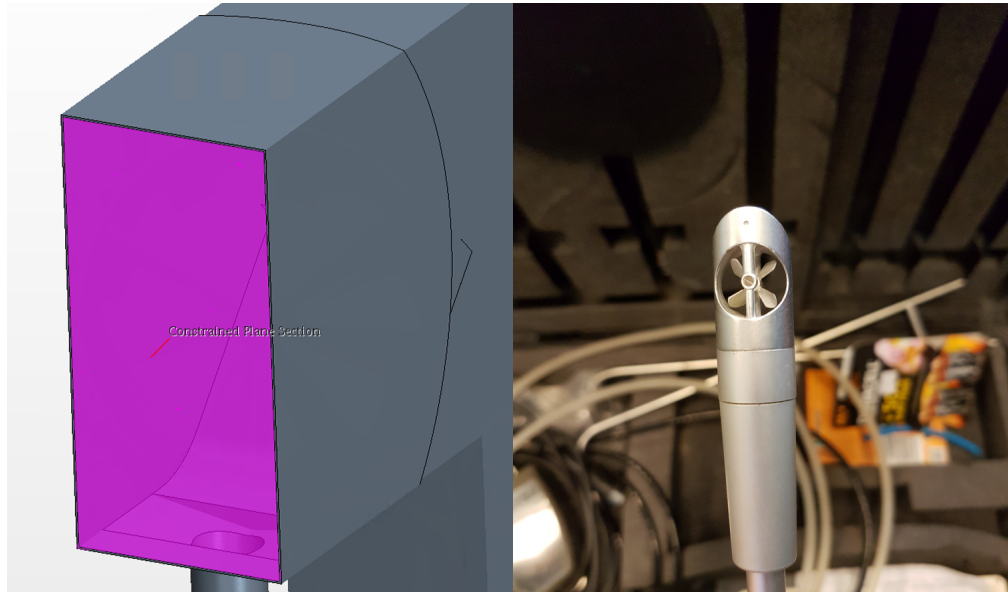


Figure 5.3: left: measurement plane for inlet velocity measurements, right: type of anemometer used

Table 5.3: INLET ORIFICE anemometer measurement locations and results at those locations

RESULTS DIAGRAM				
[m/s]	A	B	C	D
1	4.8	1.5	1.6	5
2	6.2	5.1	5	6.3
3	5.9	5.1	4.9	5.8
4	5.8	4.8	4.9	5.6
5	5.6	5.1	5.1	5.6
6	6	5.2	4.9	5.7
7	5.8	4.9	5	6.4
8	6.3	5.1	5.2	6.8
9	5.6	4.9	5	5.8
10	3.2	2.4	2.3	3.3

Table 5.4: OUTLET anemometer measurement locations and results at those locations

RESULTS DIAGRAM				
[m/s]	A	B	C	D
1	4.6	4.7	4.7	4.6
2	4.6	4.8	4.8	4.7
3	4.7	4.8	4.8	4.7
4	4.7	4.8	4.8	4.7

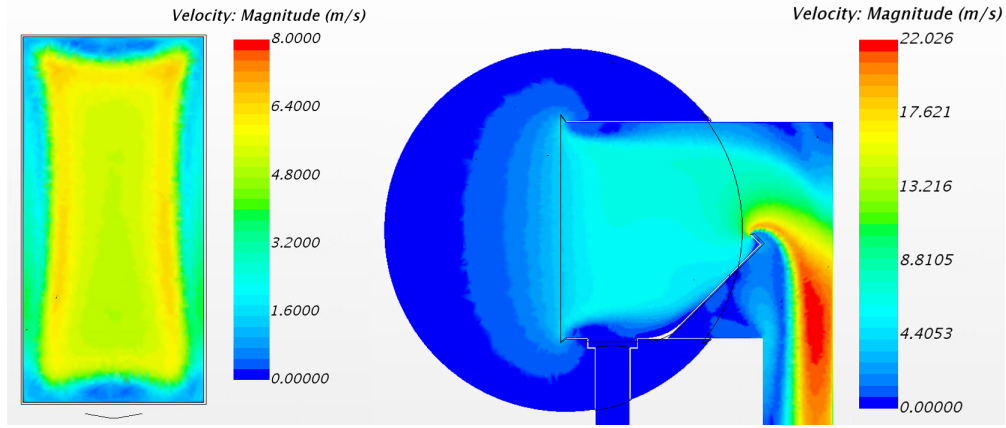


Figure 5.4: velocity scalar plot: left at inlet orifice, right at lateral cross-section

figure 5.4. By observing the contour plot, it was concluded that further investigation is needed to accurately pin point the different air velocities. Also, the air speed measured using the anemometer only represents the air particles which are moving perpendicular to the inlet; in the simulation, a measuring plane is created and only the vector component across this plane is registered. To investigate the air velocity further, a point study on the inlet surfaces was conducted similar to the grid pattern used for the measured data, only the velocity in direction equal to the anemometer direction was considered.

Table 5.5 illustrates the magnitude of the velocity simulated on the inlet of the scaled down box. In bold the values of the measurement, in italic the values of the simulation and in colour the error. The error values are colour coded to better identify highest to lowest values. Similarly, table 5.6 illustrates the magnitude of the outlet velocity.

$$error(velocity) = \left\{ \frac{|measured - simulated|}{measured} \right\} .100 \quad (5.1)$$

#### 5.2.4 Pressure Loss - Measured

One of the purposes of an enclosure is to restrict the noise level generated by the engine radiating out from the inlet orifice. Therefore, the inlet should be large enough so that it will supply the required air flow needed. However, it should be small enough so that it will constrain the noise. Because of this size limitation, the inlet acts as an orifice plate and a restriction to the air flow. As a result, the pressure inside the enclosure will change when the engine is operating. Regardless of whether the fluid particles are in motion or not, the pressure will apply to any part of the fluid domain. There are two kinds of pressure, static pressure and dynamic pressure. Static pressure is the pressure applied on a surface when the fluid is at rest relative to the flow, not the pressure created by the motion of fluid particles. Dynamic pressure is the pressure applied as a result of moving particles, and is only exerted in the direction of the flow. Therefore, measuring only the dynamic pressure is difficult and always requires some degree of calculation. Hence, every particle in the fluid domain has its own static pressure  $P_S$ , dynamic pressure  $P_D$  and total pressure  $P_T$ , regardless of the fluid speed. Thus, the total pressure along a streamline is in simplified form,

$$P_S + P_D = P_T \quad (5.2)$$

Table 5.5: INLET: velocity errors between measured and simulated - green is error between 0 and 5 percent, yellow is between 5 and 10 percent, and red is above 10 percent

inlet velocity [m/s] - bold is measured - italic is simulation - colored is error											
Point 1-A			Point 1-B			Point 1-C			Point 1-D		
4.8	5	4.2	1.5	1.4	6.7	1.6	1.8	12.5	5	5	0.0
Point 2-A			Point 2-B			Point 2-C			Point 2-D		
6.2	5.9	4.8	5.1	5.1	0.0	5	5.1	2.0	6.3	6.6	4.8
Point 3-A			Point 3-B			Point 3-C			Point 3-D		
5.9	5.9	0.0	5.1	5	2.0	5	4.7	6.0	6.3	5.5	12.7
Point 4-A			Point 4-B			Point 4-C			Point 4-D		
5.8	5.6	3.4	4.8	4.5	6.3	4.9	5	2.0	5.8	5.9	1.7
Point 5-A			Point 5-B			Point 5-C			Point 5-D		
5.6	5.6	0.0	5.1	5.4	5.9	5.1	5.4	5.9	5.6	5.9	5.4
Point 6-A			Point 6-B			Point 6-C			Point 6-D		
6	6	0.0	5.2	4.9	5.8	4.9	4.9	0.0	5.7	5.4	5.3
Point 7-A			Point 7-B			Point 7-C			Point 7-D		
5.8	5.1	12.1	4.9	5.1	4.1	5	5	0.0	6.4	6.7	4.7
Point 8-A			Point 8-B			Point 8-C			Point 8-D		
6.3	6.1	3.2	5.1	4.9	3.9	5.2	5.3	1.9	6.8	6.5	4.4
Point 9-A			Point 9-B			Point 9-C			Point 9-D		
5.6	5.9	5.4	4.9	4.9	0.0	5	5.1	2.0	5.8	6	3.4
Point 10-A			Point 10-B			Point 10-C			Point 10-D		
3.2	2.9	9.4	2.4	2.6	8.3	2.3	2.5	8.7	3.3	3.1	6.1

Table 5.6: OUTLET: velocity errors between measured and simulated - green is error between 0 and 5 percent, yellow is between 5 and 10 percent, and red is above 10 percent

outlet velocity [m/s] - bold is measured - italic is simulation - colored is error											
Point 1-A			Point 1-B			Point 1-C			Point 1-D		
4.6	4.3	6.5	4.7	4.7	0.0	4.7	4.8	2.1	4.6	4.7	2.2
Point 2-A			Point 2-B			Point 2-C			Point 2-D		
4.6	4.8	4.3	4.8	4.9	2.1	4.8	4.6	4.2	4.7	4.7	0.0
Point 3-A			Point 3-B			Point 3-C			Point 3-D		
4.7	4.9	4.3	4.8	4.8	0.0	4.8	5	4.2	4.7	4.5	4.3
Point 4-A			Point 4-B			Point 4-C			Point 4-D		
4.7	4.9	4.3	4.8	5	4.2	4.8	4.8	0.0	4.7	4.7	0.0

by applying a simplified version of Bernoulli's equation, the Equation can be written as,

$$P_S + \frac{1}{2}\rho\nu^2 = P_T \quad (5.3)$$

Where,  $\rho$  is the density of the fluid and  $\nu$  is the flow velocity. Also, static and dynamic pressures can vary during the course of the fluid flow, but the total pressure will be constant along the streamline of air flow (assuming no losses occur). Therefore, depending on the changes in dynamic pressure, static pressure will also change. Moreover, because dynamic pressure cannot be easily measured, static pressure is measured instead. So the changes in the static pressure are to some extent a reflection of the changes in dynamic pressure. The static pressure is measured relative to atmospheric pressure or relative to two points in the streamline. Using the above equation, it can be concluded that the air velocity at the inlet orifice will be higher than that in the atmosphere in front of the inlet. To explain this further: according to the conservation laws, the flow rate should be constant throughout the inlet. However, the inlet acts as an orifice to the air flow, hence air velocity is higher inside the orifice. This higher velocity will create a higher dynamic pressure. However, the total pressure should be constant along the streamline. Hence, static pressure will drop in order to accommodate the rise in dynamic pressure. While the test rig was running at the correct condition, this static pressure drop inside the inlet system was measured using the pitot tube described in the previous sections. The measurement was taken inside the outlet duct at roughly 6 times the hydraulic diameter in order to avoid turbulences and compared with atmospheric pressure as in front of the inlet orifice. An assumption was made that the static pressure values will be the same in other parts of the outlet tube. At a flowrate of  $13.5 \text{ m}^3/\text{min}$ , static pressure loss was rated at 455Pa.

### 5.2.5 Pressure Loss - Simulated

A cut plot was used to visualize the pressure across the intake system. However, since the simulation calculates and visualizes the pressure in each fluid particle, it is not recommended to calculate the pressure loss by taken 2 points. By analysing the contour plot on the cut plane a better understanding of the pressure loss is obtained. StarCCM does not plot the dynamic pressure, yet it does plot both the static and the total pressure. Comparing these 2 in combination with the velocity plot from before describes then the dynamic pressure. For compressible fluid, total pressure is calculated assuming an isentropic expansion from the total (stagnation) to the actual flow conditions. For incompressible fluid, total pressure is working static pressure + dynamic pressure. Figure 5.5 left illustrates a simplified contour plot of average static pressures in the system from a lateral viewpoint onto that middle cross-section. The higher pressure denoted in red reflects the ambient environmental pressure (101200 Pa). The simulated pressure at the inlet orifice is slightly lower than the atmospheric values. The reason for this difference is that the boundary of the fluid domain is at the half sphere representing the atmosphere and not at the entrance to the enclosure. Therefore, inside the inlet orifice there is a significant amount of air movement, thus, there is a static pressure drop. So, when calculating the simulated static pressure drop across the enclosure, the static pressure across the inlet orifice should be considered as well. Figure 5.5 right represents the total pressure contour plot on that same cross-section plan. At the atmosphere both static and total pressure are 0, confirming that dynamic pressure is zero (minimal

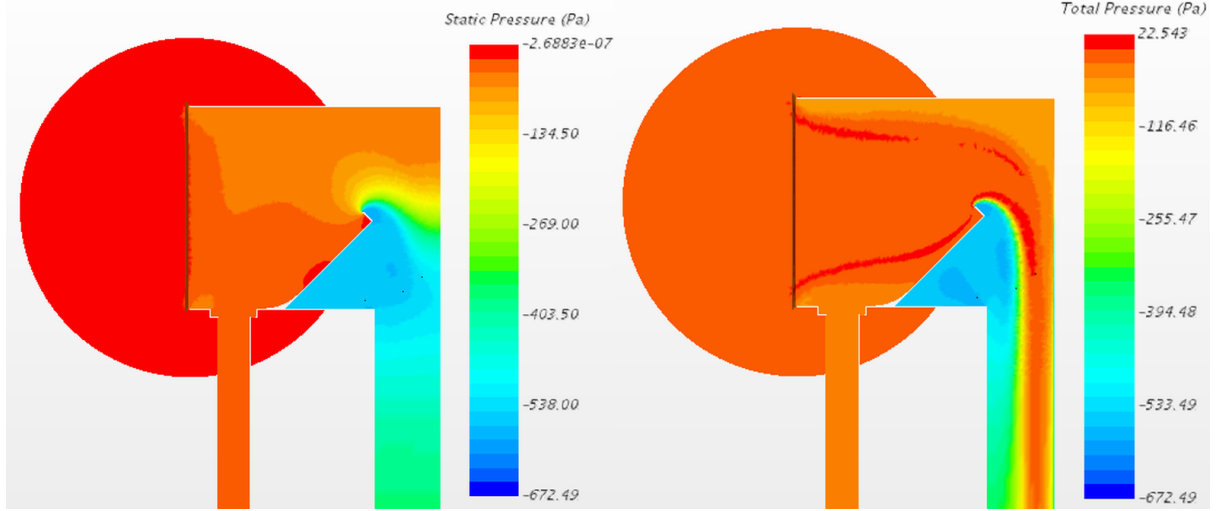


Figure 5.5: Pressure change throughout the system in Pa - LEFT: static pressure RIGHT: total pressure

airspeed at furthest points in atmosphere). To evaluate the pressure loss between atmosphere and the outlet point that was used in the experimental phase, we need to create a cross section in the outlet duct (again at 6 times the hydraulic diameter to match the experiment) and run a mass flow averaged report of the static and total pressure there. The mass flow averaged scalar quantity through a surface is computed as,

$$\frac{\oint \rho \phi |v \cdot da|}{\oint \rho |v \cdot da|} = \frac{\sum \rho_f \phi_f |v_f \cdot a_f|}{\sum \rho_f |v_f \cdot a_f|} \quad (5.4)$$

resulting in a mass flow averaged static pressure of 432 Pa, compared to the 455 Pa obtained during the experiment this leads to an error of 5 percent. However during the experiment the static pressure was measured only at a few discrete point and in the centre of the tube. When the exact values in the centre of the outlet tube in the simulation rather than the averaged value is taken this leads to a static pressure loss of 450 Pa, further reducing the error to 1.2 percent.

### 5.3 Validation of the CFD model - Water Behaviour

This is the main area of interest of the thesis. In order to observe the rain water behaviour in the computational environment of the scaled down experiment multiple solvers and physics models were combined. First the main air phase was solved with the methods described in the previous sections. Then water spray was realized by setting up Lagrangian particles at the atmosphere (as shown in figure 5.6). To simulate the surface behaviour when the droplets hit the inclined slope, multiple models have to be combined. The liquid film provides a surface where the Lagrangian particles can impact on the inclined surface, yet it only allows to set a static contact angle. The VOF model does allow setting a dynamic contact angle, yet it first needs to exist in order to accept incoming Lagrangian particles, hence the liquid film needs to be run in combination with VOF to ensure that particles are intercepted on the dry plate, figure 5.7 shows this in a schematic way. To simulate the radioactive tracer another Lagrangian particle can be setup at the top of the inclined plate (like in the experiments), however to avoid adding complexity to the sim it is decided to follow

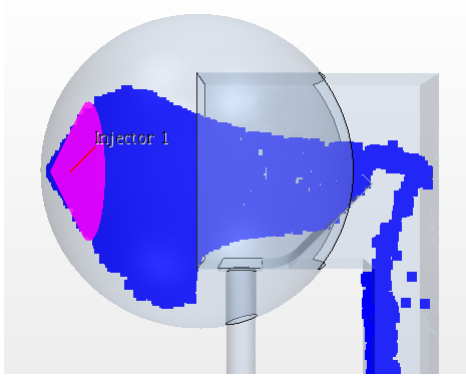


Figure 5.6: Lagrangian particles representing the water spray, moving through the system

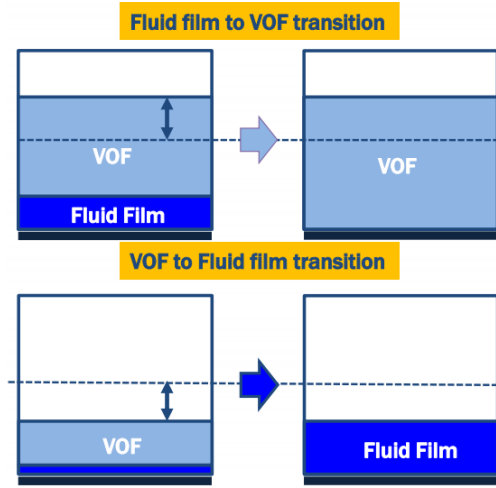


Figure 5.7: VOF and liquid film model working together to tackle dynamic contact angle problems

the investigation from the PEPT experiments, where it was shown that these particles follow the water without problem and that the particles do not influence the flow of the water whatsoever. The advantage of running a simulation is that we now can investigate and study any behaviour without being hindered by the physical properties of the prototype. For the experimental study of the water flow we needed PEPT because there was no other way to record the waterflow in such detail and in a closed steel box. We can therefore decide that due to both the radioactive particle not influencing the water and not being needed to study the flow, we no longer need to setup this particle in the simulation. For all details concerning the simulation setup refer to the appendix.

### 5.3.1 Water Phase - Setup CFD

The appendix explains in full detail the setup of the CFD parameters for the water phase. Describing the steps in this section would remove attention from the results, however some important aspects of the setup need to be highlighted. First is the creation of 2 additional coordinate systems, since the CFD model itself has a coordinate system associated that is derived from the CAD model (see figure 5.8 coordinate system A), this does not correspond automatic with the coordinate system and origin that was used in the experimental PEPT measurements. Therefore a new coordinate system needs to be created with its origin offset from the main coordinate system and the direction of the main 3 axis re-aligned with the experimental axis (see figure 5.8 coordinate system B). Special attention needs to be put into the orientation of this coordinate system so that it takes into account the coordinate system from the PEPT experiments. For this thesis this is not a problem, the main axis is the fore-aft X axis from the experiment and it is this one that needs to be aligned in the CFD setup, if the other axis like the lateral one would point in the opposite direction, this does not pose a problem. Next to the coordinate system that matches the experimental coordinate system another one needs to be created to monitor the velocity in the direction of the slope (see figure 5.8 coordinate system C), with the creation of this slope coordinate system the CFD package will then calculate for us automatic the velocity in the direction of its main axis (unlike the experimental part where we had to calculate this velocity ourselves as the vector sum



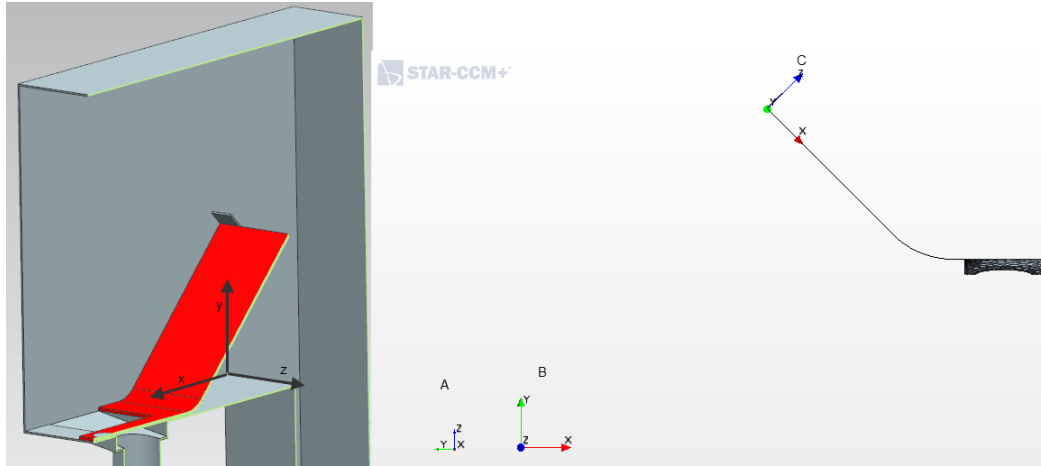


Figure 5.8: LEFT: directions of experimental setup - RIGHT: A.original coordinate system imported from the CAD geometry, B.coordinate system that matches the experimental coordinate system, C. coordinate system parallel with the slope

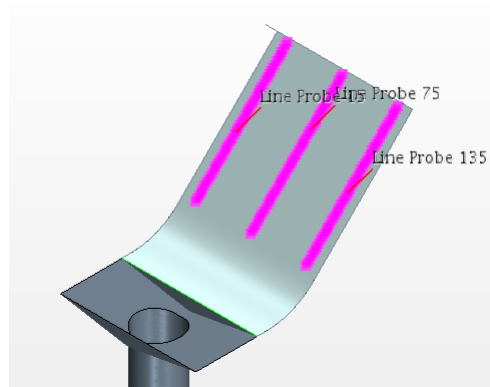


Figure 5.9: Lineprobe at 15, 75 and 135 mm displayed on top of the inclined slope, these are used to monitor and report the fluid film velocity when moving down the slope

of the velocities along the main axis. Figure 5.8 shows all 3 coordinate systems.

The second important aspect is the creation of line probes that are used to monitor and plot the velocity of the water film while moving down the slope. As mentioned before to reduce the complexity of the simulation the radioactive tracer particle is not included. However this also implies that measuring the velocity of that particle is not possible. Therefore line probes are created on top of the slope surface every 15 mm for the total width of the slope going from 0 to 150 mm. Special attention needs to be put into assigning the regions to the line probes, when also the main air phase is assigned to the probe, this probe will measure the airflow speed that is shearing upwards next to the slope. This would create velocity measurements that are pointing in the opposite direction as the waterflow (moving down the slope) and could lead to false conclusions.

The third aspect is important for the stability of the simulation: when the main flow field is first solved as a steady state solution, this solution needs to be used to initialise the unsteady part. This also matches with reality where first the main airflow is switched on and only when that is up to speed the water injection will commence. This can be achieved by creating 2 physics continua in the same simulation model. Once the steady state solution has converged, the unsteady model is then assigned to our model and the solution is continued from there on. However in order to again start with blank charts and graphs, it is important to wipe those fields without wiping the

solution itself, more information on how to do this can be found in the appendix.

The fourth aspect is choosing the correct solvers settings, in the implicit unsteady approach, each physical time-step involves some number of inner iterations to converge the solution for that given instant of time. These inner iterations can be accomplished using implicit spatial integration or explicit spatial integration schemes. You specify the physical time-step size that is used in the outer loop. The integration scheme marches inner iterations using optimal pseudo-time steps that are determined from the Courant number. With the Implicit Unsteady approach, you are required to set the physical time-step size, the Courant number, and the number of inner iterations at each physical time-step. The transient phenomena being modelled generally governs the physical time-step size. The time step must at least satisfy the Nyquist sampling criterion: more than two time-steps per period are required. In general, the guidelines for setting the Courant number in steady-state integration schemes also apply to the transient integration schemes. The number of inner iterations per physical time-step is harder to quantify. Generally, you determine this number by observing the effect that it has on results. Select a number of inner iterations, plot a monitor for one or more specific quantities against iteration, and see whether these monitors are converging within each time-step. Smaller physical time-steps generally mean that the solution is changing less from one time step to the next; fewer inner iterations are then required. There is an optimal balance of time-step size and number of inner iterations for a given problem and desired transient accuracy. The difference between the 1st and 2nd order discretisation scheme is that the 2nd order is more accurate than the 1st order. The truncation error is lower when we use the 2nd order scheme. In general the 1st order time integration is sufficient, but sometimes the 2nd order can be required if time integration of large importance. Lower order integration schemes (1st order) are less accurate, however, they are usually also more stable, because they introduce a little bit of dissipation. The Implicit Unsteady approach is appropriate if the time scales of the phenomena of interest are either of the following:

- The same order as the convection and/or diffusion processes (for example, vortex shedding).
- Related to some relatively low frequency external excitation (for example, time-varying boundary conditions or boundary motion).

### **5.3.2 Water Phase - Experimental**

The previous sections described parameters that are important to establish the validity of the CFD model for the main phase (air), these proved to be fairly straightforward to measure and to validate. Yet the centre point of this thesis is to also establish the validity of the CFD model in terms of the behaviour of the water phase. The measured values from the PEPT experiment were already described in chapter 3. The next sections will describe the simulation of this water phase in all its forms, starting from droplets in the form of a Lagrangian phase, then impinging on the inclined slope covered by the fluid film impingement models and then moving down the slope under the influence of the surface tension, shear flow from the main air phase and gravity, covered by both the liquid film model.

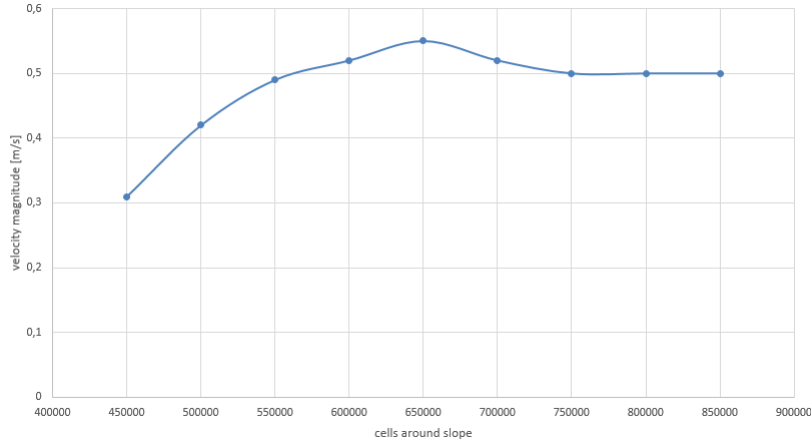


Figure 5.10: Mesh independence: velocity magnitude average on probe line stabilizing when cell count increases around slope

### 5.3.3 Water Phase - Mesh independence study

For the transient simulation where the water behaviour is studied the mesh had to be further refined (certainly around the slope area). For more information on the mesh settings used for the mesh independence study please refer to Appendix C, after the independence study a mesh of 7,500,000 cells was obtained. For the steady results an initial mesh independence study was already done in order to make sure that results such as air flow velocity, flow-rates and pressure losses of the main air phase were stable and mesh independent. Similar to this methodology this was also done for the water phase part of the simulation, the main aspect under study in this section is the movement of the water down the inclined slope. The mesh should therefore be fine enough so that it no longer influences the magnitude of fluid film velocity and other parameters under investigation when refining the mesh. Unlike in the previous section where the whole mesh was refined up until the point where the air phase results no longer varied, for the water phase only the area around the slope was refined. This enables the simulation to still be computationally cheap and at the same time provide more qualitative results. A Mesh or Grid independent solution is a solution that does not vary significantly even when you refine your mesh further. When you start with a coarse mesh and solve, you may notice difference in results as you make your mesh finer. But, there exists a limit, beyond which you won't observe any changes in the results even after you make it finer. Then we may state that we have achieved grid independence. At this point, the mesh will be fine enough to capture the most intricate details of the flow, which is why making it finer will not make any changes in the results. The answer comes through the question that emphasizes the independence of numerical solution from grid structure, also called mesh. In every computational analysis, mesh independence studies, also expressed as mesh convergence, ought to be conducted to sustain credible results. Otherwise, the results that obtained would be considered as sceptical.

### 5.3.4 Convective Courant number

The principle behind this scalar is that, for example, if a wave is moving across a discrete spatial grid and we want to compute its amplitude at discrete time steps of equal duration, then this duration must be less than the time for the wave to travel to adjacent grid points. As a corollary,

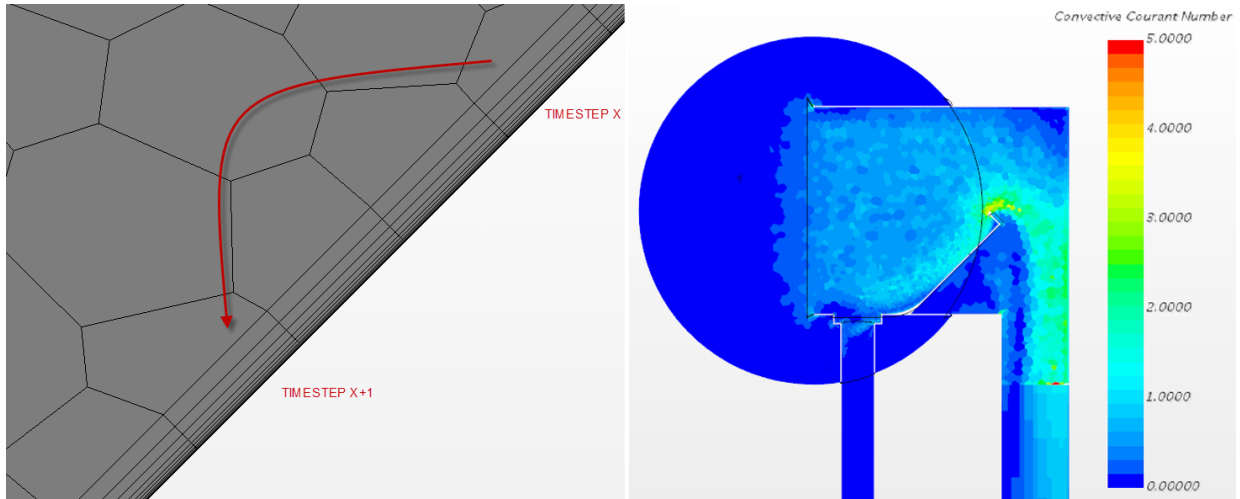


Figure 5.11: LEFT: If a timestep is too large, the simulation moves across multiple cells in between steps, leading to a convective courant number larger than 1 - RIGHT: convective courant number for main air phase - low values around slope indicate good model settings

when the grid point separation is reduced, the upper limit for the time step also decreases. In essence, the numerical domain of dependence of any point in space and time (as determined by initial conditions and the parameters of the approximation scheme) must include the analytical domain of dependence (wherein the initial conditions have an effect on the exact value of the solution at that point) to assure that the scheme can access the information required to form the solution. In the case of the fluid film moving down the slope 2 factors will influence the convective courant number, the mesh density at the slope and the timestep value defined for the simulation. Decreasing the mesh size will increase the accuracy of the model, however when the timestep is not properly reduced this could results in the fluid film moving across multiple cells in the same timestep. The convective Courant number is a helpful indication for selecting the time step size: for time-accurate simulations, the convective Courant number should be 1.0 on average in the zone of the interest. This value implies that the fluid moves by about one cell per time step. For flows with free surfaces, if a second-order scheme for time integration is used, the Courant number must be less than 0.5 in all cells. If a free surface moves more than half a cell per time step, the High-Resolution Interface-Capturing (HRIC) scheme can lead to overshoots or undershoots, and eventually to divergence. It is important to point out that it is not very useful to look at the CFL number on a fluid film. The CFL number is in fact used for making sure that the information is convected in the proper way and it can be (for explicit solvers) a limit for the stability. Bear in mind that the solver used so far are implicit ones (so no stability issues for  $CFL > 1$ ) and that in the case we have a high CFL number, it will be most likely localized in areas of high speed, again most likely for the continuous phase rather than the liquid one. The reason why the CFL number is available for VOF phase is related for the specific need of ensuring a  $CFL < 0.5$  in order to use the HRIC scheme which will describe better the interface. When only a static contact angle is used and therefore only the liquid film is activated there is no need of looking at the CFL number on the fluid film, however it should be inspected for the main air phase around the areas where it might sweep up the water phase.

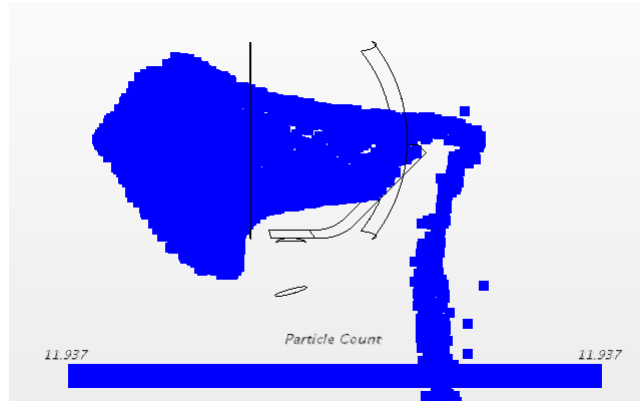


Figure 5.12: Particle count per parcel - for this image a parcel size of 10 was used, this number was increased until the value displayed was 1, indicating that each individual particle was represented by a unique parcel, providing the best accuracy

### 5.3.5 Parcel size independence study

When injecting water droplets into the system, this is done by using the Lagrangian model (see Chapter 4 for more detail). In order to obtain a realistic spray, some of the parameters will need to be optimized. Diameter, velocity and flowrate can be obtained from the experiments, however parcel size is a parameter that needs to be tuned similar to a mesh refinement study. CFD represents the true number of particles in a spray by a number of "parcels" (groups of particles) which have similar properties (diameter, velocity etc..) as each particle. Increasing this size will help add realism to the simulation, yet a value too high will affect computational time. The thing to realise is that the mass-flow of the parcel is equal to the mass-flow of the group of particles, to account for their number on the momentum exchange with the gas phase. StarCCM groups injected particles in parcels, if this number is equal to 1 it means that all particles are represented by a single parcel. This means that the simulation will treat all those particles as 1 big block which is not very realistic. Increasing this number until it matches the exact number of particles means that the simulation will add exactly 1 particle per parcel, in effect applying all the simulation setting per particle. It helps reduce the computational time as you are dealing with less calculations but still getting the diameters and velocities out. Generally the more parcels you use the more accurate the solution. Particle parcels are analogous to seeding particles in flow measurements. Seeding particles have uniform diameter, spherical shape, low lose weight, and high melting temperature and when introduced they follow flow stream lines. They are expected to have near-zero buoyancy. In measurement techniques, the velocities of these particles are considered to be the velocities of the fluid packets surrounding them.

### 5.3.6 Effect of Bai-Gosman

The impingement of incoming water droplets (or other particles for that matter) can be simulated in numerous ways. The numerical explanation of the Bai-Gosman was done in Chapter 3. Not enabling the Bai-Gosman means that any incoming particle is accepted by the fluid film as perfect impingement. With Bai-Gosman enabled all the extra options of water droplet impact are now possible adding to the realism of the simulation.

- Classic method without fluid film: incoming Lagrangian particles hit a boundary and the

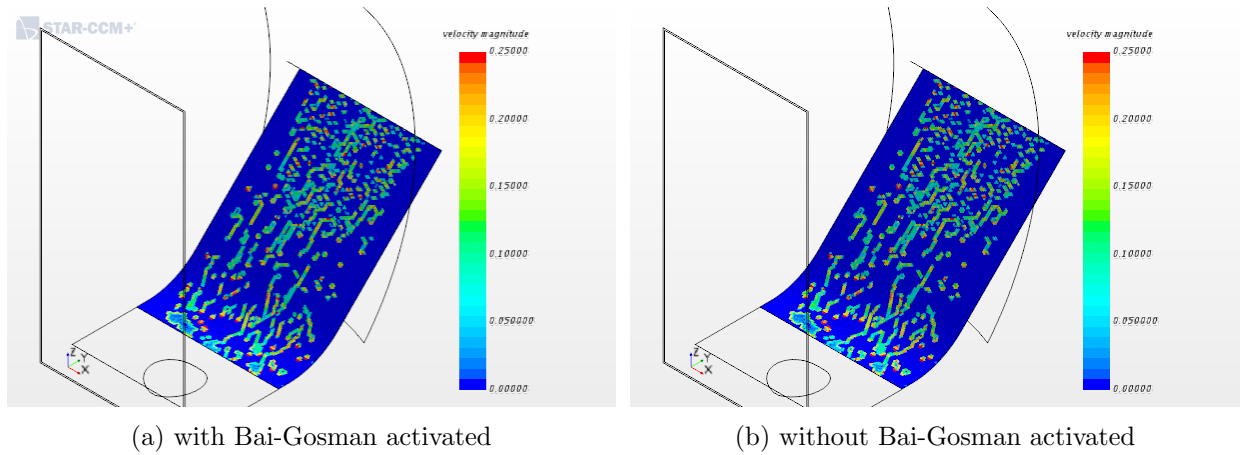


Figure 5.13: Effect of Bai-Gosman on velocity magnitude

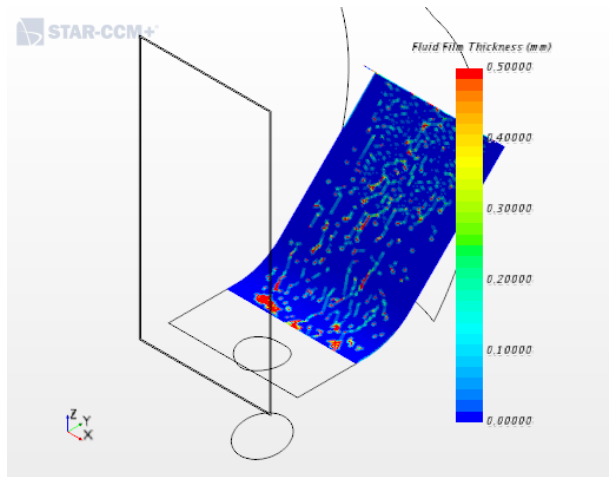
boundary can then accept these particles as escape, rebound or stick, with each time a restitution coefficient that can be set. Although this method is computationally cheap it is not very realistic and requires a detailed experimental study of the coefficient of restitution.

- Fluid Film without Bai-Gosman: the fluid film accept the incoming particles as perfect impingement, and the fluid film then takes over the modelling of the water flowing over a surface, this being already more realistic vs the prior method.
- Fluid Film with Bai-Gosman: the fluid film accepts the incoming particles no longer as perfect impingement, but allows now a wide variety of behaviours: spread, breakup, rebound, adhere and the combination of those as described in Chapter 3.

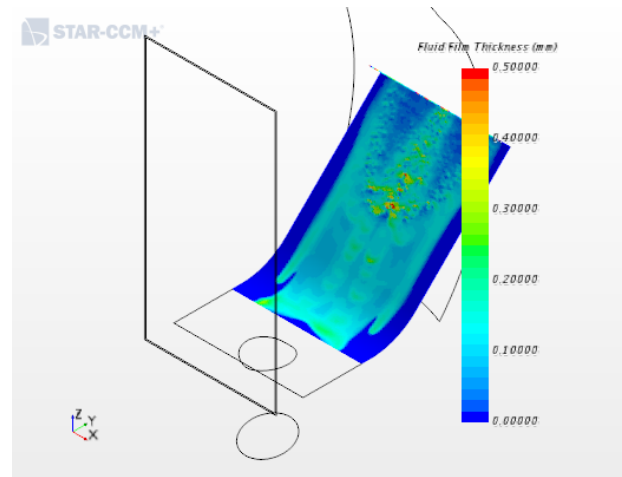
The classic method with coefficient of restitution is not used for this chapter, after all the goal of the topic under investigation was to establish validation between the PEPT experiments and the CFD model, since the PEPT model was tracing a radioactive particle sliding down a slope, the classic CFD method with coefficient of restitution would not be suitable for validation, it accepts or rebounds incoming raindrops (Lagrangian particles), it does not create a liquid film sliding down the slope, so any CFD measurement on speed down the slope like what happened in the experiments is not possible, simply because there is no liquid film being created with this method. The 2 other methods with and without Bai-Gosman impingement are simulated and compared to each other and the experimental results. Although that both methods in our setup do not provide vastly different results and one could opt for leaving the Bai-Gosman model turned off, it needs to be highlighted that this good validation without Bai-Gosman will not always be the case. When raindrop size increases or initial velocity of the spray increases (like in pressure washing), the impingement into the liquid film will occur with much more energy, hence resulting in a wider range of impingement behaviour. It is there that Bai-Gosman will make a difference. For the remainder of this investigation Bai-Gosman will be left on in order to obtain in all cases the most realistic result. However when running CFD simulations during early design work of air inlets, it could be turned off to obtain faster results, if the boundary conditions are limited to low energy impact (normal raindrops falling vertically in front of the inlet as opposed to pressure washing sprayed into the inlet).

### 5.3.7 Description of final setup and result

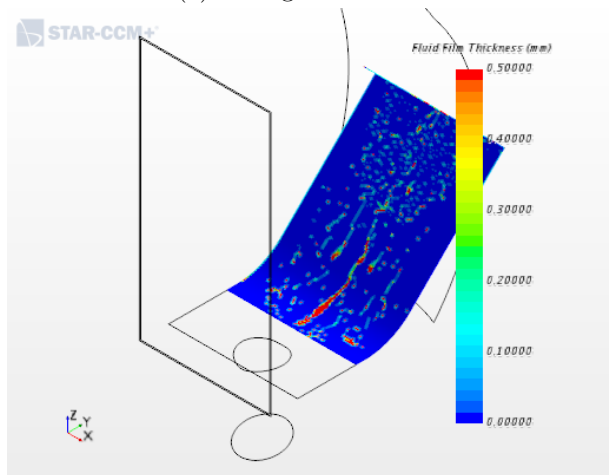
Next to the setup of the models like described in the previous sections, also the other parameters were set like in the experiment. A mesh cell count of 7,500,000 cells was needed to achieve mesh independence, describing the full StarCCM CFD setup is done in the appendices for the mesh continuum and the physics continuum. When applying the results of this thesis to another air inlet case, one needs to pay attention to both these appendices and follow the instructions to the letter. After that small variations can be made, however these type of fluid film setups will require a great deal of knowledge about the CFD software package itself, e.g. it could be opted to turn off 2-way coupling in the film physics, yet this will disable impingement physics for the fluid film, small details like these will of course greatly affect the performance of the drainage model. For the settings of the main continuum (air being pulled through the inlet system), it was fairly straightforward to copy those from the experiments. Airflow, density, temperature, atmospheric pressure etc. were all easily obtained through measurements in the lab during the PEPT run. The water phase however was more challenging, some parameters like the density, temperature and flow rate were obtained without much effort and readily available measurement techniques. However for the injected droplets the datasheet from the injector had to be used as reference. Although these values are set in the suppliers lab, conditions there are optimal. In reality the droplets formed at the injector are not a perfect match with those lab conditions and could affect the validation between the CFD and PEPT results. For example when the droplet diameter in reality is larger than the diameter that in theory should be produced by the injector, there will be fewer particle count for the same flowrate yet the droplets will be bigger, hence impacting with more energy on the plate. More of these variations will be examined in the section further analysis. For the actual validation we will follow the injector theoretical specifications in combination with the measurements for the air and water phase as described before. Figure 5.14 shows the results from the simulation, the fluid film thickness is plotted on the water surface and is shown for the four contact angles as they were used in the experiments, as expected the hydrophilic case has the most outspoken effect on the fluid film thickness, the other 3 contact angle cases are distinguishable in this type of plot. Figure 5.15 and figure 5.16 show the same style of plot (scalar plotted on top of the water surface, this time respectively the velocity magnitude and the velocity component in the direction of the slope. The results as shown in figure 5.17 show fairly good validation between the simulation and the PEPT analysis, however as mentioned some simulation settings are difficult to assess versus reality (injector setting as one example). Next to that the case with the very small contact angle did not want to converge properly, and this due to the instability that is to be expected for this contact angles, after all the impinged droplets keep on moving around on the slope. However also in real-life scenarios these extremely low contact angles are rare and only obtained in lab environments when the surfaces can be plasma treated as was done for the prototype pieces that were used the PEPT analysis. Therefore it was decided that for the further analysis in the next sections this case with very low contact angles was no longer considered.



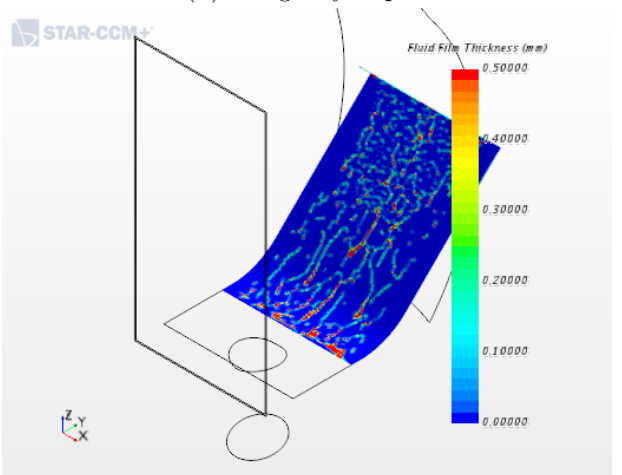
(a) 95 deg - default PE



(b) 0 deg - hydrophilic



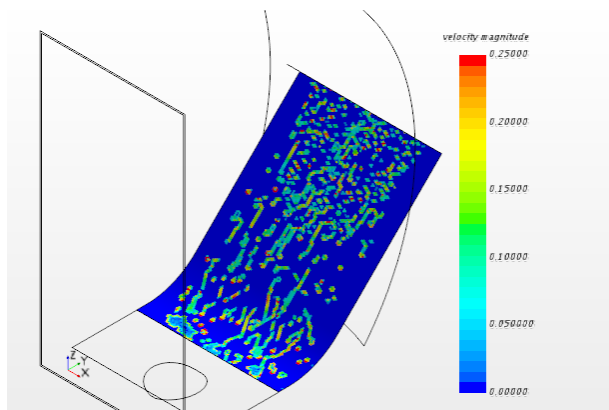
(c) 110 deg - hydrophobic



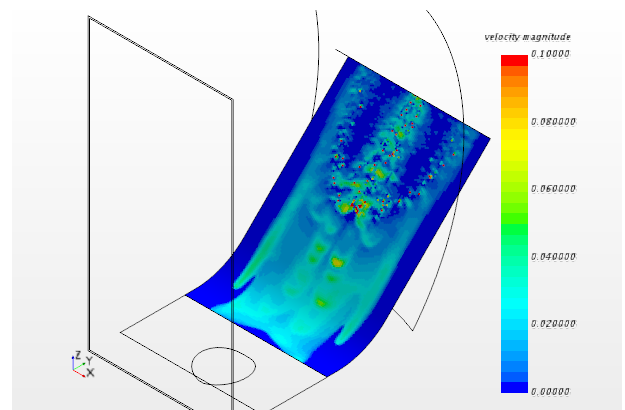
(d) 72 deg - steel

Figure 5.14: Fluid film thickness in function of the contact angle of the surface treated slope [time=5s]

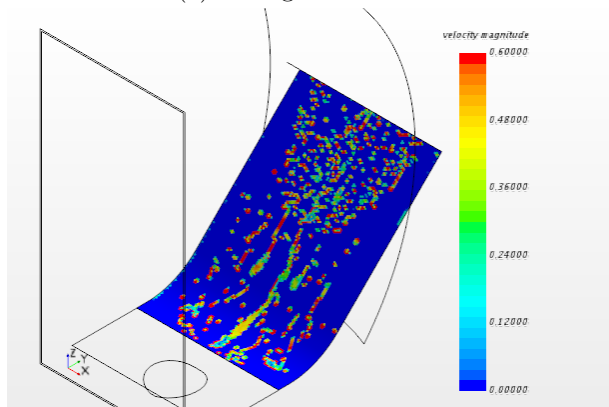




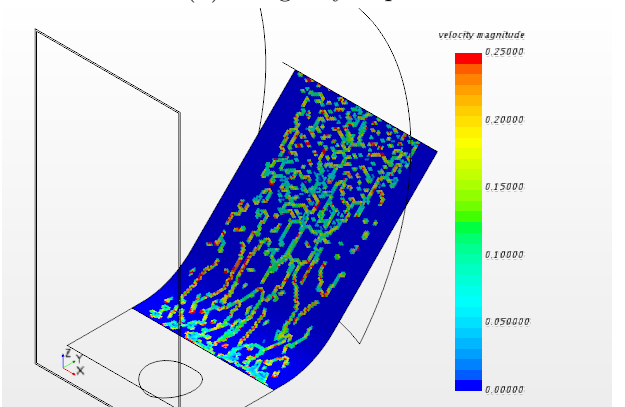
(a) 95 deg - default PE



(b) 0 deg - hydrophilic

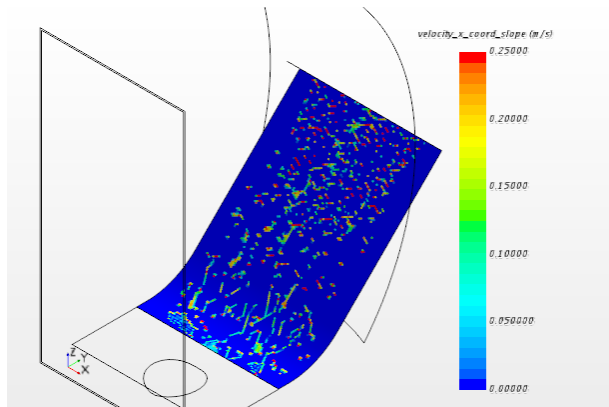


(c) 110 deg - hydrophobic

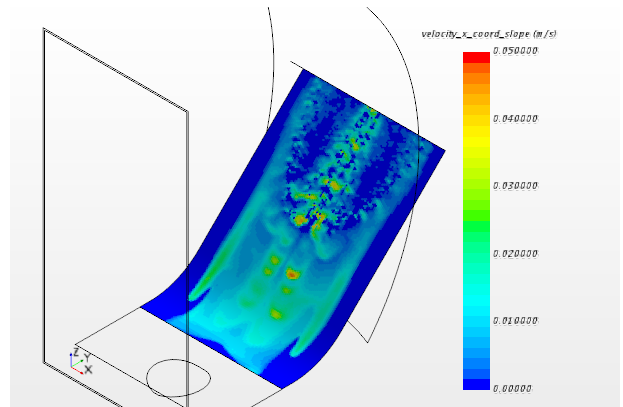


(d) 72 deg - steel

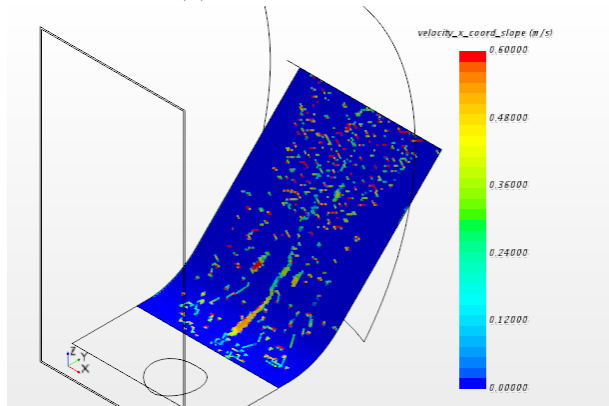
Figure 5.15: Velocity Magnitude of the fluid film on the slope, after impingement the water phase will start to slide down [time=5s]



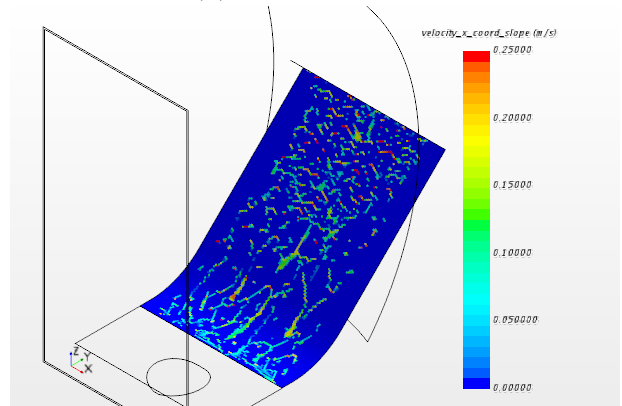
(a) 95 deg - default PE



(b) 0 deg - hydrophilic



(c) 110 deg - hydrophobic



(d) 72 deg - steel

Figure 5.16: Velocity component of the fluid film in the direction of the slope [time=5s]

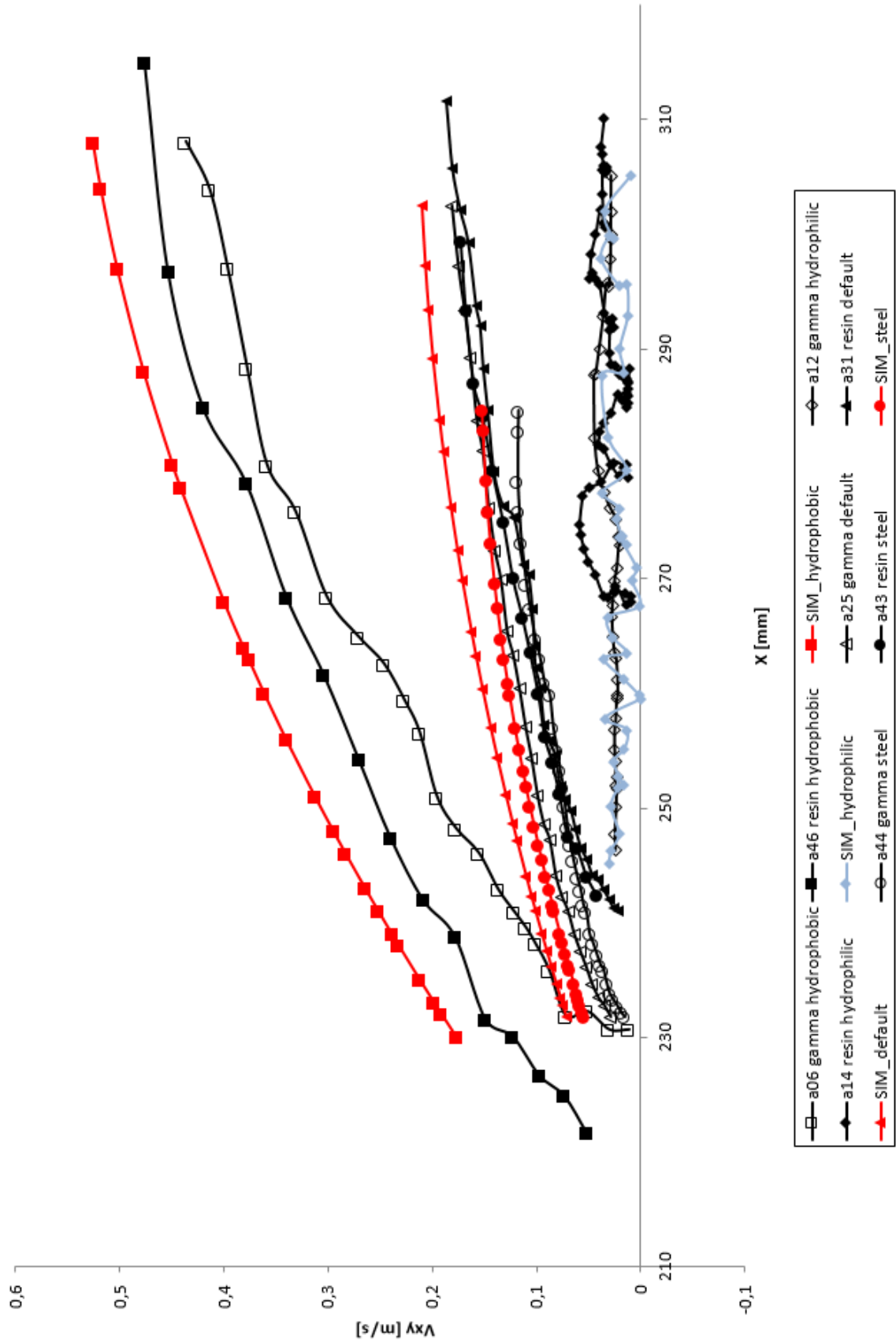


Figure 5.17: Main result of the chapter: for different contact angles the CFD setup is validated by the PEPT experimental results by comparing the velocities of the water phase sliding down the slope (hydrophilic case is plotted in grey because it is not applicable for real-life AIS cases)

## 5.4 Conclusion on validation of the CFD setup with PEPT result

As mentioned earlier, the CFD model is an approximation of the real application, meaning it is very difficult to apply all the real world conditions in a CFD model. For example, in an actual air intake system (AIS), the inside walls can be covered in dust, soot or other contaminants. These materials can act as a restriction to airflow and influence the behaviour of the water ingress. However, in the CFD model, the wall conditions were defined as an adiabatic wall. Meaning, the simulation assumes that the wall surfaces have no effect on the air flow conditions. Likewise, many other assumptions were made in the CFD model. Other examples of assumptions that were made for the CFD model, to name a few, were: heat conditions were not accounted for, vibrations were ignored and flow was considered to be in ideal conditions.

For the main air phase part of the simulation (steady state) we analysed the difference between the measured and simulated results and they showed less than 1 percent error for the velocity at the outlet. Table 5.5 and 5.6 compares the measured and simulated velocity values for the inlet orifice and outlet. This high level of validation is not uncommon for the steady state part of a simulation providing the airflow generated by the fan is done under lab conditions where it can be regulated to a highly accurate and stable value. With reference to static pressure differences between the measured and simulated situations at the outlet, the measured set only used one data point (in the centre of the tube at 6 times the hydraulic diameter, while the simulated used a mass flow averaged value. Thus, it may not contain an accurate pressure reading of the whole enclosure. However, when compared to a single value in the centre of the simulated tube, the measured static pressure loss is in validation with the experimental value.

The main topic for this thesis is however not the validation of the main air flow as described above, but the validation of the water behaviour. For the part of the simulation where we switched on the water modelling, more CFD factors became important. First off, the mesh independence study that occurred for the steady analysis, had to be redone for the unsteady simulation. The line probe results of the velocity down the slope were analysed to establish mesh independence. Secondly the convective courant number was monitored to correctly select the timestep for this problem. When the timestep would be too large, the simulation could 'skip' cells when moving down the slope. Thirdly the parcel size of the Lagrangian injectors had to be set, for this thesis it was set at its maximum, so each particle was represented by a single parcel (for rapid design iterations this could be lowered).

As described in the previous section on mesh independence, the CFD model was always ran with the optimal mesh setting (see also appendix C for full details on mesh settings used for mesh independence and appendix D for full details on the physics and boundary condition settings, meaning that values did not change any-more when refining the mesh, while solve time was reduced to a minimum. Outside of this thesis, the choice should be made by the person running the simulations, for early prototype stage analysis it could be beneficial to run the simulation with lower mesh quality in order to get faster results to already get a first understanding of the problem at hand and to do some qualitative comparisons. Like that multiple design iterations can be made relatively quick and expensive computational time can be saved. Fully detailed analysis can then be done on later models or right before rapid prototyping to validate the setup.

The validation of the CFD water behaviour down the slope with the PEPT experimental results that were obtained in chapter 3 are summarized in figure 5.17, good validation is shown for

the four different contact angles: the CFD velocity down the slope was plotted against the same velocity from the experimental setup in function of the coordinates on the X-axis (the horizontal fore-aft movement). The red plots represent the CFD results while the black plots represent the experimental PEPT results (for PEPT 2 lines are plotted each representing one kind of tracer particle). The results as shown in figure 5.17 show fairly good validation between the simulation and the PEPT analysis, however as mentioned some simulation settings are difficult to assess versus reality (injector setting as one example). Next to that the case with the very small contact angle did not want to converge properly, and this due to the instability that is to be expected for this contact angles, after all the impinged droplets keep on moving around on the slope. However also in real-life scenarios these extremely low contact angles are rare and only obtained in lab environments when the surfaces can be plasma treated as was done for the prototype pieces that were used the PEPT analysis. Therefore it was decided that for the further analysis in the next sections this case with very low contact angles was no longer considered.

## 5.5 Further Analysis on the scaled down inlet box

The same CFD model used in the previous section to illustrate comparison with PEPT experiments is modified here by changing four parameters, for the Lagrangian injector: initial velocity (the velocity with which the droplets leave the injector), droplet diameter and cone angle, for the main air phase the overall flowrate is adjusted, resulting in an increase or decrease of inlet velocity at the inlet orifice. Since the case with a 95 degree contact angle is representing the most common real life scenario, this case will be used as starting point. Running these extra simulations is not done for further validation, but for more in depth insight in how CFD models can be used in future filtration analysis to simulate also other test conditions. Furthermore the scaled down inlet box setup allows for fast exploration of these new settings compared to a full scale AIS, due to its reduced size and complexity. Off course nothing prevents the reader from also running these investigation on a full scale AIS when required. It is important before any simulation that concerns water drainage analysis to do a proper investigation into the Lagrangian phase that is injected into the system and define in detail its boundary conditions. In general, correct CFD setup is not limited to these 4 properties and also parameters such as turbulence properties, gravity, mesh settings etc will affect the results, however these are more general CFD recommendations for any type of simulation and not specific for water drainage, it is for CFD studies always advised to be thoroughly aware of the underlying algorithms and its limitations and requirements, as such results from CFD studies should always be critically studied and validated with experimental results.

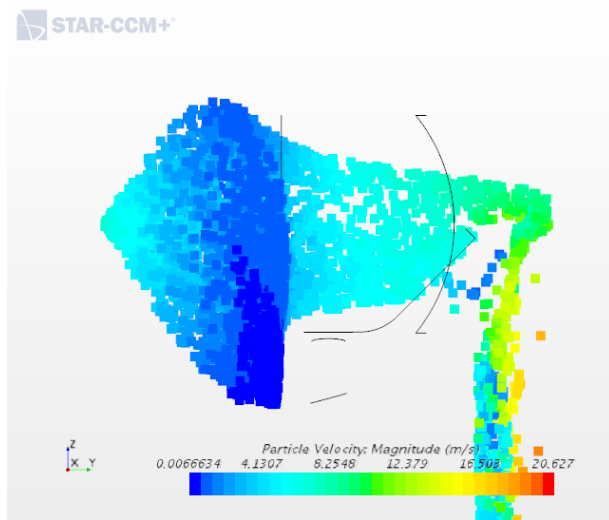
### 5.5.1 Effect of Injector Droplet initial velocity

When setting up the Lagrangian phase, one as the aspects to pay attention to is the creation of the injector and its parameters. An injector in a CFD code is a theoretical location from where Lagrangian particles are introduced into the system. In our case the injector was located at the same location as in the experiment, relative to the inlet orifice of the scaled down box. In the scalar results from the main flow field it was shown that the velocity of the air phase only increases in the actual orifice due to the sudden change in cross-area. The injector is located relatively far from this point of higher inlet velocities, in an area of the atmosphere where the surrounding air hardly has

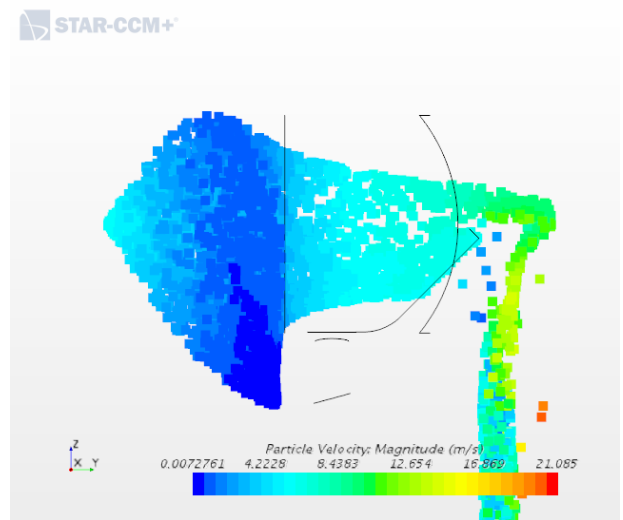
any velocity, as result the droplets would not get picked up by the air-stream and merely fall down under the influence of gravity. What needs to be done is to give the Lagrangian particles an initial velocity from their own, pointing in the direction of the air-intake similar to the initial velocity that is created by the injector nozzle from the experiments. In the previous section the validation was studied with the injector initial velocity that matched exactly the experimental value. For this section this initial velocity is changed to study its effect on the water behaviour while all the other parameters were kept the same (contact angle was kept at 95 degrees as this is the more common contact angle from the ones tested). Figure 5.18 to figure 5.21 shows the effect of this initial injector velocity on the water as it moves through the domain starting from the injected water drops to the movement of the fluid film on the inclined slope. Figure 5.18 and figure 5.19 show that the higher initial velocities allow the injected parcels to spread out further along the initial path (in this case the injector cone was set at 120 degrees in all directions). Figure 5.18d that corresponds to an injector velocity of 3 m/s (lowest velocity value) shows that the parcels get picked up by the main airflow more easy when compared to the higher velocities as in figure 5.18a, in this setup it means also that they will start to move to the centre of the flow and hence impact on the inlet geometry in a more concentrated manner. Also the plot for the fluid film thickness on the inclined slope shows this effect, figure 5.20a shows a more spread out impact zone with more distributed thickness, while figure 5.20d shows a concentrated pattern and as result a film that is showing higher thickness overall (water collect on a more concentrated patch). Similar to the fluid film thickness also the fluid film velocity in direction of the slope is now slightly higher in figure 5.21d that corresponds to the lowest injector initial velocity. A general conclusion would be that a lower initial injector velocity allows the parcels to start following the main air flow, specifically for out setup of this scaled down inlet box it means that for lower injector velocities the parcels get dragged in the main air phase that is concentrated in the centre of the inlet orifice, hence resulting in a more concentrated impingement pattern in the inclined slope resulting in higher film thickness and film drainage velocities.

### 5.5.2 Effect of Injector Droplet diameter

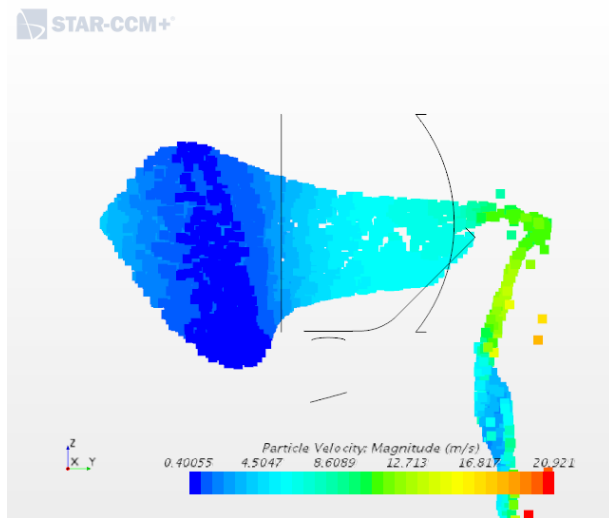
In the PEPT validation chapter the injector droplet diameter was simulated with a normal distribution rather than a fixed diameter size, this to better represent the injected spray as it is occurring in the lab test. However lorries do not always face similar conditions during operation. A noticeable exception would be the finer droplets that occur when the truck would be pass in a pressure wash. In order to evaluate the effect of droplet diameter on the water behaviour when moving through the domain, 4 extra simulations were run where the droplet diameter was either 0.5, 1.0, 1.5 or 2.0 mm. It is expected that the smaller droplets are easier to carry in the main airflow, however the larger droplets will impact heavier and are prone to breakup and potential re-entrainment. Figure 5.22 to figure 5.25 shows the effect of this injector diameter on the water as it moves through the domain starting from the injected water drops to the movement of the fluid film on the inclined slope. for this setup the initial velocity was kept identical, however when the diameter of the injected particle changes this in combination with the initial velocity will influence its trajectory. Figure 5.22d and figure 5.23d show that for larger particles there is slightly more resistance of the particle to the main flow (it doesn't get carried so quickly as the smaller particles), however this is not so outspoken as the effect of the injector velocity as described in the



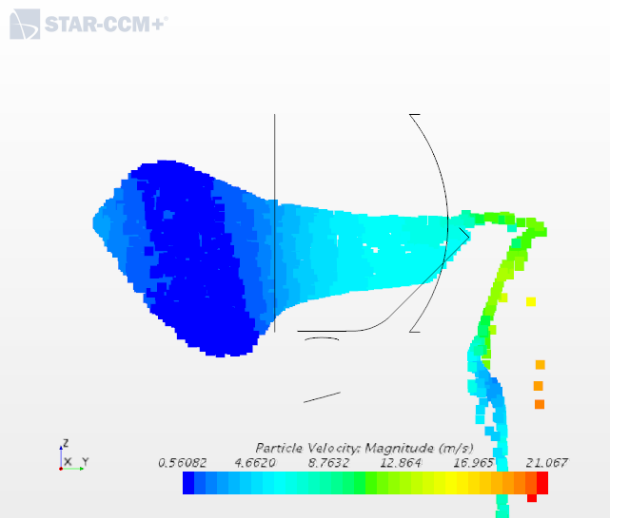
(a) 7 m/s



(b) 6 m/s

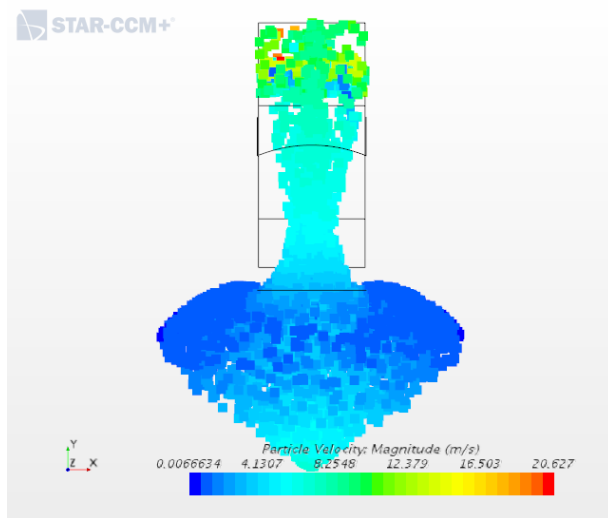


(c) 4 m/s

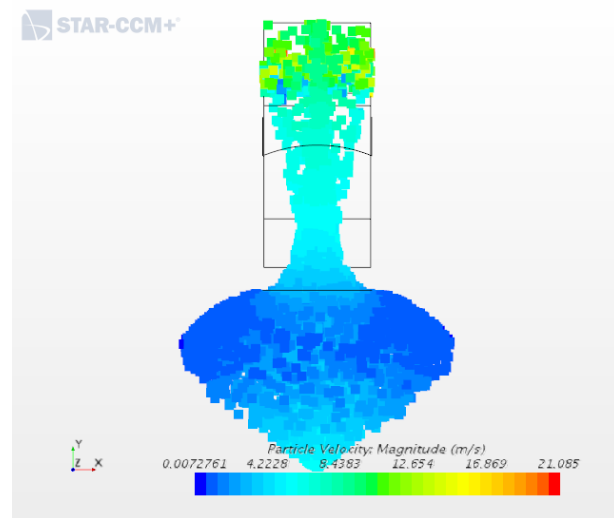


(d) 3 m/s

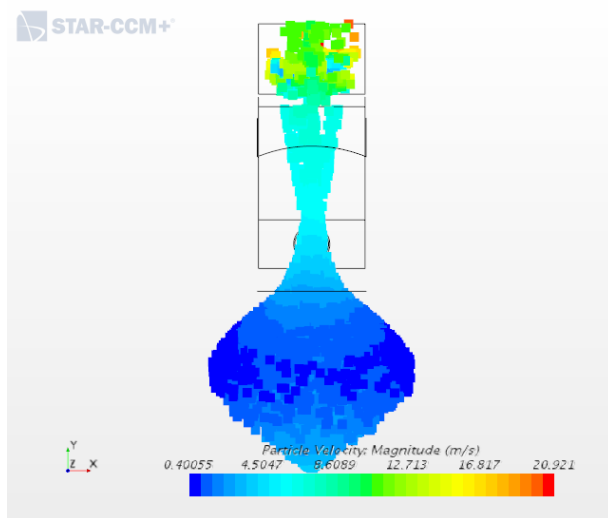
Figure 5.18: Injected droplets path (front view) in function of injector initial velocity



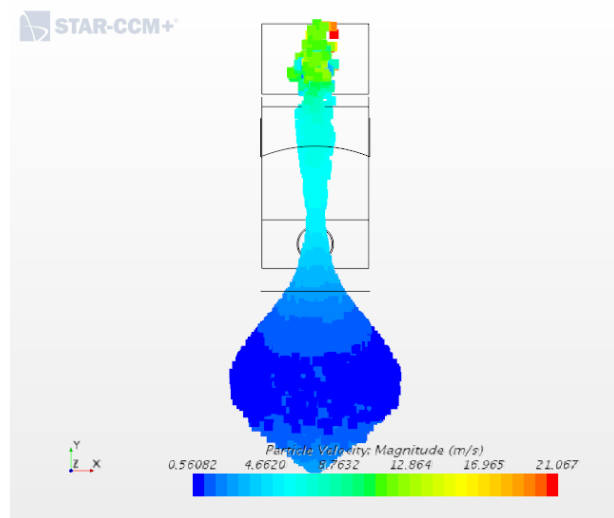
(a) 7 m/s



(b) 6 m/s



(c) 4 m/s



(d) 3 m/s

Figure 5.19: Injected droplets path (top view) in function of injector initial velocity



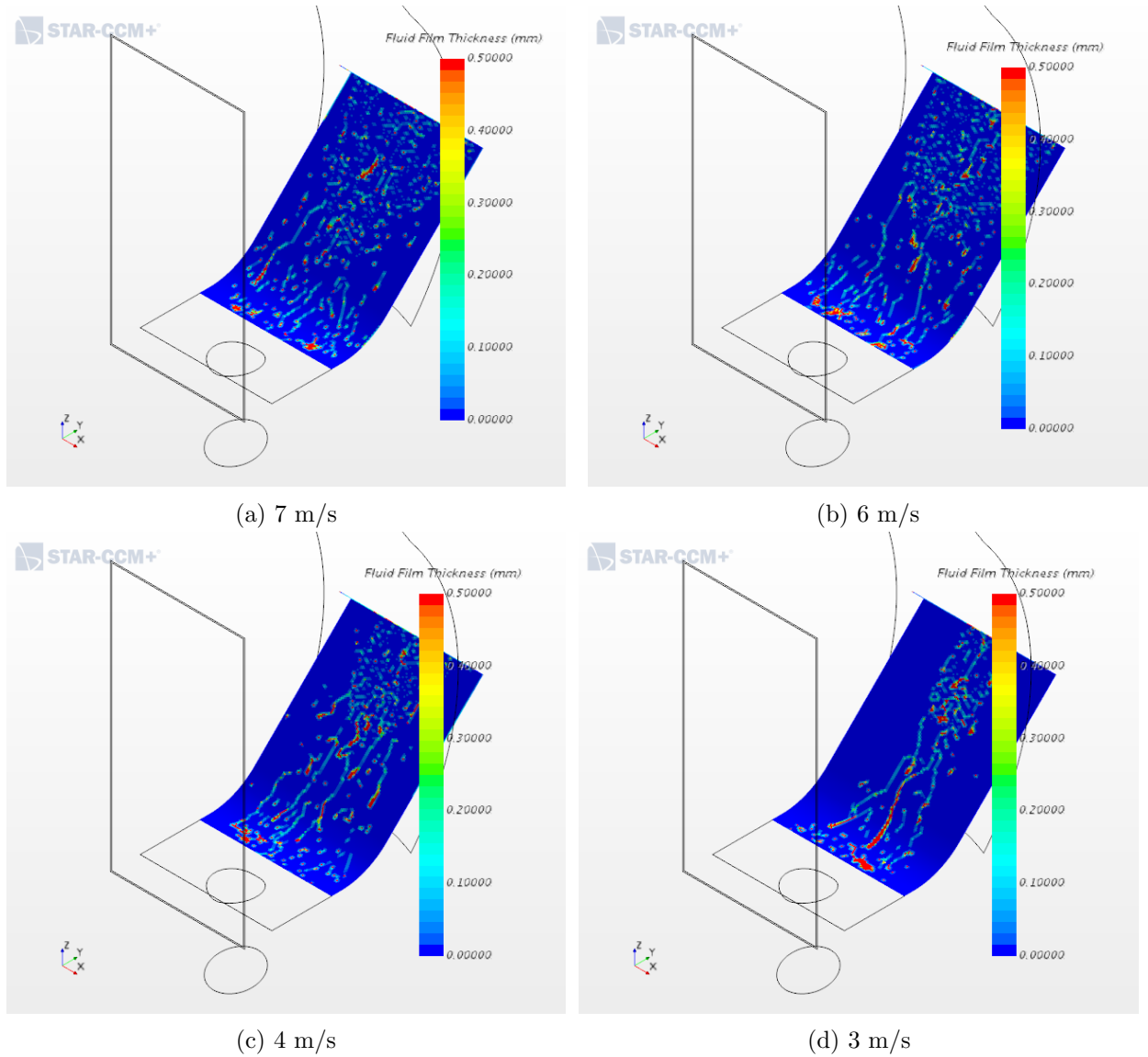


Figure 5.20: Fluid film thickness in function of injector initial velocity - when high injector velocity is used (figure a), the main air stream doesn't have the capability to pull the droplets towards the centre of the airflow, resulting in a more spread out impact pattern, in image d that has the lowest injector velocity the opposite is occurring: the main air flow is now capable of pulling the droplets to the centre of the airflow and as result the water is concentrated around the centre of the slope, with the water being concentrated in the centre also the film thickness is higher in that zone

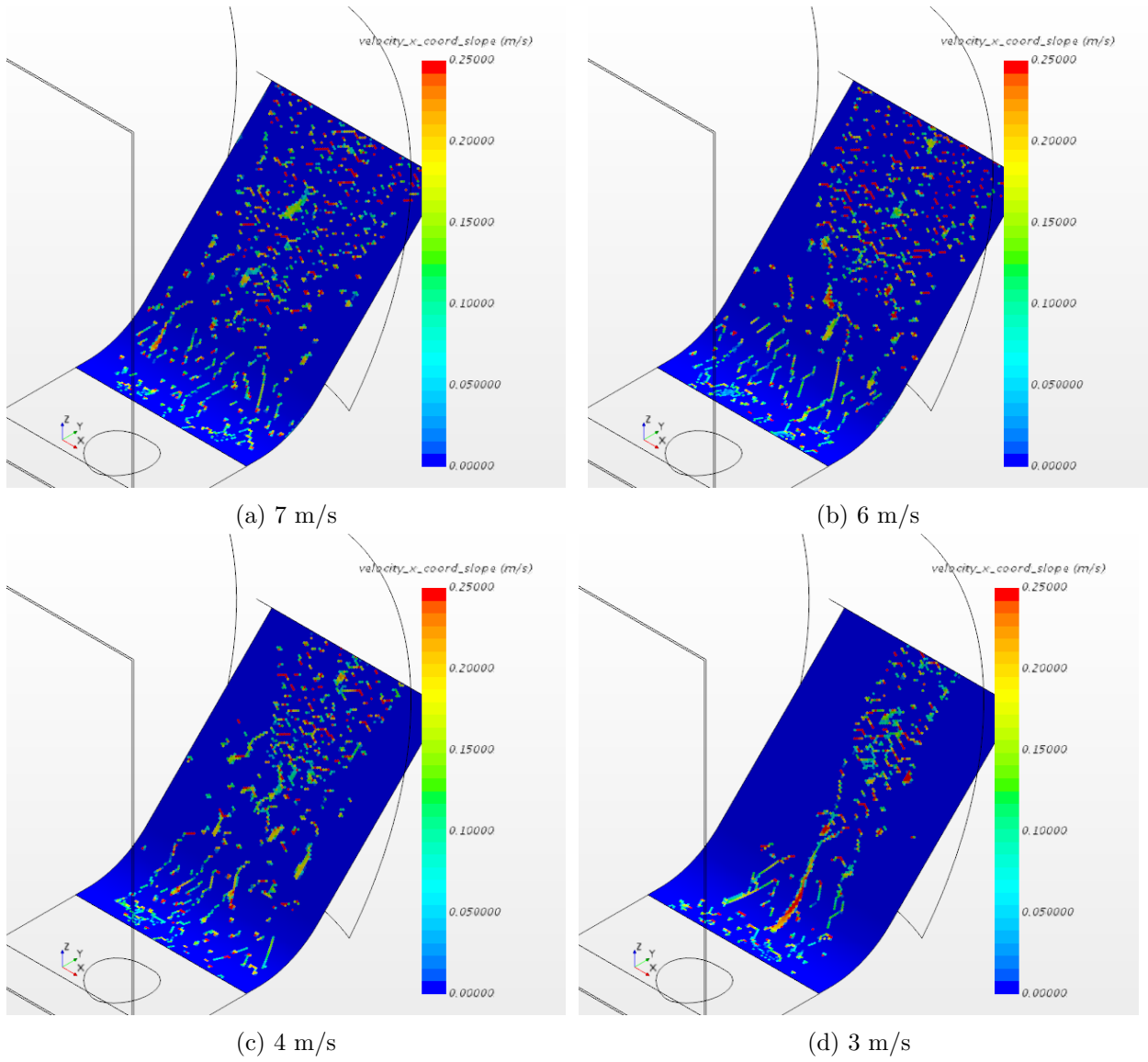


Figure 5.21: Fluid film velocity in direction of slope in function of injector initial velocity - as in figure 5.20 the injector velocity has most impact on the distribution of the droplets

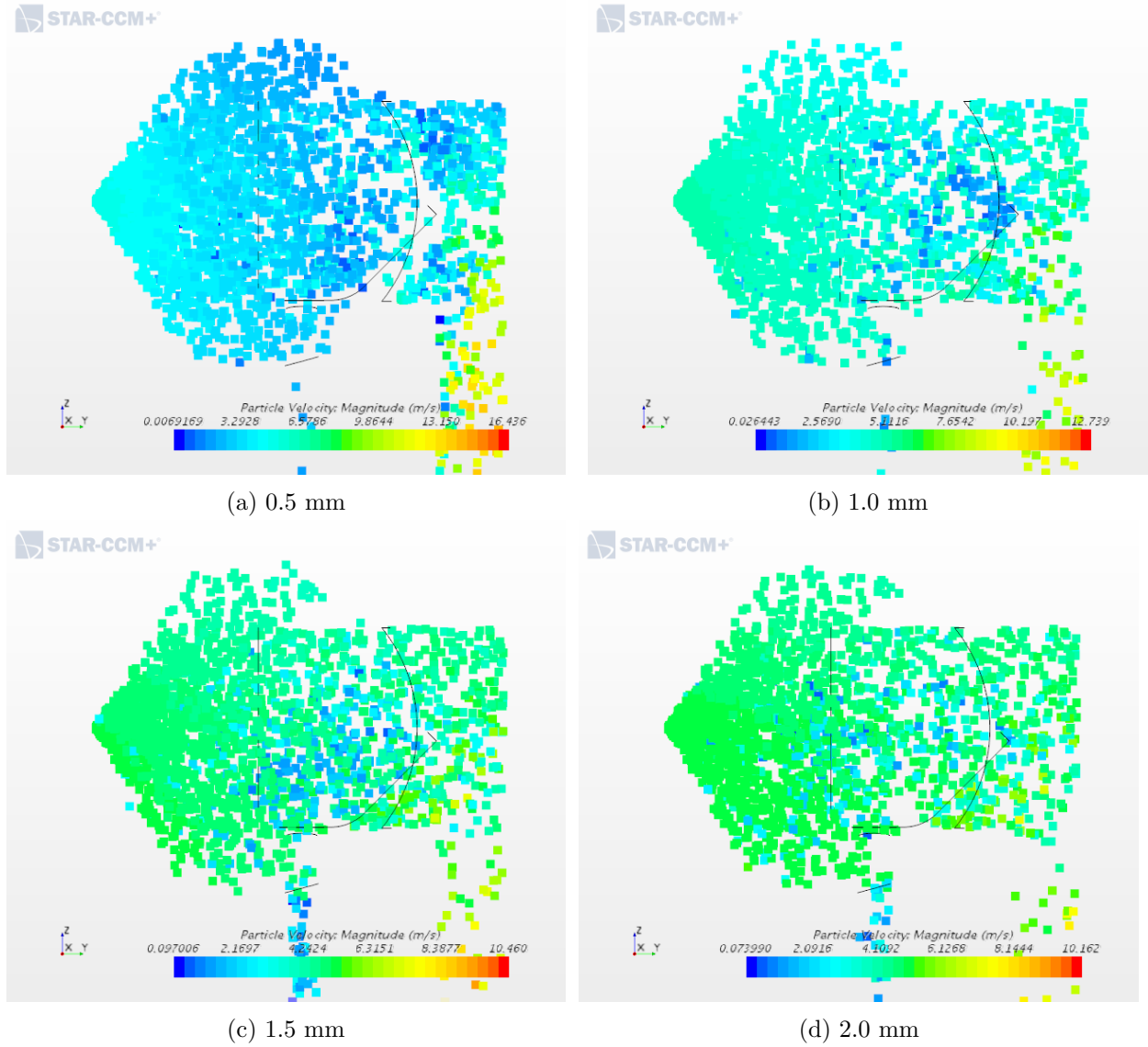
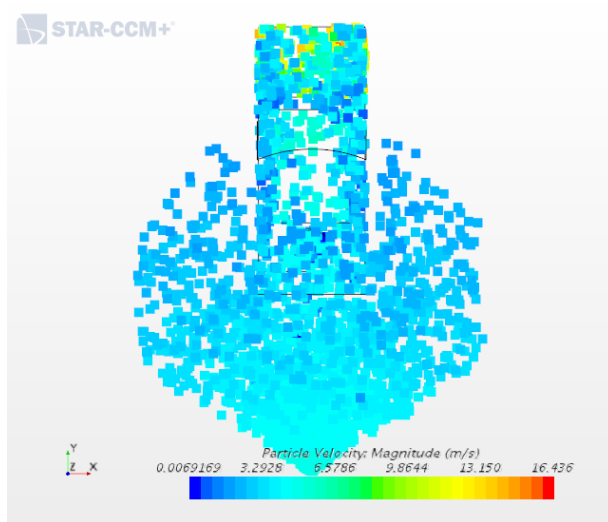


Figure 5.22: Injected droplets path (front view) in function of injector droplet size

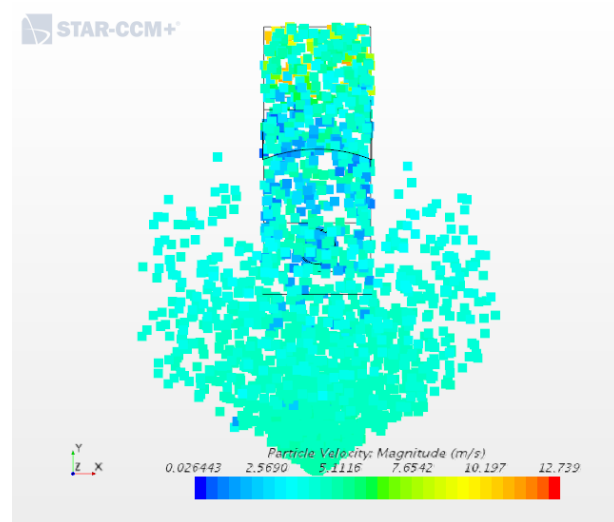
previous section. Figure 5.24 and figure 5.25 shows that there is hardly any effect and the fluid film behaviour both in terms of film thickness and velocity. For our case we can conclude that particle diameter has less impact on the behaviour in the domain when compared to changing the injector initial velocity. However this should not be a general conclusion that is applicable to any water drainage analysis, much smaller particle diameters that represent a very fine mist or spray will react differently.

### 5.5.3 Effect of Injector Cone Angle

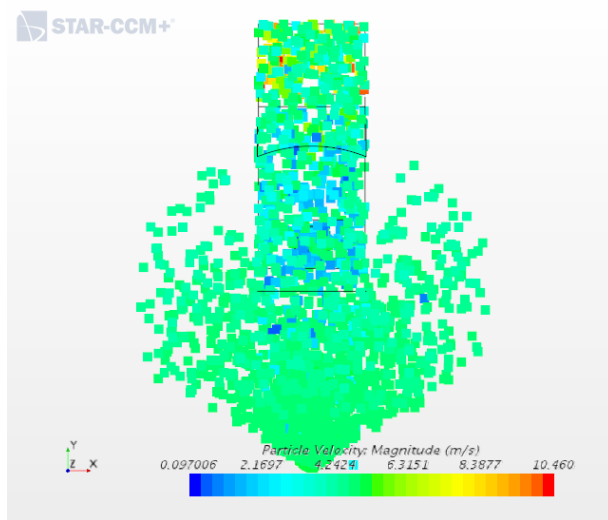
As described before, the injector act as a theoretical location from where Lagrangian particles are introduced into the system. The default setup for an injector in the CFD code is a point injector, meaning a singularity from where all particles depart in the system. However more options are available in order to better mimic real-life scenarios. Next to a point injector, we could also choose for a line injector (similar to a waterfall where all particles depart from a long narrow strip), also using a boundary surface from the CFD model could act as an injector part. For our case



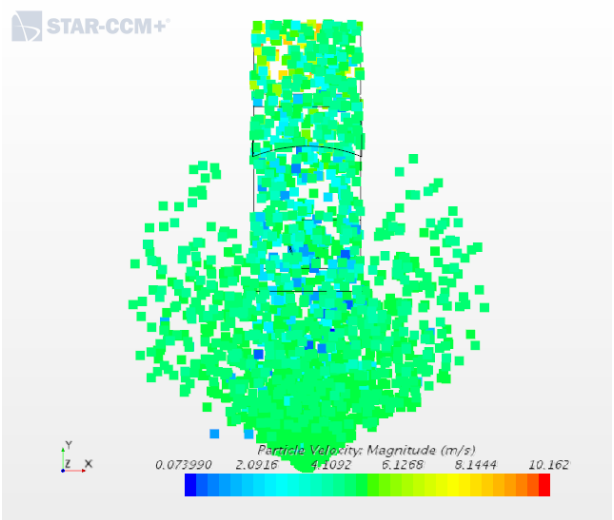
(a) 0.5 mm



(b) 1.0 mm

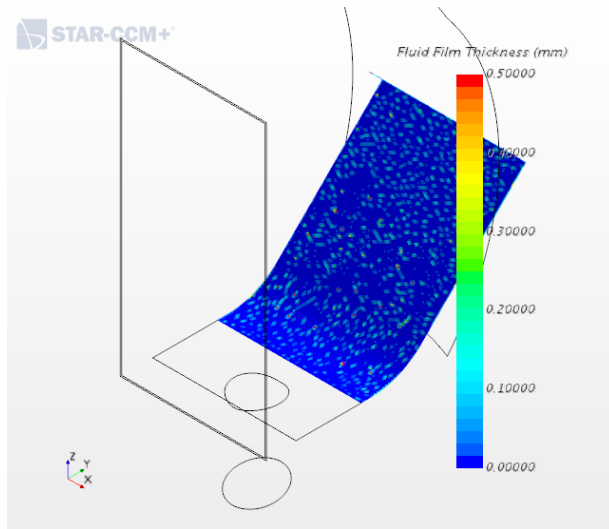


(c) 1.5 mm

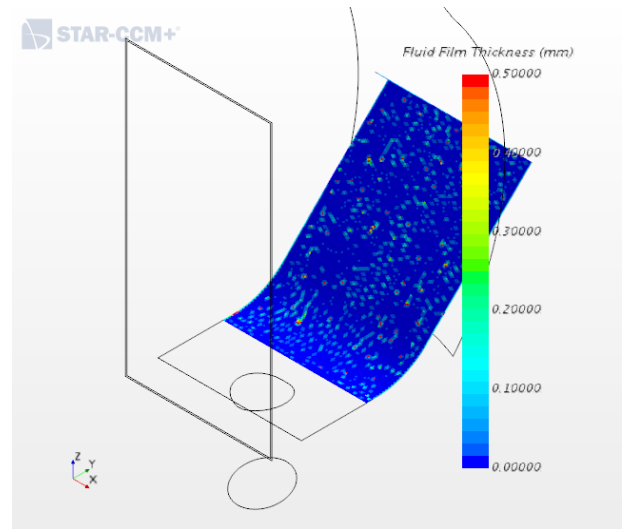


(d) 2.0 mm

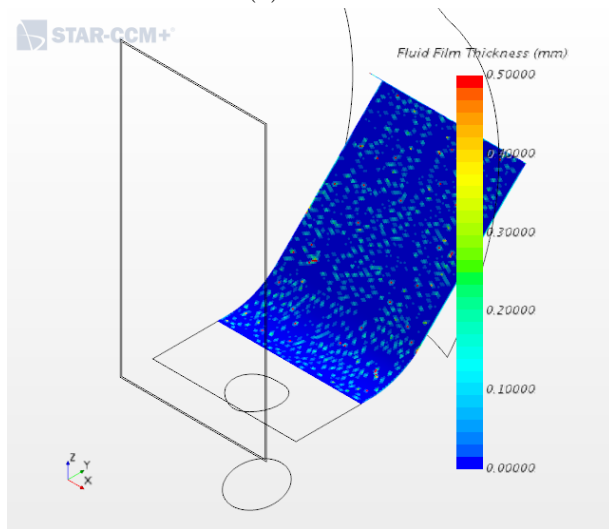
Figure 5.23: Injected droplets path (top view) in function of injector droplet size



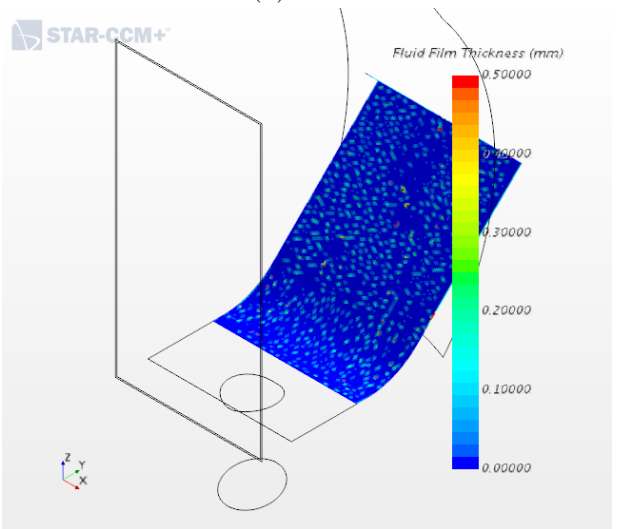
(a) 0.5 mm



(b) 1.0 mm



(c) 1.5 mm



(d) 2.0 mm

Figure 5.24: Fluid film thickness in function of injector droplet size

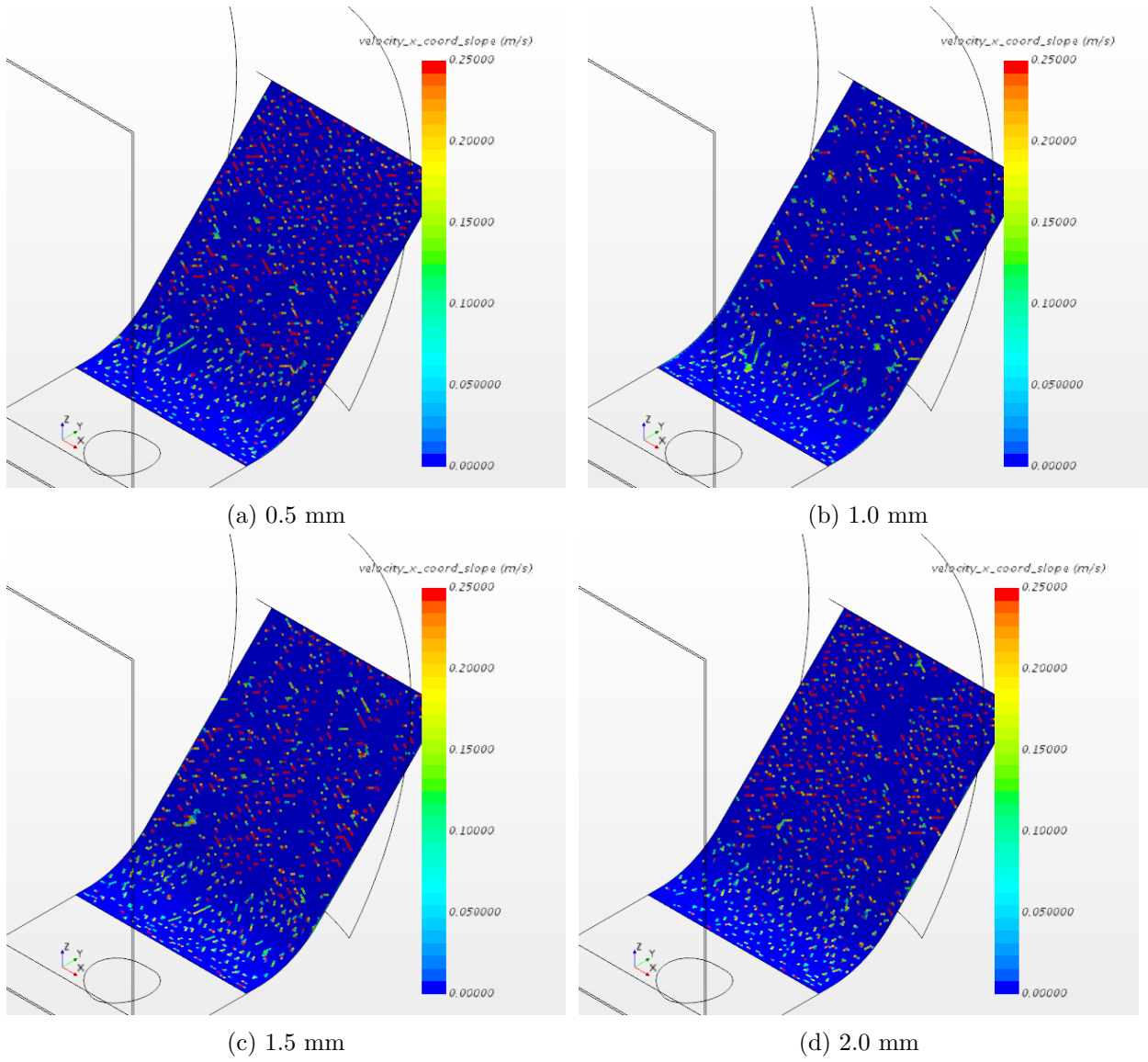


Figure 5.25: Fluid film velocity in direction of slope in function of injector droplet size

the most realistic method is the cone injector. A (hollow) cone injector injects parcels in a cone formation about an axis you specify. An injector diameter, an inner cone angle, and an outer cone angle define the cone, as shown in figure 5.26. (The diagram shows only half the cone; the injector uses a whole cone. The example shown has an injector diameter of zero). The specified number of parcel streams are injected in random directions conforming to a uniform distribution on the surface of the cone. Given the direction, the velocity is obtained using the specified velocity magnitude. In steady simulations, each iteration uses the same stochastically chosen direction and size distribution. In unsteady simulations, the direction and size distribution are randomized again and newly sampled each time-step, if you activate the Cone Randomization property. For this injector, the Inputs property is used to define the region within which the origin of the axis is located. The injector cone angle can range from 0 to 180 degrees, for the validation study a solid (inner cone angle is zero) cone injector of an angle of  $120^\circ$  was used that matched with the injector nozzle from the experiment. Figure 5.27 to figure 5.30 shows the effect of this injector diameter on the water as it moves through the domain starting from the injected water drops to the movement of the fluid film on the inclined slope. Figure 5.27 and figure 5.28 show a very pronounced effect of the injector cone angle on the path of the injected particles, of course this again depends heavily on the initial velocity of those particles (when a particle would have no initial velocity it would start to follow the main air phase almost instantaneously). In this case however there is some initial injector velocity and hence the effect of changing the cone angle is more outspoken. A wide cone angle ( $150^\circ$ ) such in figure 5.27a and figure 5.28a show a very wide trajectory and particles that even overshoot the inclined slope, allowing particles to move into the inlet without impinging and draining from the collector. Figure 5.27d and figure 5.28d show a narrow cone angle ( $30^\circ$ ) that concentrates the particle flow and make it impact on a limited patch of the inclined slope, this will create a fast formation of a draining film, and in this case also a film that is concentrated in the centre of the slope. Figure 5.29d that represents the particle path with the narrow impact shows a phenomenon that is typical for a stream of water droplets that impact a narrow area of a surface, namely right under the impact zone the fluid film thickness is not increasing, in reality the film under this area is receiving a large amount of energy from those impinging particles, while in the wide cone angle scenario that energy is more distributed. The conclusion for our setup is also valid for a more general conclusion, when there is a significant initial injector velocity then the injector cone angle will have an influence on the water behaviour further downstream. This is something that needs to be considered when running water drainage simulations and a good prior knowledge of the test conditions is required in order to obtain good validation. As discussed before a cone injector is not the only means of introducing Lagrangian parcels to the domain, other forms of injector like point injectors or a grid injector can sometimes be better suited to represent the correct boundary conditions, for our full scale analysis in a later chapter we will use a grid injector because this better represents rain drops as they are falling from the sky.

#### 5.5.4 Effect of main air phase flowrate

The main air phase is the physics continuum that was first solved with the steady state simulation. It is the continuum that represent the movement of the air into the inlet orifice and being pulled throughout the whole air intake system. In the experiment this was done by switching on the fan set and generating a suction at the outlet of air intake box. In the CFD code this is achieved

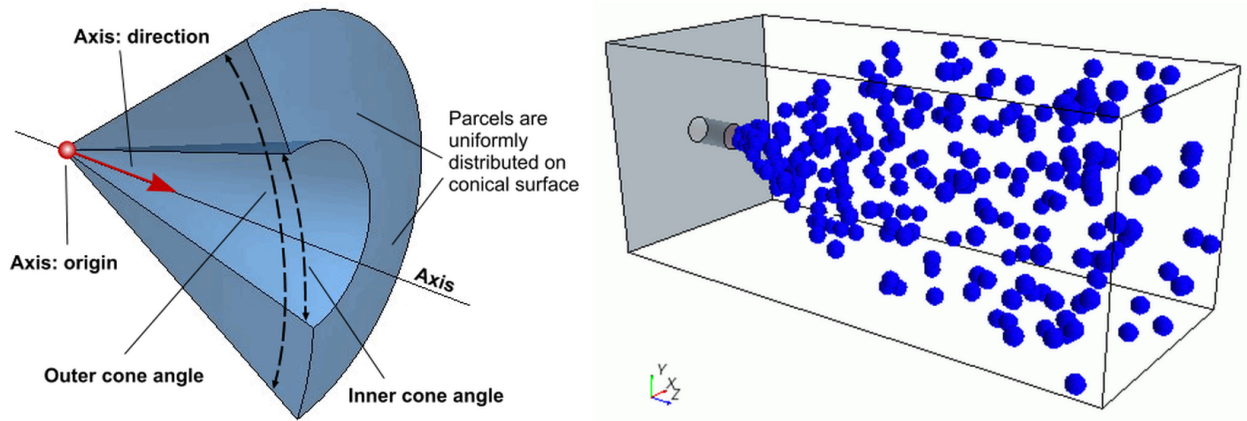


Figure 5.26: LEFT: (hollow) cone injector layout - RIGHT: resulting particle distribution from a (hollow) cone injector

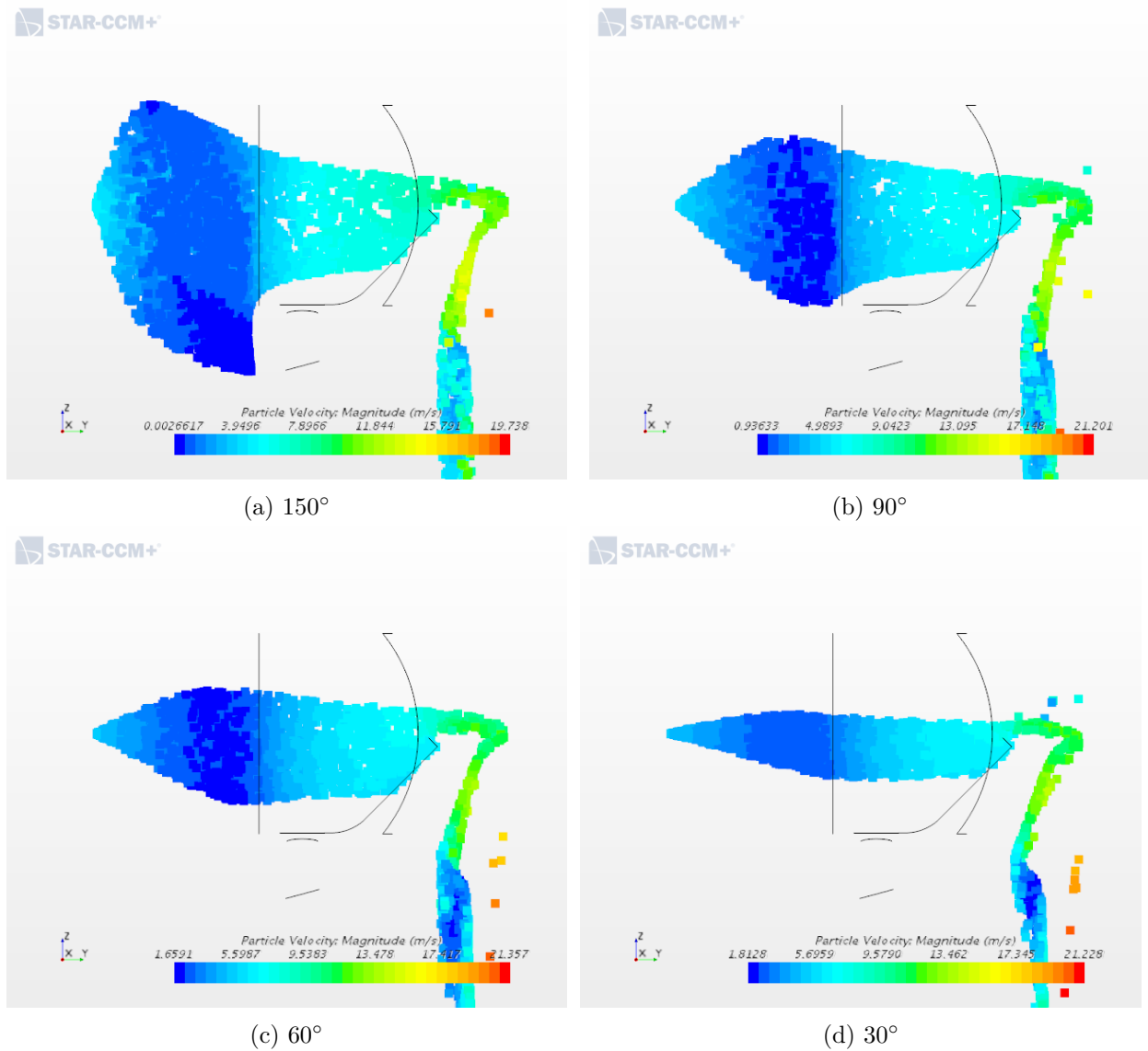
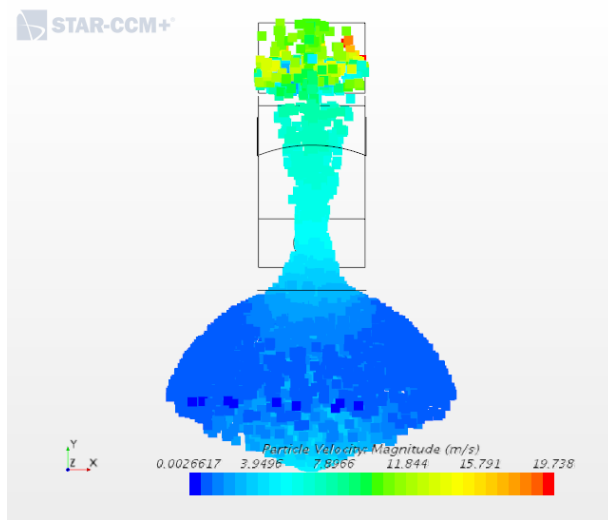
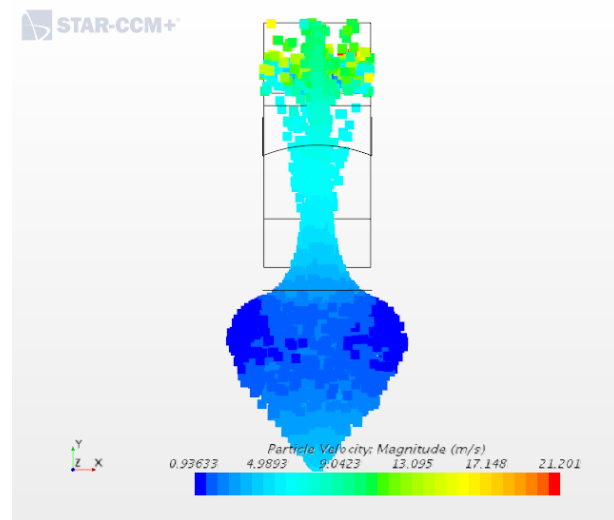


Figure 5.27: Injected droplets path (front view) in function of injector cone angle

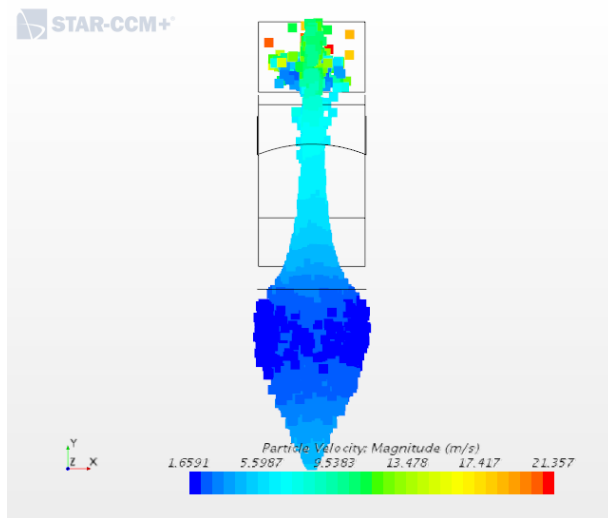




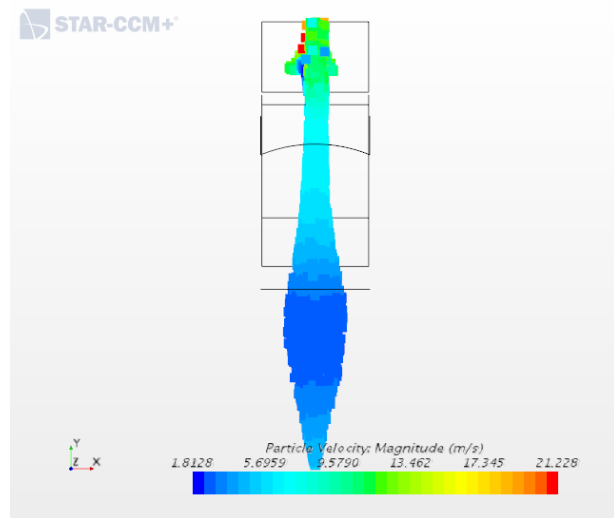
(a) 150°



(b) 90°



(c) 60°



(d) 30°

Figure 5.28: Injected droplets path (top view) in function of injector cone angle

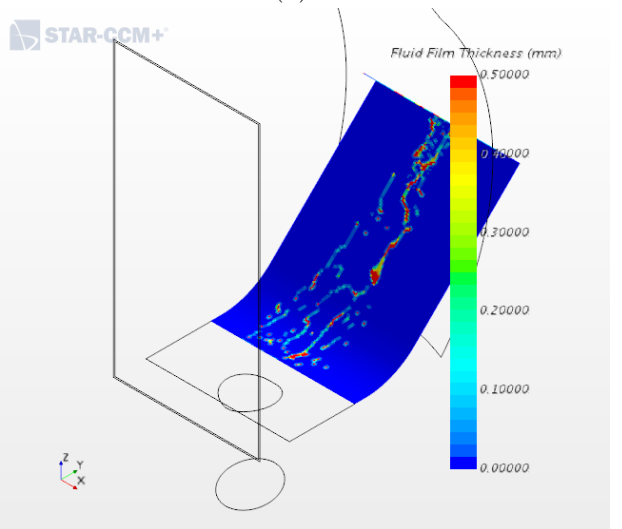
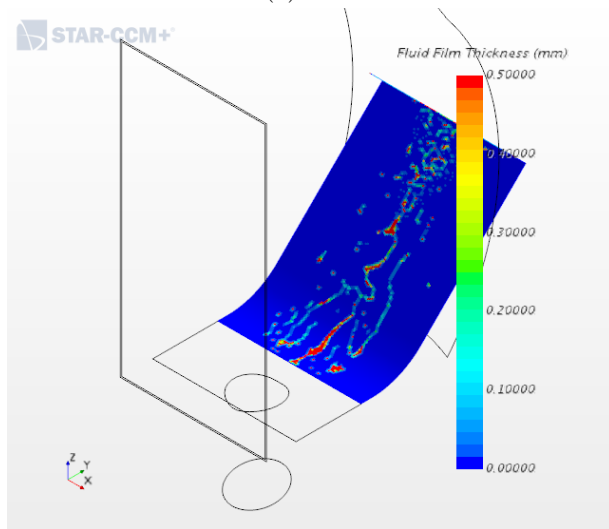
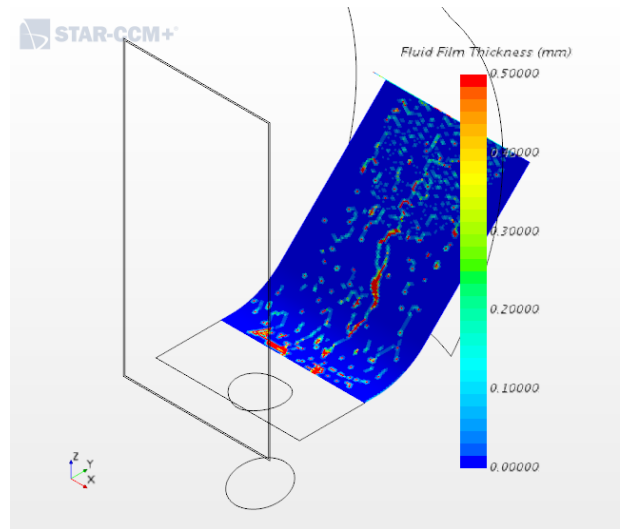
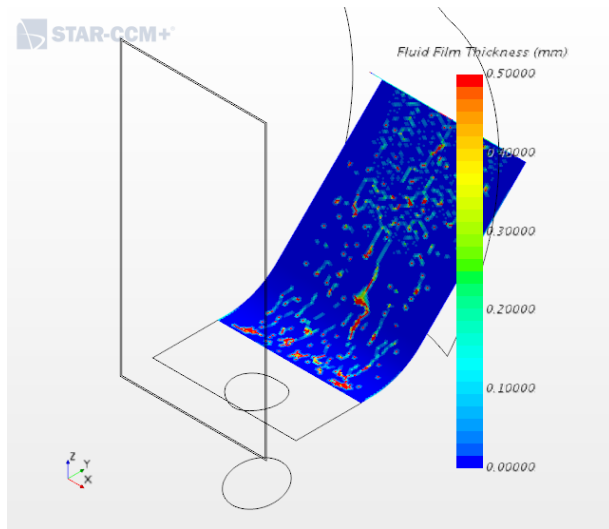


Figure 5.29: Fluid film thickness in function of injector cone angle

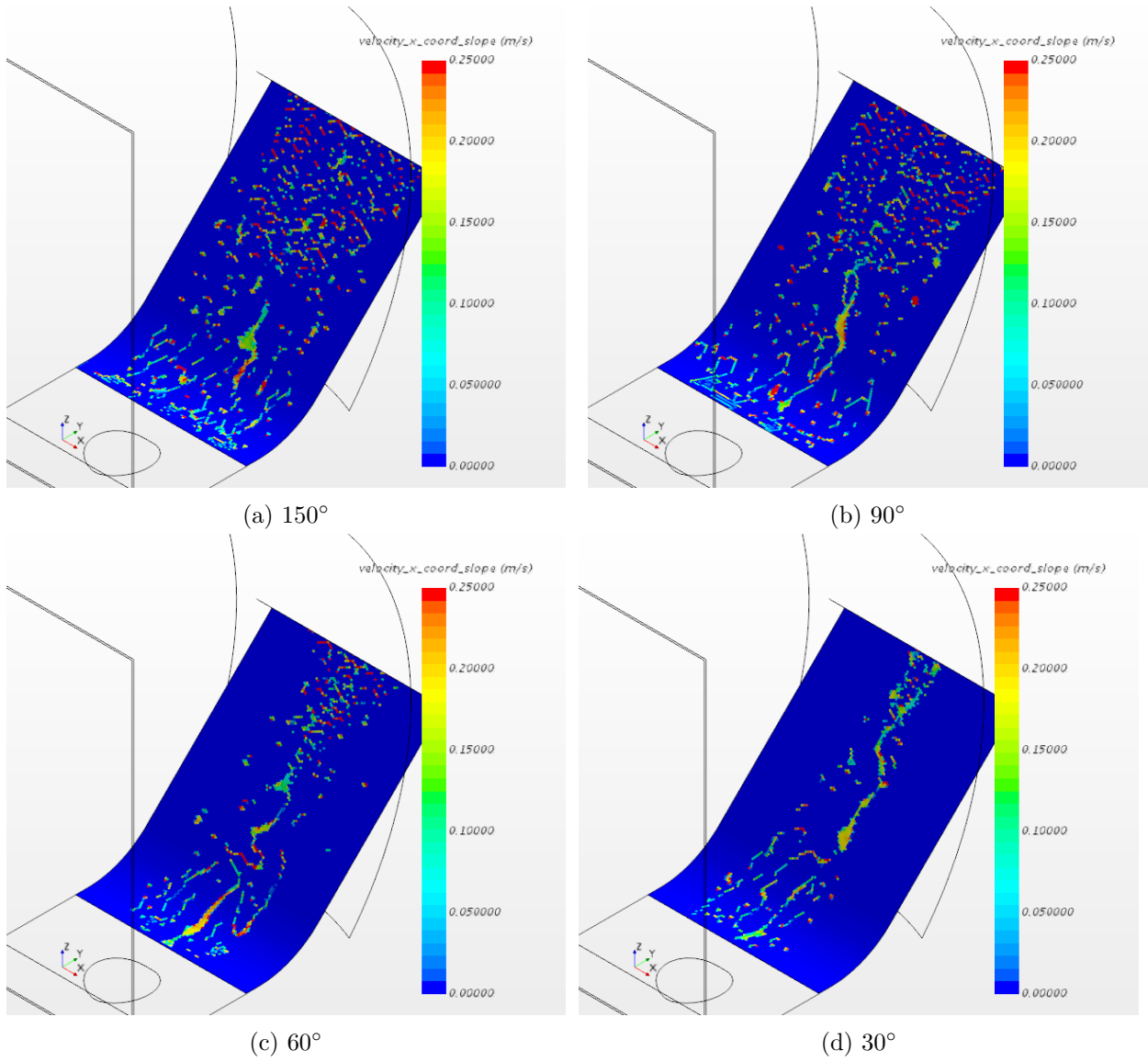
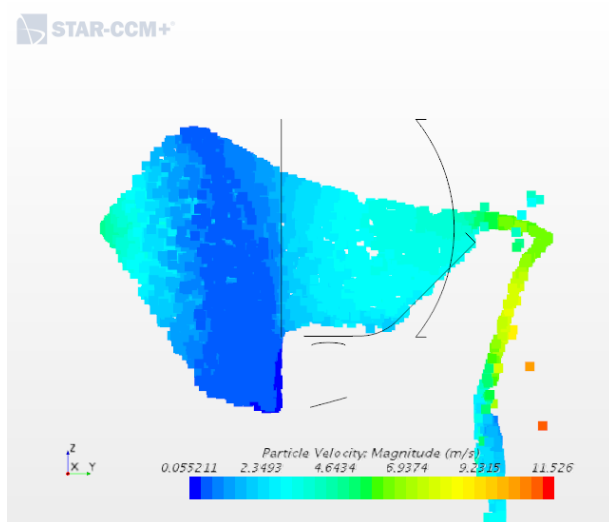
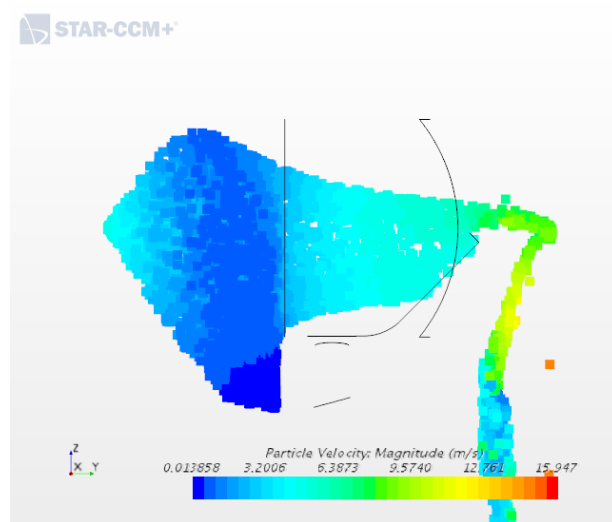


Figure 5.30: Fluid film velocity in direction of slope in function of injector cone angle

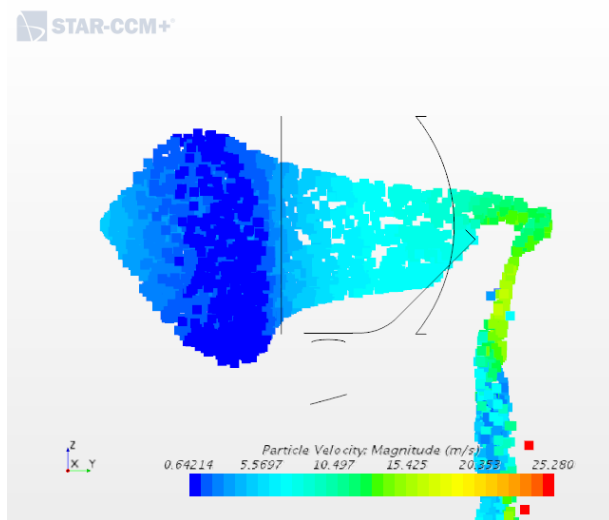
by applying a negative mass flow-rate to the outlet boundary condition. In the validation case this was done with a mass flow-rate of  $0.2665\text{kg/s}$ . Having such a large inlet cross-area available is not always a given, and space constraints for inlets (and other auxiliary components) are becoming more critical. Therefore it could occur that inlet velocities are higher than  $5\text{ m/s}$ . This subsection will investigate the effect of this increase in velocity. An extra simulation with a lowered velocity field is also performed in order to also examine that impact. An important pre-requisite for this type of analysis is the use of drag models in the simulation. The drag model simulates the effect of the air phase on the Lagrangian particles, if this would not be switched on (this is an optional model), the air phase would have no drag effect on the particles, this is only the case for very small air velocities. For our examination this is never the case and hence this model was always switched on. The drag coefficient itself can also be adapted and multiple models exist for these, however for this thesis the default value and model was kept. Figure 5.31 to figure 5.34 shows the effect of the main air phase flowrate on the water as it moves through the domain starting from the injected water drops to the movement of the fluid film on the inclined slope. The main air phase is the air that moves from the atmosphere into the air intake, it is called main phase since it is the main fluid present in the simulation, it forms the domain in where the water drops are injected. In the simulation there are 2 options to define the interaction between this main phase and the injected particles, either 1 way coupling where the main phase acts on the Lagrangian phase but not the other way around, or full 2 way coupling where also the Lagrangian phase will act on the main air phase. In our cases the injected water droplets are not significant to affect the main air phase and 1 way coupling is selected (which also has a positive effect on the calculation time). Figure 5.31a and figure 5.32a show that for a low airflow the particles are allowed to follow their own trajectory that is determined by the injector cone angle and the injector initial velocity. When the main air phase flowrate is increased (see figure 5.31d and figure 5.32d) we can observe that the particles are no longer able to swerve out so much and are picked up by the main air phase more quickly, for our case this also means that those particles will be more concentrated when impinging on the inclined slope with similar effect as described in the prior 2 sections.



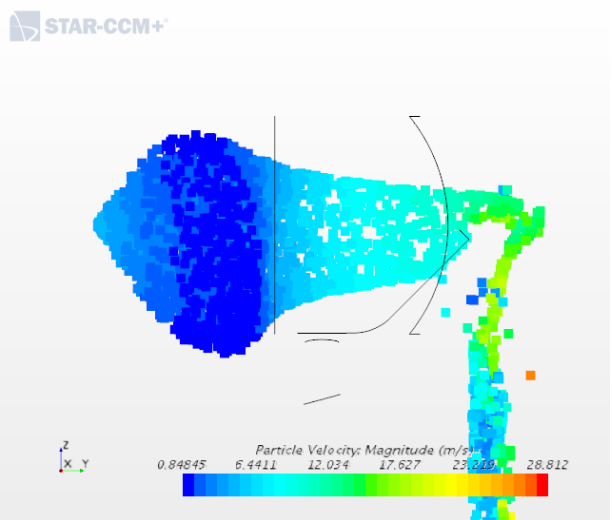
(a) 0,13325 kg/s



(b) 0,199875 kg/s

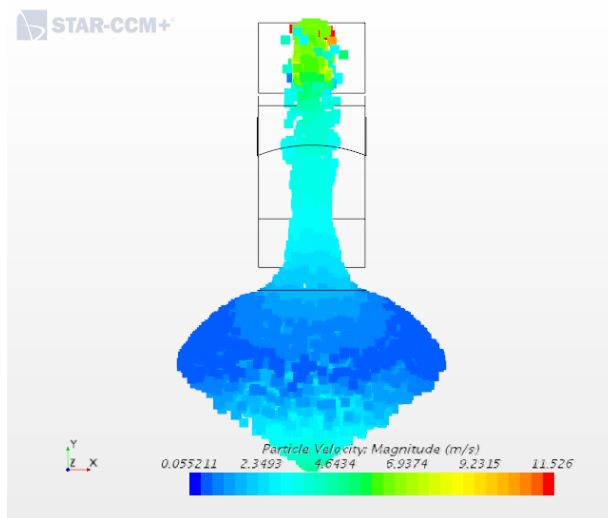


(c) 0,333125 kg/s

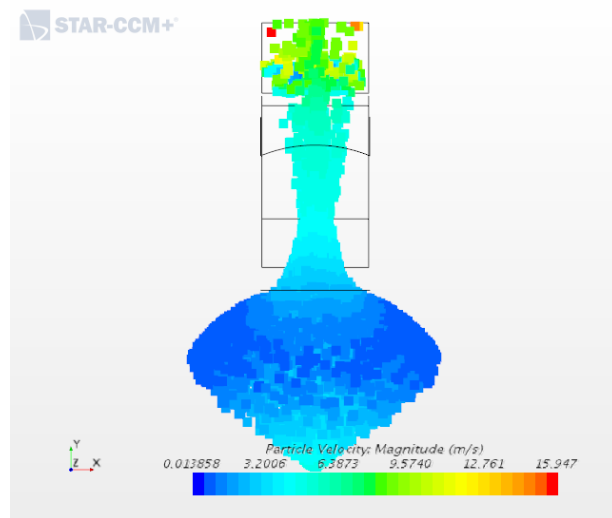


(d) 0,39975 kg/s

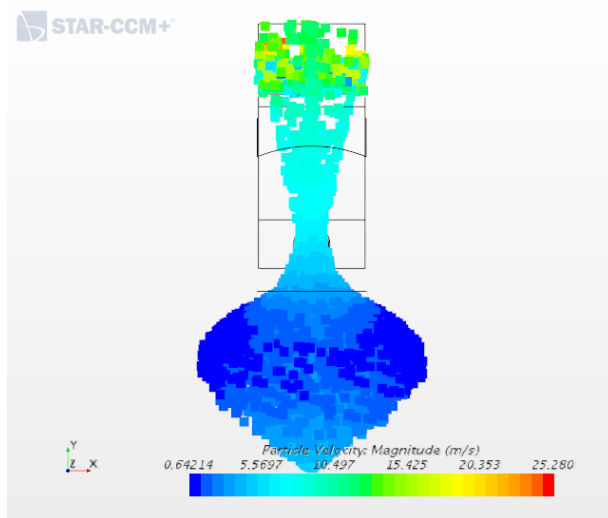
Figure 5.31: Injected droplets path (front view) in function of main air phase flowrate



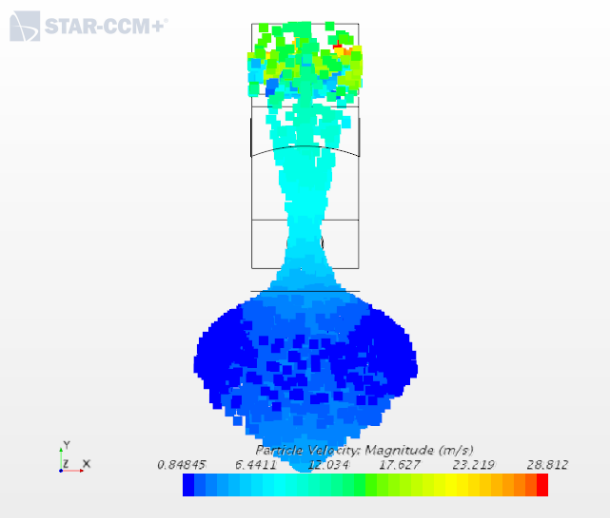
(a) 0,13325 kg/s



(b) 0,199875 kg/s

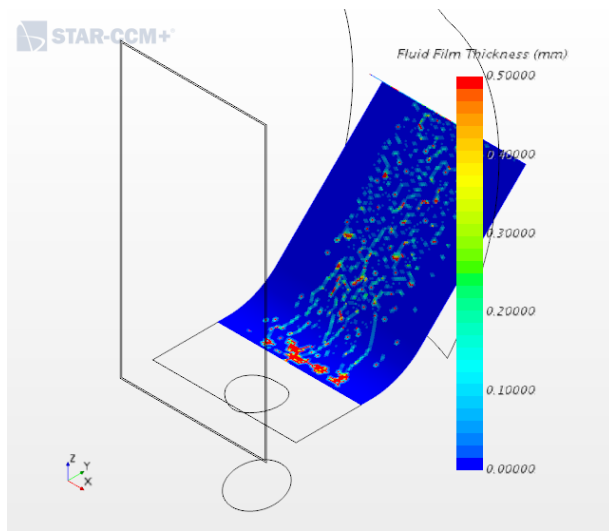


(c) 0,333125 kg/s

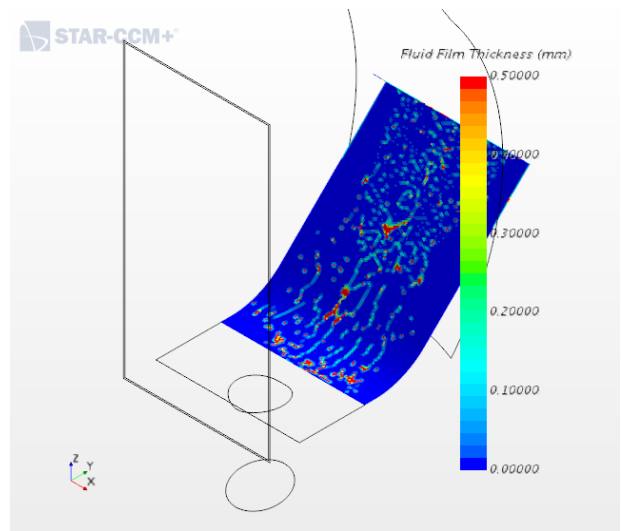


(d) 0,39975 kg/s

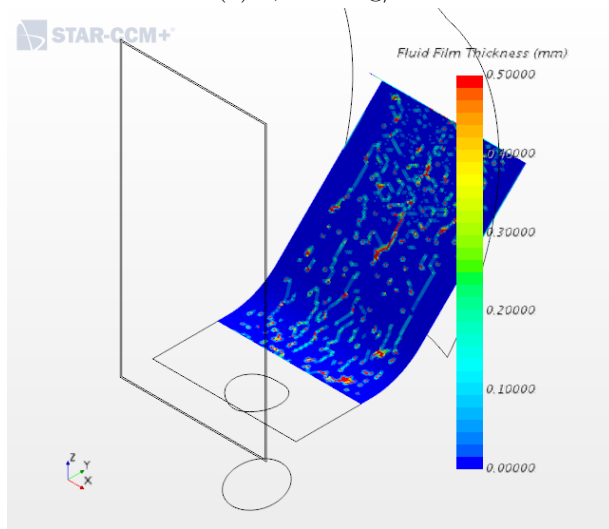
Figure 5.32: Injected droplets path (top view) in function of main air phase flowrate



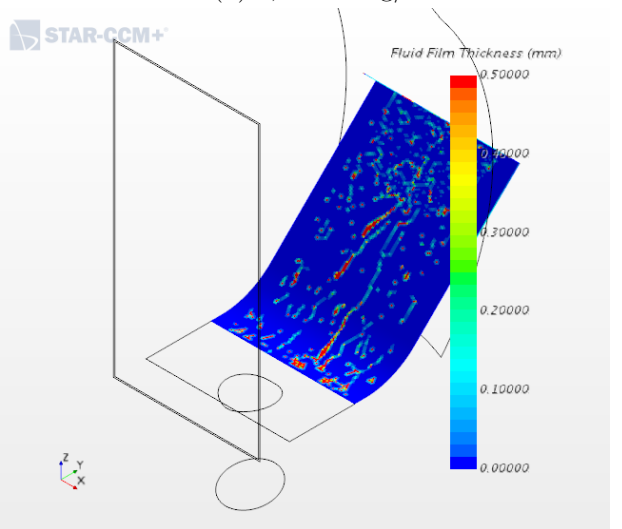
(a) 0,13325 kg/s



(b) 0,199875 kg/s

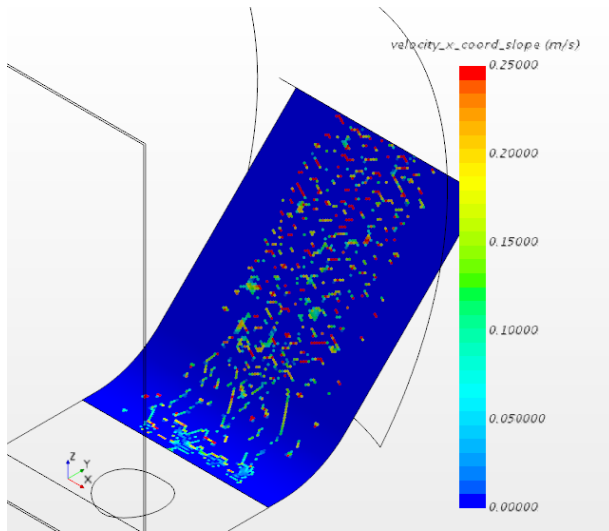


(c) 0,333125 kg/s

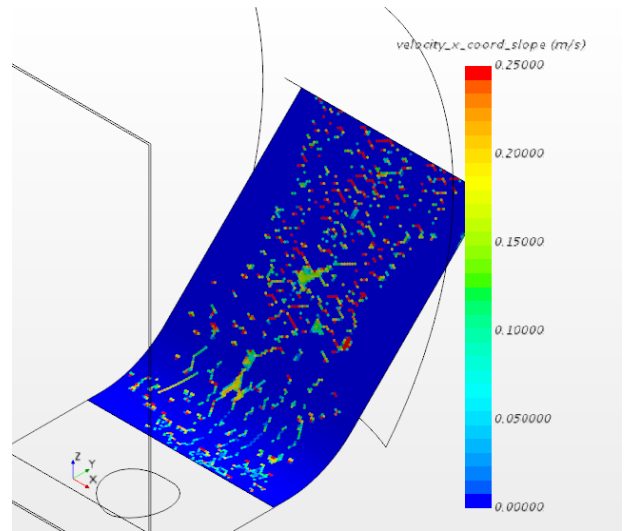


(d) 0,39975 kg/s

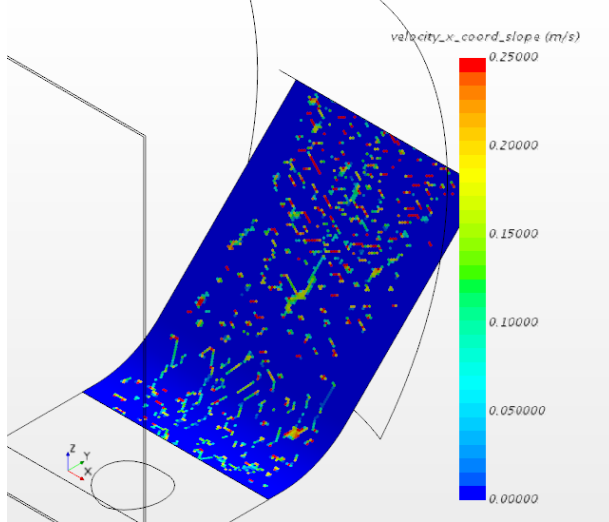
Figure 5.33: Fluid film thickness in function of main air phase flowrate



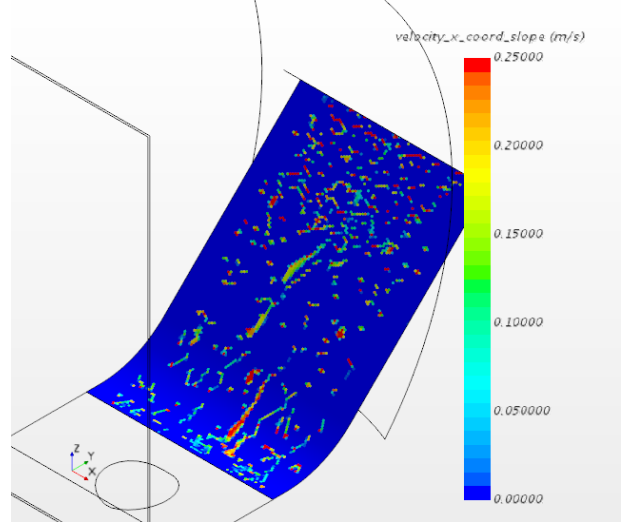
(a) 0,13325 kg/s



(b) 0,199875 kg/s



(c) 0,333125 kg/s



(d) 0,39975 kg/s

Figure 5.34: Fluid film velocity in direction of slope in function of main air phase flowrate



### **5.5.5 Conclusion from further investigation on the scaled down inlet box**

Four properties that could influence the water drainage results were investigated in more detail: injector initial velocity, injector diameter, injector cone angle and main air phase flow-rate. It's clear these will have a significant impact on results when not defined properly. It is therefore important before any simulation that concerns water drainage analysis to do a proper investigation into the Lagrangian phase that is injected into the system and define in detail its boundary conditions. Injector initial velocity can be determined in several ways depending on the type of injector, when the injected phase represents rainwater coming from the sky, numerous information can be found under what circumstances this happens, similarly for secondary road spray or power washing scenarios. When data would not be available it is always recommended to first examine the actual test or operational conditions to establish these and obtain qualitative input data for the simulation. In general, correct CFD setup is not limited to these 4 properties and also parameters such as turbulence properties, gravity, mesh settings etc will affect the results, however these are more general CFD recommendations for any type of simulation and not specific for water drainage, it is for CFD studies always advised to be thoroughly aware of the underlying algorithms and its limitations and requirements, as such results from CFD studies should always be critically studied and validated.

## Chapter 6

# Applying the validated CFD setup to a large scale AIS

This chapter takes the validated CFD models from Chapter 5 and applies these to a full scale air intake system (AIS). The purpose of running the CFD simulations on real life models allows the industry to iterate these designs before actual prototypes are being fabricated. Using CFD has the benefit that multiple design variations can be made without any significant additional cost except the man hours used at the CAD and CAE departments. For this thesis specifically this chapter runs the simulations for a commercially available air intake system, and the results can be used to further optimize this design. Important remark is that this thesis stops at publishing the results from this real life model, it does not go into design optimizations. Section 6.1 explains how a good CFD geometry is obtained from the raw CAD models and how the mesh is constructed to simulate the main air phase, since also here the main air phase will be solved in a steady state form first and then this solution is used to initialize the transient model that simulates the water behaviour. Section 6.2 explains how the rainwater is setup in the CFD code, in the full scale model the Lagrangian droplets fall down from a presentation grid to represent rain falling from the sky (this does differ from the experimental setup where the water was coming from a nozzle injector). Section 6.3, 6.4 and 6.5 then makes a comparison between 2 methods to simulate water behaviour in an air intake: section 6.4 explains the historical method that uses coefficients of restitution, with the big downside that extensive testing is needed on the final real-life model to establish these coefficients (yet we want to avoid creating costly real life AIS in the first place), section 6.5 uses the modelling method that was validated in Chapter 5 with the big advantage that a coefficient of restitution is no longer required to be measured upfront, the only prior parameters that need to be known are the surface properties of the final material used for the production of the AIS and its geometry, giving a big advantage for simulation needs very early in the design process of an air intake solution. Section 6.6 then takes this validated method further and uses it to simulate water behaviour during pressure washing (requirement from majority of clients in the commercial vehicle market), the main difference with prior modelling is that during pressure washing the water flow is now concentrated in a fine nebula with the engine running almost idle. Section 6.7 takes the validated simulation method and investigates the effect of changing the main airflow rate as until then the thesis was done with the worst case condition: the engine running at full load, for this section this flow-rate is lowered to conditions as seen during highway cruising or manoeuvring.

## 6.1 CAD and Mesh model

In an air intake of a commercial vehicle, to move air to the internal combustion engine and/or turbo, air is blown through the enclosure by means of the engine's pistons that act as air displacement device. The engine power is used to flow or push the air across the air intake system. In the engine, chemical energy is converted into mechanical energy and this enables the pistons to move. This movement converts this energy into kinetic energy in the moving air particles. However, in the full scale CFD model, the engine is not included, and it is assumed that the air is blown using an outside force. Thus, the outlet boundary condition is defined as a negative flowrate field. In some air intake systems, the inlet orifice is hidden behind body panels of the vehicle, yet for our model these conditions are neglected and the inlet orifice is exposed directly to the atmosphere (most common scenario). The engine and turbo itself do generate some heat yet since these simulations are not focused on thermal analysis, this was not considered. All internal components from the inlet duct up until the engine or turbo are considered, since the slightest change in topology can affect the flow-pattern of the incoming air and the dust and water particles that are suspended in it. Because of the complex topology of these small items, a wrapping mesh technique is used that enables creating a fluid domain in a fraction of the time of normal meshing techniques. By doing so, the inner geometry of the parts were preserved with the original shape and the outer components were removed. However, an insignificant amount of surface deformation can be observed. Finally the full inner volume of the CAD geometry is imported in the CFD software as 3 solid blocks (dirty air plenum, filter element, clean air plenum). To study the effect of water separation at the inlet louvres it is only this first section (dirty air plenum) that is considered for the CFD model.

For the mesh continuum, due to the high curvature and fine details around the inlet louvres a too coarse mesh is not capturing correctly the surface features, especially when a finer discretization is required. See figure 6.2 for the effect of a too coarse mesh on the cell skewness angle which is an important parameter for mesh quality (high skewness would imply that the form of the mesh cell would deviate strongly from the ideal form of a tetrahedron or polyhedral cell). For the mesh improvement, several steps were taken:

First, the mesh target size around the inlet louvres was refined for both the surface and polyhedral mesher and the polyhedral growth rate was increased to 1.1, this to make sure that the overall cell count still stayed acceptable. The growth is the factor that determines how fast cells will grow from the fine surface mesh on the boundaries to the wider cells in the centre of the flow. Since we are interested in the water behaviour close the louvres and not to the large scale phenomena in the centre of the air flow a growth factor of 1.1 is acceptable (and this will also be proven in the stabilization of the values under investigation after mesh refinement). Also the mesh surface size on the inlet atmosphere is increased, since this inlet represents a far field environment, more important is that the mesh refines towards the boundaries under investigation in a not to abrupt manner (controlled by the mesh growth factor).

Second, due to the number of parts with high curvature, the mesh curvature setting is increased to 72 in order to have a smoother discretization of the curved parts so that the rounded louvres would obtain a better representation, simply put increasing the curvature setting of the surface mesh ensures that more sections/splits are placed on top of a radius resulting in a finer representation of the original CAD geometry.

Third, as can be seen on a plot of the  $y^+$  values (see figure 6.3) most of the louvres are

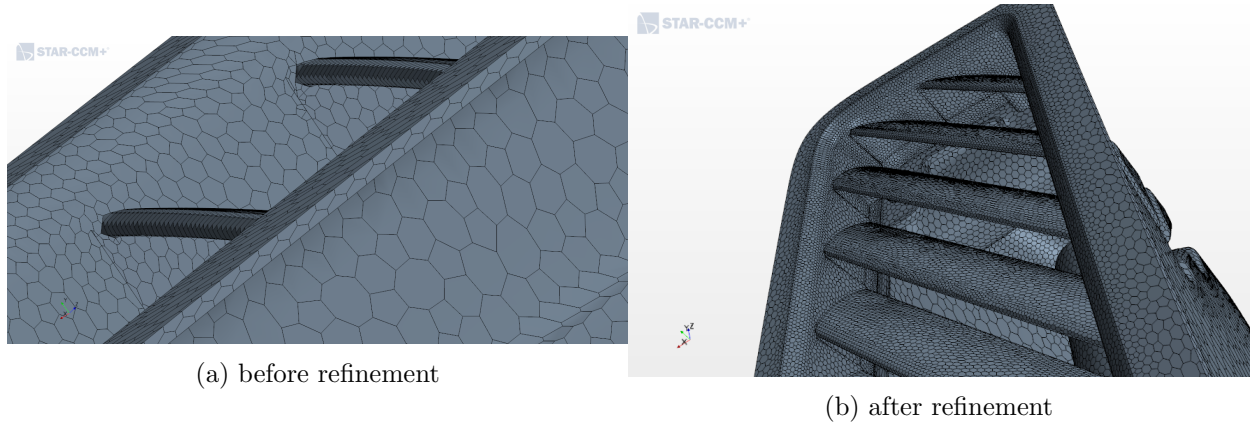


Figure 6.1: Mesh around inlet louvres before and after mesh refinement

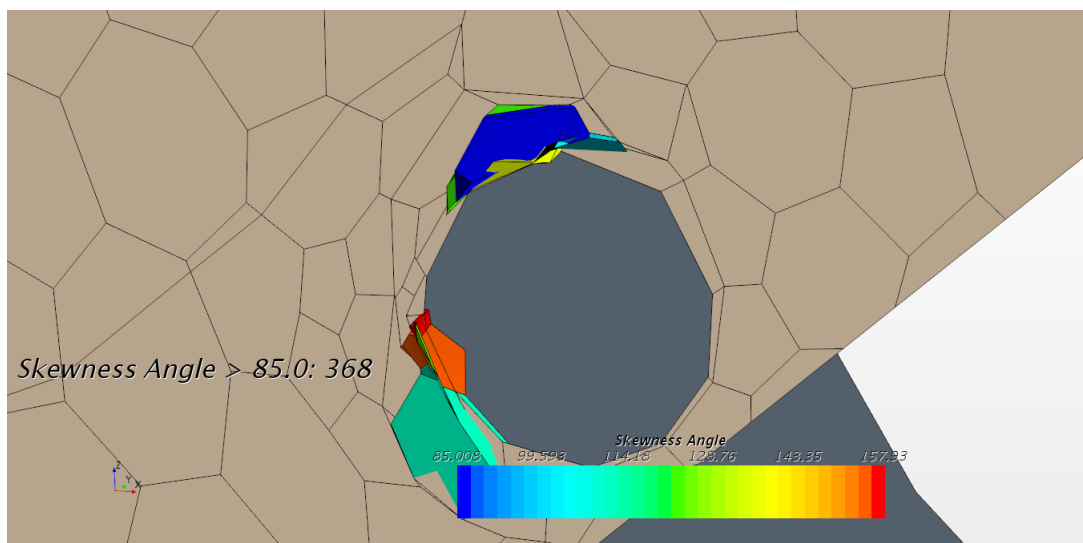
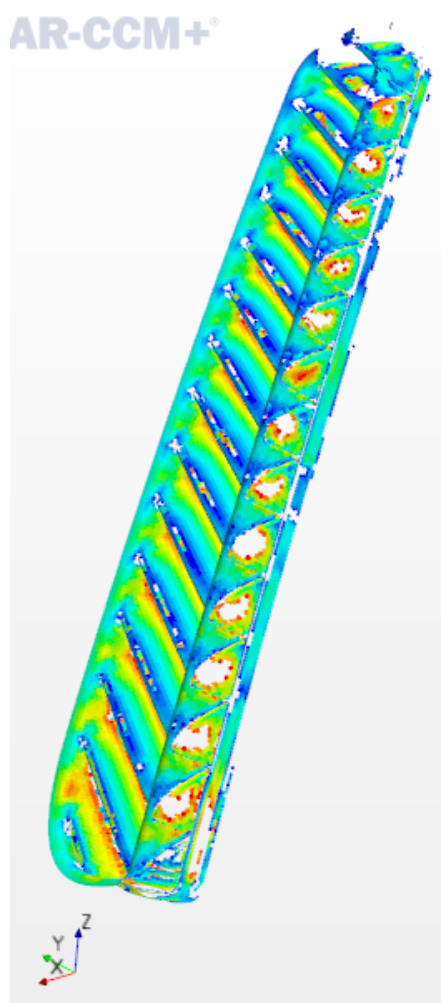


Figure 6.2: High cell skewness angles as result from a too coarse mesh

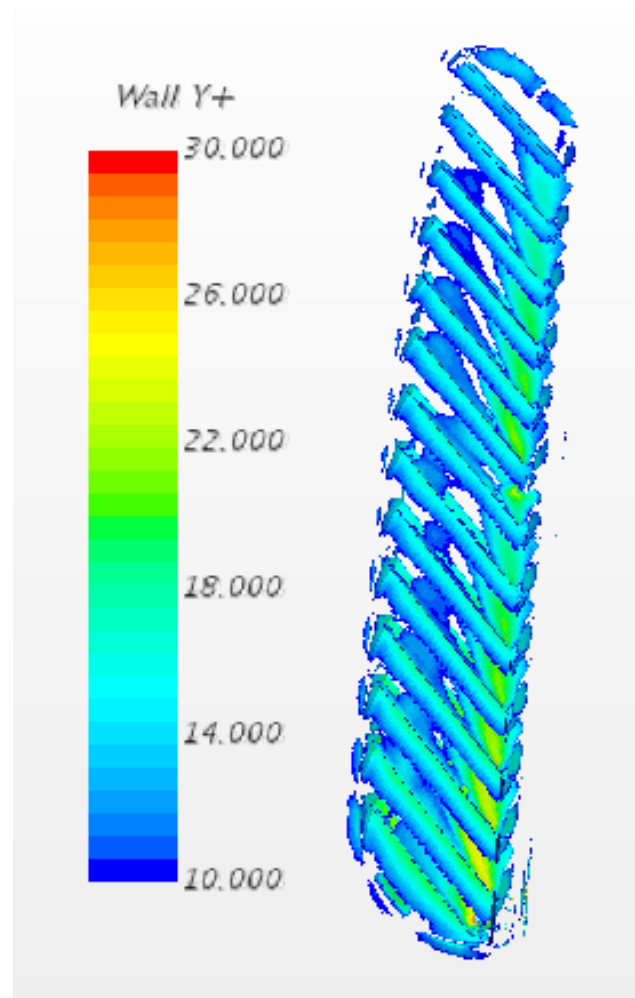
$> 1$  and so the boundaries close to the inlet have a  $y^+$  in the buffer range, which is definitely something to avoid. Hence, it makes sense increasing the number of prism layers to get a better ratio of cell height vs. cell width (more squared cells).

These steps are resulting in a finer mesh with improved mesh quality, the mesh refinement around the louvres is visible in figure 6.1

For the physics continua: special attention needs to be put into the turbulence model. K-omega is very good when there are highly recirculating flows but it is also less stable, especially in internal flow. It is advised to run the first time with k-epsilon and then running with k-omega. If k-omega works without oscillating too much, then k-omega can be used further on, otherwise keep on using k-epsilon. This can be monitored by looking at the amplitude of the oscillations of the residuals but also the values of interest such as pressure at outlet (see figure ??) and velocity throughout the model. In this case the k-epsilon model came out as more stable. Overall the oscillations before model refinement are quite small compared to the main value (2.65 percent for Pt and 0.25 percent for the mass flow), but it is worth refining the model on the points highlighted before. Once corrected, it will be possible to assess whether the oscillation is physical (related to flow oscillation) or numerically induced. Before the model refinement there is an overall count of 1,706,173 cells. The overall cell count after refinement was 1,892,431 polyhedral cells, although



(a) before refinement



(b) after refinement

Figure 6.3: Wall  $Y^+$  at louvres before and after mesh refinement

Table 6.1: Mesh settings for the optimal mesh (for the simulation of the water phase the mesh is further refined as described in section 6.5.1 - resulting mesh was acceptable for parameters under investigation and also for residuals - With these settings all variables no longer show large fluctuations and computational time is still within limits

Mesh Global settings - Fine mesh settings	
Mesh Models	Extruder
	Prism Layer Mesher
	Polyhedral Mesher
	Surface Remesher
Base size	5mm
Number of prism layers	3
prism layer stretching	1.5
prism layer thickness	33.3% relative to base
surface size - relative min	10
curvature	72
mesh growth factor	1.1
Local mesh settings - Louvres	
custom surface size min	5% relative to base
custom surface size max	25% relative to base
nr of prism layer	5
prism layer stretching	1.5
prism layer thickness	25% relative to base
Local mesh settings - Atmosphere	
custom surface size min	20% relative to base
custom surface size max	250% relative to base

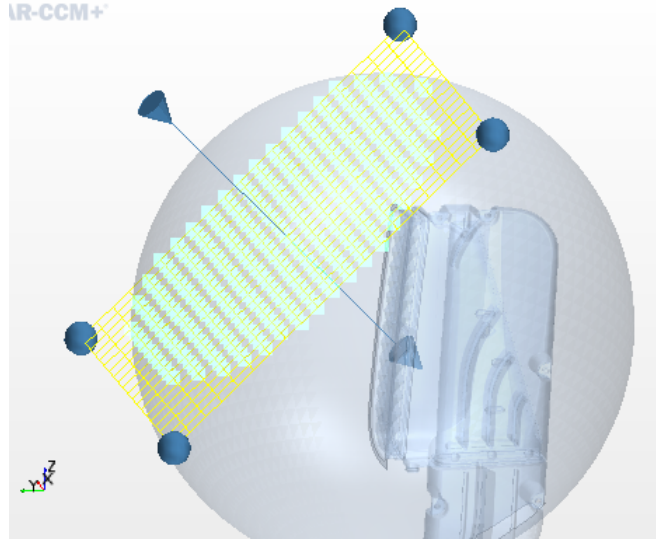


Figure 6.4: Injector grid to represent rainfall condition - each crosspoint is an injector location

this seems like only a minor increase in cell count, due to the settings described above the mesh is actually twice as dense around the area of interest while reducing the cell count around the areas that are not under investigation. Further model refinement did not show any benefits and further stabilization of the examined parameters. Hence mesh independence was obtained at 1,892,431 cells while still achieving acceptable solution times.

## 6.2 Rainwater Injection Setup

In order to simulate the free flowing water droplets, the droplet injector velocity (initial velocity of the Lagrangian droplets when they enter the domain) and the diameter of the droplets needs to be set. For the validation study in the previous chapter, the properties for the Lagrangian injector were obtained from the nozzle datasheet used in the PEPT test. However, for this full scale simulation it is more realistic to use actual rainwater properties like it is falling from above or under a slight angle. As already described in section 2.3.3 rainwater can occur in a wide range of conditions, for this full scale setup, a lower limit of 0.2 mm and an upper limit of 2.0 mm diameter were selected. The droplets were injected at a 45 degree plane with respect to the enclosure (see figure 6.4. By doing so, droplets experienced the maximum horizontal and vertical terminal velocities when they arrived at the intake orifice. At this location, the droplets encountered the air flow. We also need to consider that the main airflow at the far field will influence the droplet velocity. The air flow velocity at the injection point was at most places below 0.1 m/s. Therefore it was decided to take the calculated terminal velocities from table 2.1 as injector initial velocities and add no extra initial velocity.

The velocity, direction and size of the droplets is now determined, yet also the volumetric flowrate needs be defined. Rain intensity is the parameter that closest quantifies the flow rate. Rainfall intensity is classified according to the rate of precipitation, which depends on the considered time, in general we can speak of 4 type of conditions [72]

1. Light rain when the precipitation rate is  $< 2.5$  mm per hour

2. Moderate rain when the precipitation rate is between 2.5 mm - 7.6 mm or 10 mm per hour
3. Heavy rain when the precipitation rate is  $> 7.6$  mm per hour or between 10 mm and 50 mm per hour
4. Violent rain when the precipitation rate is  $> 50$  mm per hour

In a normal rain gauge (pluviometer), 1 mm corresponds with 1 litre of water per square meter of ground surface. If we consider for our case heavy rain and take a measurement of 25 mm, this would imply 25 litres of water per hour per square meter of ground surface. Our injector however is not perfectly  $1m^2$ , so we need to recalculate this value. From the CFD setup we know that the space between 2 injector point is 0.06 m (see figure 6.4). If we count the number of injector point we arrive at  $1.134 m^2$  for the injector surface, this leads to a volumetric flowrate in  $m^3/hr$  of:

$$25 \cdot \frac{1.134}{1} \cdot \frac{1}{1000} = 0.02835 \quad (6.1)$$

### 6.3 CFD Methods to simulate Water behaviour

As discussed in Chapter 2, Air Intake Systems should undergo rainwater penetration testing before releasing it to the market. A water droplet moving through the intake and reaching the filter medium is considered water penetration. When the engine is in full load, there are three main explanations for rain water getting into the air-stream and ingress in the air intake: Free flowing, Dripping and Splashing.

In the previous chapter simulations were run to study the CFD validation with the measured values from the PEPT experiments and it was established that simulating water ingress with the liquid film and multiphase models mentioned in that chapter are valid. In order to further observe the rain water behaviour in a full scale air inlet system further CFD studies were conducted to replicate the water behaviour. All based onto the simulation models and settings that were validated with the experiments in the previous chapters. Unlike the previous chapter where the focus was on establishing validation with experiments and obtaining the correct settings and models for studying water ingress, in this chapter we can now further investigate knowing that the models have proven themselves and a wider set of investigation can be conducted. In chapter 5 the optimal models for water ingress analysis were established based on current state of the art CFD capabilities, however historically also other methods were used, together these can be summarized as:

- Method 0 (this method is not used in this thesis): the earliest simulation method for rainwater separation was limited to steady state simulation of the air passing through the intake, by keeping the velocity around the intake orifice below a threshold of 5 m/s (see figure 6.5) good results can be obtained, yet it does not simulate the water phase in any way.
- Method 1 (this method is shown in this thesis only to show its shortcomings vs. method 2)- Steady method with coefficient of restitution: incoming Lagrangian particles hit a boundary and the boundary can then accept these particles as escape, rebound or stick, with each



time a restitution coefficient that can be set for the rebound case. Although this method is computationally cheap it is not very realistic and requires a detailed experimental study to establish the coefficient of restitution (this experimental study has to be repeated every single time when the setup changes).

- Method 2 - Transient method with Fluid Film/VOF: the fluid film accept the incoming particles as perfect impingement, and the fluid film then takes over the modelling of the water flowing over the drain surfaces, this being already more realistic versus the prior methods. Optionally the Bai-Gosman impingement model can be activated, with it the fluid film accepts the incoming particles no longer as perfect impingement, but allows now a wide variety of behaviours: spread, breakup, rebound, adhere and the combination of those as described in figure 4.8. When the film height becomes too high for the fluid film model, the VOF model takes over.

## 6.4 Method 1 - Steady method with coefficient of restitution

This method is used in this thesis to show its shortcomings vs. method 2. Historically the very first CFD method to optimize water drainage in air intakes was to not simulate the water phase at all, but to focus on the air velocities of the steady state simulation, if the velocity around the intake orifice was around 5 m/s or lower it was considered as good for water drainage (and this was also somewhat confirmed through experiments). However having large surface areas available for this orifice is not always the case, and then 5 m/s is no longer achievable. A solution was to simulate with CFD the rainwater ingress as a steady state analysis with a coefficient of restitution for each boundary where the droplets are impinging and rebounding, or alternatively setting the boundary as a perfect escape or stick.

However for the method without fluid film only the rebound effect (b in figure 4.8 will be simulated. Rebound mode is available only at walls, baffles, and contact interfaces. Rebounding particles remain active in the simulation; the mode is distinguished by its treatment of the particle velocity. The rebound velocity relative to the wall velocity is determined by the impingement velocity and user-defined restitution coefficients:

$$(v_p - v_w)^R = e_t(v_p - v_w)_t^I - e_n(v_p - v_w)_n^I \quad (6.2)$$

The superscripts R and I denote rebound and impingement respectively; the subscripts n and t denote wall-normal and tangential respectively. Since the left-hand side of the equation can be split into orthogonal n and t components, it can be split into two equations:

$$(v_p - v_w)_t^R = e_t(v_p - v_w)_t^I \quad (6.3)$$

$$(v_p - v_w)_n^R = e_n(v_p - v_w)_n^I \quad (6.4)$$

which serve to emphasize the definition of the restitution coefficients as the constants of proportionality between impingement and rebound velocities. Both coefficients may range from 0 to 1. The latter, perfect elastic rebound, is the default. The tangential velocity of a wall boundary

is zero unless a value is explicitly prescribed through a wall sliding option. In other words, it is non-zero only at no-slip walls. As result to simulate the water ingress into the inlet box we can use three differing types of wall conditions; absorption, ideal rebound and limited rebound rather than complex setup of VOF and liquid film to simulate the contact angle effect on the rainwater. Further analysis is done to examine if this is a viable method for Air Intake Systems. If the wall condition is defined as escape, the particles will be absorbed by the wall. If it is ideal rebound (coefficient of restitution set at 1), the particle will rebound in the opposite direction at the same magnitude of the impact velocity. Finally, in limited rebound condition, the user can assign the coefficient of restitution. The coefficient of restitution will depend on many variables, such as, paint, rust resistant coatings, material type, and other all affecting the contact angle. Measuring the coefficient of restitution is a cumbersome process which requires specialized testing equipment. Furthermore it also needs to be repeated each time the experimental setup changes in term of topology, surface conditions or any other parameter that would differ from the original measurement.

Although a simulation that uses a coefficient of restitution as wall condition rather than the complex setup of VOF and liquid film is more efficient in terms of solving time. It does not deliver the same qualitative results as the full fluid film setup that allows the definition of the contact angle. Also when observing the actual experiment it becomes clear that when the water moves downwards on the louvres the impingement and the film itself shows a multitude of behaviours (splashing, break-up, re-entrainment, coalescence, etc..) that is difficult to be captured in a single coefficient of restitution. More-over during the early design of a new intake system there is not always a prototype available to run test on to determine the coefficient of restitution, in those cases running the simulation with VOF and liquid film allows an early insight without making assumptions on restitution that could prove to be wrong, losing valuable engineering time. If only the contact angle of the louvres would change and all other parameters would remain constant in future design, it could be done to create a validation table between contact angle and coefficient of restitution, yet as commented before, these parameters are rarely constant (e.g. the topology of a louvre is often changed due to design constraints, as is the airflow and other conditions)

#### **6.4.1 Free flowing - wall absorption**

Because of the high air velocity and the static pressure drop created near the inlet orifice, rain water droplets can get carried through the air stream into the enclosure. In order to stop the free flowing penetration, louvre plates are placed in the intake orifice, the purpose of the louvres is to act as a barrier while directing the air flow further into the air intake system. The purpose of the louvres is to separate the water droplets from the air. Because of the change in momentum permitted by altering the direction, the relatively heavier water droplets will bump into the frontal face of the louvre while the lighter air particles will flow in their natural path. Also, there is sometimes a small ridge created across the louvres to prevent water collected on them from running over the louvre and again entering the air stream. When the direction of the air flow is suddenly changed, it creates high and low velocity areas around the louvres. The loss of velocity creates static pressure drops and influences the volumetric flow rate. Hence, an angled face is used to ease the directional change of the air flow, making the transition smoother.

The next step was to define the wall conditions. Since this analysis was focused on water

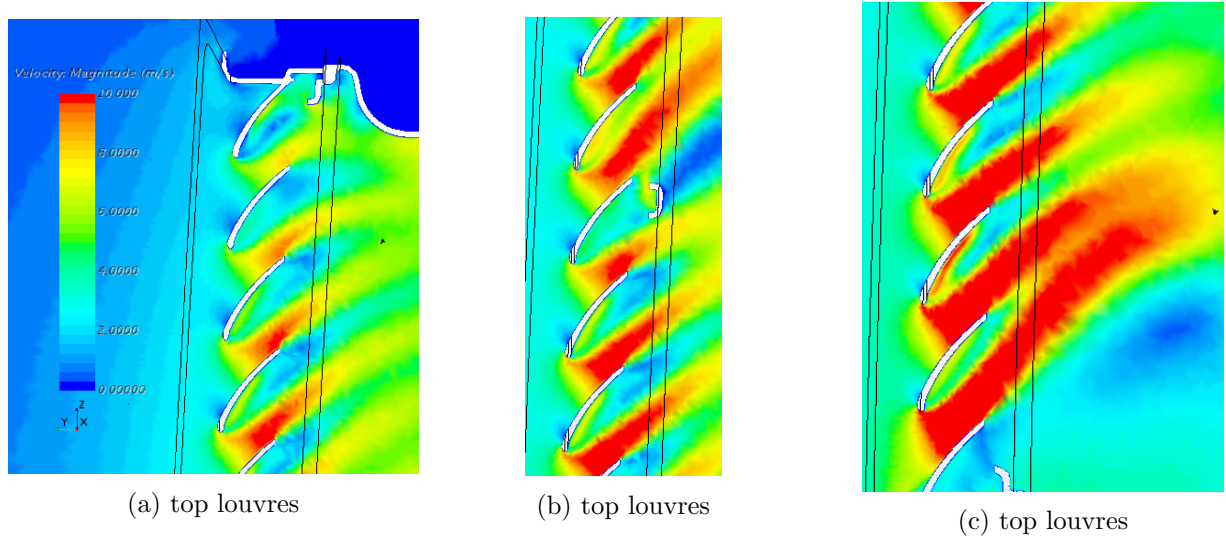
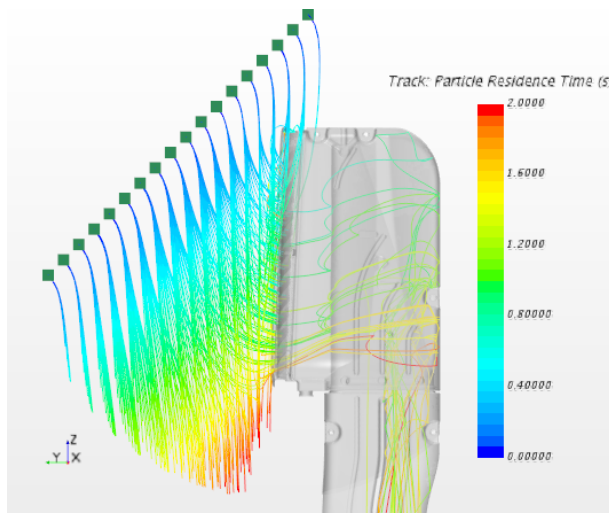


Figure 6.5: Velocity around louvres - magnitude 0-10 m/s

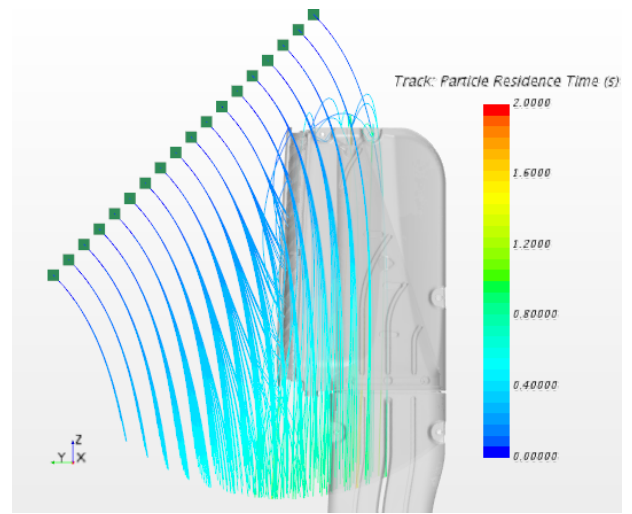
droplets that are free flowing, the behaviour of the droplets after impact on the louvres will have a significant influence. Hence, all the wall conditions except the louvres are selected as perfect rebound, the louvres itself where simulated with 4 settings (perfect escape, coefficient of restitution set to 0.3, to 0.6 and to 1). In other words, if a water droplet hits the louvres, the simulations assume the droplet is absorbed by the wall in the case of perfect escape, and will retain only parts of the droplets respective to the coefficient of restitution that was set.

In total 20 simulations were running (4 different wall absorption settings for the louvres times 5 settings for the injected droplet). To estimate the quality of water drainage at the louvres the mass flux was reported at 3 boundaries (the inlet, the outlet and the louvres itself). The mass flux is the amount of fluid that passes through a boundary expressed in kg/s, our injector volume flowrate was previously defined as  $0.02835 \text{ m}^3/\text{hr}$  which corresponds to  $0.007856 \text{ kg/s}$ . Since we are running a steady state simulation mass being inserted into the system also needs to be equal to mass exiting the system, this is shown in table 6.2 where the last column is the sum of the 3 measured exit boundaries and this matches each time the mass flow rate being injected into the system. The inlet boundary is reported because as shown on the plots in figure 6.6 the injected rainwater droplets furthest away from the inlet orifice (far left) will fall to the ground before they are even pulled into the air-stream (this is the result of having a large orifice where inlet velocities are low). The outlet boundary is reported because this will indicate how much particles will be able to pass through the louvres and thus indicate how good the louvres are in stopping the water from ingress into the system. The louvres boundary is reported as a control mechanism, as this should be the difference between the mass introduced into the system and the mass existing the system through the inlet and outlet boundaries. Figure 6.6 shows the tracks of the water droplets injected into the system and the residence time of those droplets overlaid onto those tracks. Plots shown here are for simulations A1 to A5 (louvres having perfect escape properties assigned - see table 6.2). Figure 6.6a indicates that 0.2 mm droplets with their low terminal velocities quickly lose the 45 degrees direction imposed by the injector, the gravity will start pulling those particles furthest away from the inlet orifice towards the ground quite fast, the droplets close to the inlet orifice will be affected by the velocity of the main air phase and more importantly because these

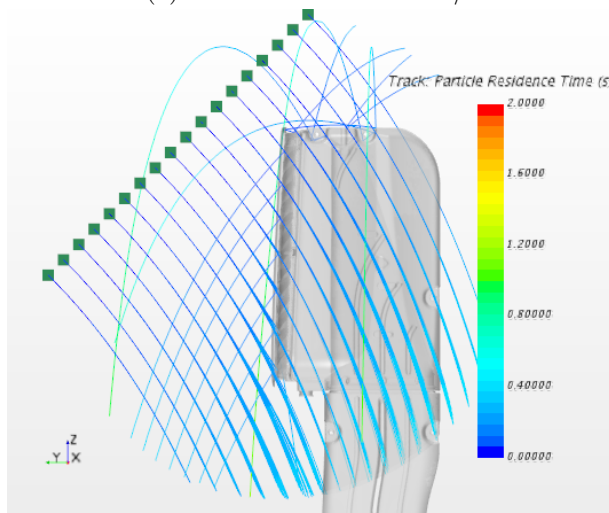
droplets are so small and light it also shown that these are able to pass the louvre geometry and can ingress further into the system all the way to the domain outlet. In reality this would imply that 0.2mm droplets (and smaller) would be able to reach to filter medium and potentially damage this (table 6.2 shows that there is indeed mass passing through the outlet boundary, indicating that the louvres were not able to stop fully the ingress of the water). For figure 6.6b to figure 6.6e the plot show increasingly smaller residence times and increasingly steeper track angles, this is behaviour that is expected since the droplet size is increasing and hence also the droplet terminal velocity. Because of these initial higher energy, droplets will start to fall to the ground much later and additionally they will also impact onto the louvres with higher energy. What is positive is that these larger size droplets are being dragged into the louvres and this also shows in the plots where no particle tracks can be observed after the louvres, also the values in table 6.2 indicate that no massflow is passing through the domain outlet, indicating that the louvres are able to intercept the incoming droplets and preventing ingress into the air inlet system. However as indicated in the table, A1 to A5 are representative for when we set the louvres to a perfect escape property, in reality this would mean that when a droplet hits the louvre, this droplet is perfectly captured and drained. In order to simulate also other scenarios where the louvres are not perfectly catching the droplets the louvre properties are changed from perfect escape to 3 different coefficients of restitution. For B1 to B5 it is set at 0.3, for C1 to C5 set to 0.6, and for D1 to D5 set to 1 (perfect rebound). Plots for these setups can be found in the appendix, table 6.2 now shows different result at the domain outlet. For the droplets of 0.2 mm (B1, C1 and D1) there is actually no difference in the amount that reaches the outlet, this again indicates that due to the small size and weight of these droplets these are easily taken along the main airflow without even touching the louvres, there is however a higher amount reaching the outlet for the case where the louvres were set at a perfect rebound (D1), this tells us that although there are 0.2mm droplets that can move past the louvres without touching the louvres, there is still an amount that touches them. For the 0.5mm droplets (A2, B2, C2, D2) the amount reaching the outlet is zero for the A2 case (implying that all droplets hit the louvres), for a coefficient of restitution set at 0.3 (B2) and 0.6 (C2), it is similar and for 1 (D2) it is in between A2 and B2/C2, this can be explained due to the fact that these larger droplets when hitting the louvres have a higher rebound velocity when compared to the 0.2mm droplets. In the case when restitution is set at 1, this implies a perfect rebound what comes down to droplets hitting the louvres and rebounding in the exact opposite direction with the same energy, hence returning to the area in front of the orifice where they then fall to the ground. For the 1mm particles (A3, B3, C3, D3) this becomes even more pronounced and now even with a coefficient of restitution set at 0.6 we already see a larger rebound resulting in less mass reaching the outlet (C3) when compared to 0.3 (B3). The same result can be observed also for the 1.5mm (A4, B4, C4, D4) and 2mm (A5, B5, C5, D5) droplets. In general we can say that a lower coefficient of restitution results in more rainwater mass reaching the domain outlet, this is expected behaviour, because a lower coefficient of restitution will cause the particles that hit the louvres to rebound with a reduction in energy and are hence more susceptible to be taken along in the main airflow.



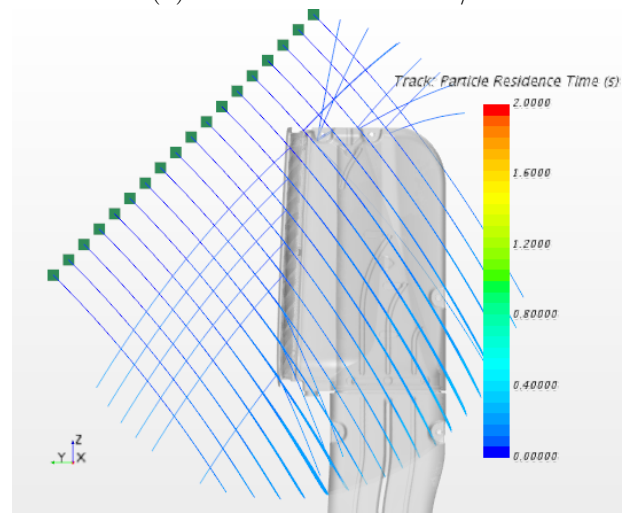
(a) A1 - 0.2 mm - 0.763 m/s



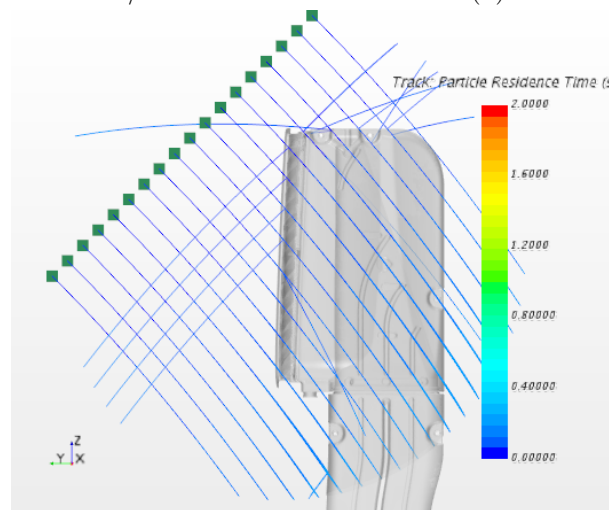
(b) A2 - 0.5 mm - 2.068 m/s



(c) A3 - 1 mm - 3.92 m/s



(d) A4 - 1.5 mm - 5.404 m/s



(e) A5 - 2 mm - 6.564 m/s

Figure 6.6: Track residence time for A1 - A5 setup (see table 6.2 for more details) - for plots B1 to D5 see appendix

Table 6.2: Mass Flux results in function of droplet parameters and coefficient of restitution  $C_r$  at louvres for the free flowing simulation

	drop size	drop vel	$C_r$	mass flux [kg/s]			
	[mm]	[m/s]		louvres	inlet	outlet	total
A1	0.2	0.763	escape	2.854E-03	4.395E-03	6.062E-04	7.856E-03
A2	0.5	2.068	escape	7.831E-04	7.073E-03	0.000E+00	7.856E-03
A3	1	3.92	escape	5.305E-04	7.325E-03	0.000E+00	7.856E-03
A4	1.5	5.404	escape	5.810E-04	7.275E-03	0.000E+00	7.856E-03
A5	2	6.564	escape	6.062E-04	7.250E-03	0.000E+00	7.856E-03
B1	0.2	0.763	0.3	8.750E-10	4.395E-03	3.461E-03	7.856E-03
B2	0.5	2.068	0.3	0.000E+00	7.073E-03	7.831E-04	7.856E-03
B3	1	3.92	0.3	1.263E-04	7.477E-03	2.526E-04	7.856E-03
B4	1.5	5.404	0.3	1.010E-04	7.628E-03	1.263E-04	7.856E-03
B5	2	6.564	0.3	2.526E-05	7.780E-03	5.052E-05	7.856E-03
C1	0.2	0.763	0.6	8.750E-10	4.395E-03	3.461E-03	7.856E-03
C2	0.5	2.068	0.6	0.000E+00	7.073E-03	7.831E-04	7.856E-03
C3	1	3.92	0.6	3.050E-10	7.805E-03	5.052E-05	7.856E-03
C4	1.5	5.404	0.6	0.000E+00	7.755E-03	1.010E-04	7.856E-03
C5	2	6.564	0.6	3.050E-10	7.805E-03	5.052E-05	7.856E-03
D1	0.2	0.763	1	8.750E-10	4.395E-03	3.461E-03	7.856E-03
D2	0.5	2.068	1	4.750E-10	7.199E-03	6.568E-04	7.856E-03
D3	1	3.92	1	3.050E-10	7.805E-03	5.052E-05	7.856E-03
D4	1.5	5.404	1	3.050E-10	7.805E-03	5.052E-05	7.856E-03
D5	2	6.564	1	9.500E-11	7.831E-03	2.526E-05	7.856E-03

### 6.4.2 Dripping

The main purpose of the angled face of the louvres is to stop water droplets from entering the enclosure. However, because of surface properties, the water droplets that collide with the louvres will attach themselves to these surfaces. Droplets can climb up on the surface of the louvres due to forces created by the air flow, and can get swept up again into the flowing air. To avoid this, several design features can be applied, a standing lip at the end of a louvre catches these droplets moving upwards, or alternatively the angle on the louvre can be made large enough so droplets are encouraged to move downwards, however once they arrive at the bottom of the louvre or at the upstanding lip the smaller drops will start to coalesce until the point that the gravitational force acting on them is higher than the surface tension, causing them to drop down the angled face. Some of these falling droplets can still get carried by the air stream into the enclosure. This occurrence is called ingestion by dripping. It is important to highlight that the diameter of the falling droplets cannot be calculated. Because the enclosure suffers vibrations and this vibration energy will affect when a droplet at the edge will be released. In other words, the combination of vibration energy and the gravitational forces are both acting on the droplets. Also, it is important to mention that heat transfer was not accounted for in the simulations, and that heat energy will affect the water's properties. Therefore the diameter of the droplets dripping from the edges is not a constant and it was assumed to range of 0.1 mm to 1.0 mm. Dripping will occur in several locations throughout the air intake system, for this study we focussed on the dripping that occurs on the louvres itself, as this is the main barrier for water ingestion.

Since this particle study is focused on the water droplet formation on the edges of the

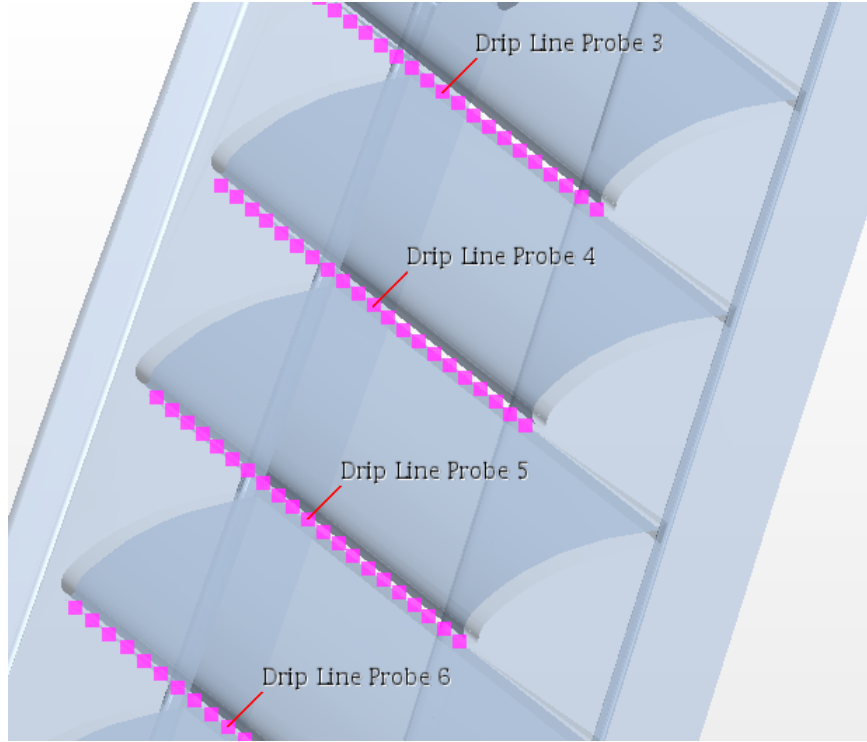


Figure 6.7: Louvre edges as drip locations

louvres, the injection point was defined as the entire surface edge of the louver (see figure 6.7). As there is more than 1 louver across the inlet orifice, it is possible for a droplet to fall from one louver to the one underneath, so we also need to define a property for that top part of the louver surface above the injector edges, the wall condition of the louver that was before defined as an escape boundary (any Lagrangian particle that touched the surface would leave the domain immediately) is now defined as a wall with perfect rebound. In this condition the droplets falling from the injectors downwards don't get immediately absorbed when they touch the louver, but are forced to move around in the domain until they reach the bottom of the inlet orifice, like it would be in reality. Moreover, wall conditions for the parts after the louvres were defined as perfect rebound. Meaning, the water droplets which collided with those surfaces were assumed to be rebound with exactly the same velocity as from impingement. As the initial velocity of dripping droplets is near zero and the simulation applies the gravitational forces to the droplets, the initial velocity was defined as zero in all three planes and the simulation then applied gravitational forces in vertical direction. The droplet diameter was set at 0.1, 0.2, 0.5 and 1 mm, higher was not considered since we already determined in the free flowing section that these droplet sizes see more influence from gravity rather than the main airflow and are not being pulled into the intake. Finally the mass flow rate needs to be determined, for this we used the extreme case from the previous chapter where the louver was set as escape (this means louver is collecting maximal number of impinging droplets). The maximal mass flowrate observed at the louvres for that condition was 0,002854  $kg/s$ . It was concluded that for the dripping scenario, when the droplet diameter is 1 mm or larger and the louver boundary condition is set the perfect rebound (B4) there are droplets that get rebounded to the area in front of the intake and due to their size get pulled down towards to earth surface. For simulation A1 to A4 the louver boundary was set to escape, yet still some mass managed to reach to the outlet, this implies that before hitting the louver underneath, the



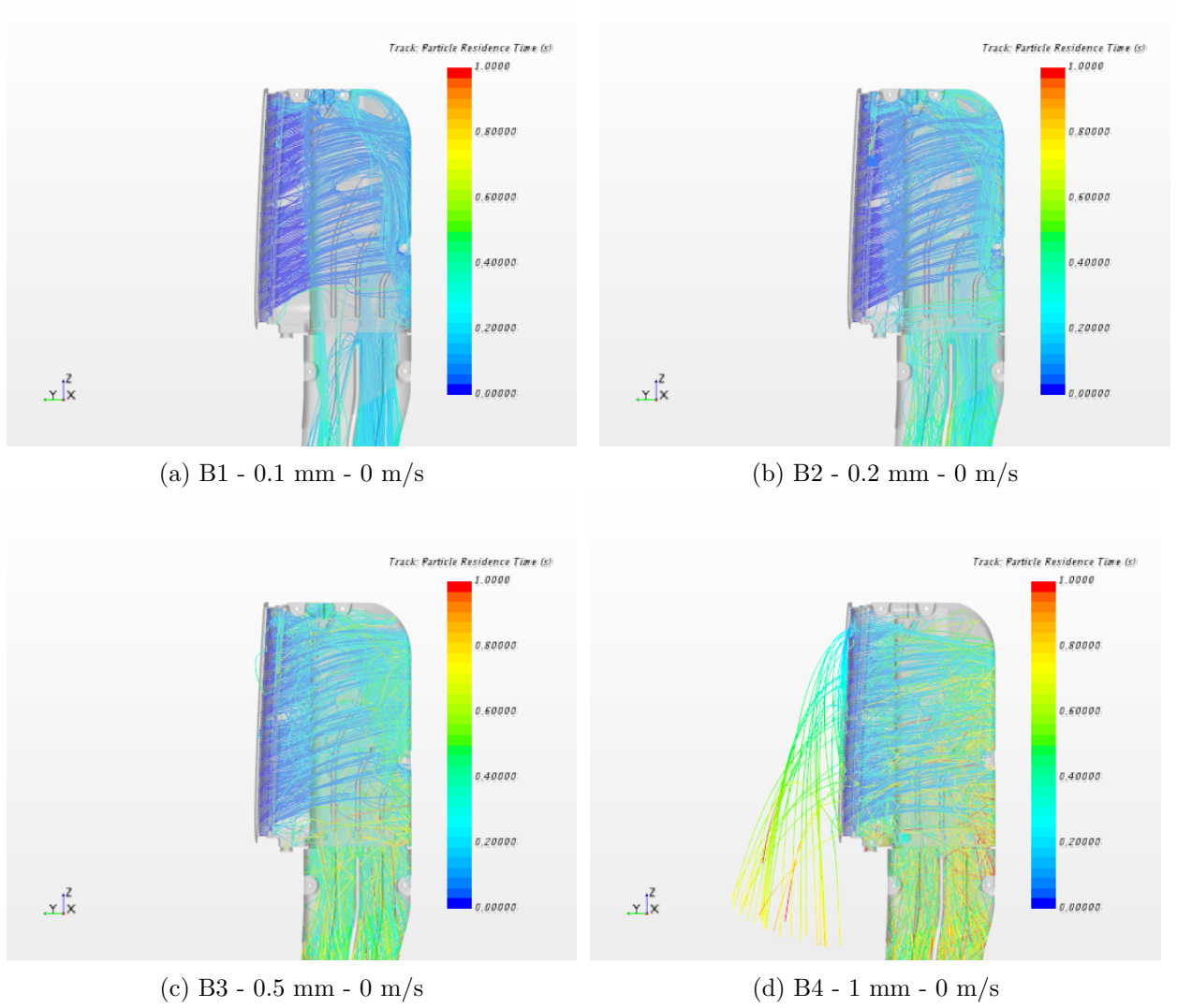


Figure 6.8: Dripping condition: track residence time for B1 - B4 setup (see table 6.3 for more details) - for plots A1 to A4 see appendix

dripping droplets are pulled into the main airstream before they manage to escape, it also shows that when increasing the droplet size (going from A1 to A4) less mass is able to ingress into the inlet, this means that larger droplets are less affected by the main airflow and just keep on falling to the underlying louvre. When the louvre boundary is set to perfect rebound (B1 to B4) more mass manages to reach the domain outlet, which makes sense since a perfect rebound will keep on re-introducing the particles into the domain, the only chance for them to escape through an exit other than the outlet boundary is when they are rebounded so much that they end up far in front of the intake orifice and can fall towards to earth surface (simulation B4).

### 6.4.3 Splashing

Splashing occurs when water droplets collide with any solid surface, breaking them into smaller droplets with different velocity profiles. In applying this principle to the air intake system, splashing can occur mainly at the louvres and at other locations where velocity is high and perpendicular to a wall. However, as mentioned before without a fluid film and a variety of impingement models



Table 6.3: Mass Flux results in function of droplet parameters and coefficient of restitution at louvres for the dripping simulation

	drop size	drop vel	resti	mass flux [kg/s]			
	[mm]	[m/s]		louvres	inlet	outlet	total
A1	0.1	0	escape	5.016E-04	0.000E+00	2.353E-03	2.854E-03
A2	0.2	0	escape	5.836E-04	0.000E+00	2.271E-03	2.854E-03
A3	0.5	0	escape	8.116E-04	0.000E+00	2.043E-03	2.854E-03
A4	1.0	0	escape	1.094E-03	0.000E+00	1.760E-03	2.854E-03
B1	0.1	0	1	0.000E+00	0.000E+00	2.854E-03	2.854E-03
B2	0.2	0	1	0.000E+00	0.000E+00	2.854E-03	2.854E-03
B3	0.5	0	1	2.736E-05	0.000E+00	2.827E-03	2.854E-03
B4	1.0	0	1	3.192E-04	2.553E-04	2.535E-03	2.854E-03

available for this method, we would need to cover this splashing behaviour by determining a coefficient of restitution that would mimic in its best way possible the splashing behaviour. Using this method will always lead to many assumptions that have to be made regarding these phenomena. Many steps would need to be undertaken experimentally to start with defining the CFD parameters to correctly simulate this behaviour. Measuring the velocity of the droplets after the impingement and rebound would need to occur for each prototype or set of environmental conditions, next to that the number of rebounded particles vs the particles that would stick to the surface would need to be measured. Extra measurements could be made to further refine the coefficient of restitution. However, coefficient of restitution only applies to those droplets that bounce back without breaking apart. The droplets created as a result of splashing will exhibit a variety of diameter size and velocity. Limits of testing equipment and thus, lack of data means that the velocity of these smaller droplets created by impact had to be assumed as well. Due to this wide array of assumptions for the splashing phenomena it becomes clear that using the CFD method with coefficient of restitution is too limited to capture this behaviour in an accurate way. Even if one would decide to use this method, a wide range of test would need to precede the simulation.

#### 6.4.4 Conclusion - Impingement with coefficient of restitution

This type of setup has its advantages, first being that the computational cost is relatively cheap versus the other method described in later sections. The mesh still needs to be fairly detailed in order to capture all the details and allow proper stabilization of the parameters under investigation, yet due to the lack of the fluid film and more complex impingement models, the droplet behaviour can be solved as a steady state model drastically cutting the solution time. However the disadvantages of this method are numerous and limit its use to a limited set of scenarios. As described in the subsections before, depending on the droplet size it can provide valuable information, but one needs to pay attention to not generalize these results and make sure to consider this method not valid for other droplet sizes or environmental conditions. Also a big limitation is the amount of assumptions that needs to be done for the coefficient of restitution and the extensive real life test that would need to occur to establish these, not to mention that they would need to be repeated each time to setup changes. During early prototyping studies of an air intake the topology and the dimensions of the design could change significantly and creating each time a rapid prototype model to again establish the coefficient of restitution would become costly and time consuming.

Not to mention that the material itself that is used for rapid prototyping can differ vastly from the actual final material used for serial production, greatly affecting its surface tension and topology. As result, we need to conclude that this method although used frequently in the past due to its low computational cost has serious limitations and needs to be used with reservation and a great deal of lab testing to support its assumptions.

## 6.5 Method 2: method validated by work in Chapter 5 - Transient method with Fluid Film/VOF

For more details on the settings for the CFD physics and mesh please consult appendix C and D. Figure 4.8 explains the different impingement possibilities when the Bai-Gosman impingement model is activated. However Bai-Gosman does add complexity to the model and is more computationally expensive. On the other hand the previous model that used rebound or perfect escape properties at the wall boundaries does not add enough realism to describe the actual phenomena. To ensure the most realistic simulations Bai-Gosman models are turned on. Where in the previous method a droplet would impact on the louvre and immediately escape the simulation irrespective if in reality a film is present or not, this method allows that the impinging particle will behave differently whether it impact into an area that is already wetted due to the presence of a film, or alternately it will impact into a dry spot and will rebound with the settings as defined by the coefficient of restitution, this is combination with the effect from the Bai-Gosman model is the closest approximation of an impingement scenario in real-life. Special attention needs to go the further setup of the CFD model, in the previous method where of coefficient of restitution was assigned to a boundary, it was sufficient to run the model as a steady state simulation and run the Lagrangian impingement in a few iterations. In this case however the selected models are to be solved through a transient simulation, hence we need to take care that timestep and the amount of inner iterations are fine enough in order to obtain proper convergence of the results. Of course refining these too much would result in a simulation that has a solution time far above the ideal one, since this transient model already is using greater solution times vs. the steady state simulation it is important to keep this solution time to a minimum in order for the simulation to be commercially still competitive to the other methods or even vs. real physical prototypes, taking into account that rapid prototyping is seeing great progress and evolution (please consult appendix C and D for more detail on these CFD settings).

### 6.5.1 Further mesh refinement

Unlike the previous method with coefficient of restitution, this fluid film based method does have some additional requirements on the mesh. Additional steps were taken to optimize the mesh, preliminary around the area of interest that are the louvres. Examining the main flow field in detail showed that local vortexes appeared around a small area of the louvres (see figure 6.9 that leads to unrealistic film height (see figure 6.10. Since these features of the CAD model would not exist after moulding the actual air intake during serial production, this feature was removed from the mesh with the wrapper technique. This wrapper technique allows wrapping a mesh around an existing geometry, similar to inflating a balloon inside an orifice where it then follows the contours of the object to mesh. the advantage is that unrealistic small details that don't contribute to the

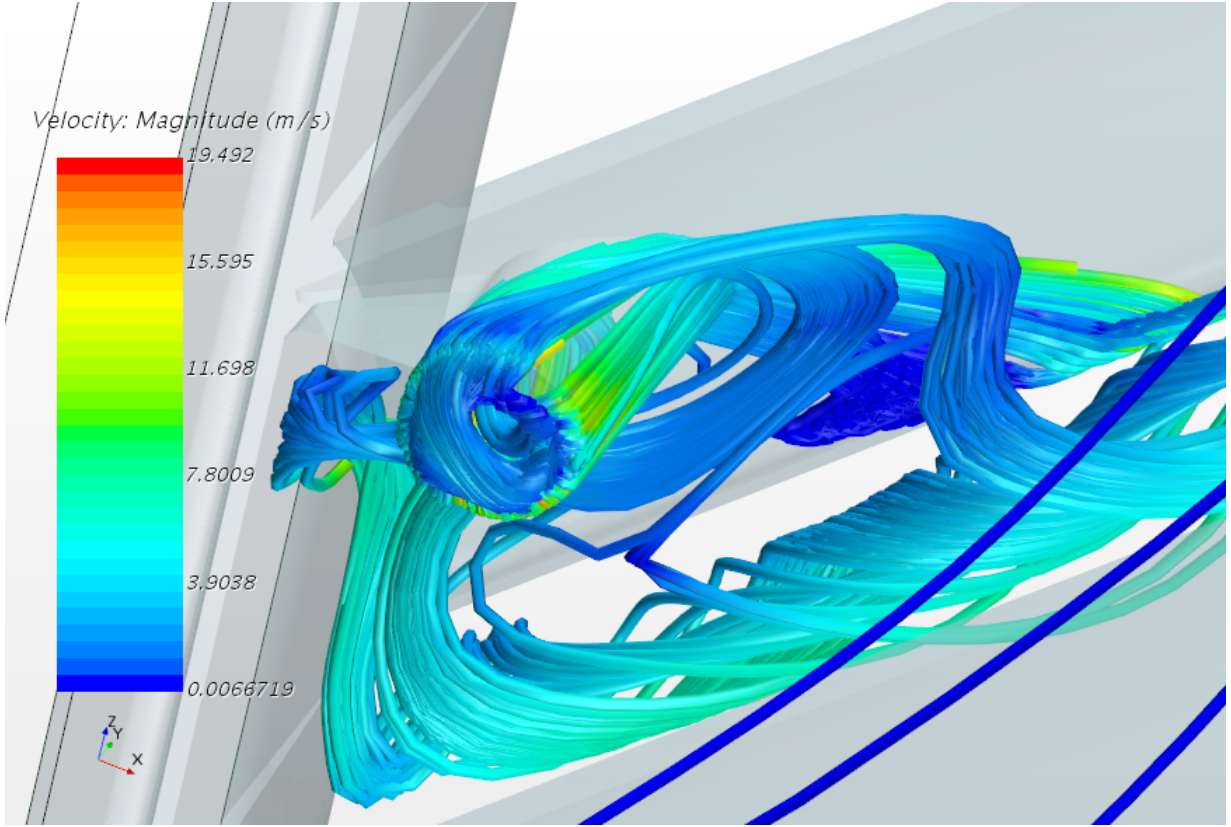


Figure 6.9: Vortex formation around small holes in the louvres, feature will be removed after surface wrapping

actual physics of the model are ignored by the mesh. Further steps include refining the boundary mesh layers in order to obtain a good film distribution and optimizing the mesh in the area around the injected particles.

For the prism layer properties following settings were used:

- Minimum thickness percentage of 1
- Layer reduction percentage of 10
- Near core aspect ratio to 0.5

Further mesh refinements for the overall domain:

- In order to avoid the very large cells near the inlet and injector area, set a Maximum cell size for the trimmer at 200
- Extrude the outlet to obtain a uniform flow at the outlet, in our case this was set at 2.5 m with 80 layers, a slightly larger value is also possible as it does not increase much the number of cells in the domain.
- Set the Template Growth Rate to be medium

### 6.5.2 Simulation Setup

As explained in Chapter 3 in the section concerning the multiphase interaction models, a combination of fluid film and VOF can be made when the simulation requires it, the 2 most common

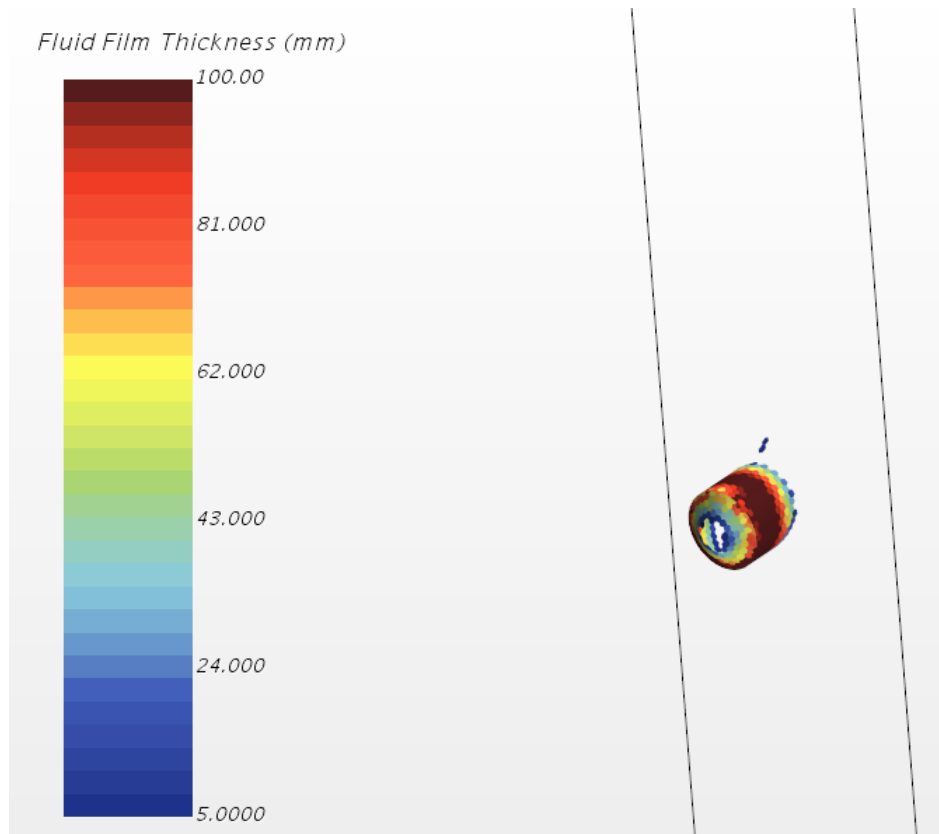


Figure 6.10: Unrealistic film height as result from small CAD features, these features are not existing in the real life AIS and are introduced in the CAD model as manufacturing aids, for the CFD model these should be removed during model preparation

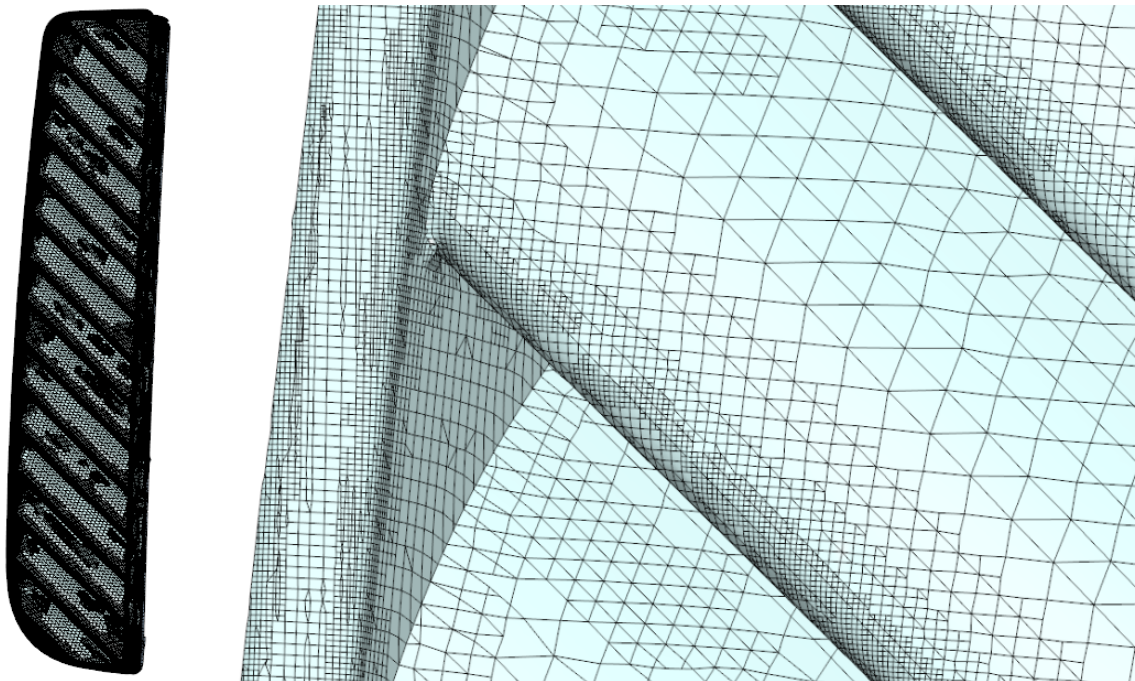


Figure 6.11: Mesh Detail around louvres

reasons are the need for a dynamic contact angle and with relatively high film heights. In our case we have a large influx of water and a film model on its own would not be able to handle this. This is also confirmed when the simulation is run with only this model activated because the simulation will not stabilize and properly converge, which is a natural results of water that increases above a height that the film model can handle.

The solver is set to 1st order already discussed previously, for this type of simulations, we always use a first order scheme for the temporal discretization. Second order scheme use is limited to a few applications, where high temporal accuracy is required and here it is very important to reduce as much as possible the numerical dissipation linked to low order schemes; a typical application is aeroacoustics. For most of the industrial applications, first order is the default practice since it is a good compromise between stability and accuracy. Clearly, there is no harm in using higher order scheme, especially when using small time-steps. However, considering potential convergence problems that can occur during the setup of our complex transient case, it is beneficial, at least in this stage, to use a first order scheme instead of a second order, in order to be sure to remove potential source of instability in the simulation. If needed, we can eventually go back to second order, but for now it is recommended to use the default practice for these type of simulation and use the 1st order scheme. Max inner iterations from is set at 10: fine running the simulation longer, ensuring a better convergence at each time step. Once setup is established it can be tried to lower the inner iterations until convergence is no longer achieved. As final step autosave is turned on: in order to later on view enough detail in the postprocessing it is recommended keep a saved version of the simulation at each 0.1 s timestep, this automatic saving can be set under the StarCCM file menu.

## **Contact Angle**

In the previous simulation setup (no VOF), we had to set up a contact angle between the boundary and the film phase. In terms of formulation, this takes into account the triple line between film, continuous phase and wall, including the surface tension effects. In the new approach, we have added the possibility of switching from fluid film to VOF whenever the film grows too large and a fluid film formulation is not suitable any longer. When and how the switching occurs is completely up to the software, which computes the relative thickness and treats differently the liquid phase. We only need to make sure that all the interaction are correctly setup and in place. When the film transitions to a proper VOF phase due to the thickness, the code will only look at the multiphase interactions set for the VOF phase in order to simulate the interaction of the liquid phase. This means that in order to keep the same contact angle even when the film grows enough to be treated as a VOF phase, we need to specify a contact angle on the boundaries of the air region too and of course define a multiphase interaction VOF water - VOF air, which is the counterpart of the Film-VOF air already available in the simulation.

## **Lagrangian Setup**

The injector is kept as described in the previous section: a grid pattern under an inclined angle with a distributed mass flowrate of  $7.86\text{E-}3$  kg/s, a particle diameter of 0.2mm (large cloud drop) and an initial velocity of 0.763 m/s. The injector parcel count is set in such a way that while solving the simulation the particle count (particles per parcels) is close to 1, this was fulfilled with

a parcel setting of 3. To print down extra information for the Lagrangian iterations the verbosity settings are changed from none too low. this will not affect the solution in any way it is only used to obtain more information from the simulation during the setup of the case. Once we have an established simulation method this setting can be switched back to 'none'.

The Lagrangian solver update frequency is set at 'recommended': The setting 'once per time step' is set for speeding up the Lagrangian simulation. The once-per time step option will simply update the Lagrangian solver at every time-step instead of at every iteration, even though the simulation is two way-coupled. This is generally fine when using a small time step, but again, in order to remove any source of error in this stage of setting up the simulation, the preference is using the more expensive and more robust approach of "recommended" update.

The Shell Source Smoothing Method for the Lagrangian solver is also activated, this controls the smoothing of Lagrangian sources arising from Lagrangian parcels impinging on a fluid film in a shell region. The impinging Lagrangian parcels can represent large mass, momentum, and energy sources to the fluid film phase. To increase numerical stability, volume source smoothing spreads the effect of the entering Lagrangian particles over several cell faces. the method of cell clustering imposes a coarse grid for evaluating exchanges of momentum, energy, mass, and species, as applicable from the Lagrangian phase to the fluid film phase. The coarse grid is a virtual grid and is constructed by clustering the cells in the Shell Regions. Sources from LMP are accumulated in the coarse cells and then distributed evenly among the component cells contained in the clusters. This method is activated when particle sizes are close to, or greater than, the smallest cell sizes in the simulation. Use the Scale property of the Cell Cluster child node to set the approximate size of the coarse-grid cells. The scale is defined as a multiple of the length of the largest cell in the original grid, and ranges from 1 to 10. The default is 1.

## **Initializing the Transient simulation**

To help stabilize the solution it is opted to first run the steady state part of the setup for the main air phase, this solution (when shown proper convergence) is then stored in a table that will act as initial values for the transient parts of the simulation. Storing these initial value in a table is done through following steps:

1. Create a Physics Continuum with the continuous phase only and run the simulation
2. Under Tools - Tables, create a XYZ Internal Table
3. Under Tools - Tables - XYZ Internal Table and choose as Part the whole region (only the region and not the boundaries); choose as scalars: Velocity, Pressure, Turbulent Kinetic Energy and Turbulent Dissipation Rate
4. Right-click on XYZ Internal Table and choose Extract
5. Now create a new Physics Continuum with Lagrangian and Fluid Film
6. In the Initial conditions of the latter Physics Continuum, you need to switch from constant to table and then select the quantity in the table.

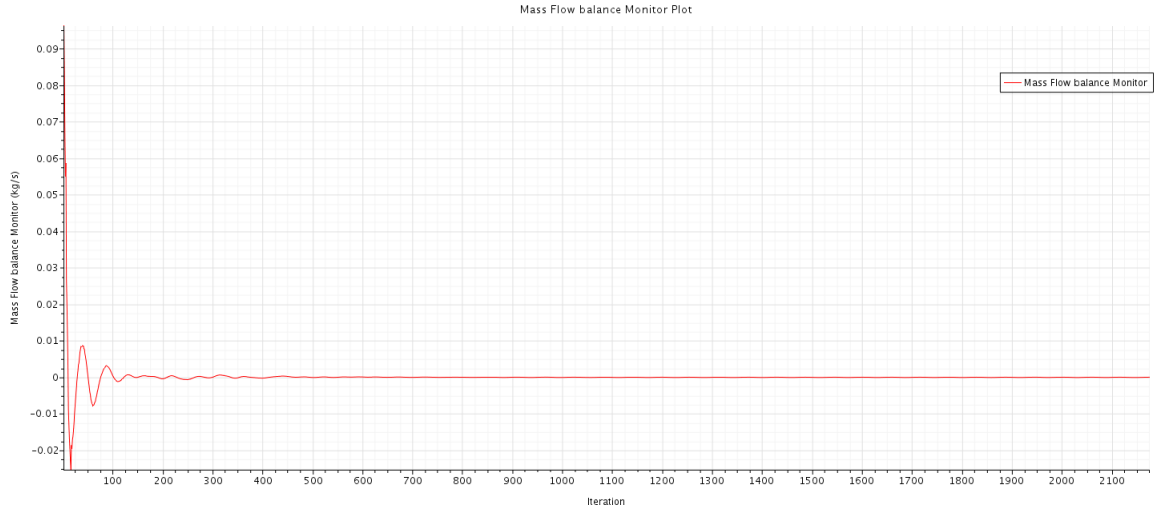


Figure 6.12: Massflow balance stabilization: difference between inlet and outlet should stabilize towards zero in order to respect mass conservation

### Monitoring the solution

For monitoring the proper convergence of the simulation, we need to focus on 2 aspects of the simulation, the main air phase and the water in all its forms moving through the domain (injected as particles, impacting on the fluid film, transferring to VOF when the film height is too high, and escaping through the outlet or film edges). The monitoring of the air phase is done with a monitor and the default residuals and some extra monitors on the mass balance, pressure at outlet and the maximum velocity in the system. Mass Balance is the difference of the massflow entering the system at the inlet and existing the system at the outlet, this difference should be stable around zero, anything else would indicate improper convergence of the simulation. The default residuals form an indication for the overall stability of the simulation (averaged values) the goal here is that these do not form any peaks or fluctuating behaviour. the maximum velocity in the system is focused on one area of the domain where the largest velocity of the air is observed, the absolute value of this monitor should be realistic relative to the imposed massflowrate, more importantly however this value should be fairly stable towards when the simulation starts to converge.

For the water phase the monitor is put on the film height, in a good converging simulation the value of the maximum and minimum film height is monitored. the minimum film height should always fluctuate around zero (our louvres will never be fully wetted, so there should always be a spot where minimum film height is zero, anything else would indicate abnormal behaviour for the film), the maximum film height is also monitored, this value should be realistic in function of the simulation that was setup. In our case we have a combination of VOF and film and as explained in chapter 3 this simulation will calculate itself when the film transfers from film to VOF, for our setup this would mean that film height above 2 mm need extra investigation. However for this monitor to be of any meaning we should pay attention to not clip the film model max height in the Fluid Film physics model. This can be completely fine and it is useful for increasing the stability of the solver. However, when starting with a simulation setup it should be avoided as it can hide a bigger problem related to mass conservation. A high correction for the film thickness for each time-step would indicate a solution that is clearly non-physical. Once a simulation setup has been

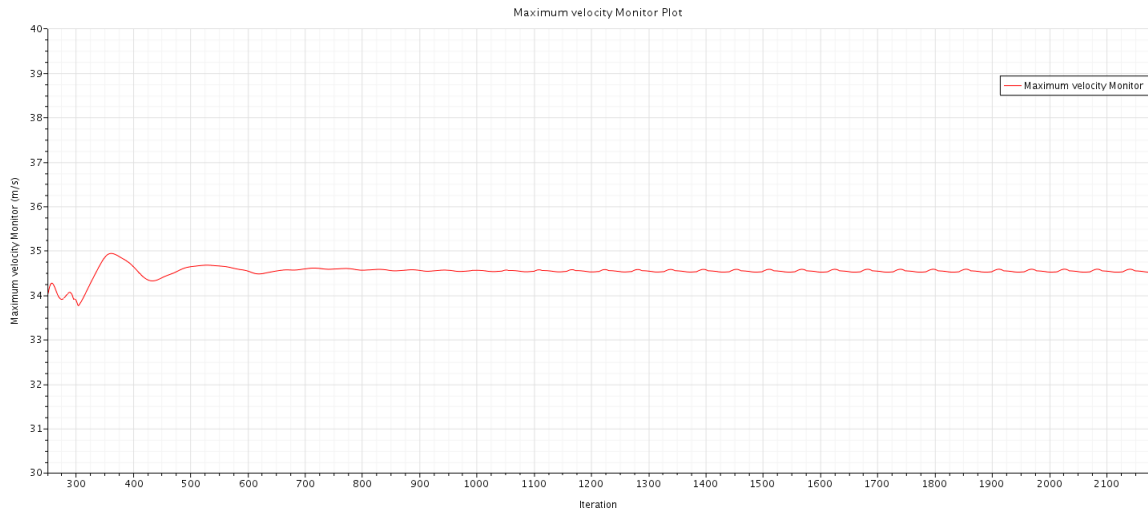


Figure 6.13: Maximum velocity: this the largest velocity value observed in a cell from the domain, when this fluctuates too much this implies the steady state solution is not stabilized. In our case the value fluctuates around 35 m/s with a variation around  $\pm 0.1$  percent, which is certainly allowed for this case

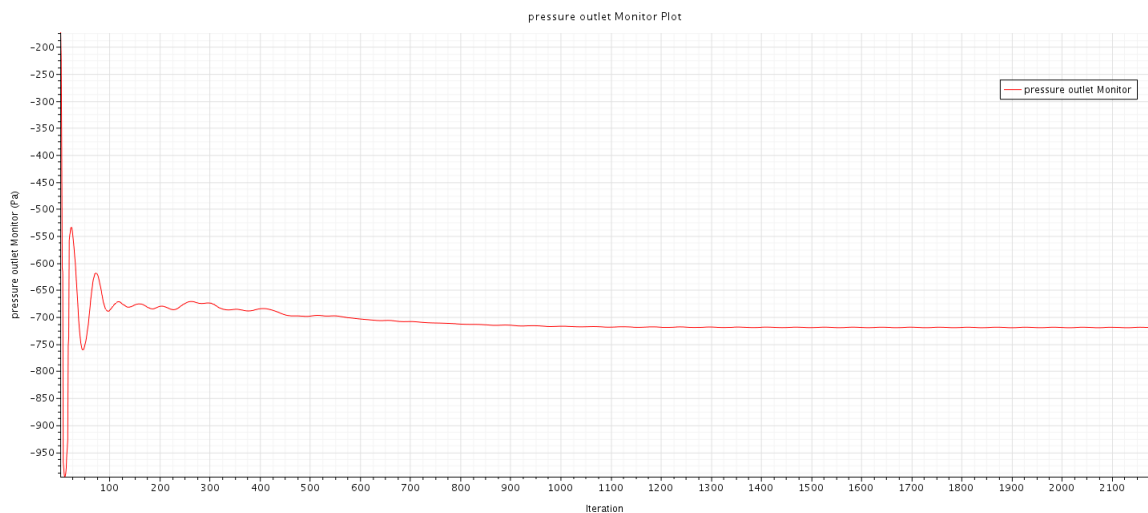


Figure 6.14: Pressure at outlet: for our steady state case this value should stabilize around a realistic value, for our case this is the case



shown to be stable it can be beneficial to again impose this film clipping, but if compute resources are of no issue its better to avoid this. This should make sure that we are not clipping away the fluid film thickness and that we are not forcing the equation to change, giving us the true value of the film residuals. For the water moving through the domain we need to monitor the cumulative mass quantities from the water in the system in kilogram (to observe these monitors a plot is created that tracks these values across the timesteps of the simulation):

1. Particles mass entering the system through the injectors
  - Create a new field function: Injector mass flow x time-step, this needs to happen manually, as there is no field function that can be called out for injector massflow, so in this case take the exact value of the injector volume flowrate and multiply it with the density, take that exact number and multiply it with the timestep: IMPORTANT - when we update the flowrate in the injector specifications, make sure to also update this field function. The dimensions of this field function should be set to mass=1
  - Create a new Field sum Monitor using Input Parts: Inlet and Field Function: the one created in step 1
  - Create a Maximum Report for the sum field function, then create a monitor from this report.
2. Particles mass flowing OUT of the system through the outlet
  - Create a new Particle Mass Flow Report using Input Parts: Outlet and Phase: Lagrangian
  - Create a new field function defined as Report \* timeStep and set dimension to mass=1
  - Create a new field sum monitor using Input Parts Outlet and Field Function: the one defined in step 2
  - Create maximum report with Field function from step 3 and create a monitor from it
3. Particles mass flowing OUT of the system through the atmosphere: repeat steps as described for outlet
4. Particles mass suspended in the system: Create a Sum Report using Field Function: Parcel Mass and Parts: Lagrangian Phase
5. Mass transferred into VOF
  - create field function: density \* Volumefractionwater \* Volume
  - create sum report with field function as described created above and input parts the main region
6. Film mass being generated out of the impinging particles
  - Create a new field function: film density \* Film thickness \* mag(Area)
  - Create a Sum Report using Input Parts: the boundary inside the shell region and Field Function: the one defined in step 1

### 6.5.3 Available steps to optimize the transient solution time

There are a few steps that can be taken to reduce the computational time and still maintaining proper converge and good results. Typically in any unsteady simulation you can make the simulation run faster by increasing the time step size, reducing the number of inner iterations or by reducing the mesh size into a more efficient mesh, however you must check that you are still reaching convergence at each time step. There are 6 approaches to help reduce the simulation time (see also the appendix for more detail):

1. Reduce the update frequency
2. Use the Active parcel fraction cut-off
3. Re-partition the mesh based on Lagrangian loading
4. Reduce the number of parcels
5. Stop tracking Parcels when they leave the area of interest
6. Remove insignificant parcels from the domain using a field function

#### Reduce the update frequency

The update frequency is how often the Lagrangian sources to the continuous phase are updated, because there is a computational expense for calculating the sources we want to reduce the update frequency as much as possible. In our simulation we definitely use the transient approach due to the fluid film model, however our time-step is sufficiently small enough to set the update frequency as once per time-step rather than every iteration. For a Transient analysis the update frequency is recommended, when Two-Way Coupling is enabled then the update is once per iteration, conversely it is once per time step when Two-Way Coupling is disabled. If the time step is small then the continuous phase solution will be approximately the same at the beginning and end of the time step so updating the sources once per time step is sufficient. Reduce the update frequency: when you have a two-way coupled simulation, the sources are updated every iteration, in order to provide a strong coupling between fluid and particles. If the time step is very small (and consequently the CFL as well), the flow won't change much between time-steps: this means that the Lagrangian sources can be updated at every time-step without adding a big error.

#### Use the Active parcel fraction cut-off

This feature removes the need to spend significant effort in tracking the final movements of a very small number of parcels (think about a few particles trapped in a recirculation area), the fraction is defined as the percentage of active parcels compared to the maximum number seen at any other sub-step. When the fraction is reached then the sub-stepping is stopped and the Lagrangian tracking for the iteration ends. The default fraction value is 0.0 which means it is inactive, you can specify a small percentage to enable the feature. The value used in our simulation is 0.001 or 0.1 percent.

## Re-partition the mesh based on Lagrangian loading

Load balancing will make sure that parcels and cells are always distributed in an optimal way between the different processors, paying more attention to the particle distribution. To use our hardware efficiently we want the loads to be balanced on each core. The Lagrangian sub-stepping will not scale well if all of our parcels are in the same mesh partition so we can enable the load balancing in the Lagrangian solver to re-partition the domain based on the Lagrangian load information.

- The parcel weight controls the relative weight of the parcel versus the cell, the weight can range from 1 (the default), as Lagrangian as possible, to 0, strictly Eulerian.
- The rebalance limit is the ratio of the most and least loaded domains, once satisfied the load balance solver stops. Setting the value close to 1 results in 'always rebalance,' in most cases this is undesirable because you are rebalancing beyond useful levels. The value of 0.8 should be appropriate for most applications.

There is a computational expense for re-partitioning, the default value for the rebalance frequency is every iteration, this is not desirable because it is likely that the solution changes slowly and so the current partitioning is suitable for a number of future iterations.

## Reduce the number of parcels

This method is not used for our rain water simulation, for reasons explained below. Because the run time of the solution is strictly dependent on the number of parcels in the simulation, reducing the number of parcels will speed up the simulation, note that this will increase the mass of each parcel. If you have a single point injector, the number of parcels is equal to the number of parcel streams, for a steady state analysis this is a finite number, but for a transient simulation this is the number of parcels injected at each time step when the mass flow rate is above zero. This approach should be used with extreme caution where you have a particle size distribution and/or complex physics (evaporation/fluid film) because we need a statistically significant number of parcels to represent our size distribution and if the mass of each parcel becomes large then it can cause convergence problems.

## Stop tracking Parcels when they leave the area of interest

Another possible solution to speed up the simulation is setting the boundary after the louvre as escape, but this should be used as last attempt or during very early stage simulation runs to get quick confirmation if the sim setup is ok and in case we have problems making the simulation faster with the settings listed above. If we are only interested in tracking parcels in the area of interest, we can allow parcels to escape, stick or evaporate by setting the wall interaction which can be for the continuum or locally at specific walls, the continuum wall interaction is set in the Physics continua - Lagrangian Multiphase - Boundary Conditions. To have a custom behaviour at a specific boundary you need to enable the Lagrangian specification and then an additional node called 'phase conditions,' appears where the behaviour mode can be chosen. For interfaces you will need to convert the interface to a porous baffle and then specify the behaviour at the continuum

level (Physics continua - Lagrangian Multiphase - Boundary Conditions) as it is not possible to locally specify the behaviour. Note that the default porous resistance is zero so there will be no pressure drop across the baffle and that if your parcels are evaporating then it would be best to change the baffle thermal option to 'conducting,' so that energy is extracted from the cells at either side of the interface.

### **Remove insignificant parcels from the domain**

We can use the parcel depletion physical model to remove insignificant parcels using a field function to avoid tracking them indefinitely, you should be aware that the parcels essentially escape and the mass is lost. It is an optional model in the Lagrangian physical model selection. In the sim file there are a number of particles with very high velocity, which are very few compared to the total number of particles. In particular, only 0.1 percent of the particles have a velocity higher than 30 m/s, but we will spend a lot of time running the simulation for tracking those particles (high velocity means smaller substep and so more time for substepping the Lagrangian simulation). The particle depletion model is activated using a criterion based on the maximum velocity of 30m/s. This model allows us to specify a depletion criteria using a logical expression or field function, parcels are removed when the expression evaluates to a non-zero value.

### **6.5.4 Results and analysis - effect of contact angle**

As described in chapter 2 an AIS (Air Intake System) will generate a strong airflow towards the engine that will cause potential rainwater to be sucked into the orifice. The previous sections described methods that were used in the past to evaluate this phenomena and the efficiency of means to prevent this (e.g. louvres), however the downsides of these methods was also highlighted. In this section we have opted to choose for simulation method that mimics closest the real life conditions. The mix of different physics allow the simulation of the main airflow, incoming raindrops falling from above, surface properties of the AIS that affect its contact angle and gravity pulling down the raindrops. A first observation from running simulations with this setup is that although they offer the highest amount of realism, they also require a significant increase in computation cost, whereas the previous method was able to run in under 12 hours on a 12 core machine, this method with all the physics models activated requires over 240 hours on a 140 core server. A good conclusion based on the runtime alone would be to use this method only when compute resources are readily available and to avoid running too many iterations of these design on other words, to run these type of simulations when some first qualitative analysis has been based on simpler less expensive methods. Due to small nature of the physics involved and the small timesteps these occur, there is limited means to increase the overall calculation time. The transfer of raindrops into the water film due to impingement requires a relative fine mesh in order to capture this phenomena properly and to allow the solution to converge, also the transfer between fluid film and VOF requires a fine mesh and fine timestep to avoid a diverging simulation in this area. To study the effect of the contact angle on the water movement throughout the system multiple values were analysed and visualized. As described in the previous section, the water mass was plotted vs time in all its forms (going from the injected Lagrangian particles to the drops that fall back to the earth, to drops being transferred into the film and VOF and eventually the mass of water that is escaping the domain through the outlet and the louvres draining location). Figure ?? and 6.15 show the water

particles as they fall from the sky under a slight angle. Figure 6.16 and figure 6.17 show water mass distribution in kg spread out in the domain, the water enters in the form of injected Lagrangian particles (blue line) and is distributed across the domain, most of the waterdrops do not even enter the air intake system, as they are being pulled down by gravity before the main airflow can pull them into the system, these are exiting the domain through the atmosphere around the AIS (red line). Figure 6.18 and 6.19 zoom in on the water suspended in the system that represent the mass that is injected and did not escape or transfer into another domain just yet (purple line), the first drops start getting deposited on the louvres film (wetting is light blue line) and the when the film becomes too high this is then transferred to the VOF model (brown line). In these more detailed images the differences between the contact angle settings become clearer. Although the wetting start in both cases around 0.4 seconds when the first drops start hitting the louvres. It is the 00 deg case that sees the mass being present in the film being higher than the 95 deg case, however this does not necessary mean that this 00 deg case is draining more water, it could also be that do the effect of the low contact angle our film height does not reached critical height and hence is not transferred into the VOF model hence being able to start amassing more incoming water mass. When looking at that VOF mass (brown line) it is indeed shown that the 95 degree case is showing higher mass being accumulated in the VOF model, which confirm our expectation that higher contact angles would lead higher film height and hence more transfer into the VOF model. When the film accumulated mass and the VOF accumulated mass are summarized this does show a much higher mass content for the 00 deg case (more pronounced at higher times) leading to the conclusion that the 00 deg case is managing to accumulate more water mass on the louvres. Figure 6.20 and 6.21 zoom in the parts with lowest water mass content, after a while the water film starts to increase in height due to the continuous feeding of new particles into the system and since we are running a hybrid film-VOF approach this is then transferred into a VOF (brown line). When we zoom in on the water that is deposited around the louvres, we can see that drainage starts around 1.4 seconds (yellow line) for the 00 deg case, while for the 95 deg this is only starting around 3.4 seconds - also a small amount of particles is able to pass past the louvres and run all the way to the outlet of the air intake system (green line), however in both cases this is very minimal. In chapter 3 where the PEPT test results were described, it was the low contact angle case that was showing the lowest speeds for the water film moving down the slope. In the simulations we just described this is not directly observable as we analysed the water mass content in several areas. However when comparing the fluid film distribution and thickness, figure 6.23 for the 95 degrees contact angle shows more smeared out patterns vs figure 6.22 for the 00 deg contact angle. The prior analysis already showed that for 95 deg the film height more rapidly increases, resulting in the faster formation of rivulets that can be caught by the air that is shearing across the louvres and as result creating higher speeds in the water moving around on top of the louvres. So for the low contact angle, better wetting is indeed leading to better draining as rivulets are not formed so easily and hence have less chance to get re-entrained into the shearing airflow.

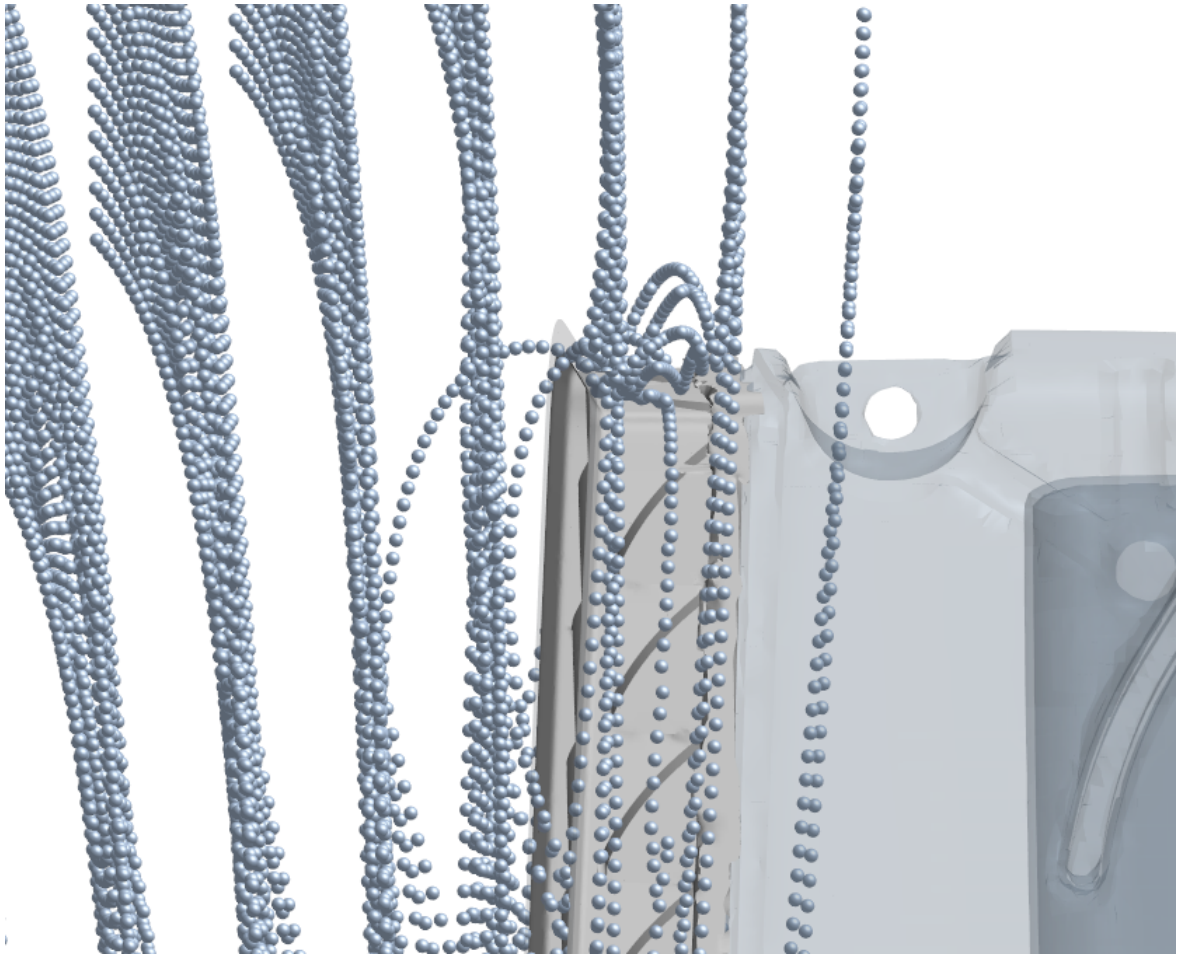


Figure 6.15: Raindrops falling onto the outer surface of the air intake system, rebounding particles have lost some kinetic energy and are seen as entraining into the intake further down.

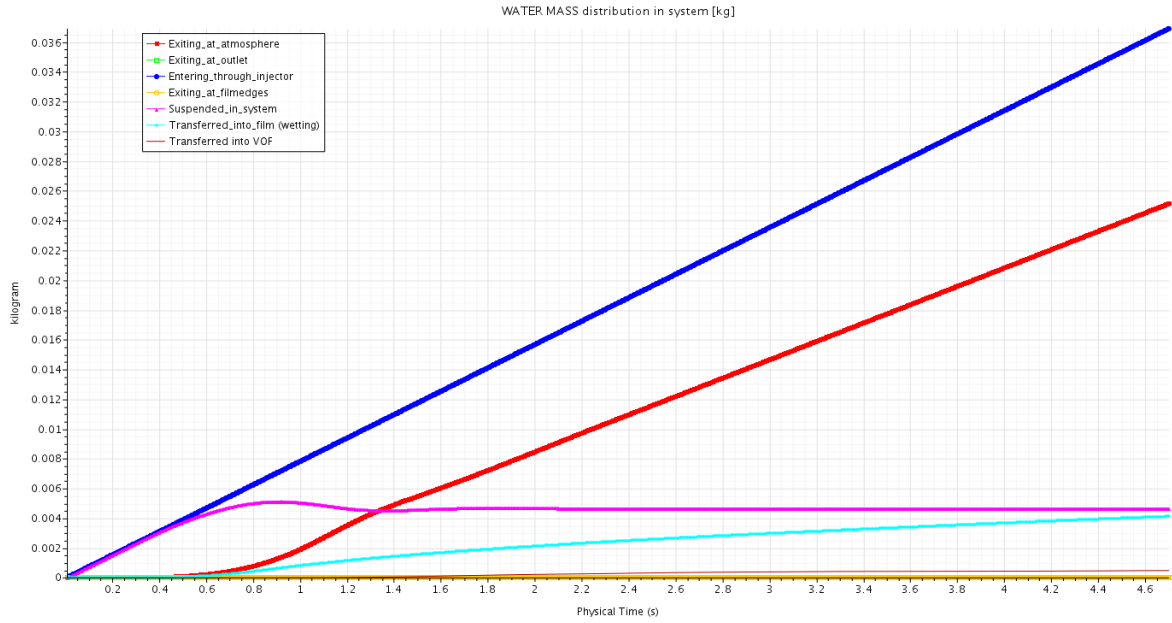


Figure 6.16: 0 deg contact angle: water mass distribution in kg spread out in the domain, the water enters in the form of injected Lagrangian particles (blue line) and is distributed across the domain, most of the water drops do not even enter the air intake system, as they are being pulled down by gravity before the main airflow can pull them into the system, these are exiting the domain through the atmosphere around the AIS (red line).

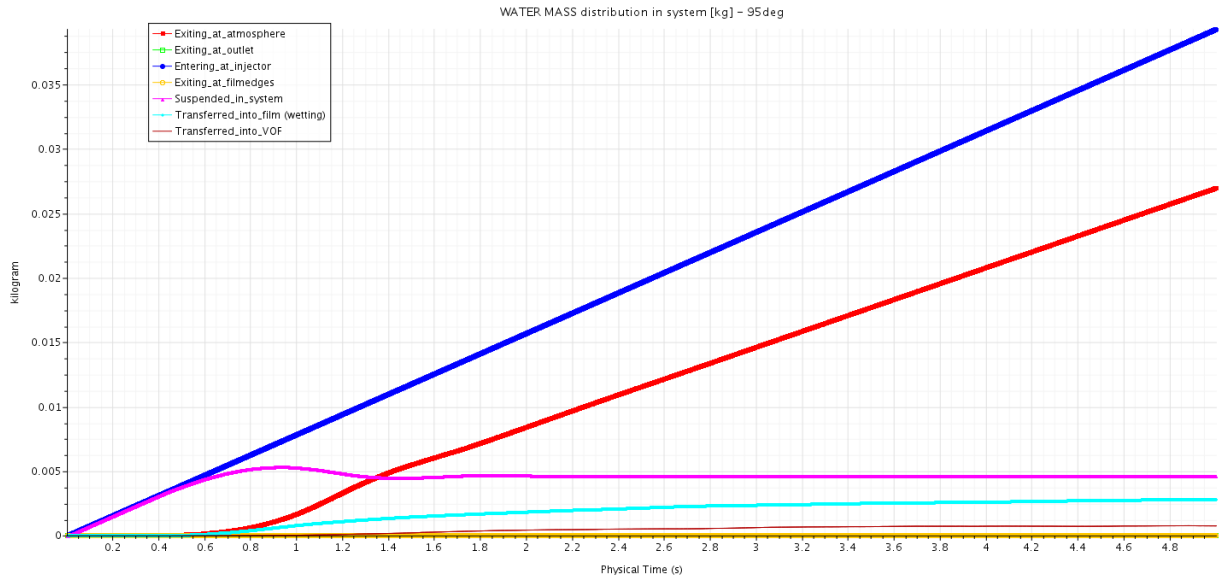


Figure 6.17: 95 deg contact angle: water mass distribution in kg spread out in the domain, the water enters in the form of injected Lagrangian particles (blue line) and is distributed across the domain, most of the water drops do not even enter the air intake system, as they are being pulled down by gravity before the main airflow can pull them into the system, these are exiting the domain through the atmosphere around the AIS (red line).

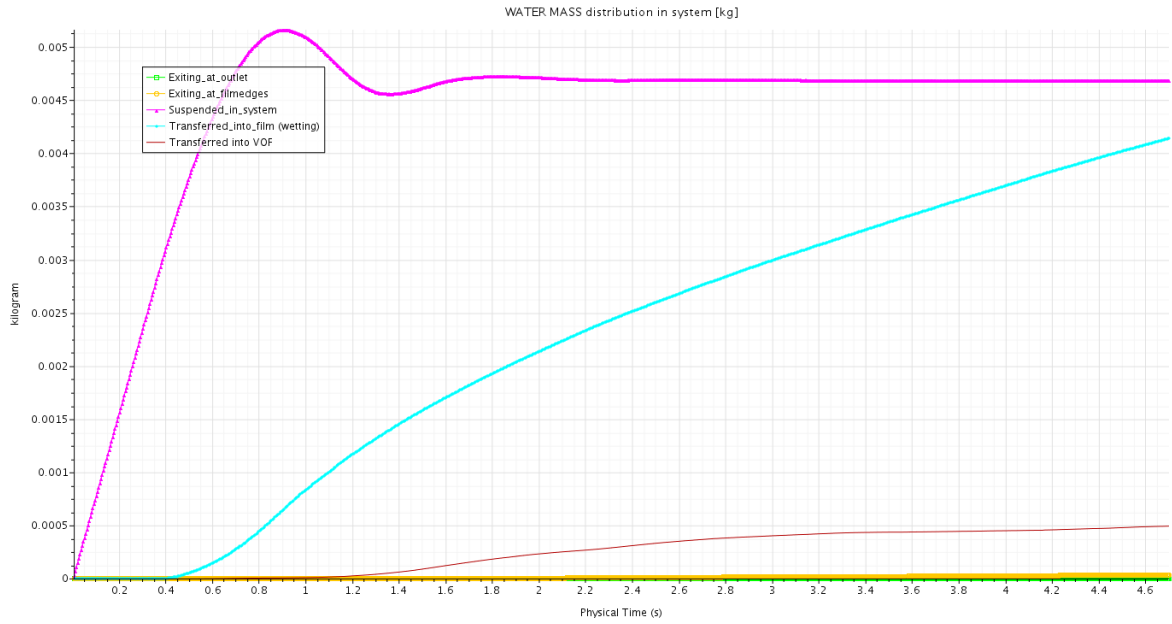


Figure 6.18: 0 deg contact angle: the water suspended in the system represent the mass that is injected and did not escape or transfer into another domain just yet (purple line), around 0.4 seconds the first drops start getting deposited on the louvres film (wetting is light blue line)

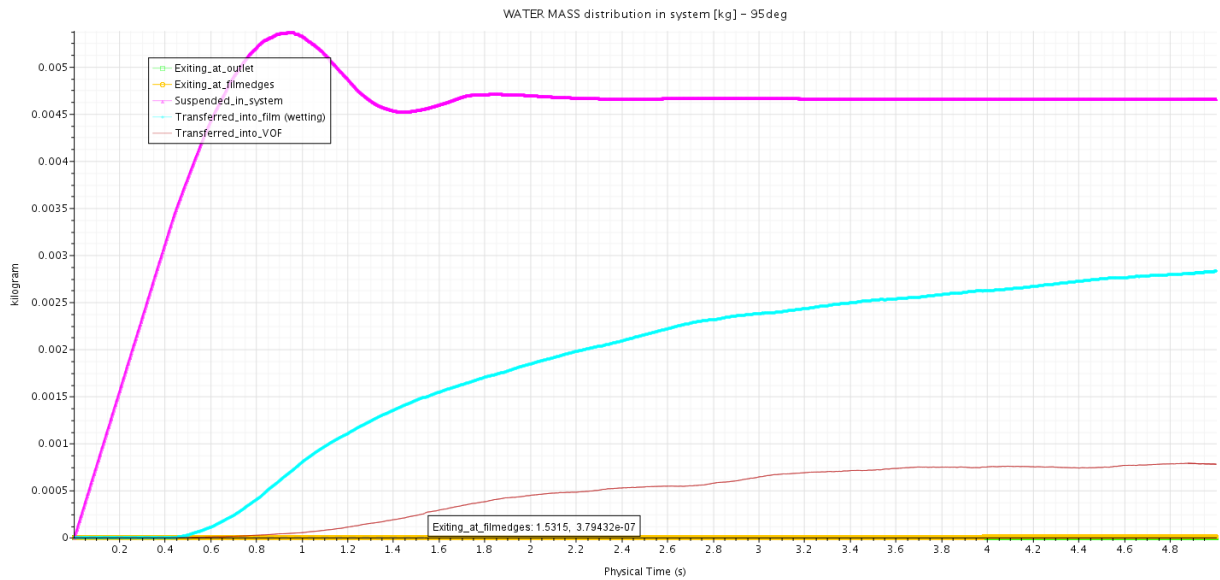


Figure 6.19: 95 deg contact angle: not much difference vs the 00 deg case can be observed on this zoomed out level, what can be seen is that the water is hitting the louvres at the same time, which is expected behaviour, after all the contact angle of the louvres have no effect on the incoming airflow and suspended water particles



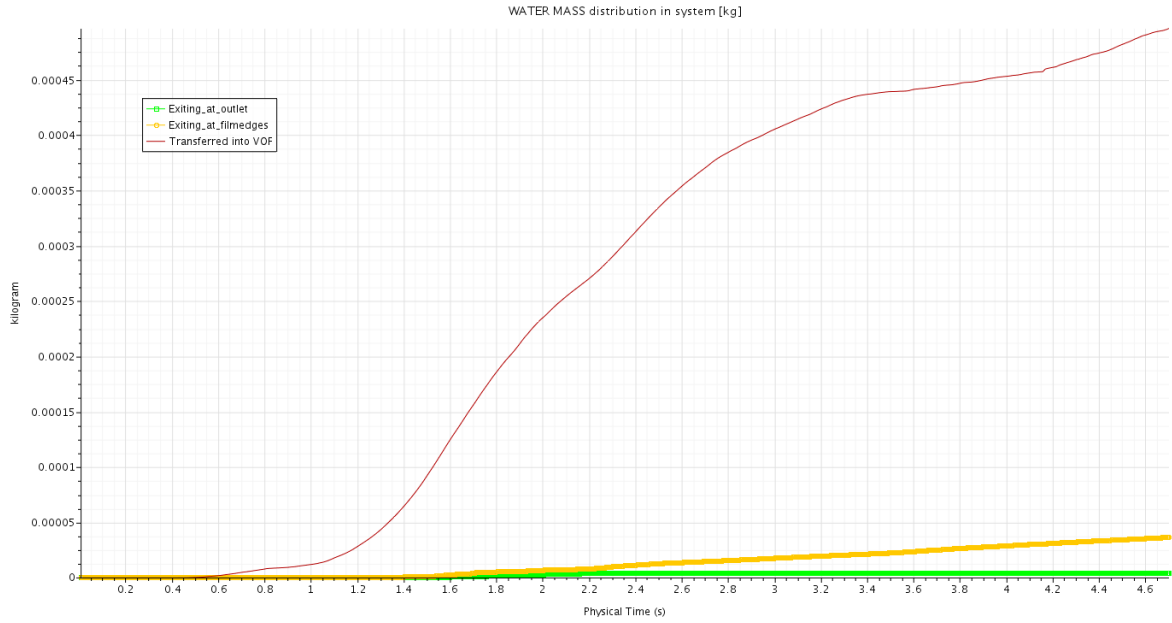


Figure 6.20: 0 deg contact angle: around 1.1 seconds the water film starts to increase in height due to the continuous feeding of new particles into the system and since we are running a hybrid film-VOF approach this is then transferred into a VOF (brown line). When we zoom in on the water that is deposited around the louvres, we can see that drainage starts around 1.4 seconds (yellow line) - also a small number of particles is able to pass past the louvres and run all the way to the outlet of the air intake system (green line)

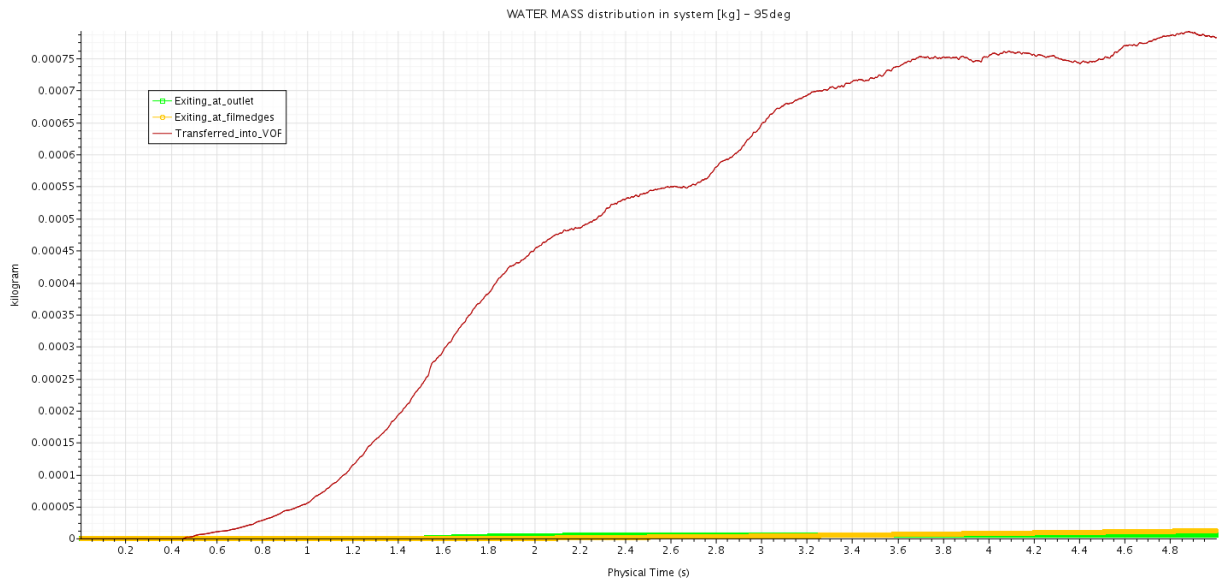


Figure 6.21: 95 deg contact angle: water draining at the edges is clearly lower around 5s into the simulation, leading to the conclusion that lower contact angle (better wetting) leads to better drainage

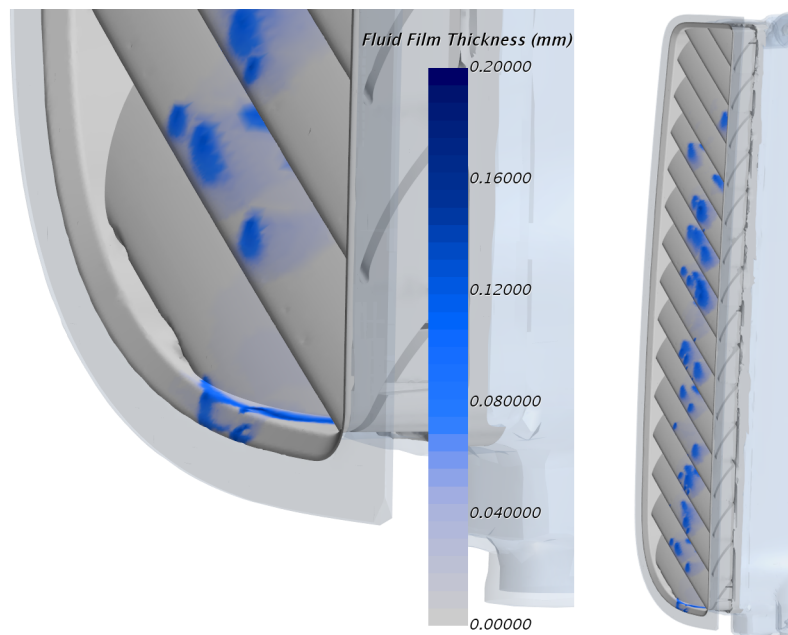


Figure 6.22: 0 deg contact angle: fluid Film thickness distribution, at the bottom there is water draining (running out at the edges)

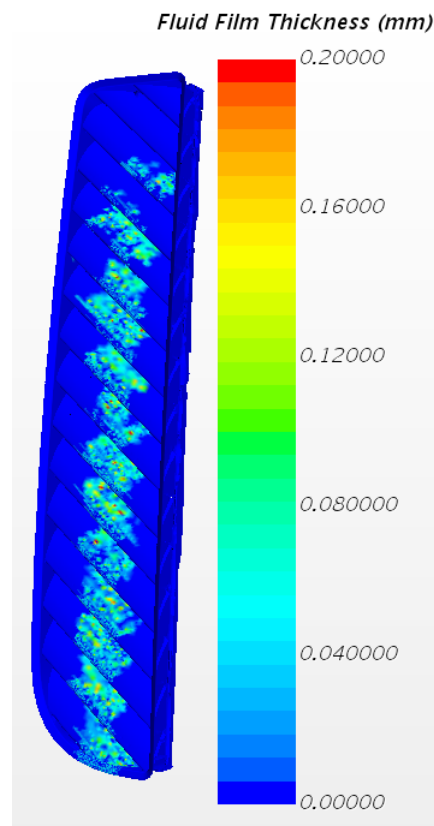


Figure 6.23: 95 deg contact angle: fluid film is more smeared out vs 00 deg case

## 6.6 Effect of Pressure (power) washing on water separation

Until now we have been considering a droplet injector placed under an angle and above the intake orifice and spraying droplets in the direction of the inlet similar to conditions like observed during a rainy day. However when a truck would pass through a pressure wash, droplets are directed perpendicular to the inlet orifice and have high initial velocity when leaving the pressure wash nozzles. To examine the effect of these pressure wash conditions, the droplet injector is moved towards the front of the simulation so that it creates droplets that spray directly towards the inlet. When the truck is standing still with the motor switch off there is no air being pulled into the intake, however more often than not automatic pressure washers do require the truck to keep the engine running as it is moving through the washing street. Also for this type of simulation the droplet diameter will have an impact on the amount of water being pulled into the main air stream. Since the effect of the droplet diameter was already studied in the prior section, we will limit our investigation to 1 droplet size that is relevant for pressure washing, typically these form very fine drizzle, so droplet size used is 0.02 mm but this time with a much higher initial velocity. The initial velocity can be calculated from the pressure that is used for the power wash equipment. Assuming no viscosity, we compute the velocity at the exit of the nozzle from the pressure and the density of the liquid (using Bernoulli's equation):

$$\frac{1}{2}\rho v^2 = \Delta p \quad (6.5)$$

For water at 135 bar, that gives a velocity of approximately

$$v = \sqrt{\frac{2\Delta p}{\rho}} = 165 \text{ m/s} \quad (6.6)$$

Like the pressure also the flowrate can be obtained from a typical pressure washer datasheet, on average this is around 12 litres per minute

$$Q = 12 \text{ lpm} = 0,0002 \text{ m}^3/\text{s} = 0,2 \text{ kg/s} \quad (6.7)$$

Also the injector form is now changed from a plane that simulated the rainwater to a cone injector with a very narrow angle of 30 degrees. As for the simulation model itself, previous sections established that using a coefficient of restitution has its limitations, certainly when particles impinge with rather high energy, this is certainly the case in this scenario so it was opted to go immediately for the fluid film analysis with Bai-Gosman activated.

The results confirm that power washing leads to a concentrated jet of water that is impinging on the louvres (see figure 6.24), a majority of particles actually rebound after hitting the louvres forming the nebula in front of the intake, the part of the jet that is able to penetrate the intake is then rebounding on the inner walls and structures of the AIS with some of them bouncing back into the area in front of louvres. When this jet impinges on the intake it did not have the time to disperse, leading to a fluid film that is concentrated around the area where the main jet impinges on the louvres, this result is obtained after only 0.04 seconds, giving an idea of how fast the water jet is moving towards the intake. Figure 6.25 and figure 6.26 show the amount of water present at different parts of the domain and also here it is clear that power washing leads to more water

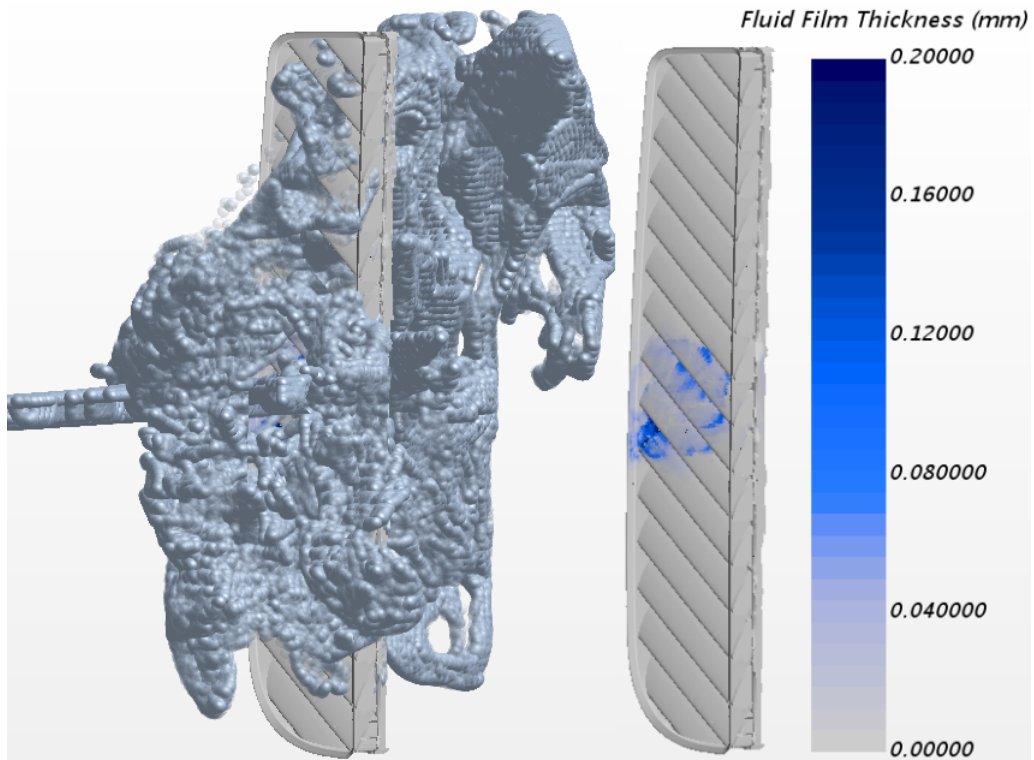


Figure 6.24: Left: power washing leads to a concentrated jet of water that is impinging on the louvres, a majority of particles actually rebound after hitting the louvres and then move into the intake orifice (even though there is no main airflow during power washing that could pull the particles in) - Right: the fluid film is concentrated around the area where the main jet impinges on the louvres, this result is obtained after only 0.04 seconds.

being injected into the system in a short amount of time. This behaviour is also observed during tests at Donaldson where power washing leads to a high amount of water being able to pass the louvres. Therefore the instruction manuals and advice to the client is always to not point power washing equipment directly into the air intake, in case some water would be able to penetrate the system due to neglect, even then the system is able to cope with this is the form of water drainage solution further downstream of the louvres, yet these only function on the premise that the engine is not running during the power washing and the instruction that when water was able to enter the system the power washing is turned off and 15 minutes is given to let the water drain from the intake.

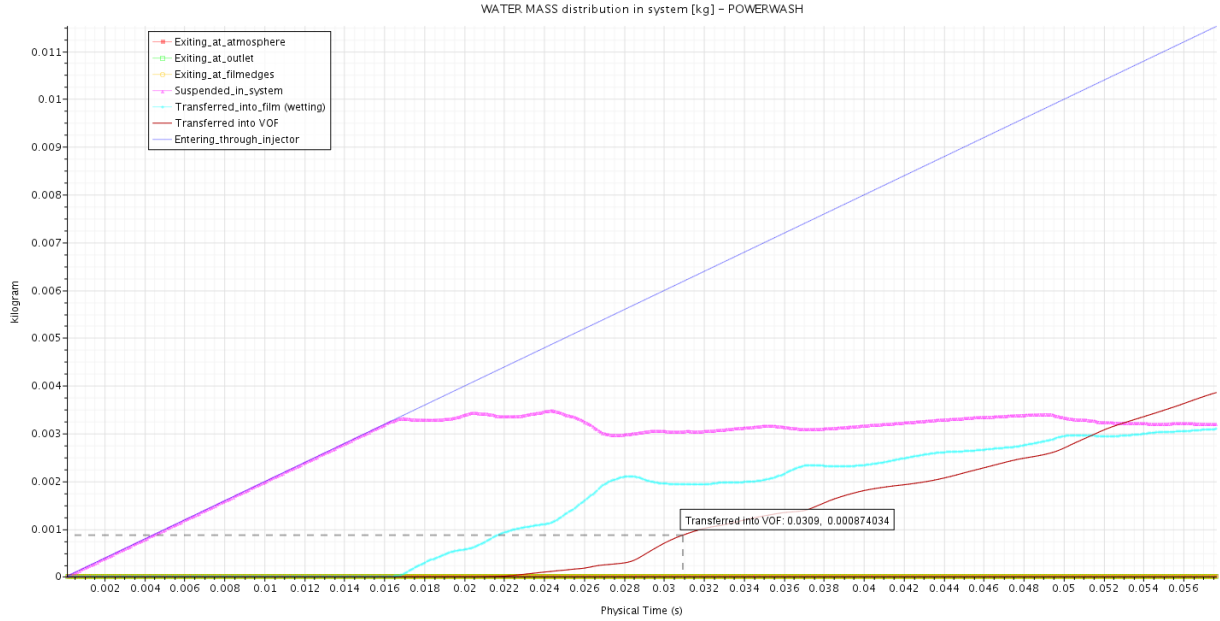


Figure 6.25: Mass distribution in the CFD model: the blue line represents the mass that is being injected from the source in the form of Lagrangian particles, compared to previous rainwater simulations, the power washing scenario injects far more water into the system, at 0.05 seconds there is already 0.01 kg of water that entered the domain. Since the particles are travelling at higher speeds, also the transferring of this injected mass into film and VOF happens faster (around 0.016 s).

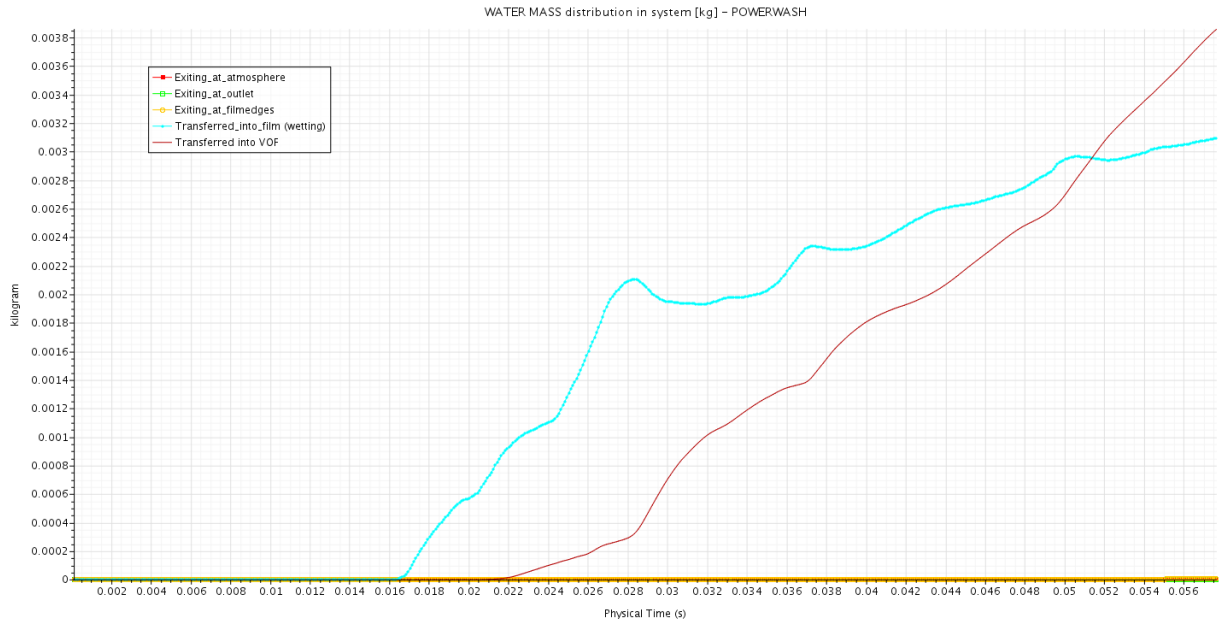


Figure 6.26: Zoomed in on the mass distribution on the film and VOF, this confirm again the observation from the prior image, the film starts to grow already at 0.016 s, and not much later the film height starts to rise above the threshold value and the mass is transferred into the VOF model. The incoming injected flow of water is actually so high that the film cannot distribute properly and film height keeps on rising much more than in the previous simulation, this is shown by the red line (VOF model) that is growing larger vs. the blue line (film model), meaning that the VOF model is handling the majority of the incoming water.

## 6.7 Effect of main air phase flowrate in the full-scale AIS

Chapter 5.5.4 already investigated the effect of the main airflow for the scaled down inlet box, figure 5.31a and figure 5.32a showed that for a low airflow the particles are allowed to follow their own trajectory that is determined by the injector cone angle and the injector initial velocity. when the main air phase flowrate is increased (see figure 5.31d and figure 5.32d) we can observe that the particles are no longer able to swerve out so much and are picked up by the main air phase more quickly. The main airflow for the full scale AIS is the air that is being pulled from the atmosphere into the air intake system that feeds it through a filter to the internal combustion engine. In the prior sections the simulation has been run with a mass airflow-rate of 0.595 kg/s that corresponds to the engine running at full load (maximal air intake). In terms of water ingression this is off course the worst case scenario since it will create the largest velocities around the intake louvres, and its these zones of high velocity that can pull in air and the raindrops contained in it from in front of the orifice. In the following simulation the airflow was reduced by 50 percent, to analyse the effect on the water ingression and drainage. Normally it would be expected that due to lower orifice velocities less water would be entering into the system. When comparing figure 6.28 for the low airflow vs figure 6.18 for the high airflow, the blue starts to ramp up later (around 0.5s for the low airflow vs 0.4 for the high airflow), this is expected behaviour as the lower airflow means that particles will get dragged along slower and arrive at the louvres a bit later. When the simulation is running for 4.5 seconds this effect is even more pronounced, as for the high airflow 0.004 kg of water has hit the louvres and is transferred into the film, while for the low airflow only 0.0018 kg of water is transferred into the film. However the red line that represent the water that is being transferred into VOF (so the water from the film that achieves a certain height) is higher for the low airflow (0.0007 kg vs 0.0005 kg). A conclusion here would be that with the high airflow the film cannot grow to a certain height, the shearing airflow would just pick up those thick drops and rivulets, while for the low airflow the water running down the louvres are less hindered. This effect is more visible on the yellow and green lines in figure 6.30 and 6.20, the yellow line represents the mass of water that is draining from the system at the edges of the louvres, for the low airflow this is 0.00007 kg at 0.45s, for the high airflow this is 0.000035 kg at 0.45s, thus indicating that the low airflow allows better drainage, certainly considering that the high airflow is receiving more water mass coming in.

Table 6.4: Mass airflowrate of the main air phase - the main air phase it the air that is being pulled through the air intake system by the running engine. 0.595 kg/s is th engine running at full load. To simulate an engine running at lower rpm like on the motorway also a mass air flowrate at 50 percent is simulated

condition	mass flowrate	percentage
engine running at full load	0.595 kg/s	100
engine running in half load (motorway conditions)	0.2975 kg/s	50

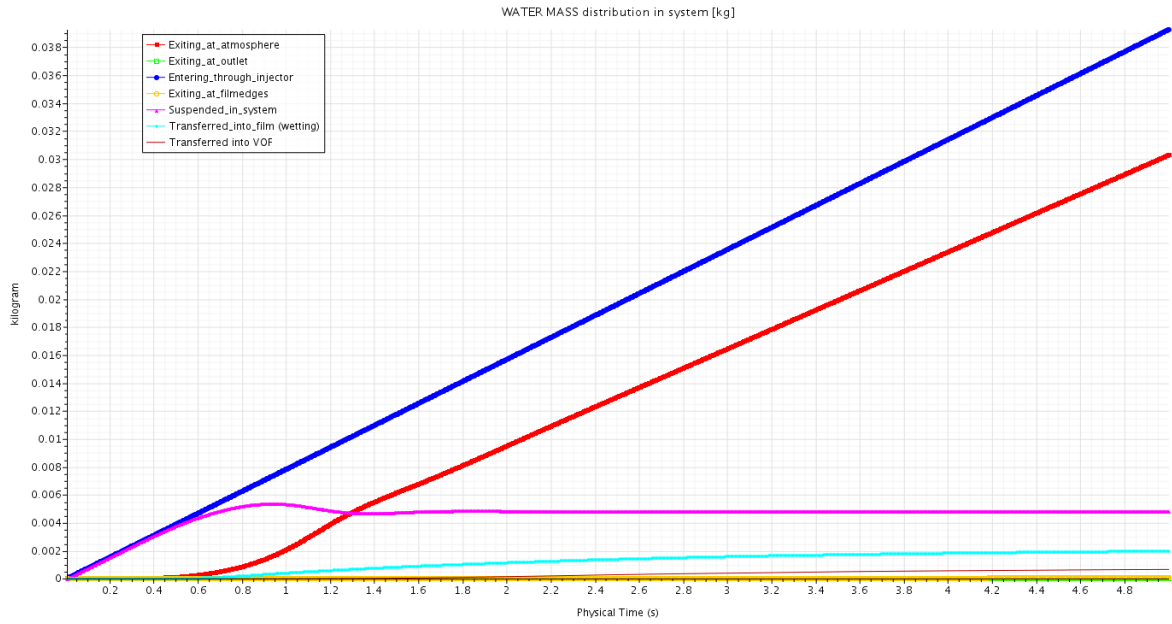


Figure 6.27: Lower airflow: Water mass distribution in kg spread out in the domain, the water enters in the form of injected Lagrangian particles (blue line) and is distributed across the domain, most of the water drops do not even enter the air intake system, as they are being pulled down by gravity before the main airflow can pull them into the system, these are exiting the domain through the atmosphere around the AIS (red line).

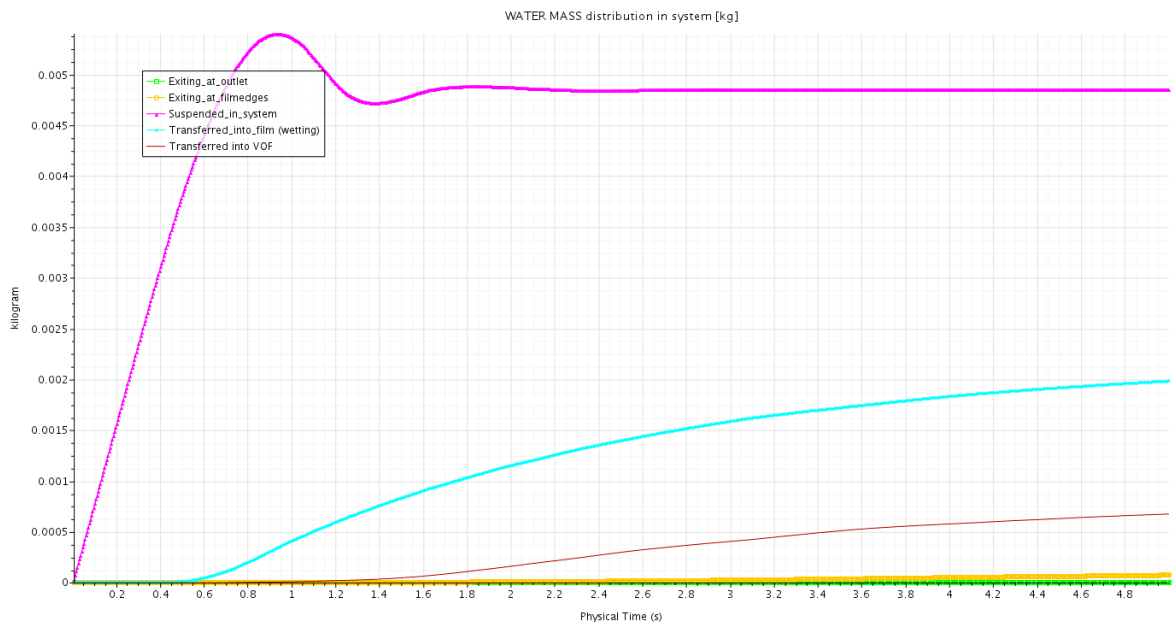


Figure 6.28: Lower airflow: The water suspended in the system represent the mass that is injected and did not escape or transfer into another domain just yet (purple line), around 0.4 seconds the first drops start getting deposited on the louvres film (wetting is light blue line)

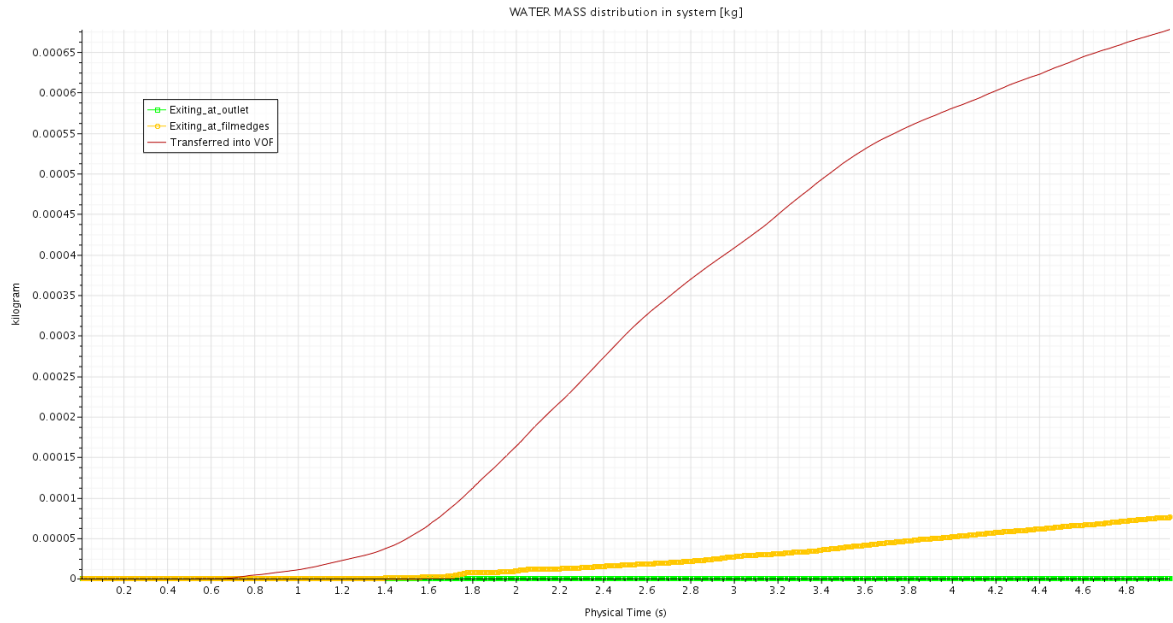


Figure 6.29: Lower airflow: Around 1.1 seconds the water film starts to increase in height due to the continuous feeding of new particles into the system and since we are running a hybrid film-VOF approach this is then transferred into a VOF (brown line). When we zoom in on the water that is deposited around the louvres, we can see that drainage starts around 1.4 seconds (yellow line) - also a small number of particles is able to pass past the louvres and run all the way to the outlet of the air intake system (green line)

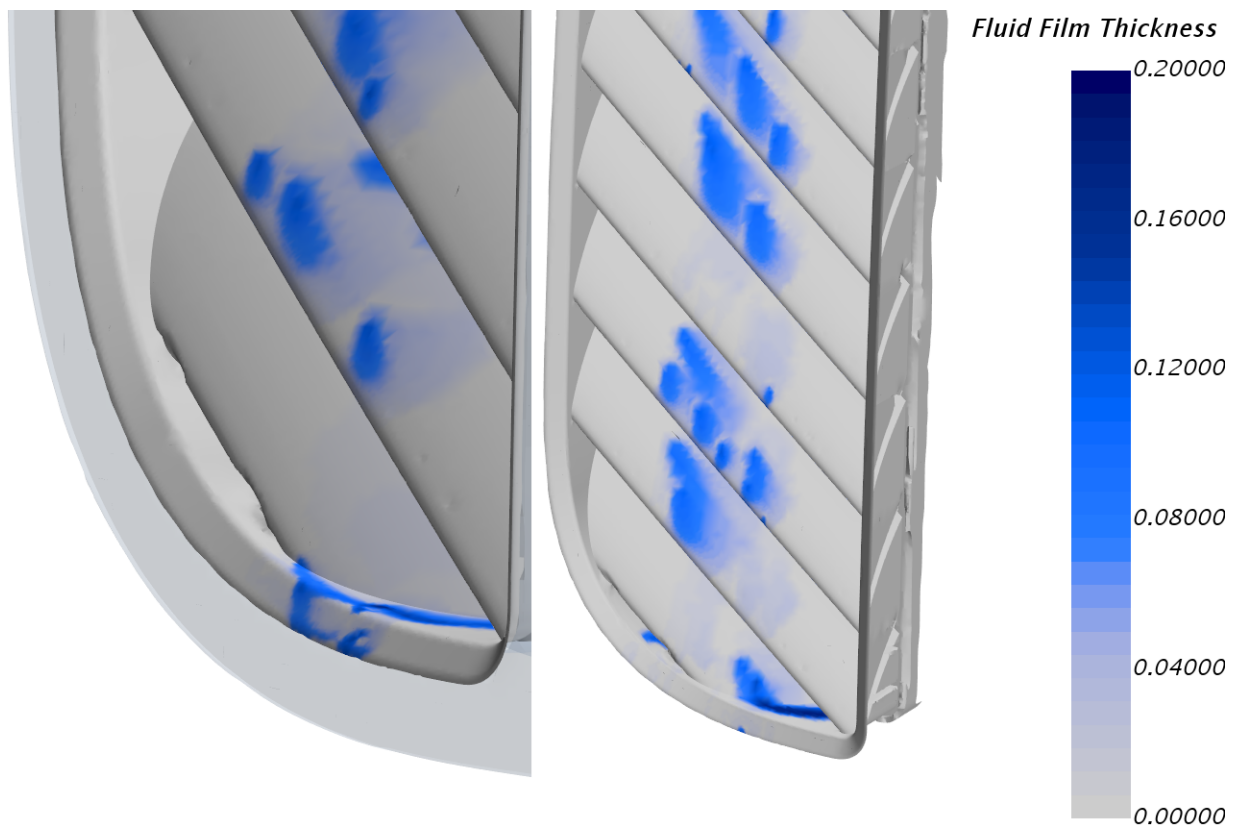


Figure 6.30: Fluid Film Thickness, detail at bottom of louvres where film is draining after 5 seconds of ingress: left - high airflow, right - low airflow: as expected the lower airflow is pulling in less rainwater and as result is not draining yet, while the setup with the higher airflow collected at the same already more rainwater and is already draining at the edges



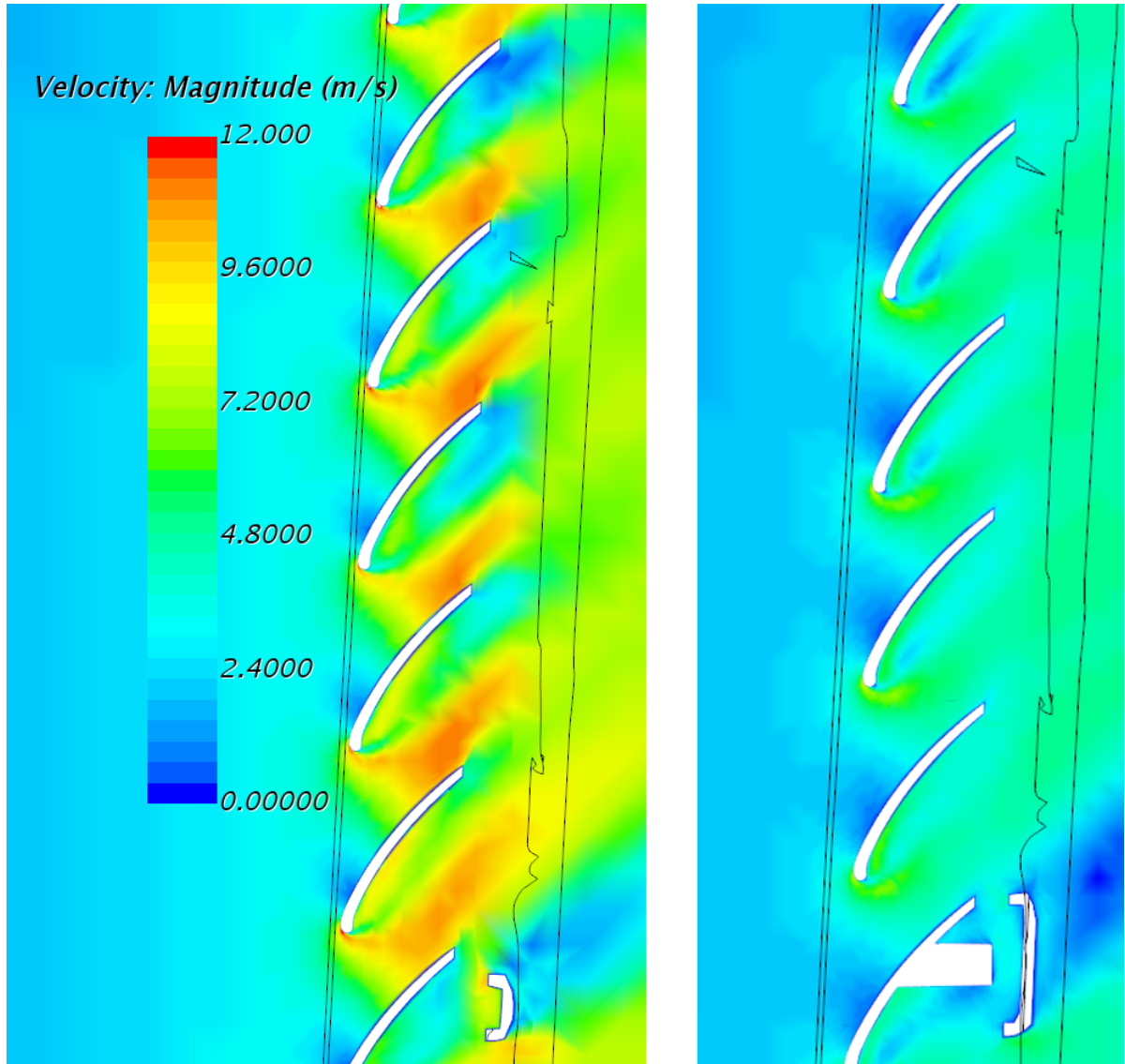


Figure 6.31: Velocity distribution around the intake louvers, left: high airflow - right: low airflow, the plots show a significant difference for the velocity magnitude around the intake louvers, this will affect the ingress of air and the suspended rainwater in front of the intake orifice (see table 6.4 for air flowrates).

## Chapter 7

# Conclusion

As explained in Chapter 1, the objective of the research was to validate CFD water behaviour models used during the design of air intake systems through validation with experimental PEPT results. Preventing water to reach a filter medium is fundamental for good and durable filtration results. To design and improve water drainage solutions for an air intake system, CFD simulations are used to provide a better understanding of the fluid flow (droplet coalescence, re-entry, accumulation, instability) and to provide fundamental insights to develop and improve separation techniques, such as inclined louvres, baffle plates, drop-out zones, drainage channels and others.

Chapter 2 describes the function of an air intake system (AIS). The main purpose of the AIS is to guide the incoming air to the cylinders in which the air will take part in the combustion process. The second purpose of the AIS is to clean the incoming air from contaminants such as dust, leaves, snow, water etc. An additional function of the filter is to reduce noise from the engine. Note that this description is a broad and general outline of an air intake system (AIS). In real life the intake system may come in a plethora of different shapes and variations. Vehicles in general and lorries in particular, have an extensive air intake system for both engine-, compressed- and cabin-air (see figure 2.1). These filters are intended to remove fine particles from the inlet air, but suffer from water ingress (rain, spray, wash) in the main filter body. Currently water drainage systems are installed prior to the cellulose or polymer filters, but a better understanding of the drainage process is needed. The installed solutions intend to achieve better water removal, yet their design is based on a trial and error process during the prototype phase. The ultimate objective of this research is the development of a numerical model that would allow for a more accurate design prior the prototype phase. Yet, before using such a numerical model, a validation of the phenomena with experimental values is essential.

Chapter 3 explains the method that was selected for the validation of the water drainage model and the results. To build a proper CFD water separation model, it is required to do validation with experimental values. The experimental method that was selected for this validation exercise is PEPT. Chapter 3 summarizes the principles and background of Positron Emission Particle Tracking (PEPT). The experimental results presented in this thesis were obtained from PEPT runs on a scaled down inlet, safety concerns with the radioactive method that PEPT is, prevented us from using a full scale air inlet that would require substantial higher flow-rates to run, hence increasing the risk of radioactive tracer particles being ejected into the lab environment. To give the reader a sound understanding of the technique, a comprehensive description of PEPTs

development in Birmingham, the location algorithm, particle labelling and recent developments in the camera system are given in chapter 3. The end goal of the PEPT experiments was to establish a confirmed trust into the selected CFD models that will be used in the simulations for years to come. Other methods besides PEPT were considered, such as Laser Doppler velocimetry (LDV), Laser Doppler anemometry (LDA) and Particle Image Velocimetry (PIV). However, the optically-based experimental measurements are constrained to transparent systems resulting in limited practical use for our experiment, after all changing the material from the air inlet under investigation to an opaque material would change its surface properties and this was exactly the property that was under investigation. Positron Emission Particle Tracking (PEPT) is capable to investigate the localized information for opaque systems. Positron emission particle tracking (PEPT) is used to study particle dynamics, granular systems and multiphase flows. PEPT allows a non-invasive 3D spatial detection of a single radioactive particle as it moves through the system under study. Because this study involves the impact of surface energy on the fluid flow, an experimental method was needed that would allow the use of the original intake orifice materials including mostly opaque materials (PA, PP). In PEPT, as there is only one point-like source particle within the field of view, the statistics necessary to provide a precise location are much less than the equivalent required for a volume image. Thus, the time-scale over which data becomes statistically significant is greatly reduced and comparable to typical physical and engineering time-scales. Dynamic systems such as our rainwater drainage can hence be studied using positron imaging techniques. To get a better understanding of the effect of the surface treatment, 4 measurement representing each individual surface condition (default PE, hydrophobic, hydrophilic and stainless steel plate) were selected and overlaid. Measurements showed consistent results for each plate. When we zoom in on the time-frame where the actual motion is occurring we see a distinctive difference between the plates with different surface condition, confirming that the PEPT measurement was able to capture the phenomena we were looking for (influence of surface energy on spatial time distribution of particles). Table 3.4 represents the median values for these parameters. And figure 3.15 plots these differences relative to the position X. Figure 3.16 is the plot that was used for further study. The hydrophilic case showed to be the most unstable during PEPT testing, also in later chapters during simulation it will show high instability during the calculations, in reality this type of surface condition (contact angle = 0 degrees) will never occur in air intake systems, hence the results for the hydrophilic plate are plotted here for reference only and is not considered further in the thesis.

Chapter 4 introduces the reader to the variety of CFD models and solvers that be used to study water drainage in inlet configurations. The principle of CFD technique is analysing the fluid flow phenomena by solving a set of governing equations that describe the fluid dynamics. CFD modelling has significant advances, for example, its ability to provide the comprehensive fundamental conceptions which are experimentally expensive or unobtainable such as the local hydrodynamics, phase distribution, and heat and mass transfer. In addition, CFD has helped with some important design criteria on developing intake system such as low air flow resistance and good distribution of air. The term phase usually refers to the thermodynamic state of matter (Solid, Liquid or Gas) In modelling terms, it can also refer to other characteristics, i.e. liquids of different density, bubbles of different size, solid granules of different size and/or weight. Concerning multiphase flows, the Eulerian-Lagrangian approach (Euler-Lagrange, Lagrangian Multiphase, LMP) where the observer tracks parcels of particles as they move through space and time, simu-

lates the solid phase as a discrete phase and so allows particle tracking, in addition, the physical effects such as the particle-turbulence interaction on the particle motion can be modelled. The Lagrangian phase allows the Navier-Stokes equations are solved for the continuous phase while the equations of motion are solved for representative parcels of the dispersed phase as they pass through the system. This model is well suited for cases where the volume fraction of the dispersed phase is relatively small, and where interaction with solid boundaries is important, i.e. vehicle soiling, spray coating, cyclone separation, erosion, aerosol dispersion, liquid fuel combustion, spray cooling. When those Lagrangian particles that represent our incoming water spray are finally impacting on the inlet geometry there is also a need for multiphase interaction models. Multiple phenomena need to be covered: the particles that impinge on a dry plate initially or after some time when the plate is already wetted that also impinge on wet areas, initially the impinging is limited however after a while large areas of water film will be formed and in some areas even rivulets with some height that can potentially be picked up again by the main air phase shearing past the intake geometry, as result several CFD solution methods where combined to capture this multiphase interaction, Section 4.6 explains this in more detail. The balance that always need to be found in industrial CFD setups is the amount of compute time vs. the result expectation (e.g. when it is faster to build physical prototypes, CFD becomes less relevant although it can still offer insight that experiments cannot).

Chapter 5 handles the CFD modelling of the scaled down inlet bow that was used for the PEPT experiments, this chapter is key to understanding the validation with the PEPT data and the capability of CFD models to capture properly the effects of surface properties on water drainage in air inlet systems. validation was not only performed for the multiphase interaction models, but also for the more common properties under investigation such as velocity and pressure distribution of the main flow field. The CFD model is an approximation of the real application. Also, it is very difficult to apply all the real world conditions in a CFD model. For example, in an actual AIS, the inside walls can be covered in dust, sooth or other contaminants. These materials can act as a restriction to airflow and influence the behaviour of the water ingression. However, in the CFD model, the wall conditions were defined as an adiabatic wall. Meaning, the simulation assumes that the wall surfaces have no effect on the air flow conditions. Likewise, many other assumptions were made in the CFD model. Other examples of assumptions that were not considered in the CFD model, to name a few, were: heat conditions were not accounted for, vibrations were ignored and flow was considered to be in ideal conditions. Analysing the difference between the measured and simulated results for the steady analysis showed less than 1 percent error for the velocity at the outlet. Even though there are differences between the simulated and measured velocities, the measured and simulated velocities exhibit similar patterns. Table 5.5 and 5.6 compares the measured and simulated velocity values for the inlet and outlet. This high level of validation is not uncommon for the steady state part of a simulation providing the airflow generated by the fan is done under lab conditions where it can be regulated to a highly accurate and stable value. For the part of the simulation where we switched on the rainwater analysis, more validation factors became important. First off, the mesh independence study that occurred for the steady analysis, had to be redone for the unsteady simulation. The line probe results of the velocity down the slope, and the fluid film thickness where 2 parameters that were analysed to establish mesh independence. Secondly the convective courant number was monitored to correctly select the timestep for this

problem. When the timestep would be too large, the simulation could 'skip' cells when moving down the slope. To conclude, overall the CFD model showed good validation with the measured data in regard to the velocity, pressure and flowrate. Water behaviour proved to be more challenging and there good validation is shown for the settings with large contact angle, but validation diminishes when contact angle reduces to zero. However, there is not a conventional ratio that differentiates between a good model and bad model. Also, the mesh setting plays an important role in the model calculations. For an example, the CFD model can solve the simulation within 5 hours or it can solve it within 48 or more hours. However, between the 5 hour solver and 48 hour solver, the pressure loss was significantly lower. The CFD model was always ran with the optimal mesh setting, meaning that values did not change any-more when refining the mesh, while solve time was reduced to a minimum. Outside of this thesis, the choice should be made by the person running the simulations, for early prototype stage analysis it could be beneficial to run the simulation with lower mesh quality in order to get faster results to already get a first understanding of the problem at hand. Like that multiple design iterations can be made relatively quick and expensive computational time can be saved. Fully detailed analysis can then be done on later models or right before rapid prototyping to validate the setup.

Chapter 6 takes the confirmed CFD models from Chapter 5 and then applies these to the full scale air intake system (as explained in chapter 3, full scale was not possible due to PEPT radioactive concerns at such high airflows). First a small introduction is given on the challenges of handling such large intake models in a CFD environment and how to properly prepare the domain for rainwater analysis. Also the setup of the incoming water is now changed vs. Chapter 5, no longer is the water coming from an experimental setup that uses an injection nozzle. It is now rain falling from the sky, as would be seen during the normal operation of a commercial vehicle. To realistically simulate rainwater, properties such as terminal velocity, droplet diameter and incoming angle were derived and used as input in the CFD model. Two methods for water drainage simulation was explained in more detail. Method 1 is the classical method that had been used for many years to obtain fast result, it uses a steady state approach where the impinging water is handled by a coefficient of restitution however as shown this methods depends heavily on the correctness of this coefficient of restitution. Since this coefficient changes for each surface from the moment any change is made to the topology, material or other boundary condition of the air intake system, this method requires significant experimental tests to be repeated before it is trustworthy. Method 2 is the method that was proven in chapter 5 through the PEPT validation. The advantage of this method 2 is that it includes the contact angle as a parameter in the CFD setup, hence no longer requiring to do experimental measurements each time this property changes. Section 6.5 discusses this method in detail and results are repeated for 2 setups: one with a low contact angle and one with a high contact angle. When reviewing those results they confirm the conclusions from Chapter 3 and 4 on the effect of the contact angle. The main disadvantage of this method is that due to the large number of CFD models that are involved in combination with the fine mesh setting that are required to capture accurately the rain water drainage on the louvres, it does require significant compute resources and computation time. Based on those same settings, additional studies were done to further examine the validity of this specific air intake geometry. The effect of pressure washing on the intake showed some interesting results, however it should be noted that pressure washing in reality depends heavily on the end-user and his understanding of

the user instruction (don't point water jet directly at intake orifice). Also the effect of reducing the main airflow was examined, as in reality a lorry is not always driving at max load of the engine.

End conclusion is that with the spatial time data and the derived velocity data of the PEPT experiments we were able to validate our CFD models and come to a setup that is capable of modelling the water behaviour in an air intake system, taking into account the effect of the material choice on the surface properties. This provides trust in our modelling capabilities and as result can lead to less costly and time consuming physical prototypes that need to be built during the development of such air intake systems.

# Appendix A

## PEPT test setup

The PEPT facility at the university of Birmingham uses scanners that were previously used at medical facilities, these are then adapted to suit the test facility (figure A.1 to A.5). For the experiment that is using radioactive tracers, safety precautions needed to be taken. One of these was to use a setup with limited flow-rate to avoid radioactive tracers that would escape the final filter and get dispersed around the test facility, because the full scale inlet model requires substantially higher flow-rates to represent realistic scenarios it was decided to create a scaled down inlet box. Furthermore this box also allowed easy changing of the surface parameters by sliding in plastic plates with different surface properties (obtained through plasma treatment). The box is made from stainless steel 1,5 mm and the inlet orifice and other important dimensional parameters are scaled down in such a way that they respects the ratios of a typical air intake inlet. The upstanding louvre consists of a steel backing plate with a plastic insert (red part in figure A.7) on top of it. This plastic insert can easily be replaced and allows for rapid changing of surface properties. Four types of surface properties were considered for the test: the base steel plate, a default PE insert, a hydrophobic treated PE plate and a hydrophilic treated PE plate. PEPT data is put through several steps to obtain useful data for the validation study. Step 1 is the raw data measured at the detector plates of the PEPT installation, Step 2 converts these values in particle locations in 3D space (see table A.2), step 3 is the filtering of these location data (removing error runs, duplicates, etcetera), step 4 is converting this location data into velocity data using the 6 point method describes in the PEPT chapter.

Table A.1: For reference a tracer was held in the 4 extremities of the baseplate, these are the coordinates

baseplate	x	y	z
top left corner	210	290	135
top right corner	210	290	240
bottom left	320	190	135
bottom right	320	190	240



Figure A.1: PEPT test equipment used for the scaled down experiment

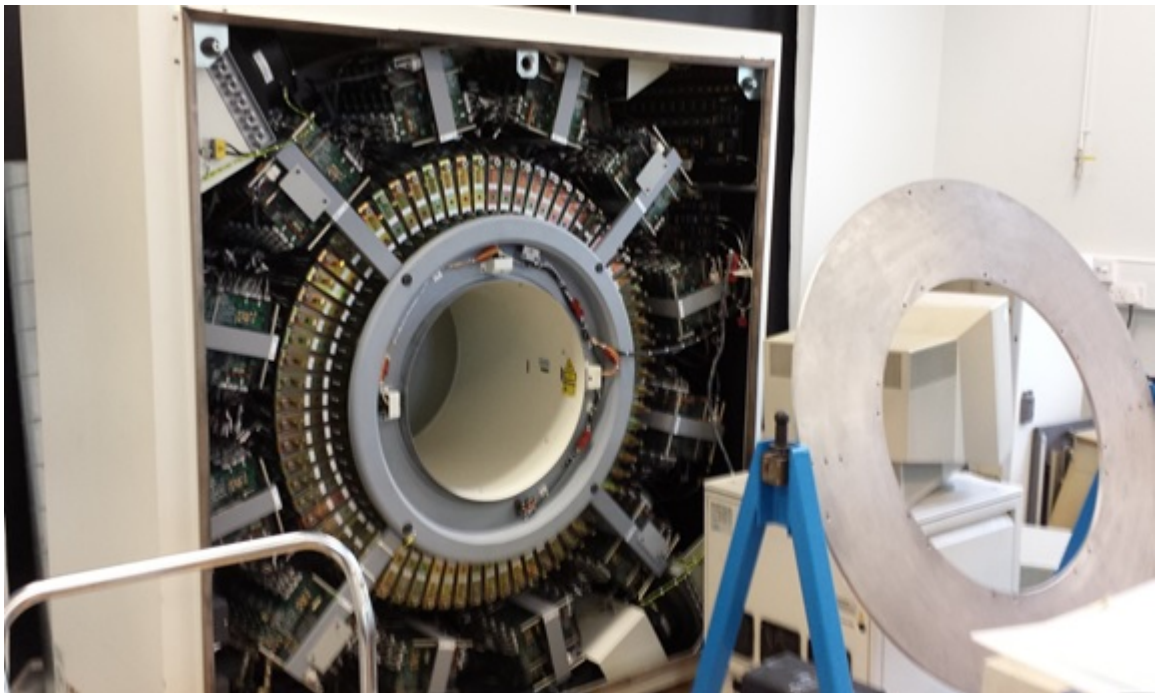


Figure A.2: Cover removed





Figure A.3: Inlet box is placed in between the 2 main detector plates (cameras)



Figure A.4: Lateral view from the test rig

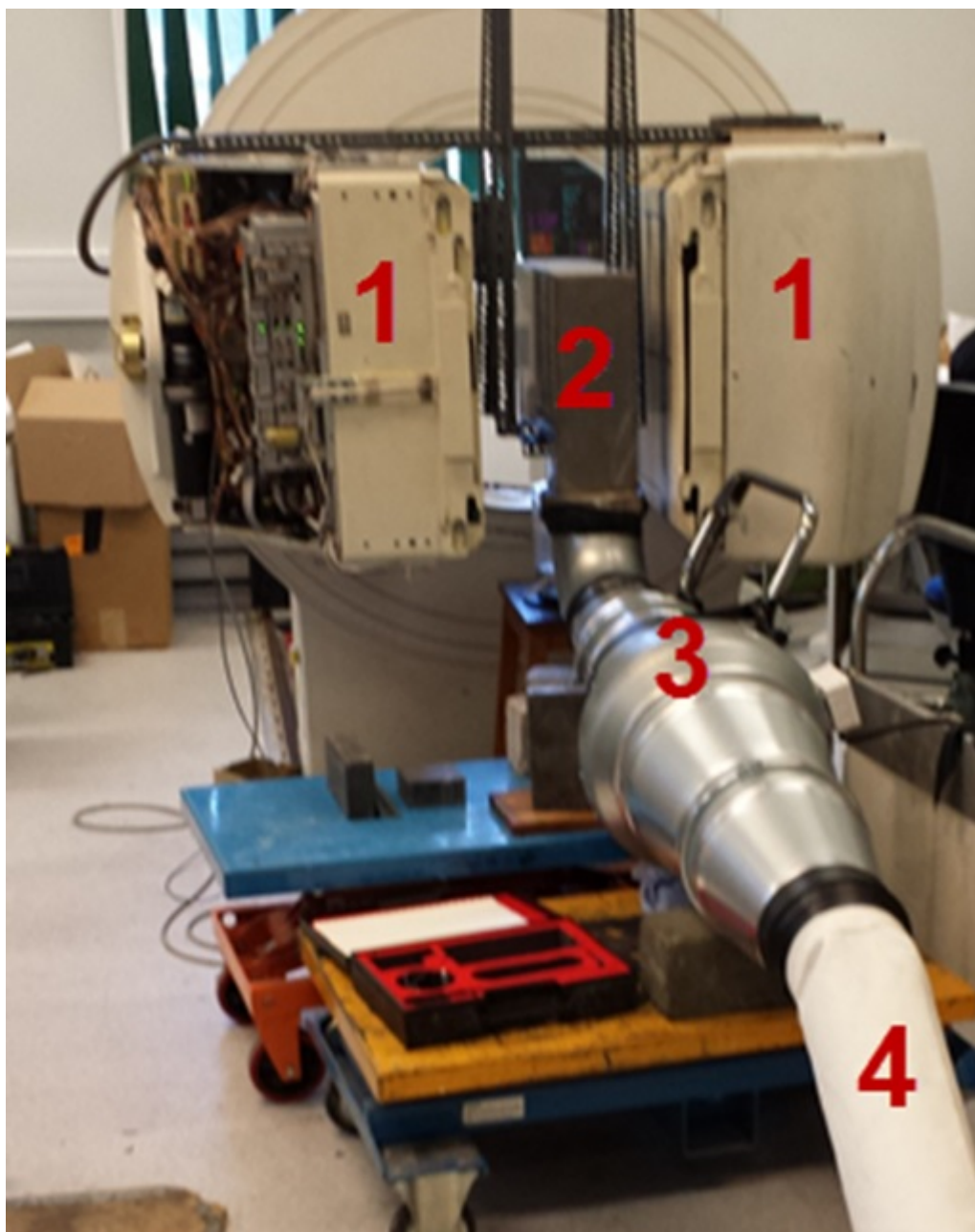
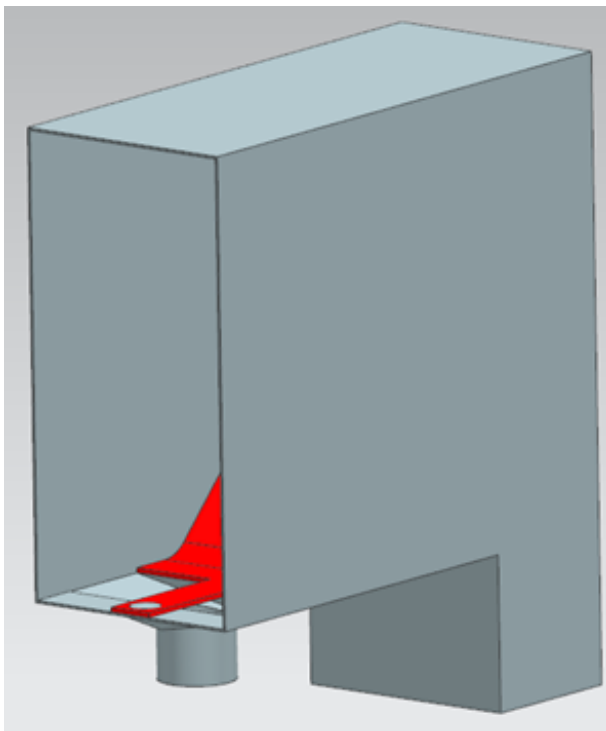


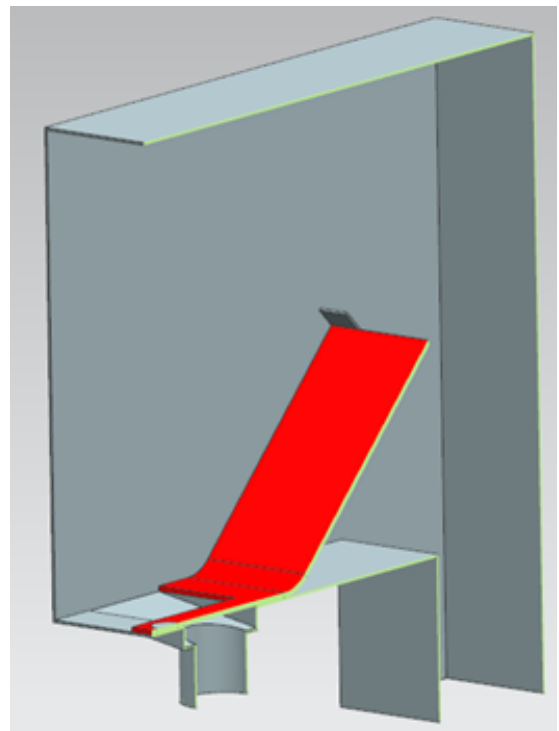
Figure A.5: 1.cameras - 2.inlet box with inclined louver - 3.fan to generate intake air flow - 4.filter bag to trap tracer particle if escaped from 2



Figure A.6: AirPro measuring probe to measure airflow in outlet duct



(a) side view



(b) section view

Figure A.7: Scaled down inlet box CAD model - red plate is interchangeable and is placed on the slope, this mimics the louvre action from the full scale model. Making it interchangeable allows for plates with a variety of surface conditions to be tested.

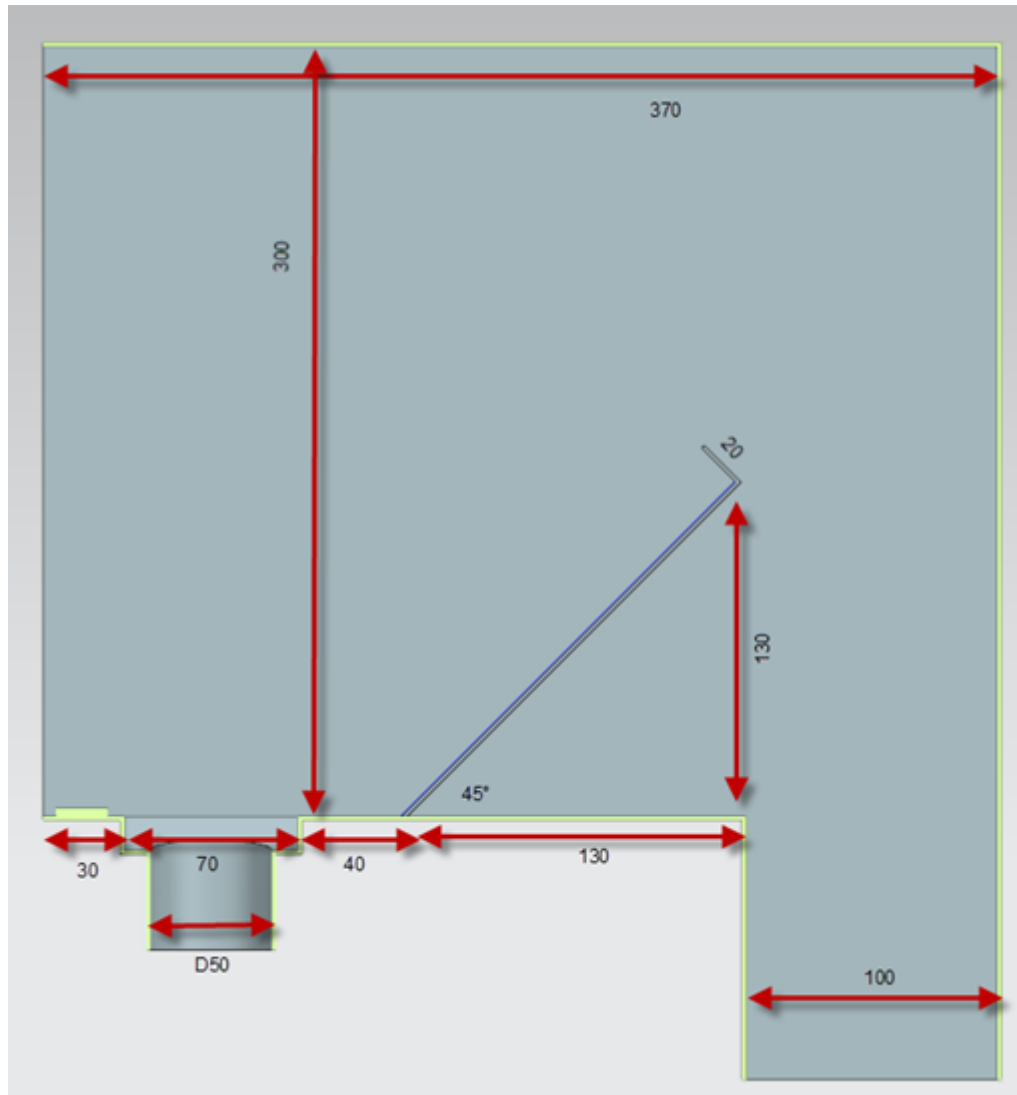


Figure A.8: Overall dimensions of scaled down inlet box

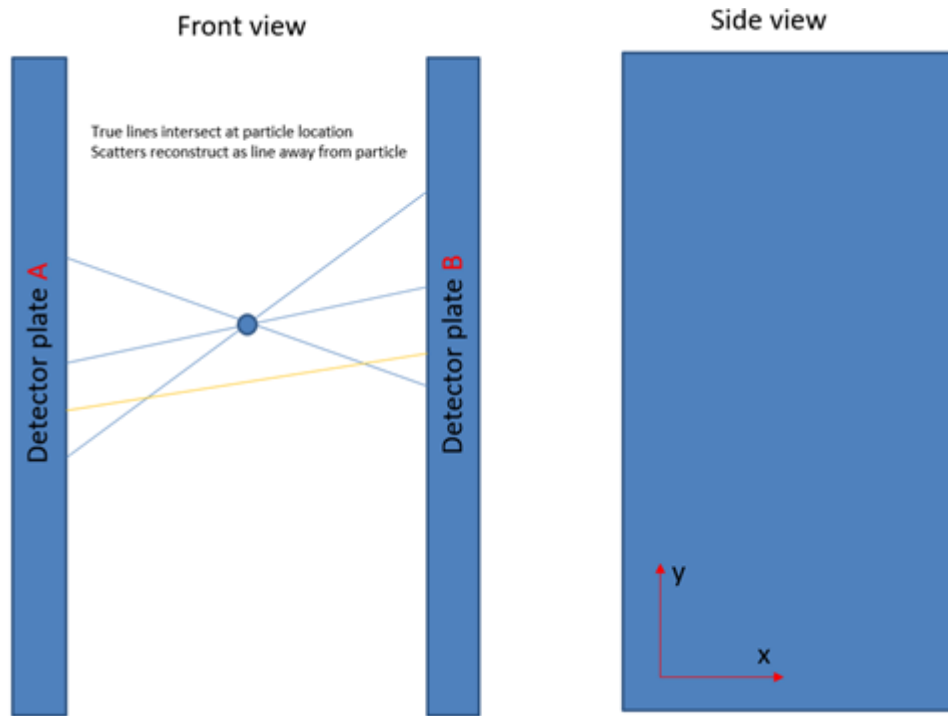


Figure A.9: Raw data [time,Ax,Ay,Bx,By] is measured at detector plates

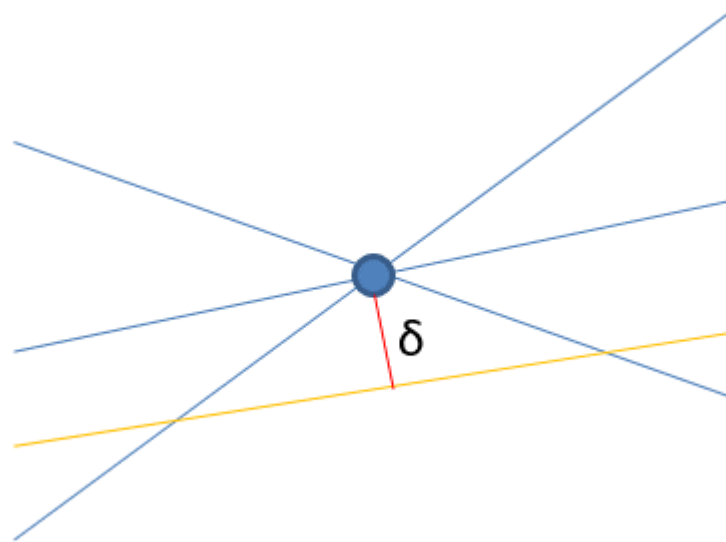


Figure A.10: True lines intersect at particle location, scatter reconstructs as line away from particle. PEPT algorithm detects 'noise' from scatter and attenuates it

time	x	y	z	delta	0	0	Nused
ms	mm	mm	mm	mm			
50.7	215.3	285.8	183.1	1.1	0.0	0.00	11
68.6	214.2	285.0	182.7	0.8	0.0	0.00	11
86.3	212.4	284.9	181.7	1.0	0.0	0.00	11
105.9	212.4	285.8	179.5	0.8	0.0	0.00	11
127.9	212.7	287.4	183.0	0.8	0.0	0.00	11
146.3	214.7	286.4	179.6	0.8	0.0	0.00	11
165.0	214.4	286.2	180.6	0.8	0.0	0.00	11
183.9	213.1	286.0	179.7	0.8	0.0	0.00	11
202.1	213.4	285.9	181.1	0.8	0.0	0.00	11
222.1	214.1	286.7	180.4	0.8	0.0	0.00	11
239.9	213.7	287.4	182.4	1.0	0.0	0.00	11
255.1	214.4	285.8	182.0	0.7	0.0	0.00	11
275.8	213.9	288.4	179.6	0.7	0.0	0.00	11
299.9	214.1	284.7	179.7	1.0	0.0	0.00	11
319.4	214.3	286.5	179.7	0.7	0.0	0.00	11
337.1	213.5	285.4	183.0	0.7	0.0	0.00	11
355.8	214.3	285.5	182.9	0.8	0.0	0.00	11
379.9	213.8	286.3	178.9	0.8	0.0	0.00	11
397.9	214.3	286.1	182.0	0.7	0.0	0.00	11
422.3	212.6	286.3	181.3	1.0	0.0	0.00	11
444.1	214.6	284.9	185.4	1.1	0.0	0.00	11
459.4	214.3	286.1	180.1	0.8	0.0	0.00	11
484.4	213.9	286.2	179.1	1.2	0.0	0.00	11

Table A.2: Raw data at the detector plates is converted to location data: typically this consist of more than 50,000 lines, only a small selection is shown in table as example - Delta reports the average deviation of the photon trajectories from the location point, it tells about the quality of the location, lower values are preferred. The two 0 columns are unused. The final column Nused tells how many final photon trajectories have been used for the location (approx.  $F \cdot N$ )



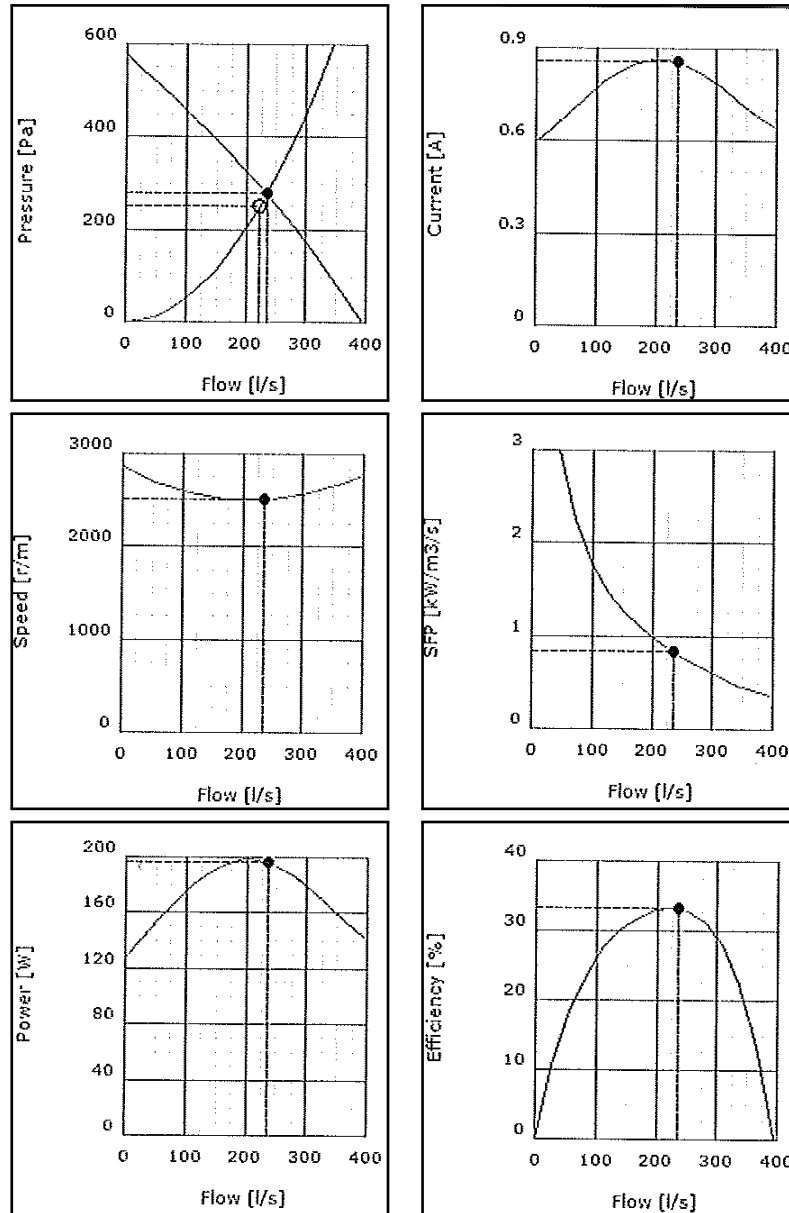
## Appendix B

### Fanset properties

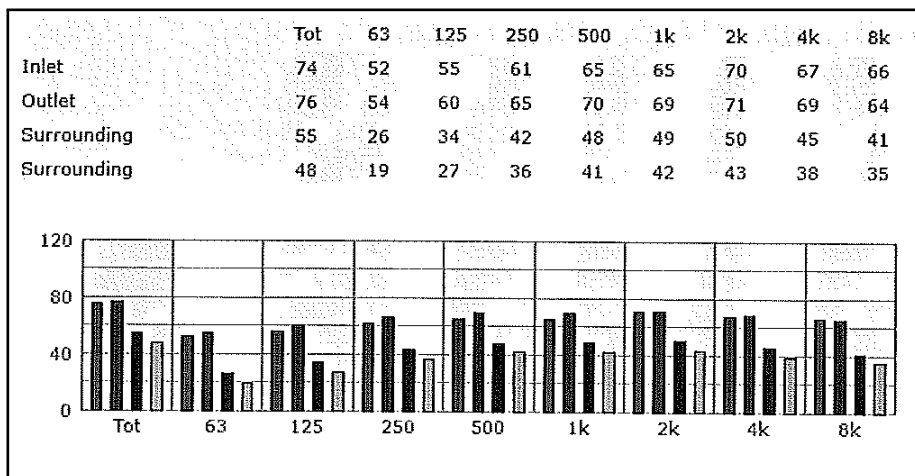
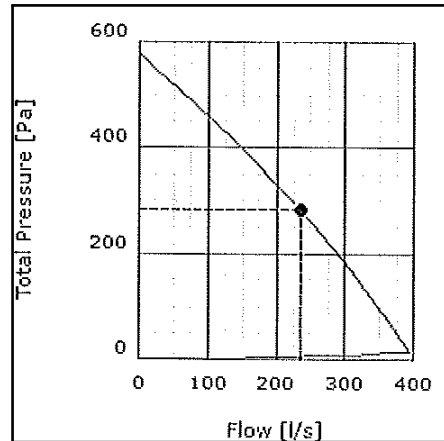
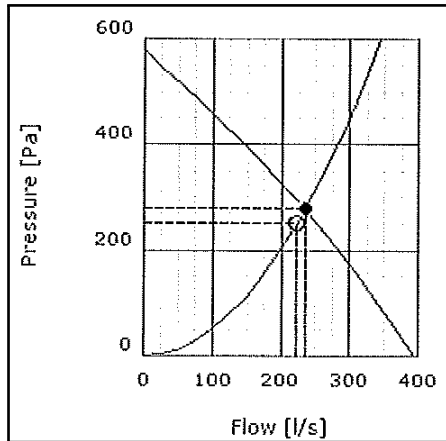
The CK is an in-line centrifugal duct fan with high capacity and excellent reliability. The straight through radial fan is compact and very easy to install. It can cope with high pressure and long duct runs, whilst still operating at acceptable sound levels. The CK range of fans have casings manufactured from galvanized steel and are moisture resistant. They are approved for installation in humid or damp environments being rated IP44 when installed in a duct system. The fan speed can be controlled by voltage variation regulators. Several fans can be connected to the same controller providing the total rating of the controller is not exceeded. The motors are an external rotor type asynchrony motor. They have maintenance free sealed ball bearings and are protected from overheating by thermo-contacts. The fans must not be used for transporting grinding dust, soot or similar.

Parameter	Value	Unit
Voltage	230	V
Phase	1	
Frequency	50	Hz
Power	190	W
Current	0.84	A
R.p.m	2465	r/m
Max. temperature of transported air	50	°C
Max. temperature of transported air when speed-controlled	50	°C
Sound pressure level at 3m	47	dB(A)
Length	255	mm
Width	402	mm
Height	402	mm
Weight	6.1	kg
Enclosure class, motor	44	IP
Insulation class, motor	F	
Capacitor	5	$\mu$ F





Our intake orifice measures 300 x 150 mm and we want to achieve an average speed of 5 m/s at the inlet, as result we need an airflow-rate of 225 l/s, this fan with its working point around 222 l/s is therefore the perfect match for this test setup.

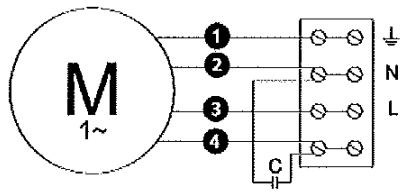


### Parameter

Distance	3.000
Propagation type	Hemi-spherical
Equivalent absorption	20.00
Flow	235l/s
Static pressure	278Pa
Power	196W
Speed	2506r/m
Current	0.86A
Voltage	230V
Efficiency	33.237%
SPF	0.84W/m3/s
Flow	222l/s
Static pressure	250Pa

## Wiring Diagram

4040001



- Ⓜ = Fan Motor
- Ⓜ1 = Fan Motor
- Ⓜ2 = Fan Motor
- Ⓜ3 = Rotor Motor
- ① = Yellow/Green
- ② = Black
- ③ = Blue
- ④ = Brown
- ⑤ = White (TW)
- ⑥ = Orange
- ⑦ = Grey
- ⑧ = Red
- ⑨ = Green

## Appendix C

### CFD - Mesh Settings

The goal of a mesh independence study is to refine the mesh up until the point where variables of interest stay stable (in this case for minimum 20 iterations between an asymptotic value of min/max 0,5% of the nominal value), yet further refining the mesh would lead to excessive calculations times. The outcome is then a mesh that is optimized for the problem under investigation. Below are some of the runs that were done to optimize the mesh. A first run was done with coarse settings, a second run introduced some local mesh refinements, and the 3rd and final run achieved the optimal mesh settings by further reducing the overall mesh base size. Refining beyond this optimal setting was done to confirm the mesh independence, but the mesh used for simulation was the one with the optimal setting. Cell independence study for the unsteady case: the velocity magnitude of the fluid film on the inclined slope was reported on probe lines, the average of 1 probe line was reported while refining the mesh around the slope. Other simulation settings were not changed and were not related to 1 specific case under examination, just in the same magnitude.

Table C.1: Mesh settings for the 1st mesh independence run - resulting mesh was too coarse

Mesh Global settings - Coarse Values	
Mesh Models	Extruder
	Prism Layer Mesher
	Polyhedral Mesher
	Surface Remesher
Base size	15mm
Number of prism layers	3
prism layer stretching	1.5
prism layer thickness	33.3% relative to base
surface size - relative min	25
Local mesh settings - Box around inclined slope face	
custom surface size min	na
custom surface size max	na
nr of prism layer	na
prism layer stretching	na
prism layer thickness	na

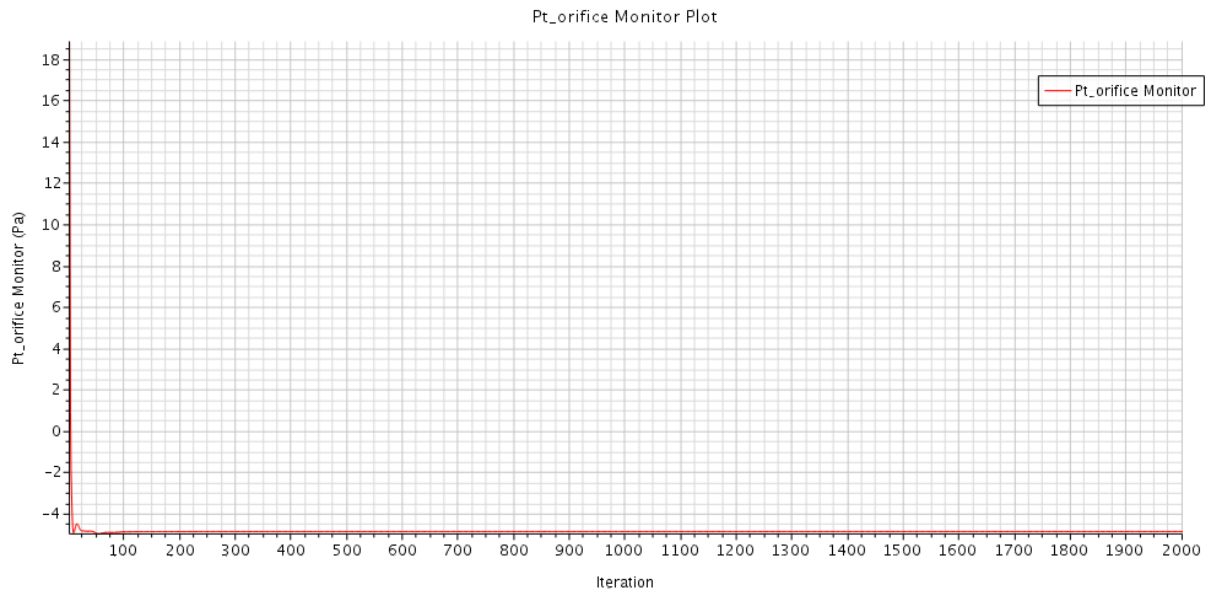


Figure C.1: Total pressure at inlet orifice -4,8647 Pa fluctuating between +0,5 and 0,5 Pa

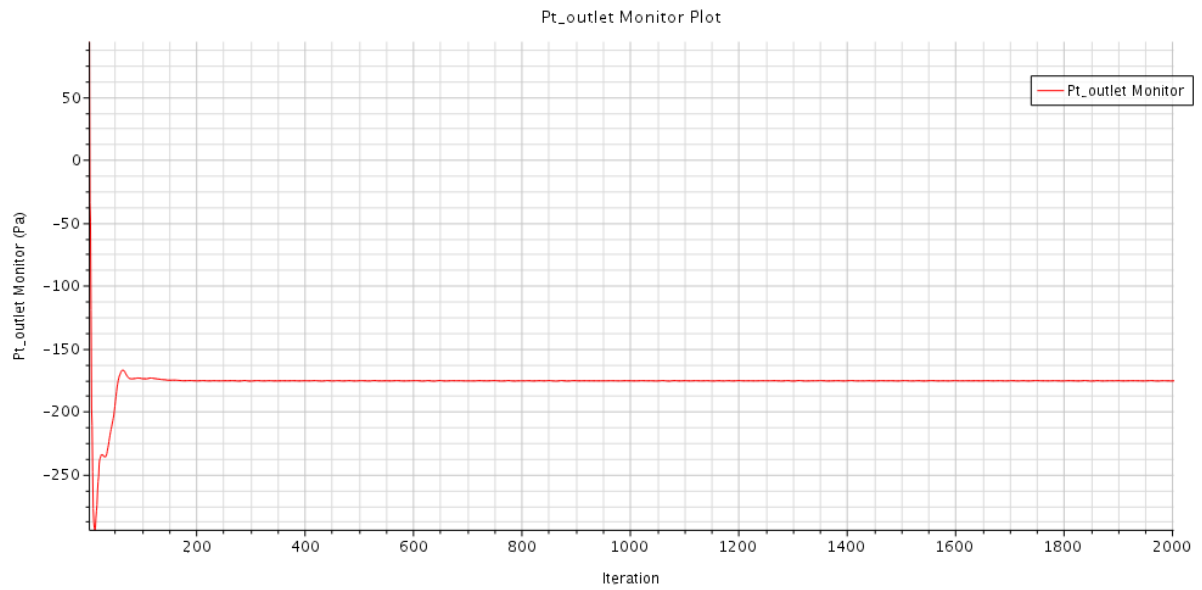


Figure C.2: Total pressure at outlet orifice -175,5 Pa fluctuating between +0,5 and 0,5 Pa



Figure C.3: Velocity magnitude at inlet orifice 6,21 m/s fluctuating between -0,1 and -0,1 m/s

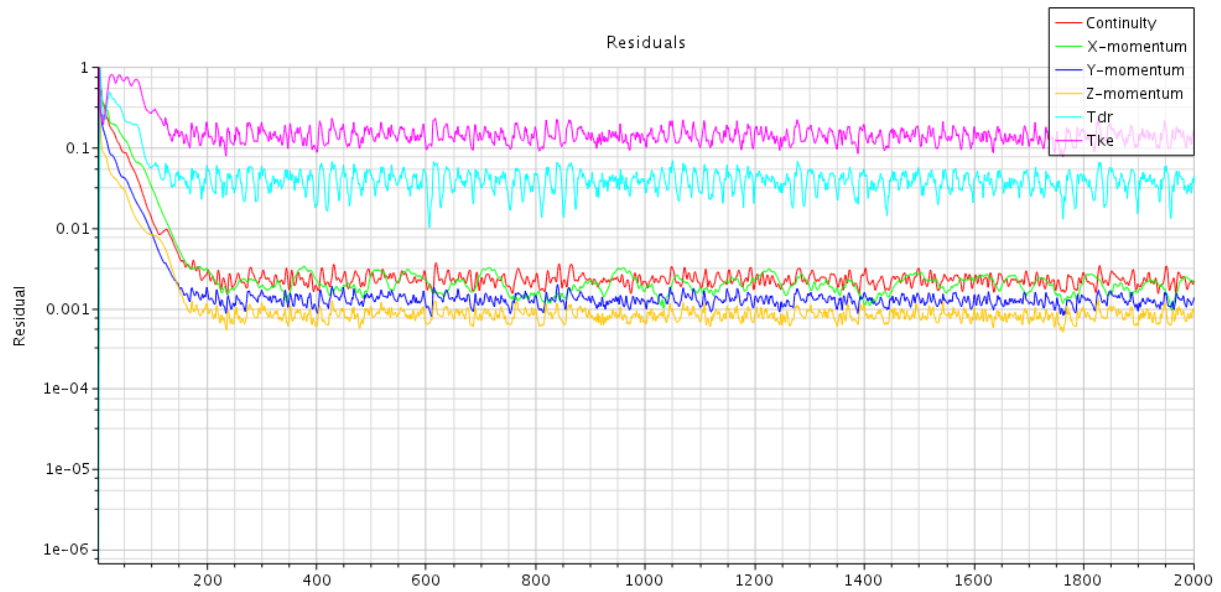


Figure C.4: Residuals show high fluctuations, this combined with other variables fluctuations show that this mesh settings are too coarse

Table C.2: Mesh settings for the 2nd mesh independence run - resulting mesh was acceptable for parameters under investigation but residuals were still fluctuating too much

Mesh Global settings - Medium Values	
Mesh Models	Extruder
	Prism Layer Mesher
	Polyhedral Mesher
	Surface Remesher
Base size	10mm
Number of prism layers	3
prism layer stretching	1.5
prism layer thickness	33.3% relative to base
surface size - relative min	25
Local mesh settings - Box around inclined face	
custom surface size min	na
custom surface size max	na
nr of prism layer	na
prism layer stretching	na
prism layer thickness	na

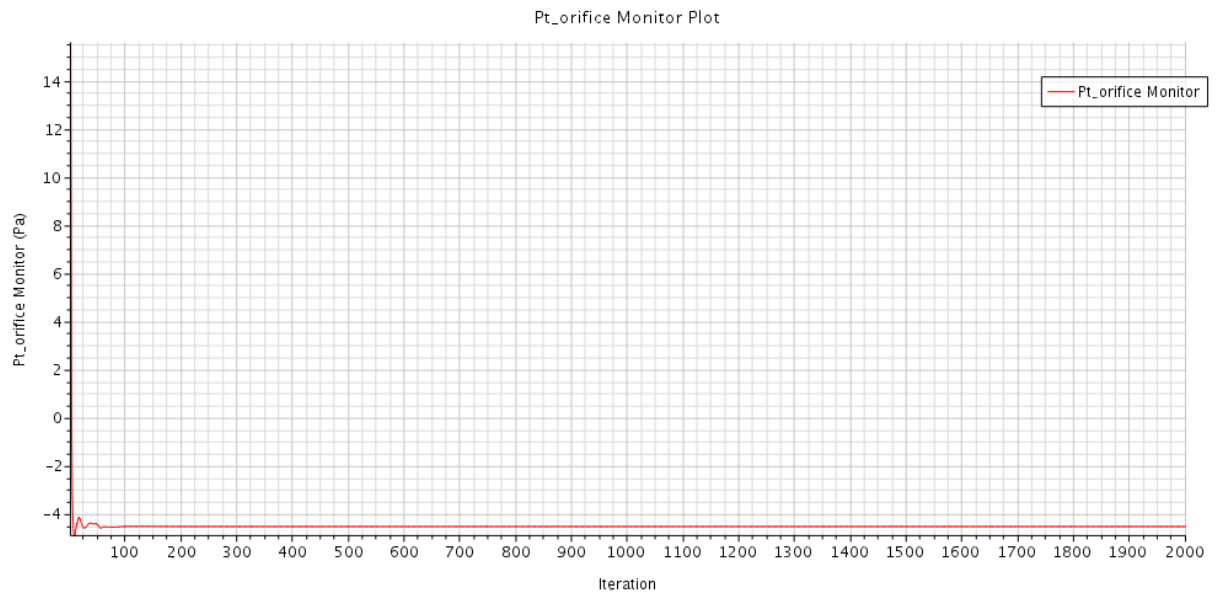


Figure C.5: Total pressure at inlet orifice -4.5 Pa fluctuating between +0.2 and -0.2 Pa

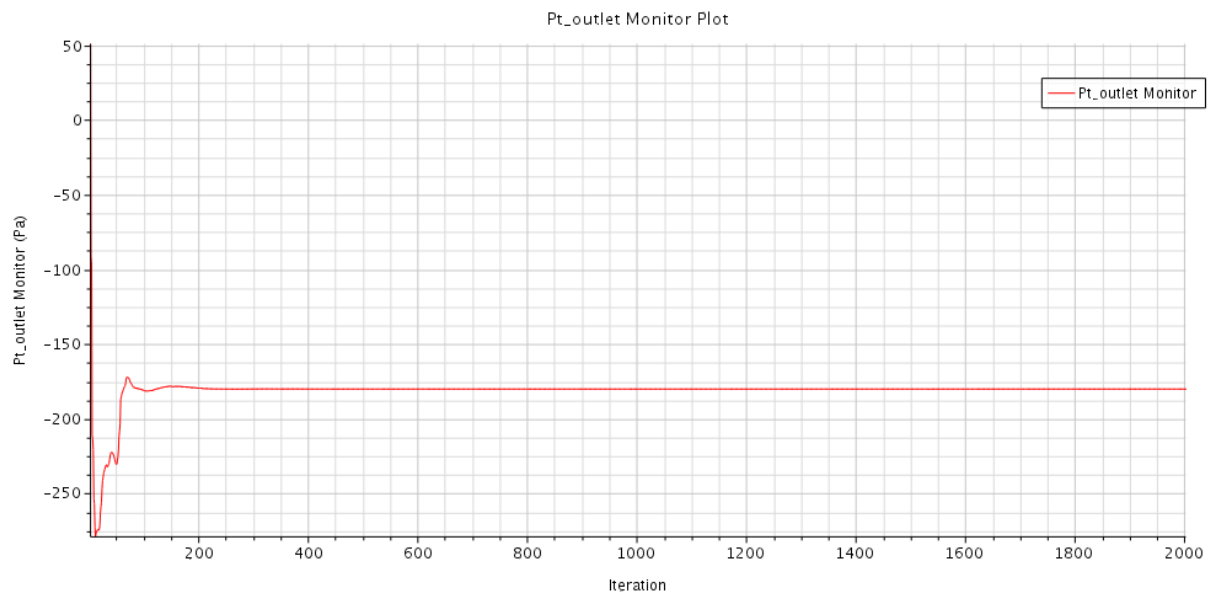


Figure C.6: Total pressure at outlet orifice -210 Pa fluctuating between +0.2 and -0.2 Pa



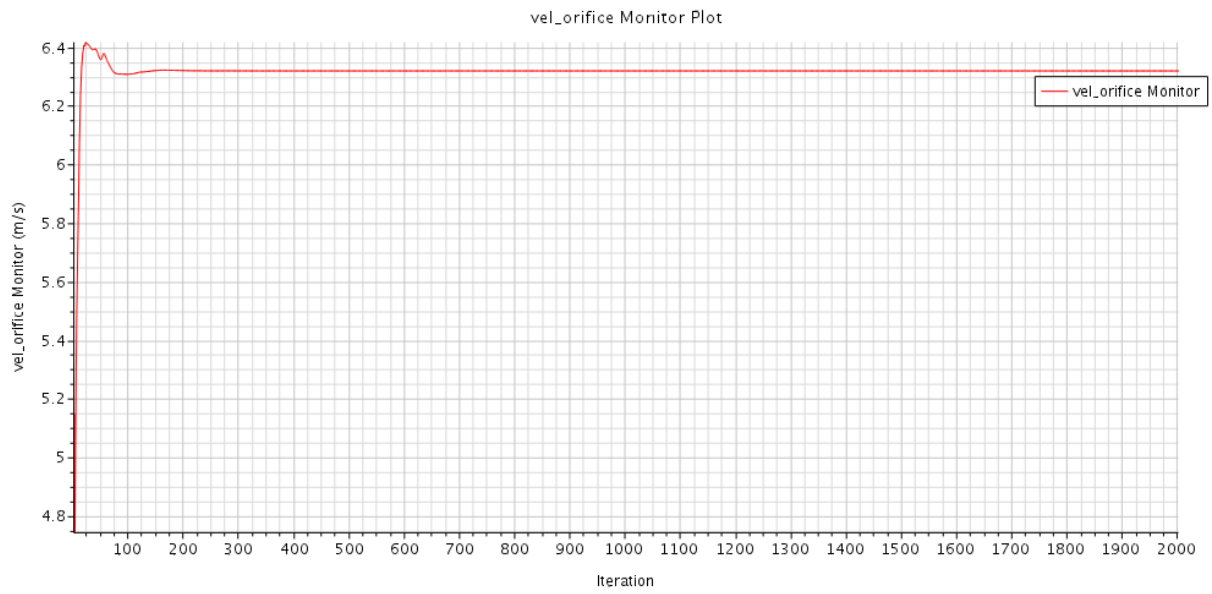


Figure C.7: Velocity magnitude at inlet orifice 6.3 m/s fluctuating between -0.05 and -0.05 m/s

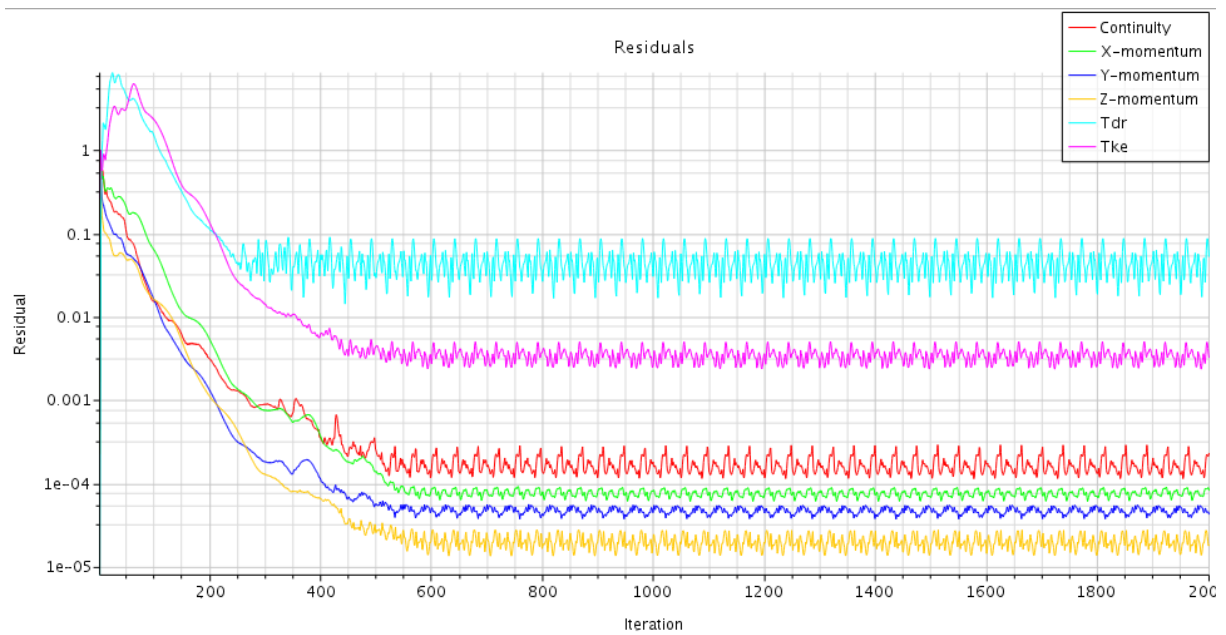


Figure C.8: Residuals still show high fluctuations, the other variables are of acceptable level

Table C.3: Mesh settings for the optimal mesh - resulting mesh was acceptable for parameters under investigation and also for residuals - With these settings all variables no longer show stable values and computational time is still within limits

Mesh Global settings - Fine mesh settings	
Mesh Models	Extruder
	Prism Layer Mesher
	Polyhedral Mesher
	Surface Remesher
Base size	5mm
Number of prism layers	3
prism layer stretching	1.5
prism layer thickness	33.3% relative to base
surface size - relative min	10
Local mesh settings - Box around inclined face	
custom surface size min	5% relative to base
custom surface size max	100% relative to base
nr of prism layer	5
prism layer stretching	1.5
prism layer thickness	25% relative to base

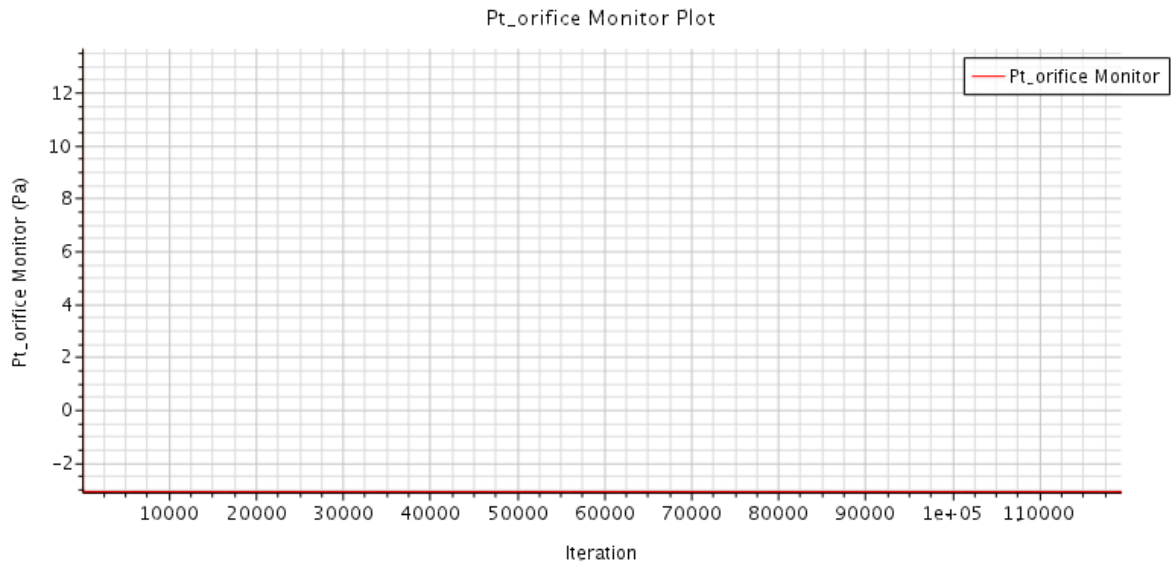


Figure C.9: Total pressure at inlet orifice -3.12 Pa fluctuating between +0.05 and 0.05 Pa

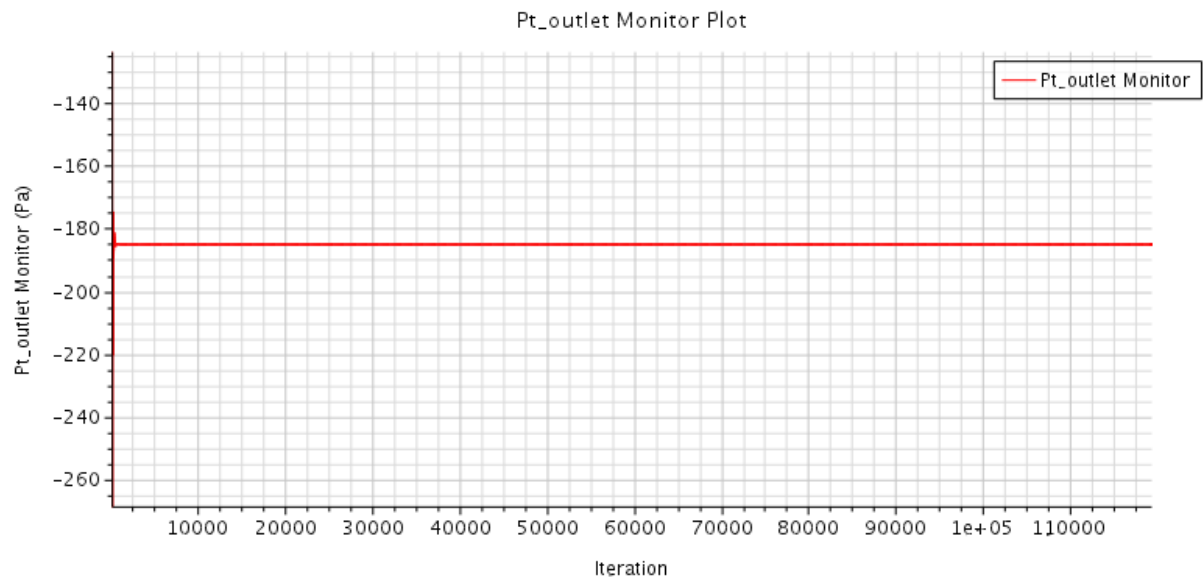


Figure C.10: Total pressure at outlet orifice -185 Pa fluctuating between +0.05 and -0.05 Pa

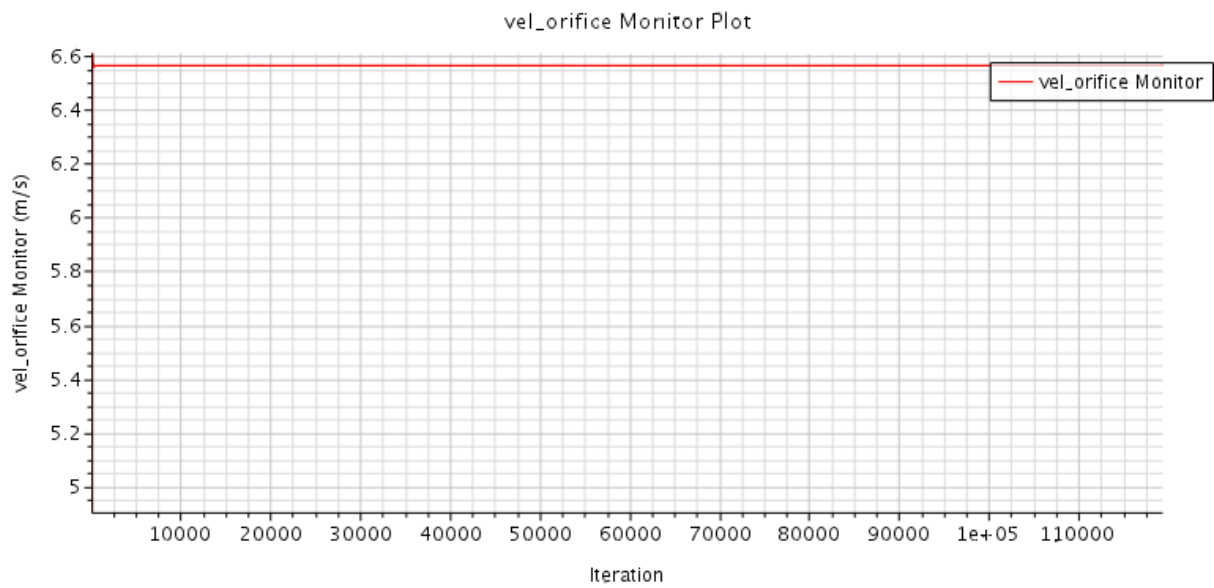


Figure C.11: Velocity magnitude at inlet orifice 6.56 m/s fluctuating between -0.02 and -0.02 m/s

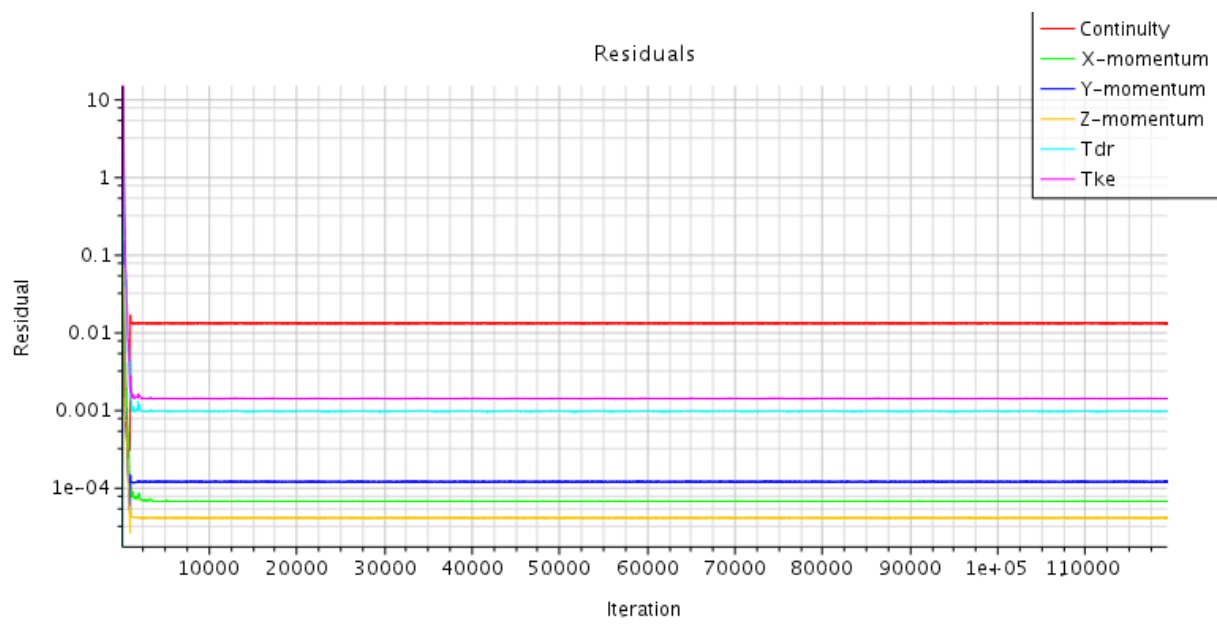
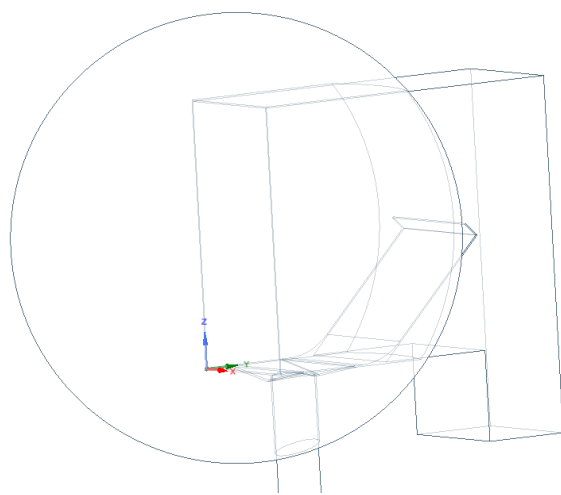
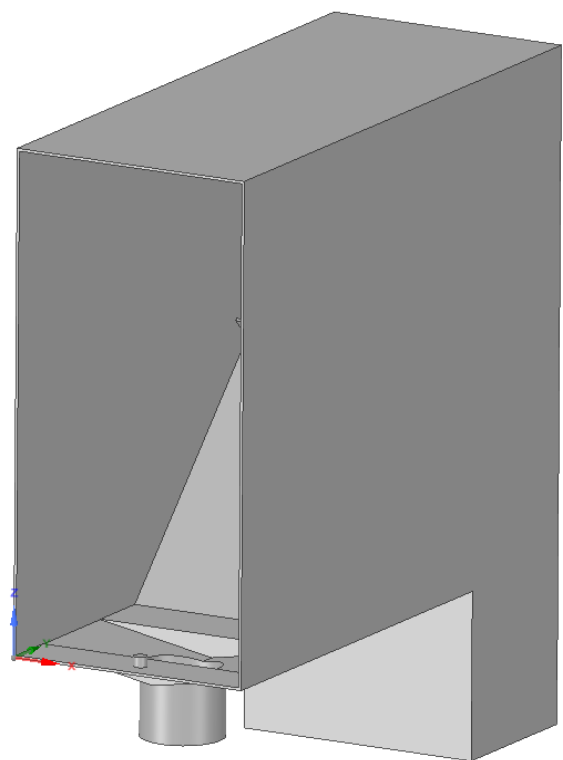


Figure C.12: Residuals no longer show high fluctuations



(a) CAD model with atmosphere included



(b) CAD model before CFD prep

Figure C.13: CAD model before meshing

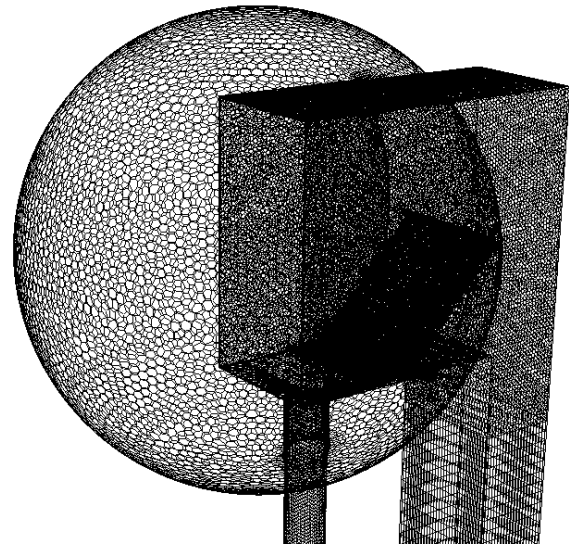
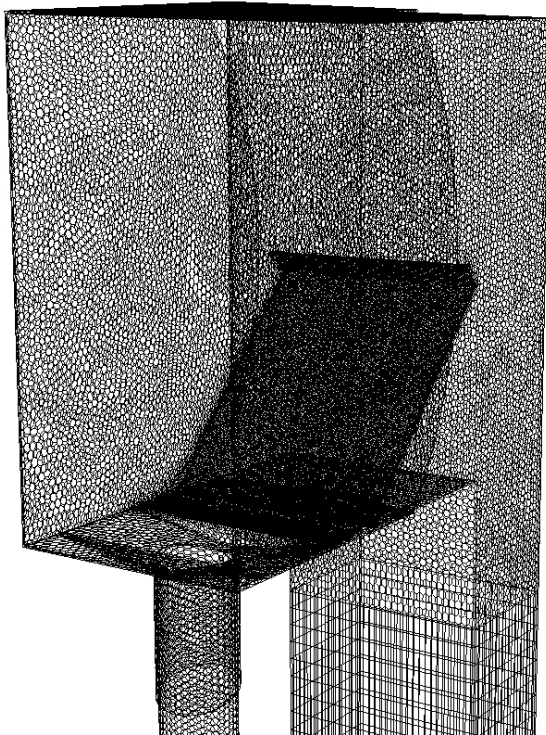
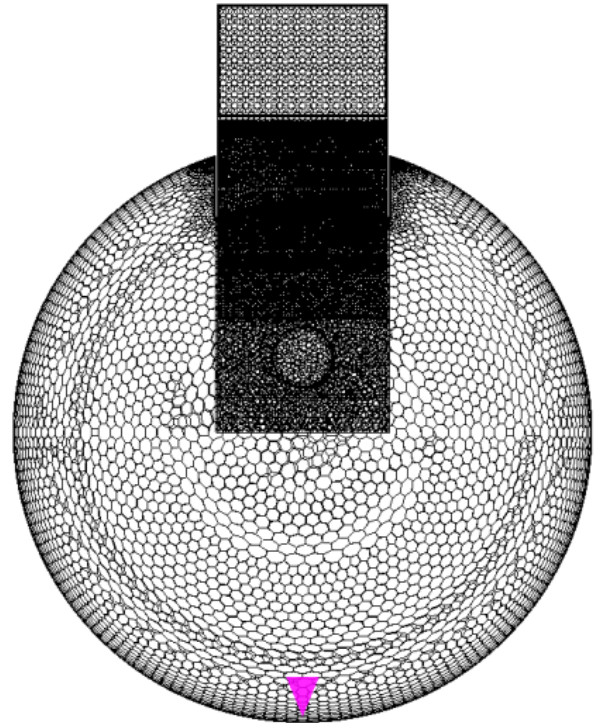
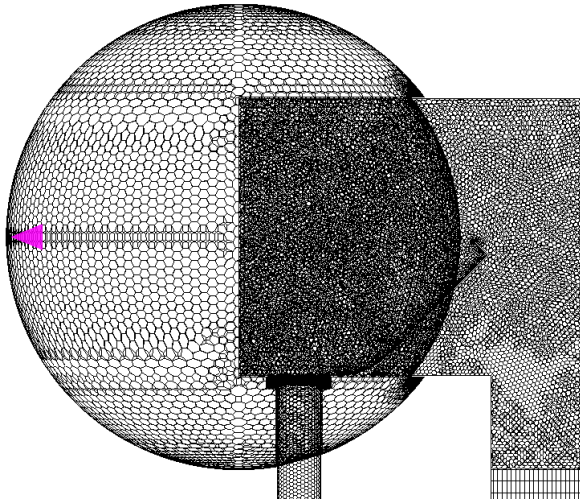


Figure C.14: Meshed CFD models (pink is the injector nozzle for the water spray)



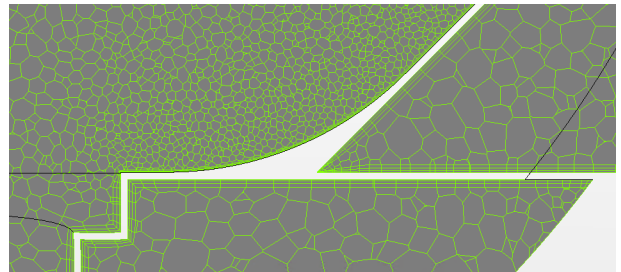
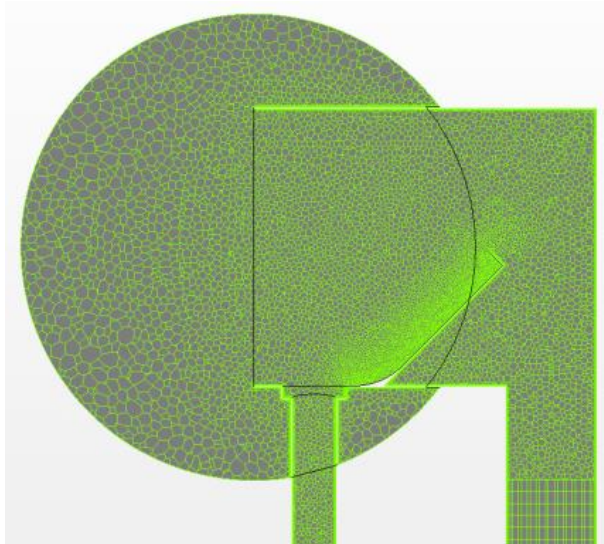
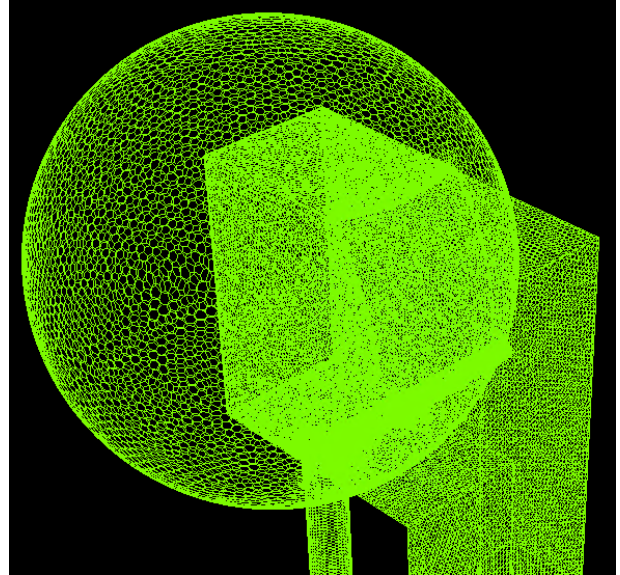
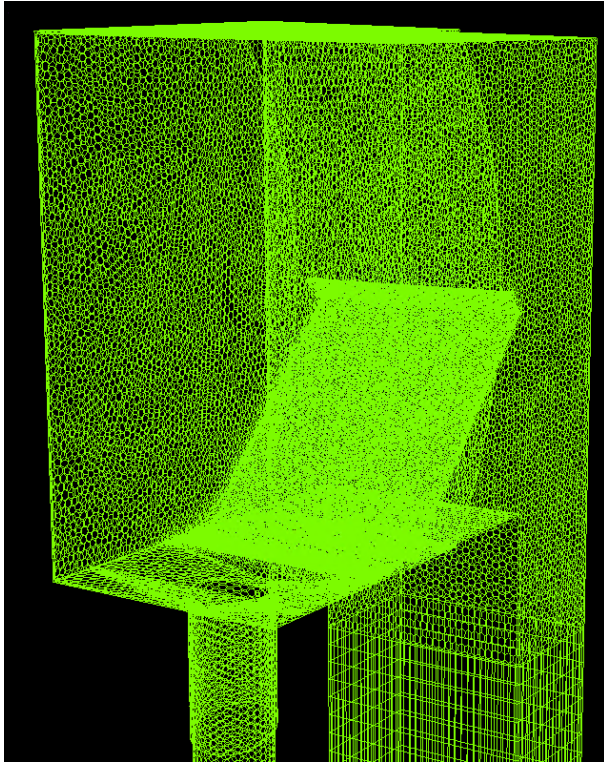


Figure C.15: Meshed CFD models - additional detail

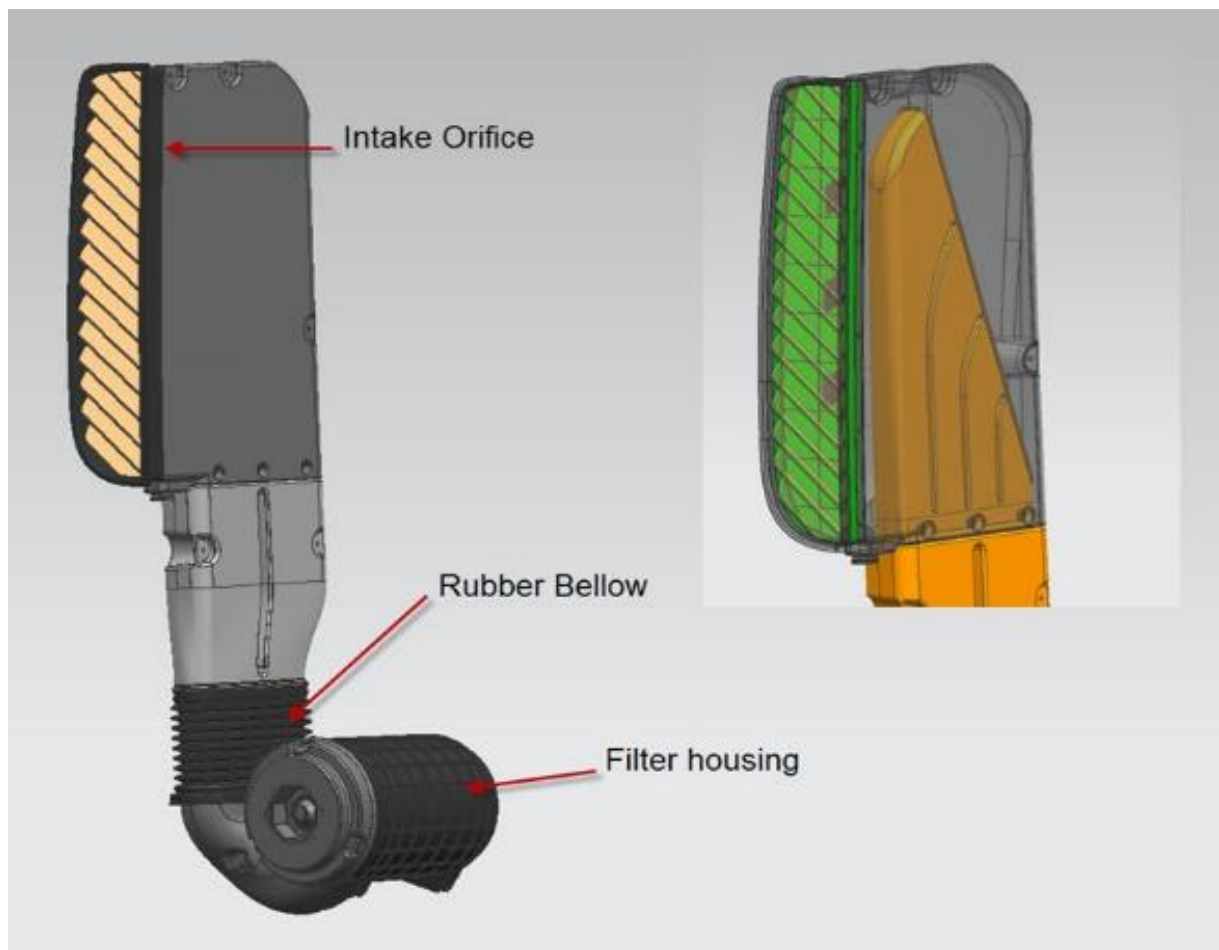


Figure C.16: Full scale inlet - CAD model

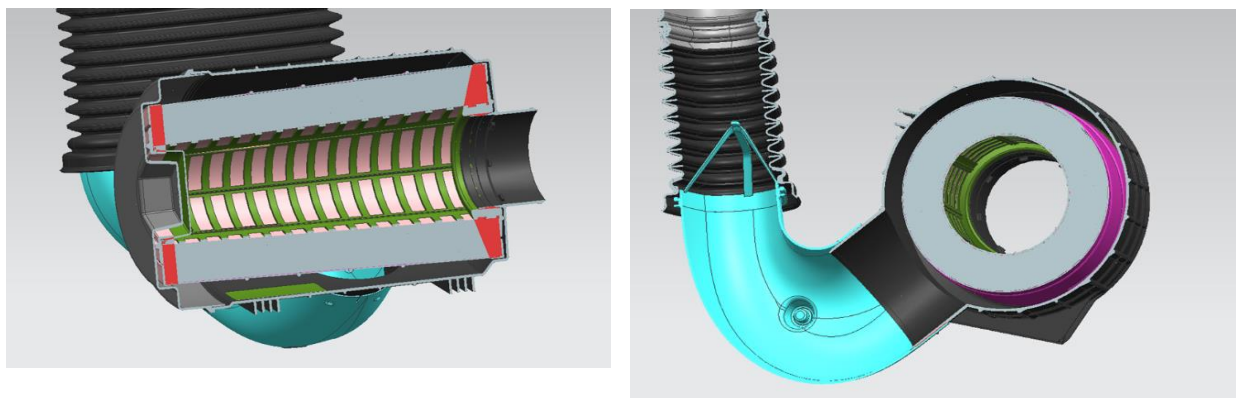


Figure C.17: Full scale inlet - CAD details

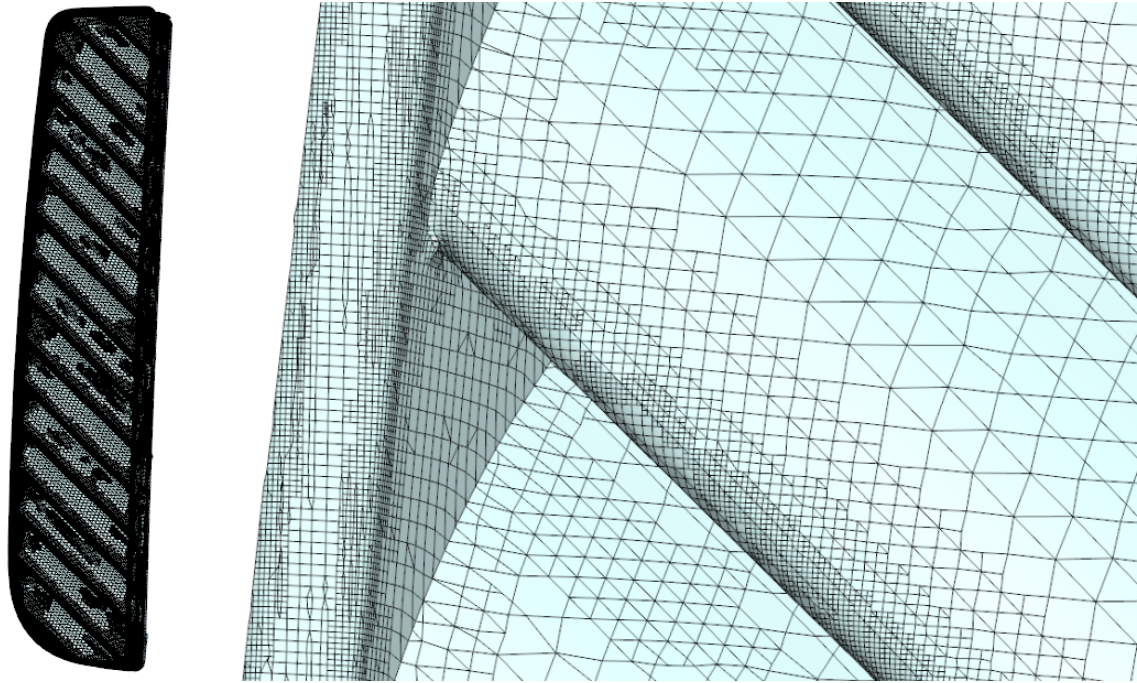


Figure C.18: Mesh Detail around louvres

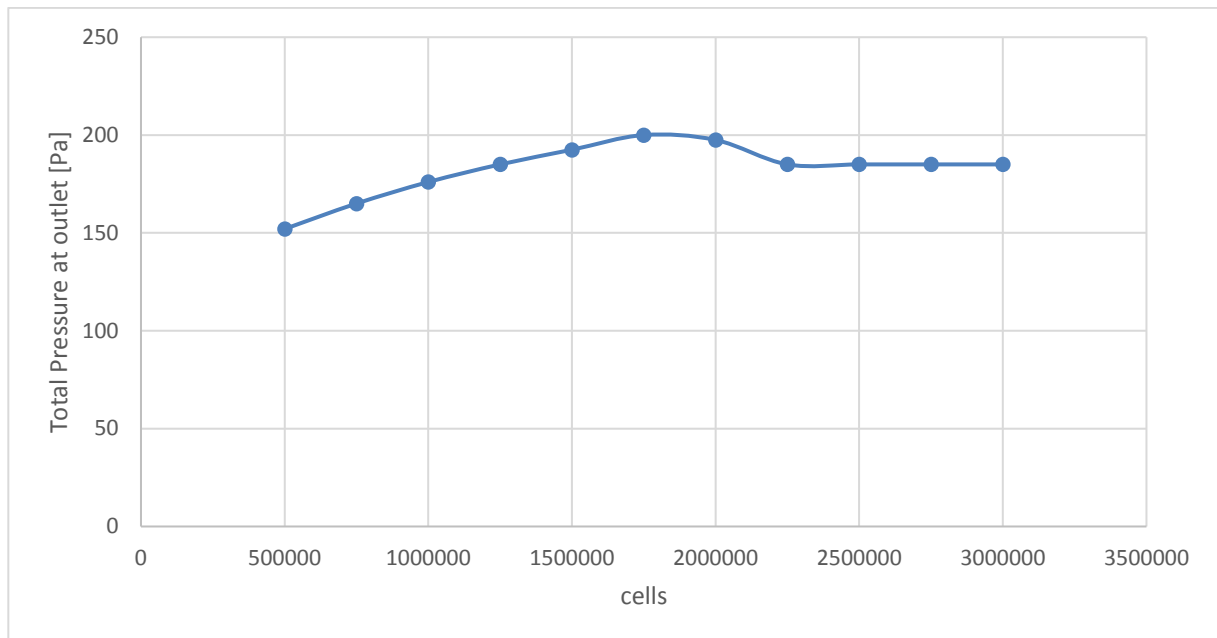


Figure C.19: Full scale Inlet - Total pressure at outlet: when refining the mesh (increasing number of cell on horizontal axis) the parameters under investigation start to stabilize during the run, this is the moment when mesh independence for that parameter is achieved



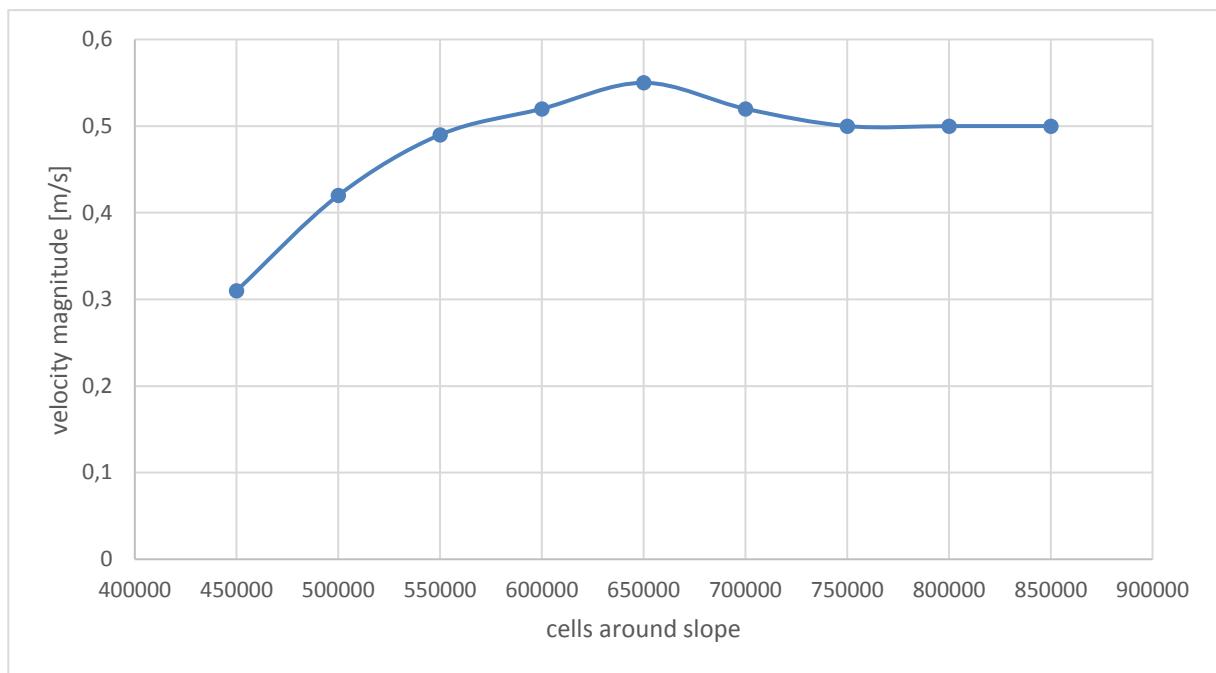


Figure C.20: Full scale Inlet - Velocity Magnitude at inlet orifice: when refining the mesh (increasing number of cell on horizontal axis) the parameters under investigation start to stabilize during the run, this is the moment when mesh independence for that parameter is achieved

## Appendix D

# CFD Settings - Mesh and Physics

### D.1 Simulation Settings - Small Scale Model

System info	
CFD Software	CD-Adapco StarCCM v13
Computer Name	LVNMINI01
CPU	4x Intel Xeon W3565 @ 3,2 Ghz
Memory	192 Gb DDR3 ECC
OS	Windows Server 2016
CAD software	Siemens NX 8.5
Project Info	
CAD model	scaled_downbox.x_t
Project name	scaled_downbox.sim
Unit System	mKs
Coordinate System	Global coordinate system
Reference axis	X
Import surface options	
import mode	create new part
parasolid transmit options	no cad edges
	merge parts by name
	create part contact from coincident faces
coincidence tolerance	1.0E-5
tessellation density	medium
Mesh Global settings	
Mesh Models	Extruder
	Prism Layer Mesher
	Polyhedral Mesher
	Surface Remesher
Reference Values	
Base size	5mm
Number of prism layers	3

prism layer stretching	1.5
prism layer thickness	33.3 % relative to base
surface size - relative min	10mm
Local mesh settings - Box around inclined face	
custom surface size min	5 % relative to base
custom surface size max	100 % relative to base
nr of prism layer	5
prism layer stretching	1.5
prism layer thickness	25 % relative to base
Boundary Conditions Inlet	
type	mass flow inlet
inlet coordinate system	global coordinate system
inlet reference axis	X
inlet flow parameters	flow vector normal to face
flowrate	225 l/s
Boundary Conditions outlet	
type	pressure outlet
inlet coordinate system	global coordinate system
inlet reference axis	X
inlet flow parameters	flow vector normal to face
thermodynamic parameters	101300 Pa 20C (Atmosphere)
General physics models and settings	
Gravity	ON
Turbulence	k-eps
Gas	constant density
Fluid Film	
cst density	1000 kg/m3
flow model	laminar
Gravity [m/s2]	
X component	0
Y component	-9.81
Z component	0
Initial conditions	
Static pressure	0 Pa
Temperature	20C
Velocity X	0
Velocity Y	0
Velocity Z	0
Multiphase Materials	
Air specific heat (Cp/Cv)	1.399
Air molecular mass	0.0290 kg/mol

Injected water drops	
cst Density	1000 kg/m3
Drag force	Schiller-Naumann
Spherical particles	
One-Way Coupling	
Multiphase interaction Film-Lag	Bai-gosman impingement
Multiphase interaction Film-Continuum	Surface tension 1E-5m
Convergence Settings average Static Pressure	
type	surface goal
calculate	average value
faces	outlet
iterations	10 iterations
delta	5 Pa
logic function	AND
Convergence Settings average Massflowrate	
type	surface goal
calculate	average value
faces	inlet
iterations	10 iterations
delta	0.01 kg/s

## D.2 Simulation Settings - Full Scale Model

System info	
CFD Software	CD-Adapco StarCCM v13
Computer Name	LVNMINI01
CPU	4x Intel Xeon W3565 @ 3,2 Ghz
Memory	192 Gb DDR3 ECC
OS	Windows Server 2016
CAD software	Siemens NX 8.5
Project Info	
CAD model	scaled_downbox.x_t
Project name	scaled_downbox.sim
Unit System	mKs
Coordinate System	Global coordinate system
Reference axis	X
Import surface options	
import mode	create new part
parasolid transmit options	no cad edges
	merge parts by name
	create part contact from coincident faces

coincidence tolerance	1.0E-5
tessellation density	medium
Mesh Global settings	
Mesh Models	Extruder
	Prism Layer Mesher
	Trimmer Mesher
	Surface Remesher
Reference Values	
Base size	17.5 mm
Number of prism layers	3
prism layer stretching	1.5
prism layer thickness	33.3 % relative to base
surface size - relative min	
Local mesh settings - Area around louvres	
custom surface size min	3% relative to base
custom surface size max	20% relative to base
nr of prism layer	3
prism layer stretching	1.5
prism layer thickness	20% relative to base
Boundary Conditions Inlet	
type	mass flow inlet
inlet coordinate system	global coordinate system
inlet reference axis	X
inlet flow parameters	flow vector normal to face
flowrate	0.595 kg/s
Boundary Conditions outlet	
type	pressure outlet
inlet coordinate system	global coordinate system
inlet reference axis	X
inlet flow parameters	flow vector normal to face
thermodynamic parameters	101300 Pa 20C (atmosphere)
General physics models and settings	
Gravity	ON
Turbulence	k-eps
Gas	constant density
Fluid Film	
cst density	1000 kg/m3
flow model	laminar
Gravity [m/s2]	
X component	0
Y component	-9.81

Z component	0
Initial conditions	
Static pressure	Table
Temperature	20C
Velocity X	Table
Velocity Y	Table
Velocity Z	Table
Multiphase Materials	
Air specific heat (Cp/Cv)	1.399
Air molecular mass	0.0290 kg/mol
Injected water drops	
cst Density	1000 kg/m3
Drag force	Schiller-Naumann
Spherical particles	
One-Way Coupling	
Multiphase interaction Film-Lag	Bai-gosman impingement
Multiphase interaction Film-Continuum	Surface tension 1E-5m
Convergence Settings average Static Pressure	
type	surface goal
calculate	average value
faces	outlet
iterations	10 iterations
delta	5 Pa
logic function	AND
Convergence Settings average Massflowrate	
type	surface goal
calculate	average value
faces	inlet
iterations	10 iterations
delta	0.01 kg/s

# Appendix E

## CFD - Post processing Settings

This appendix explains step by step on how to setup a water drainage simulation in CD-adapco StarCCM, if certain terminology is unfamiliar you can use the StarCCM help files to retrieve these. Not all steps will be explained in full detail, it is assumed that the reader has an understanding of CFD software and how to setup basic simulations.

### E.1 MAIN FLOWFIELD

#### E.1.1 CAD preparation and boundary types

Upload the cad geometry into the CFD software, split faces into recognizable boundaries. Then assign parts to respective region

- drain surface
- drain pipe
- gutter
- inlet: pressure outlet
- outlet: mass flow inlet with negative flow -0,2665 kg/s (is roughly 5 m/s at orifice) not velocity inlet because that forces a uniform field at the boundary leading to an unstable convergence
- slope
- wall-inner
- wall-outer

#### E.1.2 Mesh preparation

Trimmer and surface remesher mesh methodologies are selected for the full scale inlet, base settings for these can be found in the simulation file (these were obtained after mesh independence described on other chapters of the thesis). The outlet is extruded in order to obtain a better and more stable far field scenario. The atmosphere inlet is meshed with a coarser mesh and that surface mesh is then grown finer towards the inlet orifice (In order to avoid the very large cells near the inlet, set

a Maximum cell size for the trimmer to be something around 200%). On the louvres and inlet orifice the mesh settings are refined on the boundaries itself and also a very fine prism layer mesh is created in order to track the fluid film properly. Derived section planes are then created to plot the mesh for inspection. Thresholds for certain mesh quality criteria such as skewness are used to further inspect mesh quality.

### **E.1.3 Coordinate systems**

1. Create Cartesian coordinate system parallel with the slope, x direction of slope downwards, y lateral on slope, z perpendicular to slope
2. Create Cartesian coordinate system that represent the experimental coordinate system: pay attention because in StarCCM only right hand coordinate systems are allowed, the experimental system was left hand. However only the X direction (fore-aft) is important for our research. Make sure this X points in the same direction as during the experiment. The origin is also moved to the 0,0,0 of the experiment.

## **E.2 Lagrangian Injector**

A Lagrangian phase is created to simulate water spray injection, in the physics section of the simulation file add Lagrangian phase and select following models:

- Liquid,
- Spherical
- Cst density
- Drag force ON to enable airstream to take the parcels along in the main flow
- 2 way coupling OFF
- Bai-gosman for impingement (optional)

Then create a solid cone injector, a grid injector and some line injectors under injectors. Assign the Lagrangian water phase to the respective type of injector under investigation. For the exact settings of each respective injector please investigate the sim file and adjust settings to match reality (for the values used in this thesis please refer to the chapter where the CFD models are explained). Adjust origin of cone injector to its correct location and also adjust its direction so its spray in direction of the orifice. Solve with track file enabled, and inspect track: particle residence time to see if solution is ok.

### **E.2.1 Optimize the Lagrangian solution time**

As described in section 6.4 further steps can be taken to optimize the solution time of a Lagrangian setup.

1. Reduce the update frequency



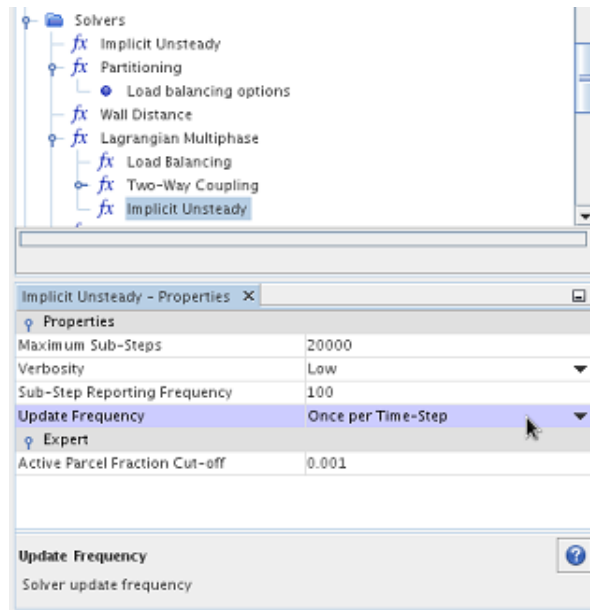


Figure E.1: Solver Settings: Lagrangian multiphase - Implicit Unsteady: Update frequency

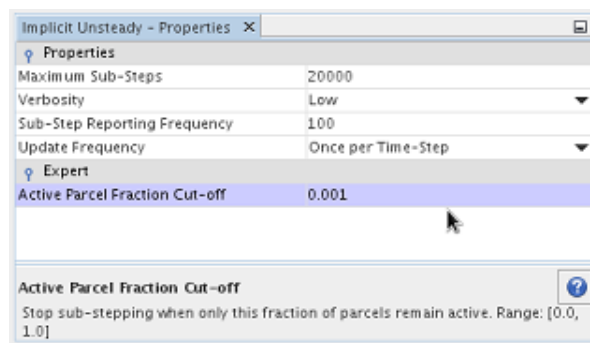


Figure E.2: Solver Settings: Lagrangian multiphase - Implicit Unsteady: Active parcel fraction cut-off

2. Use the Active parcel fraction cut-off
3. Re-partition the mesh based on Lagrangian loading
4. Reduce the number of parcels
5. Stop tracking Parcels when they leave the area of interest
6. Remove insignificant parcels from the domain using a field function

## E.3 Fluid Film Settings

### E.3.1 Fluid Film Physics

Start with creating a shell region on the slope (right click on boundary and create shell region). Under the physics section create a new physics continuum, call it 'transient physics' and select following models:

1. Implicit unsteady

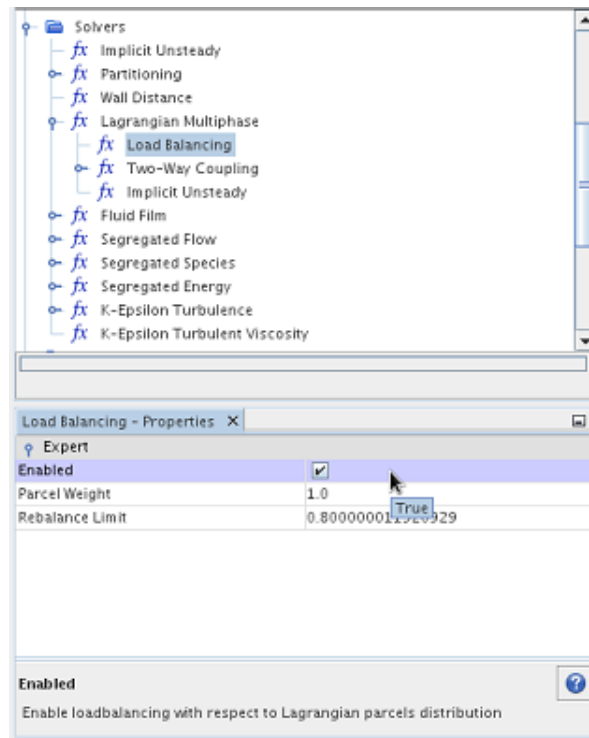


Figure E.3: Solver Settings: Lagrangian multiphase - Load Balancing

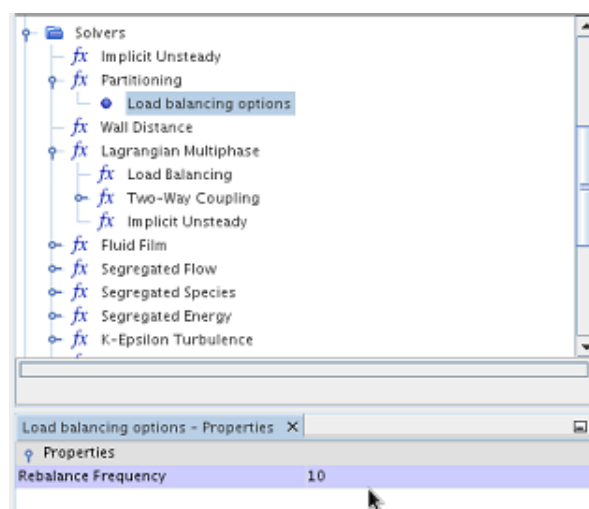


Figure E.4: Solver Settings: Partitioning - Load Balancing options - Rebalance frequency

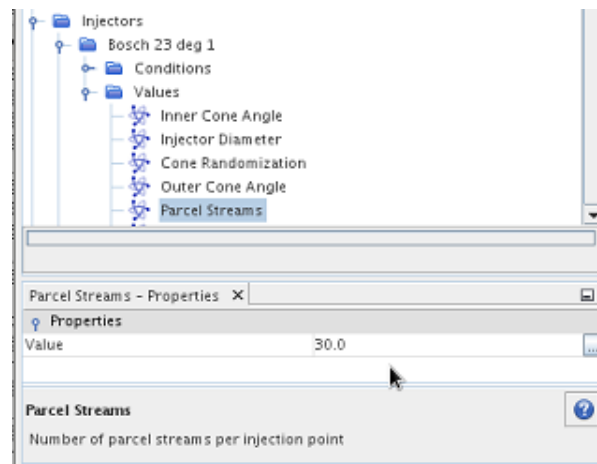


Figure E.5: Injector Settings: Values - Parcel streams

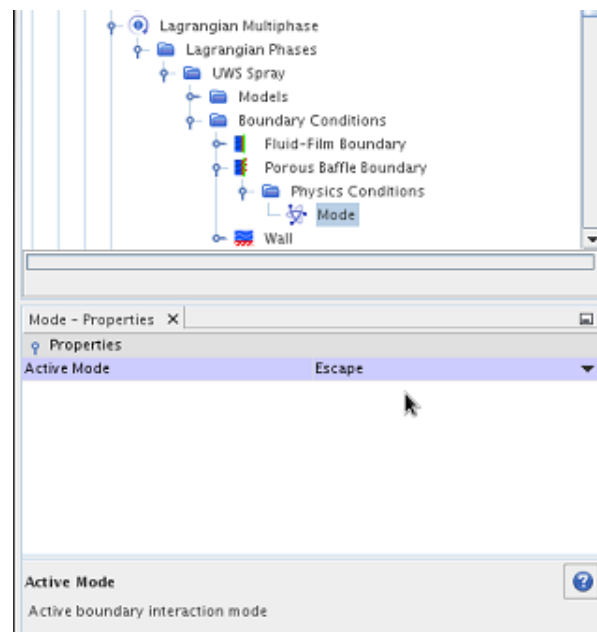


Figure E.6: Physics continua Settings: Lagrangian Multiphase - Boundary Conditions

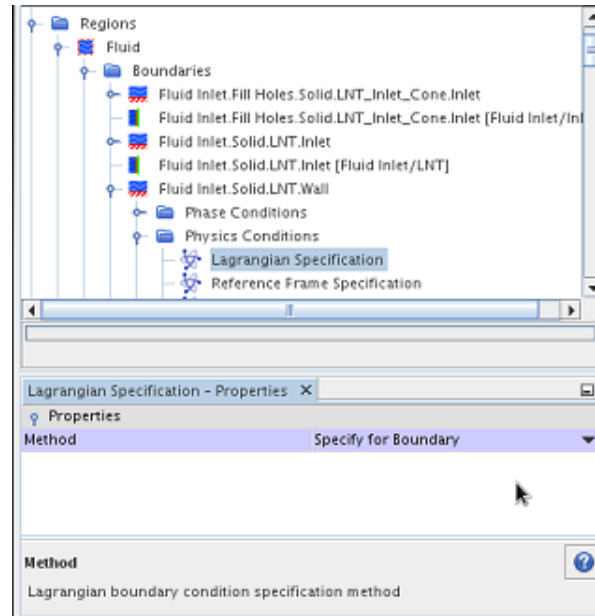


Figure E.7: Phase Boundary Settings: Lagrangian Specification

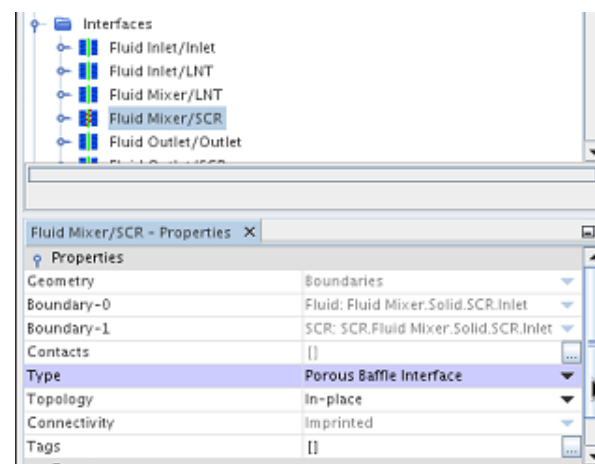


Figure E.8: Interface Settings: Porous baffle interface

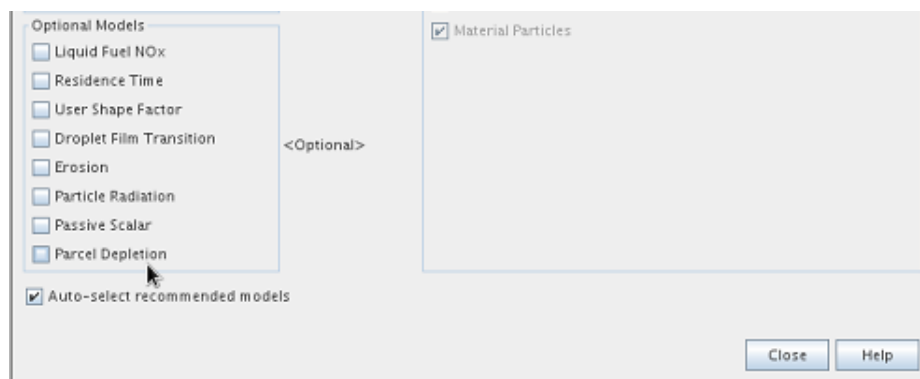


Figure E.9: Lagrangian physical model selection: Parcel depletion

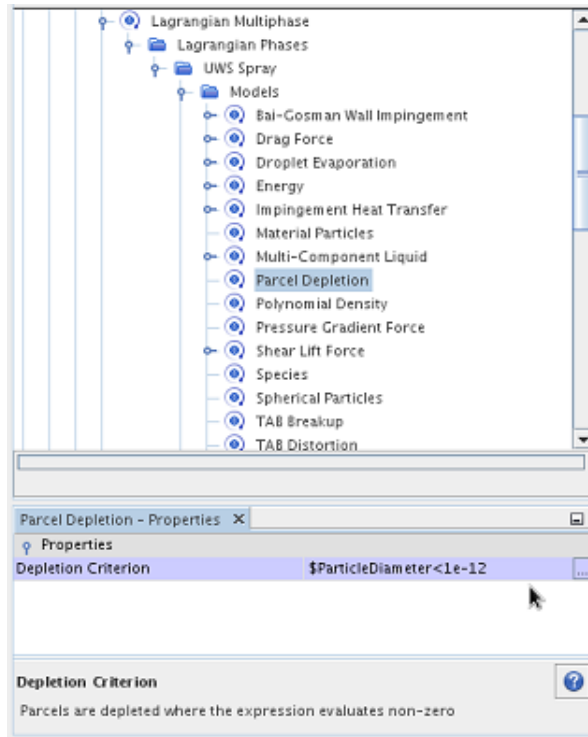


Figure E.10: Lagrangian physical model selection: Parcel depletion

2. Eulerian multiphase (optional, normally in v12 fluid film can also solve with contact angle)
3. Multiphase interaction
4. VOF (optional, normally in v12 fluid film can also solve with contact angle)
5. Multiphase equation of state
6. Fluid Film
7. Segregated Flow
8. K-eps realizable two layer all  $y^+$  wall treatment
9. Lagrangian multiphase
10. Gravity
11. Gas
12. Segregated Flow
13. Constant density

### E.3.2 Fluid Film Boundary Conditions

Under Boundary Conditions, select:

- Fluid film boundary mode: fluid film
- Wall Mode: rebound

### E.3.3 Fluid Film - Create phase

Right click fluid film model and create new phase, call it water film and select following models:

- Shell three dimensional
- Laminar
- Liquid
- Constant density

Check if liquid is water and initial conditions film thickness 0m (no thickness represents dry wall to start).

### E.3.4 Multiphase interaction

#### Film-Lagrangian

In physics models right click multiphase interaction and create new multiphase interaction subset, rename it film\_Lagrangian and select following multiphase interaction models:

- Impingement
- Film-Lagrangian phase interaction
- Lagrangian phase injected\_water\_drops
- Lagrangian phase water film

#### Film-Continuum

In physics models right click multiphase interaction and create new multiphase interaction subset, rename it film\_continuum and select following models and settings:

- surface tension activated and settings kept default
- minimum film thickness =  $1.0e-5\text{m}$
- alpha tuning = 1
- beta tuning = 1
- multiphase material surface tension = default  $0.072\text{ N/m}$
- need to define liquid phase (water film) as primary phase

Now that the phases are created and the phase interaction models received the correct settings, make sure to assign them to the correct boundary conditions and region. In the shell region set Continuum = water film and type = fluid region then set gutter edges to flow split outlet.

## E.4 Solver Settings

Implicit unsteady

Timestep 0.0005 s

2nd order

Lagrangian multiphase

Implicit unsteady verbosity: none

## E.5 Stopping criteria

Maximum inner iterations

Enabled

10

OR

Maximum physical time

Enabled

5s

OR

Max Steps

DISABLED

## E.6 Post processing

Create derived part isosurface

Scalar- volume fraction of water

No displayer

Create Scalar Scene (only for VOF) rename to isosurface water

Parts isosurface

Scalar field convective courant number max value at 0.5 auto range off

Attributes: update save to file with name scalar\_isosurface\_water trigger timestep

Create Scalar Scene (only for liquid Film) Convective Courant Film

Parts interface air region

Scalar field convective courant number

Attributes: update save to file with name scalar\_isosurface\_water trigger timestep

Create scalar Scene rename to fluid film thickness

Parts all shell region

Scalar field: fluid film thickness auto range min value clip off max 1e-5m

Attributes: update save to file with name scalar\_fluidfilm\_thickness trigger timestep

Create Scalar Scene rename to velocity film

Parts shell interface

Scalar field velocity magnitude

Attributes: update save to file with name scalar\_velocity\_water trigger timestep

Water drainage report massflow film outlet at moment

Create section plane at shell out outlet (need to be created only on shell region boundaries not needed, only fluid film mass flow is needed, not air mass flow)

Mass flow report on that outlet

Water drainage report massflow film outlet total over time

Use previous mass flow report

Expression report defined as  $\{\text{TimeStep}\} * \{\text{MassFlow1Report}\}$

Create sum monitor using the section plane as part and the sum monitor as field function

Create a maximum report using as part again the plane section and the sum monitor field as field function

Probes

Under Derived Parts, you can create a new probe line on the slope (and referred only to the Shell Region) and evaluate the velocity vectors on those points. By creating multiple probe lines, you would be able to map the velocity over the slope.

Create probe in geometry scene, snapping to slope is not possible due to curved surface, best to drag the slope star and endpoint to the area right above the slope, like that the probes will be able to pick up the properties of the water film sliding down the plate.

Orientation views

Views: +X -Y +Z up +Z

### E.6.1 Isosurface settings

Situations occur where a thin film of liquid forms on a solid surface, for example our air intake louvres system that has rainwater ingress into it. This film can flow and accumulate, and gradually grow into a "thick" film, or a pool of liquid that can no longer be described as a fluid film. These situations are multi-scale problems which, if resolved on all scales (using the VOF multiphase model), would require significant computer resources. Simcenter STAR-CCM+ offers a modelling approach to solve these types of problems in an efficient way. You can combine the VOF model and the thin fluid film model, such that the VOF model is used in areas where the mesh is sufficiently fine to resolve the flow of liquid, and the fluid film model is used in areas where the mesh size is larger than the film thickness, or as in our method described, we use the fluid film for the areas with low film height and transfer to VOF when it increases in height (relative to the mesh size), for example when drops of water that are impacting on the louvres start to accumulate and form a rivulet that is flowing down the louvre. Figure E.11 is showing a general representation of this behaviour.

1. Create an isosurface with a volume fraction value of 0.5 that represents the VOF resolved water film surface



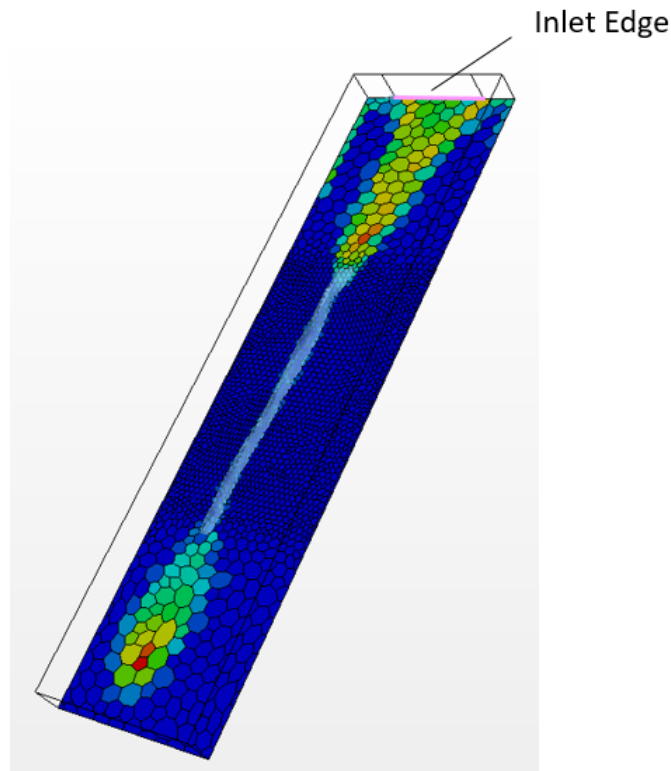


Figure E.11: The mesh resolution is not uniform. The upper and lower regions of the inclined plane use a coarse mesh, but the central region uses a finer mesh. In this case, the mesh in the central region is sufficiently fine to resolve the flow of liquid, so the VOF model is used. The fluid film model is used in the upper and lower regions

- Right-click the Derived Parts node and select New Part - Isosurface. The Create Isosurface dialog appears in the Edit window.
  - In the Input Parts box, select Body1.
  - Set the Scalar function to Volume Fraction - Volume Fraction of Water.
  - Set the Extraction Mode to Single Value.
  - Set the Isovalue to 0.5.
  - In the Display group box, select No Displayer.
  - Click Create and then click Close, A new derived part, Isosurface, is created.
2. Right-click the Scenes node, and select New Scene - Scalar.
  3. Select the Scalar Scene 1 node and then set Mesh Override to Show All Meshes.
  4. Manipulate the scene to make the view orientation suitable to see both fluid film and the resolved VOF
  5. Rename the scalar scene as Combined Fluid film - resolved water VOF Scene
  6. Select this scene its displayers node and set the following properties:
    - VOF displayer
      - Outline 1 Opacity = 0.6

- colour Mode = Constant
- Mesh colour = Sky Blue
- Parts = Derived Parts - Isosurface
- Fluid film displayer
  - Scalar 1 Contour Style = Filled
  - Parts = Regions - PartiallyWetSurface shell - Boundaries - Interface to Body 1 [In-place 1]
  - Scalar Field Function = Fluid Film Thickness
  - colour Bar Orientation = Vertical
  - colour Bar Position = [0.05, 0.1]

## 7. Save the simulation

## Appendix F

### CFD - Results

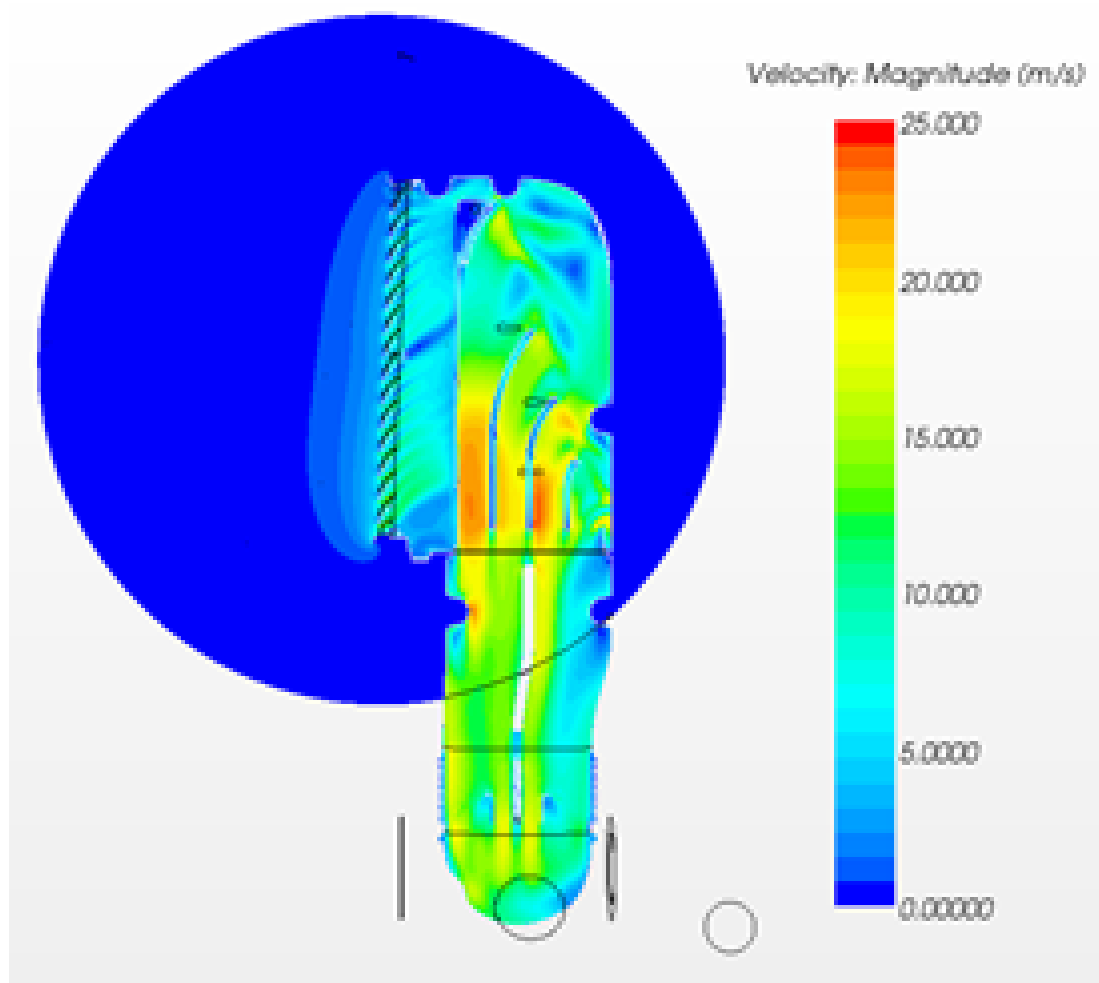


Figure F.1: Velocity Magnitude plot in the dirty air plenum of the air intake system (AIS)

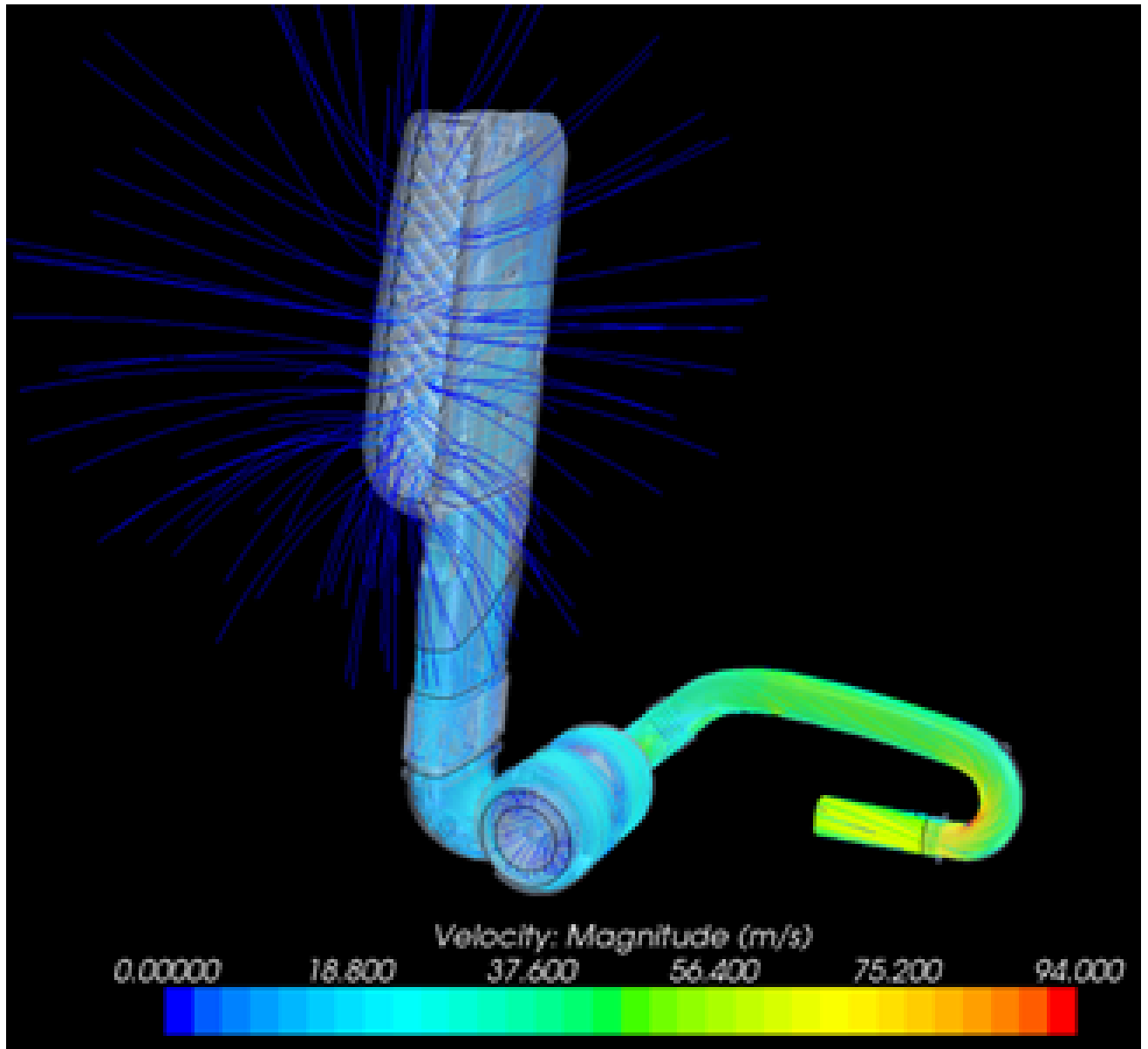


Figure F.2: Velocity Magnitude plotted on streamlines running through the full air intake system, starting from atmosphere until engine intake plenum

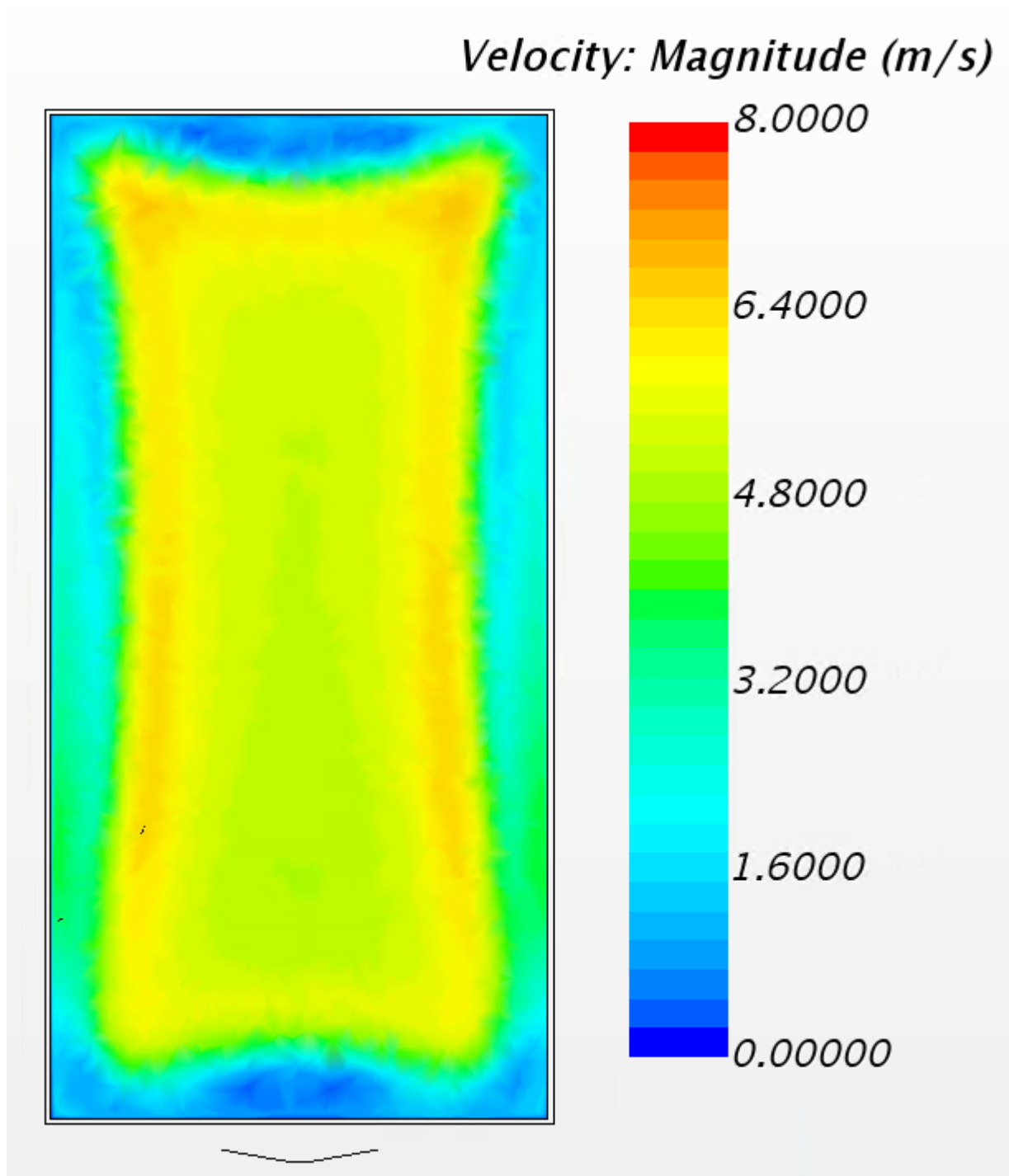


Figure F.3: Velocity Magnitude for the small scale inlet box, plotted on a plane perpendicular to the inlet orifice

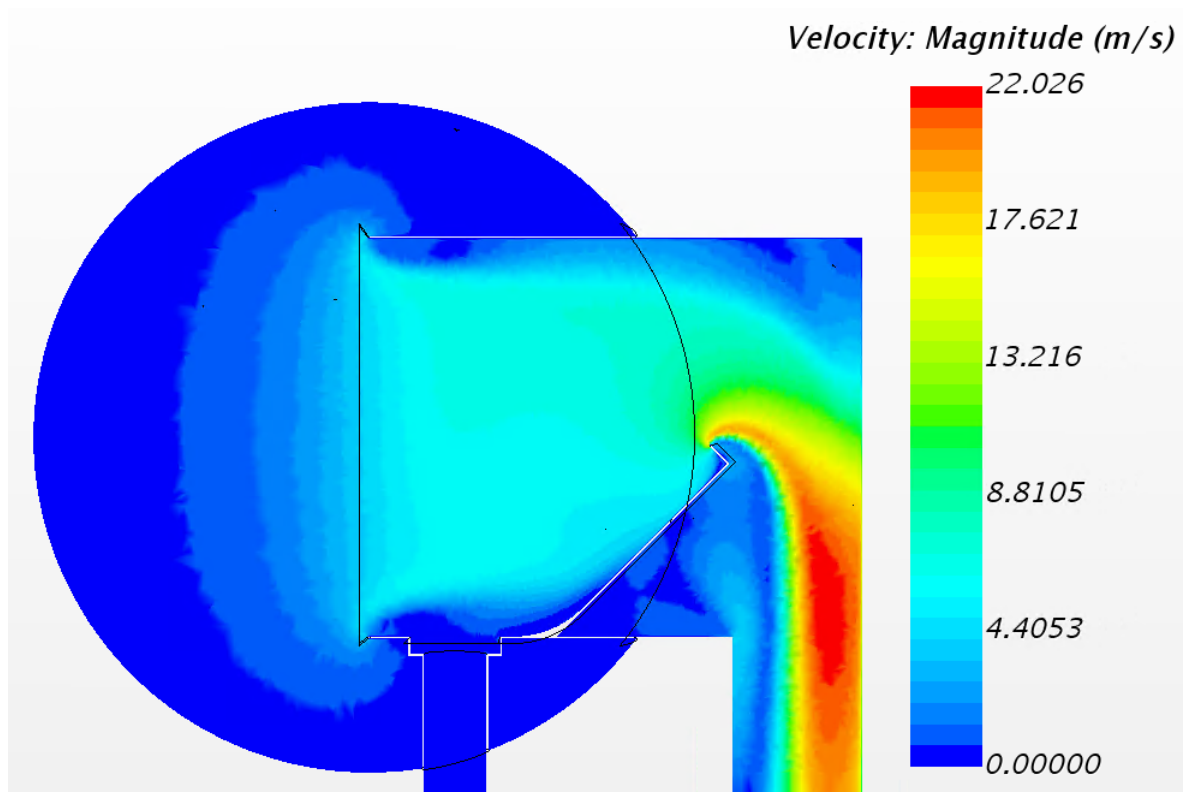


Figure F.4: Velocity Magnitude for the small scale inlet box, plotted on a half section plane between the 2 side walls

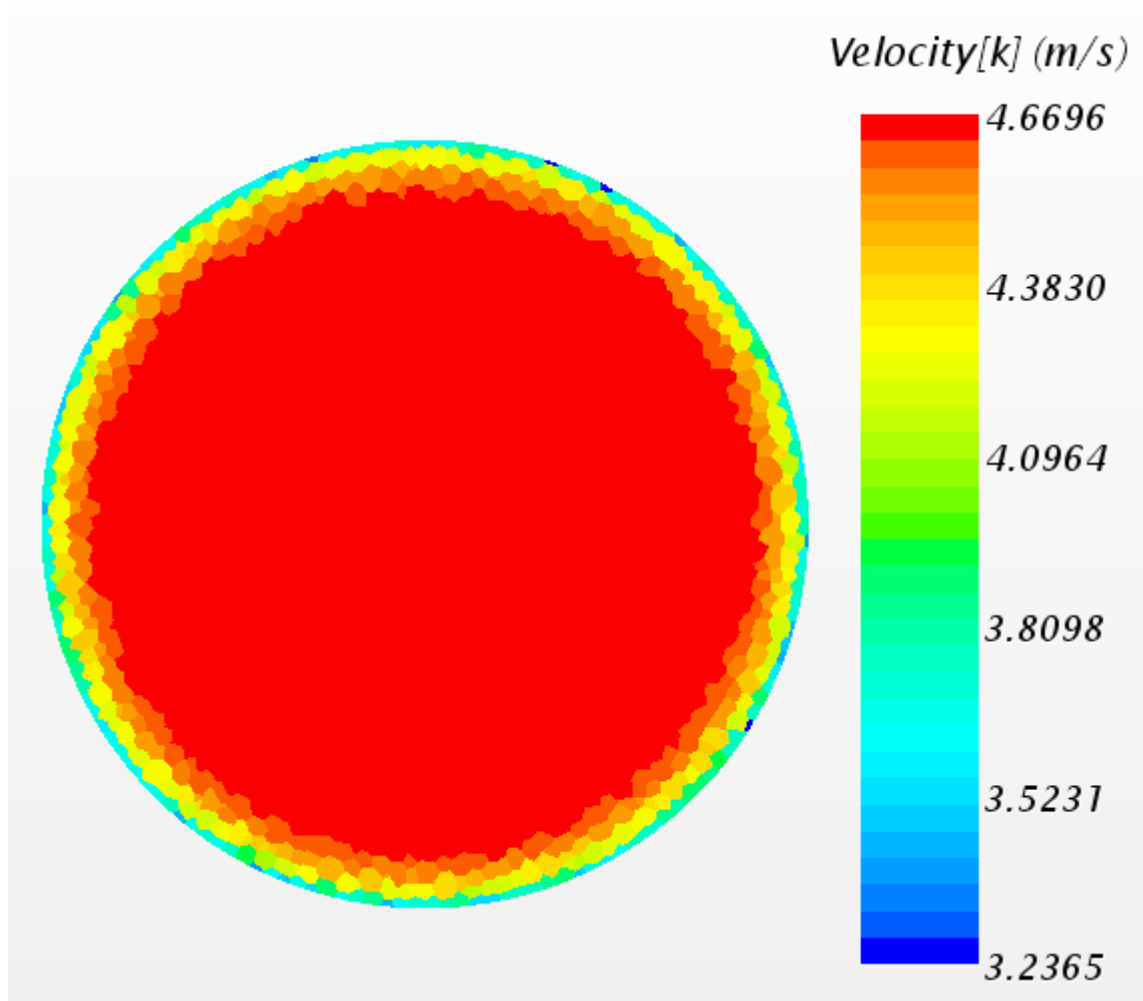


Figure F.5: Velocity Magnitude plot for the small scale inlet box, plotted at a plane perpendicular to the outlet



# Appendix G

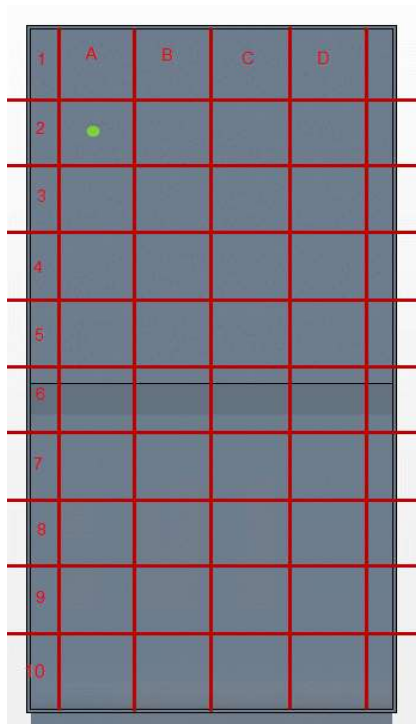
## Measured Results

Table G.1: Environmental conditions during PEPT measurements

temp	293	K
altitude	31	m
wind spd	0	m/s
RH	17	%
air dens	1,17845	kg/m3
date	23/05/2015	

### G.1 Measured Velocity - Small Scale Box: Inlet

Velocity measurements were done across the inlet orifice of the scaled down model, velocity is measured with anemometer at the centre of each section (e.g.. green dot for A-2), airflow is then calculated based on cross area of each individual sections, size of the full inlet orifice: 150 x 300 mm.



m/s	A	B	C	D
1	4.8	1.5	1.6	5
2	6.2	5.1	5	6.3
3	5.9	5.1	4.9	5.8
4	5.8	4.8	4.9	5.8
5	5.6	5.1	5.1	5.6
6	6	5.2	4.9	5.7
7	5.8	4.9	5	6.4
8	6.3	5.1	5.2	6.8
9	5.6	4.9	5	5.8
10	3.2	2.4	2.3	3.3

Table G.2: Measured velocities for each section of the image to the left: the small scale box inlet is divided into multiple sections, and the anemometer is used to measure the velocity in each of these

<b>Point 1-A</b>			<b>Point 1-B</b>			<b>Point 1-C</b>			<b>Point 1-D</b>		
vel	4.8	m/s	vel	1.5	m/s	vel	1.6	m/s	vel	5	m/s
area	957.4	$mm^2$	area	957.4	$mm^2$	area	957.4	$mm^2$	area	957.4	$mm^2$
area	0.0010	$m^2$	area	0.0010	$m^2$	area	0.0010	$m^2$	area	0.0010	$m^2$
flow	0.2757	$\frac{m^3}{min}$	flow	0.0862	$\frac{m^3}{min}$	flow	0.0919	$\frac{m^3}{min}$	flow	0.2872	$\frac{m^3}{min}$
<b>Point 2-A</b>			<b>Point 2-B</b>			<b>Point 2-C</b>			<b>Point 2-D</b>		
vel	6.2	m/s	vel	5.1	m/s	vel	5	m/s	vel	6.3	m/s
area	957.4	$mm^2$	area	957.4	$mm^2$	area	957.4	$mm^2$	area	957.4	$mm^2$
area	0.0010	$m^2$	area	0.0010	$m^2$	area	0.0010	$m^2$	area	0.0010	$m^2$
flow	0.3562	$\frac{m^3}{min}$	flow	0.2930	$\frac{m^3}{min}$	flow	0.2872	$\frac{m^3}{min}$	flow	0.3619	$\frac{m^3}{min}$
<b>Point 3-A</b>			<b>Point 3-B</b>			<b>Point 3-C</b>			<b>Point 3-D</b>		
vel	5.9	m/s	vel	5.1	m/s	vel	4.9	m/s	vel	5.8	m/s
area	957.4	$mm^2$	area	957.4	$mm^2$	area	957.4	$mm^2$	area	957.4	$mm^2$
area	0.0010	$m^2$	area	0.0010	$m^2$	area	0.0010	$m^2$	area	0.0010	$m^2$
flow	0.3389	$\frac{m^3}{min}$	flow	0.2930	$\frac{m^3}{min}$	flow	0.2815	$\frac{m^3}{min}$	flow	0.3332	$\frac{m^3}{min}$
<b>Point 4-A</b>			<b>Point 4-B</b>			<b>Point 4-C</b>			<b>Point 4-D</b>		
vel	5.8	m/s	vel	4.8	m/s	vel	4.9	m/s	vel	5.6	m/s
area	957.4	$mm^2$	area	957.4	$mm^2$	area	957.4	$mm^2$	area	957.4	$mm^2$
area	0.0010	$m^2$	area	0.0010	$m^2$	area	0.0010	$m^2$	area	0.0010	$m^2$
flow	0.3332	$\frac{m^3}{min}$	flow	0.2757	$\frac{m^3}{min}$	flow	0.2815	$\frac{m^3}{min}$	flow	0.3217	$\frac{m^3}{min}$
<b>Point 5-A</b>			<b>Point 5-B</b>			<b>Point 5-C</b>			<b>Point 5-D</b>		
vel	5.6	m/s	vel	5.1	m/s	vel	5.1	m/s	vel	5.6	m/s
area	957.4	$mm^2$	area	957.4	$mm^2$	area	957.4	$mm^2$	area	957.4	$mm^2$
area	0.0010	$m^2$	area	0.0010	$m^2$	area	0.0010	$m^2$	area	0.0010	$m^2$
flow	0.3217	$\frac{m^3}{min}$	flow	0.2930	$\frac{m^3}{min}$	flow	0.2930	$\frac{m^3}{min}$	flow	0.3217	$\frac{m^3}{min}$
<b>Point 6-A</b>			<b>Point 6-B</b>			<b>Point 6-C</b>			<b>Point 6-D</b>		
vel	6	m/s	vel	5.2	m/s	vel	4.9	m/s	vel	5.7	m/s
area	957.4	$mm^2$	area	957.4	$mm^2$	area	957.4	$mm^2$	area	957.4	$mm^2$
area	0.0010	$m^2$	area	0.0010	$m^2$	area	0.0010	$m^2$	area	0.0010	$m^2$
flow	0.3447	$\frac{m^3}{min}$	flow	0.2987	$\frac{m^3}{min}$	flow	0.2815	$\frac{m^3}{min}$	flow	0.3274	$\frac{m^3}{min}$
<b>Point 7-A</b>			<b>Point 7-B</b>			<b>Point 7-C</b>			<b>Point 7-D</b>		
vel	5.8	m/s	vel	4.9	m/s	vel	5	m/s	vel	6.4	m/s
area	957.4	$mm^2$	area	957.4	$mm^2$	area	957.4	$mm^2$	area	957.4	$mm^2$
area	0.0010	$m^2$	area	0.0010	$m^2$	area	0.0010	$m^2$	area	0.0010	$m^2$
flow	0.3332	$\frac{m^3}{min}$	flow	0.2815	$\frac{m^3}{min}$	flow	0.2872	$\frac{m^3}{min}$	flow	0.3677	$\frac{m^3}{min}$

Point 8-A			Point 8-B			Point 8-C			Point 8-D		
vel	6.3	m/s	vel	5.1	m/s	vel	5.2	m/s	vel	6.8	m/s
area	957.4	$mm^2$	area	957.4	$mm^2$	area	957.4	$mm^2$	area	957.4	$mm^2$
area	0.0010	$m^2$	area	0.0010	$m^2$	area	0.0010	$m^2$	area	0.0010	$m^2$
flow	0.3619	$\frac{m^3}{min}$	flow	0.2930	$\frac{m^3}{min}$	flow	0.2987	$\frac{m^3}{min}$	flow	0.3906	$\frac{m^3}{min}$

Point 9-A			Point 9-B			Point 9-C			Point 9-D		
vel	5.6	m/s	vel	4.9	m/s	vel	5	m/s	vel	5.8	m/s
area	957.4	$mm^2$	area	957.4	$mm^2$	area	957.4	$mm^2$	area	957.4	$mm^2$
area	0.0010	$m^2$	area	0.0010	$m^2$	area	0.0010	$m^2$	area	0.0010	$m^2$
flow	0.3217	$\frac{m^3}{min}$	flow	0.2815	$\frac{m^3}{min}$	flow	0.2872	$\frac{m^3}{min}$	flow	0.3332	$\frac{m^3}{min}$

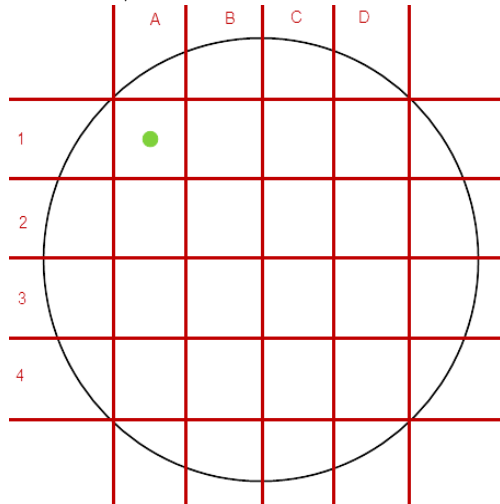
Point 10-A			Point 10-B			Point 10-C			Point 10-D		
vel	3.2	m/s	vel	2.4	m/s	vel	2.3	m/s	vel	3.3	m/s
area	957.4	$mm^2$	area	957.4	$mm^2$	area	957.4	$mm^2$	area	957.4	$mm^2$
area	0.0010	$m^2$	area	0.0010	$m^2$	area	0.0010	$m^2$	area	0.0010	$m^2$
flow	0.1838	$\frac{m^3}{min}$	flow	0.1379	$\frac{m^3}{min}$	flow	0.1321	$\frac{m^3}{min}$	flow	0.1896	$\frac{m^3}{min}$

The difference in flow-rate between the sum airflow and the fan airflow is explained by the sum not taking into account all the surfaces (like the small surfaces on the side of the grid illustration), only the measured areas.

avg vel	4.9875	m/s
sum airflow	11.461	$\frac{m^3}{min}$
fan set airflow	13.5	$\frac{m^3}{min}$

## G.2 Measured Velocity - Small Scale Box: Outlet

Velocity measurements were also done across the outlet of the scaled down model. velocity is measured with a pitot meter that is inserted into the outlet tube and measurements are done at the centre of each section (e.g. green dot for A-1) The airflow is then calculated based on cross area of individual sections. The size of the outlet duct is 250 mm and the imposed fanset airflow is set at 225 l/s, in the straight outlet duct we therefore expect velocities around 4,6 m/s.



m/s	A	B	C	D
1	4.6	4.7	4.7	4.6
2	4.6	4.8	4.8	4.7
3	4.7	4.8	4.8	4.7
4	4.7	4.8	4.8	4.7

Table G.4: Measured velocities for each section of the outlet section as illustrated in the left image: the outlet is divided into multiple sections, and the pitot is used to measure the velocity in each of these

<b>Point 1-A</b>			<b>Point 1-B</b>			<b>Point 1-C</b>			<b>Point 1-D</b>		
vel	4.6	m/s	vel	4.7	m/s	vel	4.7	m/s	vel	4.6	m/s
area	1600	$mm^2$	area	1600	$mm^2$	area	1600	$mm^2$	area	1600	$mm^2$
area	0.0016	$m^2$	area	0.0016	$m^2$	area	0.0016	$m^2$	area	0.0016	$m^2$
flow	0.4416	$\frac{m^3}{min}$	flow	0.4512	$\frac{m^3}{min}$	flow	0.4512	$\frac{m^3}{min}$	flow	0.4416	$\frac{m^3}{min}$

<b>Point 2-A</b>			<b>Point 2-B</b>			<b>Point 2-C</b>			<b>Point 2-D</b>		
vel	4.6	m/s	vel	4.8	m/s	vel	4.8	m/s	vel	4.7	m/s
area	1600	$mm^2$	area	1600	$mm^2$	area	1600	$mm^2$	area	1600	$mm^2$
area	0.0016	$m^2$	area	0.0016	$m^2$	area	0.0016	$m^2$	area	0.0016	$m^2$
flow	0.4416	$\frac{m^3}{min}$	flow	0.4608	$\frac{m^3}{min}$	flow	0.4608	$\frac{m^3}{min}$	flow	0.4512	$\frac{m^3}{min}$

<b>Point 3-A</b>			<b>Point 3-B</b>			<b>Point 3-C</b>			<b>Point 3-D</b>		
vel	4.7	m/s	vel	4.8	m/s	vel	4.8	m/s	vel	4.7	m/s
area	1600	$mm^2$	area	1600	$mm^2$	area	1600	$mm^2$	area	1600	$mm^2$
area	0.0016	$m^2$	area	0.0016	$m^2$	area	0.0016	$m^2$	area	0.0016	$m^2$
flow	0.451	$\frac{m^3}{min}$	flow	0.4608	$\frac{m^3}{min}$	flow	0.4608	$\frac{m^3}{min}$	flow	0.4512	$\frac{m^3}{min}$

<b>Point 4-A</b>			<b>Point 4-B</b>			<b>Point 4-C</b>			<b>Point 4-D</b>		
vel	4.7	m/s	vel	4.8	m/s	vel	4.8	m/s	vel	4.7	m/s
area	1600	$mm^2$	area	1600	$mm^2$	area	1600	$mm^2$	area	1600	$mm^2$
area	0.0016	$m^2$	area	0.0016	$m^2$	area	0.0016	$m^2$	area	0.0016	$m^2$
flow	0.4512	$\frac{m^3}{min}$	flow	0.460	$\frac{m^3}{min}$	flow	0.4608	$\frac{m^3}{min}$	flow	0.4512	$\frac{m^3}{min}$

The difference in flow-rate between the sum airflow and the fan airflow is explained by the sum not taking into account all the surfaces (like the small surfaces on the side of the grid illustration), only the measured areas.

avg vel	4.71875	m/s
sum airflow	7.248	$\frac{m^3}{min}$
fan set airflow	13.5	$\frac{m^3}{min}$

# Bibliography

- [1] L.E. Patruno, P.A. Marchioro Ystad, C.B. Jenssen, J.M. Marchetti, C.A. Dorao, H.F. Svendsen, H.A. Jakobsen, “Droplet size distribution for a low surface tension mixture”, *Chemical Engineering Science* **65** 5272-5284
- [2] Uplinger, William G., *Conference on Radar Meteorology of the American Meteorological Society* **20** 389-391 (1981)
- [3] American Society of Agricultural and Biological Engineers [ASABE], “Spray Nozzle Classification by Droplet Spectra”, *ANSI/ASAE S572.1 W/Corr 1 MAR2009* (2013)
- [4] Bormashenko, E., *Wetting of Real Surfaces* 2013
- [5] D.I. Wilson, B.L. Le, H.D.a. Dao, K.Y. Lai, K.R. Morison, J.F. Davidson, “Surface flow and drainage films created by horizontal impinging liquid jets”, *Chem. Eng. Sci.* **68** 449-460 (2012)
- [6] T. Wang, D. Faria, L.J. Stevens, J.S.C. Tan, J.F. Davidson, D.I. Wilson, “Flow patterns and draining films created by horizontal and inclined coherent water jets impinging on vertical walls”, *Chem. Eng. Sci.* **102** 585-601 2013
- [7] Bert Blocken, Jan Carmeliet, “On the accuracy of wind-driven rain measurements on buildings”, *Building and Environment Volume 41* **12** 1798-1810 (2006)
- [8] Lagubeau, et al., “Spreading dynamics of drop impacts”, *Journal of Fluid Mechanics* **713** 50-60
- [9] Durickovic, Varland, “Between bounding and splashing: water drops on a solid surface”, (2005)
- [10] Villiermaux, Bossa, “Drop fragmentation on impact”, *Journal of Fluid Mechanics* **668** 412-435 (2011)
- [11] Randy L. Vander Wal, Gordon M. Berger, Steven D. Mozes, “The splash/non-splash boundary upon a dry surface and thin fluid film”, *Experiments in Fluids* **40** **1** 5359 (2006)
- [12] Moaath N.Oqielat, Ian W.Turner, John A.Belward, Scott W.McCue, “Modelling water droplet movement on a leaf surface”, *Mathematics and Computers in Simulation* **81** **8** 1553-1571 (2011)
- [13] Ross Gunn and Gilbert D. Kinzer, “The terminal velocity of fall for water droplets in stagnant air”, *Journal of Meteorology* (1949)
- [14] Yuehua Yuan, T. Randall Lee, “Contact Angle and Wetting Properties”, *Surface Science Techniques* 3-34 (2013)

- [15] J. Baeyens, D. Geldart, S.Y. Wu, “Elutriation of fines from gas fluidized beds of Geldart A-type powders effect of adding superfines” *Powder Technology Volume 71* **1** 71-80 (1992)
- [16] Bakalis, S., Cox, P. W., Russell, A. B., Parker, D. J., Fryer, P. J., “Development and use of positron emitting particle tracking (PEPT) for velocity measurements in viscous fluids in pilot scale equipment”, *Chemical Engineering Science* **61** 1864-1877 (2006)
- [17] Barigou, M., “Particle tracking in opaque mixing systems: An overview of the capabilities of PET and PEPT”, *Chemical Engineering Research and Design* **82** 1258-1267 (2004)
- [18] Bridgwater, J., Parker, D. J., “Granular flow over a flat bladed stirrer”, *Chemical Engineering Science* **56** 4257-4271 2001
- [19] Burnard, D., Gargiuli, J., Leadbeater, T., Parker, D. J., Griffiths, W. D., “The application of positron emission particle tracking (PEPT) to study inclusions in the casting process”, *Materials Science Forum* **690** 25-28 2011
- [20] Fan, X., Parker, D. J., Smith, M. D., “Labelling a single particle for positron emission particle tracking using direct activation and ion exchange techniques”, *Nuclear Instruments and Methods in Physics Research Section A* **562** 345-350 2006
- [21] Fan, X., Parker, D. J., Smith, M. D., “Enhancing  $^{18}\text{F}$  uptake in a single particle for positron emission particle tracking through modification of solid surface chemistry”, *Nuclear Instrument and Methods in Physics Research Section A* **558** 542-546 2006
- [22] Guida, A. Nienow, A. W., Barigou, M., “Lagrangian tools for the analysis of mixing in single-phase and multiphase flow systems”, *Aiche Journal* **58** 31-45 (2011)
- [23] Guida, A., Fan, X., Parker, D. J., Nienow, A. W., Barigou, M., “Positron emission particle tracking in a mechanically agitated solidliquid suspension of coarse particles” *Chemical Engineering Research and Design* **87** 421-429 (2009)
- [24] Parker, D. J., Fan, X., “Positron emission particle tracking: Application and labelling techniques”, *Particuology* **6** 16-23 (2008)
- [25] Seville, J. P. K., Ingram, A., Parker, D. J., “Probing processes using positrons”, *Chemical Engineering Research and Design* **83** 788-793 (2005)
- [26] Stein, M., Ding, Y. L., Seville, J. P. K., Parker, D. J., “Solids motion in bubbling gas fluidised beds”, *Chemical Engineering Science* **55** 5291-5300
- [27] D.I. Wilson, B.L. Le, H.D.a. Dao, K.Y. Lai, K.R. Morison, J.F. Davidson, “Surface flow and drainage films created by horizontal impinging liquid jets”, *Chem. Eng. Sci.* **68** 449-460 (2012)
- [28] T. Wang, D. Faria, L.J. Stevens, J.S.C. Tan, J.F. Davidson, D.I. Wilson, “Flow patterns and draining films created by horizontal and inclined coherent water jets impinging on vertical walls”, *Chem. Eng. Sci.* **102** 585-601 (2013)
- [29] S. Bakalis, P.J. Fryer, D.J. Parker, “Measuring velocity distributions of viscous fluids using positron emission particle tracking (PEPT)”, *AIChE J.* **50** 1606-1613 (2004)

- [30] M. Eesa, M. Barigou, “Horizontal laminar flow of coarse nearly-neutrally buoyant particles in non-Newtonian conveying fluids: CFD and PEPT experiments compared”, *Int. J. Multiph. Flow* **34** 997-1007 (2008)
- [31] L. Liu, M. Barigou, “Numerical modelling of velocity field and phase distribution in dense monodisperse solidliquid suspensions under different regimes of agitation: CFD and PEPT experiments”, *Chem. Eng. Sci.* **101** 837-850 (2013)
- [32] P. Pianko-Oprych, a.W. Nienow, M. Barigou, “Positron emission particle tracking (PEPT) compared to particle image velocimetry (PIV) for studying the flow generated by a pitched-blade turbine in single phase and multi-phase systems”, *Chem. Eng. Sci.* **64** 4955-4968 (2009)
- [33] D.J. Parker, X. Fan, “Positron emission particle tracking application and labelling techniques”, *Particuology* **6** 16-23 (2008)
- [34] J.A. Schetz, A.E. Fuhs (Eds.), “Handbook of Fluid Dynamics and Fluid Machinery: Fundamentals of Fluid Dynamics”, John Wiley Sons Inc, (1996)
- [35] F. Chiti, S. Bakalis, W. Bujalski, M. Barigou, A. Eaglesham, A.W. Nienow, “Using positron emission particle tracking (PEPT) to study the turbulent flow in a baffled vessel agitated by a Rushton turbine: improving data treatment and validation”, *Chem. Eng. Res. Des.* **89** 1947-1960 (2011)
- [36] D.J. Parker, C.J. Broadbent, P. Fowles, M.R. Hawkesworth, P. McNeil, “Positron emission particle tracking a technique for studying flow within engineering equipment”, *Nucl. Instrum. Methods Phys. Res. Sect. A* **326** 592-607 (1993)
- [37] L.E. Patruno, P.A. Marchioro Ystad, C.B. Jenssen, J.M. Marchetti, C.A. Dorao, H.F. Svendsen, H.A. Jakobsen, “Liquid entrainment Droplet size distribution for a low surface tension mixture”, *Chemical Engineering Science* **65** 5272-5284 (2010)
- [38] Mahmoudi, S, Baeyens J., Seville, “The solids flow in the CFB-riser quantified by single radioactive particle tracking”, *Powder Technology Volume 211* **1** 135-143 (2011)
- [39] Chian W. Chan, Jonathan P.K. Seville, David J. Parker, Jan Baeyens, “Particle velocities and their residence time distribution in the riser of a CFB”, *Powder Technology* **203** **2** 187-197 (2010)
- [40] Chian W. Chan, Jonathan Seville, Xianfeng Fan, Jan Baeyens, “Particle motion in L-valve as observed by positron emission particle tracking”, *Powder Technology* **193** **2** 137-149 (2009)
- [41] Chan CW, Seville JPK, fan X, Baeyens J, “Particle motion in CFB cyclones as observed by positron emission particle tracking”, *Industrial and engineering chemistry research* **48** 253-261 (2009)
- [42] K Yokoi, D Vadiello, J, Hinch, and I Hutchings, “Numerical studies of the influence of the dynamic contact angle on a droplet impacting on a dry surface”, *Phys. Fluids* **21** (2009)
- [43] Versteeg and Malalasekera, *An Introduction to Computational Fluid Dynamics - The Finite Volume Method*



- [44] M.A. Ceviz , M. Akn, “Design of a new SI engine intake manifold with variable length plenum” 2010
- [45] Pedley, *Introduction to Fluid Dynamics*
- [46] Bungartz, Zimmer , Buchholz, Pfluger, *Modellbildung und Simulation Eine anwendungsorientierte Einfhruung*
- [47] Hauke G, *An Introduction to Fluid Mechanics and Transport Phenomena*
- [48] Rieutord, Michel, *Fluid Dynamics An Introduction*
- [49] Pozrikidis, *Fluid Dynamics Theory, Computation and Numerical Simulation, 2nd edition*
- [50] Kleinstreuer, *Modern Fluid Dynamics*
- [51] Donea, Huerta, Ponthot, Rodriguez-Ferran, *Arbitrary Lagrangian Eulerian Methods*
- [52] Zikanov, *Essential Computational Fluid Dynamics*
- [53] John F. Wendt, John David Anderson, Von Karman Institute for Fluid Dynamics, *Computational fluid dynamics: an introduction*
- [54] Kaplan S. Basniev, Nikolay M. Dmitriev, George V. Chilingar, Misha Gorfunkle, Amir G. Mohammed Nejad, *Mechanics of Fluid Flow*
- [55] Jiyuan Tu, Guan Heng Yeoh, Chaoqun Liu, *Computational Fluid Dynamics: A Practical Approach*
- [56] Meredith, K.V., Heather, A., de Vries, J. Xin, Y., “A numerical model for partially-wetted flow of thin liquid films”, *Computational Methods in Multiphase Flow* **6** 239-250 (2011)
- [57] Landau, L.D., Lifshitz, E.M., *Fluid Mechanics, Second Edition: Volume 6 (Course of Theoretical Physics)* (1984)
- [58] Brackbill, J. U., Kothe, D. B., and Zemach, C. 1992. “A Continuum method for modelling surface tension”, *J. Comp. Physics* **100** 335-354
- [59] Kistler, S. F. 1993, “Hydrodynamics of wetting”, *Surfactant Science Series* **49** 311-316 (1993)
- [60] Bai C., “modelling of spray impingement processes”, Ph.D Thesis University of London
- [61] Bai C., Gosman A.D., “Development of methodology for spray impingement simulation”, *SAE Technical Paper Series 950283*
- [62] Bai, C.X., Rusche, H., and Gosman, A.D. 2002, “modelling of gasoline spray impingement”, *Atomization and Sprays* **12** 1-27.
- [63] A. Marmur, “Thermodynamic aspects of contact angle hysteresis”, *Advances in Colloid and Interface Science* **50** 121-126 (2011)
- [64] I. Gao and T.J. McCarthy, “Contact angle hysteresis explained”, *Langmuir* **22** 6234-6237 (2006)

- [65] L. Feng, S. Li, Y. Li, H. Li, L. Zhang, J. Zhai, Y. Song, B. Liu, L. Jiang and D. Zhu, “Superhydrophobic surfaces: From natural to artificial”, *Advanced materials* **14** 1857 (2002)
- [66] R. Blossey, “Self-cleaning surfaces - virtual realities”, *Nature Materials* **2** 301 (2003)
- [67] Maroteaux, F., Llory, D., Le Coz, J-F., Habchi, C., “Liquid film atomization on wall edges separation criterion and droplets formation model”, *J. Fluids Engineering* **124** 565-575 (2002)
- [68] Gubaidullin, A., “Comments on Liquid film atomization on wall edges separation criterion and droplets formation model”, *J. Fluids Engineering* **129** 665-666 (2007)
- [69] Friedrich, M. A., Lan, H., Drallmeier, J. A., Armaly, B. F., “A separation criterion with experimental validation for shear-driven films in separated flows”, *ASME J. Fluids Engineering* (2007)
- [70] Arai, T., Hashimoto, H., “Disintegration of a thin liquid sheet in a concurrent gas stream”, *Proceedings of the Third International Conference on Liquid atomization and Spray Systems, London* (1985)
- [71] Foote, G.B. and DuToit, P.S., “Terminal velocity of raindrops aloft” *J. Appl. Meteor.* **8** 249-253 (1969)
- [72] Monjo, R., “Measure of rainfall time structure using the dimensionless n-index”, *Climate Research* **67** 71-86 (2016)